Mitotic spindle dynamics in stretched epithelial tissue *in vivo* and *in silico*

A thesis submitted to the University of Manchester for the degree of
Doctor of Philosophy
in the Faculty of Biology, Medicine and Health

2023

Dionn Hargreaves
School of Biological Sciences
Division of Cell Matrix Biology and Regenerative Medicine

Contents

Word Count: 46043

List of figures

List of tables

Terms and abbreviations

1D	One dimensional
2D	Two dimensional
APC/C	Anaphase promoting complex/cyclosome
BFP	Blue fluorescent protein
BRAF	Serine/threonine-protein kinase B-Raf
BSA	Bovine serum albumin
Ca^{2+}	Calcium
CDK	Cyclin-dependent kinase
DFA	Danilchik's for Amy explant culture media
DNA	Deoxyribonucleic acid
ERK	Extracellular-signal-regulated kinase
F-actin	Filamentous actin
GDP	Guanosine diphosphate
GFP	Green fluorescent protein
GPR1/2	G protein regulator 1/2
GTP	Guanosine triphosphate
HCG	Human chorionic gonadotrophin
IQR	Interquartile range
KD	Knockdown
kDa	Kilodalton
LGN	Leucin/glycine/asparagine-repeat-containing protein
MDCK	Madin-Darby canine kidney
MMR	Marc's modified Ringer's solution
MO	Morpholino
MT	Microtubule
MTOC	Microtubule organising centre
Mud	Mushroom body defect
NED	Nuclear envelope breakdown
NuMA	Nuclear mitotic apparatus
ODE	Ordinary differential equation
PBS	Phosphate buffered saline
PDE	Partial differential equation
PDMS	Polydimethylsiloxane
Pins	Partner of Inscuteable
Plk1	Pole-like Kinase 1
PMSG	Pregnant mare's serum gonadotrophin

PNC	Pronuclear complex
RhoA	Ras homolog family member A
RNA	Ribonucleic acid
ROCK1	Rho-associated coiled-coil containing protein kinase 1
SDS	Sodium dodecyl sulfate
SEM	Standard error of the mean
TCV	Tricellular vertices

Abstract

Cell division is vital for the growth and homeostasis of tissues. The outcome of division, for example a contribution to tissue spreading or tissue stratification, depends upon its spatial orientation within the tissue. In turn, the external environment of the tissue feeds back to determine cell division orientation, with divisions commonly aligning with an axis of greatest tensile force. Division orientation is determined by the orientation of the mitotic spindle. From its assembly until chromosome segregation, the spindle dynamically rotates and explores the cell by the interaction of its astral microtubules with protein complexes at the cell periphery. The nuclear mitotic apparatus protein (NuMA) is one such element implicated in spindle positioning which is localised dynamically to the cell cortex during cell division and to the spindle poles during cell division. As such, NuMA has been highlighted as a key candidate in driving the orientation of division with external force. Recent unpublished work in the Woolner lab has revealed that NuMA localisation to the cortex is sensitive to tissue tension and is perturbed in cells experiencing an externally applied force, though the precise mechanism by which NuMA functions to orient divisions with external force remains unclear.

To determine how mechanosensitive spindle orientation is regulated, we used a combination of biological and mathematical approaches to analyse dynamic movements of the mitotic spindle. We utilised the tightly adhered epithelial layer of the *Xenopus laevis* animal cap to study spindle movements in stretched and unstretched tissues to assess the impact of stretch on the spindle rotational and translational dynamics. We find that the mitotic spindles undergo oscillatory movements as they seek out their division axis. The period of these oscillations is insensitive to external forces but we see an affinity for oscillating which is higher in unstretched tissues rather than stretched tissues. Crucially, the period of oscillation is sensitive to the depletion of NuMA.

We develop a model of spindle pole displacements due to cortical pulling forces and microtubule-based restoring forces, using stochastic simulations, Fokker-planck equations, ODEs and an algebraic formulation. By systematically reducing the mathematical system we highlight the key relationships between parameters which promote dynamic movements of the spindle pole. We also show that oscillations in the position of a single spindle pole may occur in a select region of parameter space. Our results suggest that depletion of NuMA reduces the restoring force acting on the spindle which allows the spindle to oscillate with a longer period at lower numbers of cortical pulling elements. We highlight new avenues to explore to determine the role of NuMA in mechanosensitive orientation, through the use of interdisciplinary techniques that allow us to vary properties of cortical force generators *in silico*.

Declaration of originality

I hereby confirm that no portion of the work referred to in the thesis has been submitted in support of an application for another degree or qualification of this or any other university or other institute of learning.

Copyright statement

i The author of this thesis (including any appendices and/or schedules to this thesis) owns certain copyright or related rights in it (the "Copyright") and s/he has given The University of Manchester certain rights to use such Copyright, including for administrative purposes.

ii Copies of this thesis, either in full or in extracts and whether in hard or electronic copy, may be made *only* in accordance with the Copyright, Designs and Patents Act 1988 (as amended) and regulations issued under it or, where appropriate, in accordance with licensing agreements which the University has from time to time. This page must form part of any such copies made.

iii The ownership of certain Copyright, patents, designs, trademarks and other intellectual property (the "Intellectual Property") and any reproductions of copyright works in the thesis, for example graphs and tables ("Reproductions"), which may be described in this thesis, may not be owned by the author and may be owned by third parties. Such Intellectual Property and Reproductions cannot and must not be made available for use without the prior written permission of the owner(s) of the relevant Intellectual Property and/or Reproductions.

iv Further information on the conditions under which disclosure, publication and commercialisation of this thesis, the Copyright and any Intellectual Property and/or Reproductions described in it may take place is available in the University IP Policy (see `http://documents.manchester.ac.uk/DocuInfo.aspx?DocID=24420`), in any relevant Thesis restriction declarations deposited in the University Library, The University Library's regulations (see `http://www.library.manchester.ac.uk/about/regulations/`) and in The University's policy on Presentation of Theses.

Acknowledgements

I would like to begin by thanking my two incredible supervisors Sarah Woolner and Oliver Jensen. Their support and guidance through this PhD has been unparalleled. I can't imagine I could have been blessed with a better team.

The Woolner lab members who have kept me going through the day-to-day challenges of lab work and particularly in writing this thesis: Georgina Goddard, Nawseen Tarannum, Iona Norwood, Irwin Phanada, Natasha Cowley, Emma Johns, and Lucy Cheeseman. Some of whom have left but are forever cherished. I'm so sorry they had to teach me how to excise animal caps - I can only imagine how many times they considered suggesting I become a full time mathematician before I became competent.

A massive thank you to Peter March, Roger Meadows and Steve Marsden, for all of their help with microscopy. I am also incredibly grateful to Joseph Pennock and Vicky Taylor, who care so much for the frogs and were always willing to answer my numerous questions. Also a thank you to the frogs, without them this wouldn't have been possible.

Of course I need to thank the C-Wing darlings: Mukti Singh, Samantha Borland, Christina Hayward, Joan Chang. All truly wonderful women and scientists, who make being a woman in STEM something to be proud of. I also thank the QBBees. Special mentions to Hel Ray, Ellie Appleton, Jess Forsyth, and Josh Hawley. They have all played such a large part in my life over the course of this PhD. An additional thank you to Chris Revell, who provided excellent technical and emotional support over the years.

Thank you to Laura Jones and Abigail Higton. They've been with me from my undergraduate degree through to now. They've brought me care packages, love and laughter, and I am forever grateful. A special thank you goes to the Stockport Spartans and extended weightlifting friends - my strong team. They kept me going when times were particularly rough. Particular acknowledgements to James Stonehewer, head coach and my biggest supporter. Without him, life would be considerably worse. Sean Mcloughlin, who's been with me from the very beginning of this PhD. Without his love and friendship I wouldn't be half the person I am today. Thank you. Georgie Rastall - her (literally) daily support and validation can never be repaid.

And finally a thank you to the families that supported me. Thank you to the Scrase family, who took me in during the scariest time and showed me unwavering love and kindness. Thank you to my own family, who have never let me believe I wasn't good enough to do anything I wanted to do. They bring me joy, love and laughter. And a final and most important thank you to Antonio Capavanni (and Bonnie) who has been my rock, particularly while writing this thesis.

Preface

Dionn Hargreaves has an undergraduate masters in mathematics and physics (MMath&Phys) from the University of Manchester.

Chapter 1

Introduction

Embryos develop, on the most basic level, as a result of one cell dividing into two cells. In a tissue, the orientation of cell division is an important factor in determining either the outcome for the daughter cells (e.g. cell fate) or the tissue as a whole (e.g. tissue and organ architecture) [1], [2]. During the course of development, the dividing cells are subject to a host of different environments and forces as the tissues and organs are formed [3]–[7]. How cells perceive and ultimately respond to the changing mechanical environment is important for robust development [8]–[11]. Studies into the effect of mechanical forces on cell division have begun to unpick the processes at play, although there is still uncertainty into exactly what the exact mechanisms may be.

In recent years, many studies have shown that cell divisions will align along an axis of tensile (stretching) stress [4], [12]–[15]. However, a clear example of uncertainty in this area of study is whether or not the direction of cell division is directly regulated by mechanical forces [12], [13], [16], or whether it is regulated indirectly via changes to the cell shape [17]–[20]. Indeed, the application of an external mechanical force in the form of a uniaxial stretch is sufficient to deform the shape of even tissue-bound cells [8], [12], [15], [17], [21]. As such, force-based and shape-based effects are inextricably linked. As both cell division rate and orientation are shown to be altered under mechanical perturbation [15], we will consider in this thesis whether or not other cell-intrinsic processes are altered under mechanical stretch. In particular, we aim to explore the effect that mechanical perturbation has on mitotic spindle dynamics.

The mitotic spindle is the structure which segregates the genetic material of a cell into two daughter cells, and its orientation within the cell determines the orientation of division. While much is known about the functions involved in spindle orientation [22], [23], the detailed response to external forces is less well established. A key player involved in spindle positioning is the nuclear mitotic apparatus protein (NuMA), which has roles in maintaining spindle integrity [24], [25] and in spindle positioning due to its association with dynein/dynactin and LGN at the cell cortex [26]. Crucially, recent unpublished work in the Woolner lab has implicated NuMA in tension-sensitive spindle orientation and positioning [27], owing to its tension sensitive localisation to the cell cortex and its ability to orient spindles with cell shape in stretched tissue cells [27].

We aim to contribute to the understanding of mechanosensitive spindle positioning by per-

forming detailed spindle movement analysis in stretched and unstretched epithelial tissues. Furthermore, we will investigate how depletion of NuMA in stretched tissues alters these spindle dynamics. To help interpret the results from our biological experiments, we will develop mathematical models of spindle pole movements which combine pulling forces from the cortical NuMA/dynactin/dynein machinery with restoring forces by growing microtubules, and use these models to explore the properties of the spindle orienting machinery which affect spindle dynamics. We will then combine the results of the mathematical model with the results of our experiments in order to elucidate how spindle dynamics are impacted by tissue stretch and shed new light on the role that NuMA may play in mechanosensitive spindle orientation.

1.1 Cell division: An overview

The cell cycle is the sequence by which cells are prepared for and commit to division. The progression through the cycle is controlled by cyclins which activate cyclin-dependent protein kinases (CDKs) to trigger cell-cycle events [28]. Following chromosome duplication in S-phase, the M-phase (mitosis) is triggered by an increase in mitotic CDK (M-CDK) activity which sets in motion the process of chromosome segragation into two complete daughter cells [28].

1.1.1 Mitosis

Mitosis can be divided into five main phases: prophase, prometaphase, metaphase, anaphase and telophase. These are followed by cytokinesis where the cell is physically separatated into two new daughter cells [28]. These phases are distinguished from one another based on the behaviour of the chromosomes. Here we describe the processes which define the five phases and also introduce the mitotic spindle; an array of microtubules which connects to the chromosomes and plays a central role in their positioning and segregation into the two daughter cells. The structure and function of the mitotic spindle will be explored in more detail in section 1.2.

At prophase, the duplicated chromosomes condense and the mitotic spindle begins to form between the two centrosomes [28], [29]. In many animal cells, the cell undergoes a dramatic rounding due to an increase in actomyosin contractility (actomyosin contractility is discussed further in section 1.3.1) [30]. This is followed by prometaphase which is characterised by the M-CDK mediated breakdown of the nuclear envelope, allowing the association of the condensed chromosomes with the mitotic spindle via their kinetochores [28], [29]. At metaphase, the chromosomes have aligned at the spindle equator to form what will be referred to as the ‘metaphase plate’ for the duration of this work [28]. Then the anaphase-promoting complex (APC/C) targets the protein securin for destruction, which results in the activation of securin’s binding partner separase [28]. Separase cleaves the duplicated chromosomes from one another resulting in their separation at anaphase. The upreg-

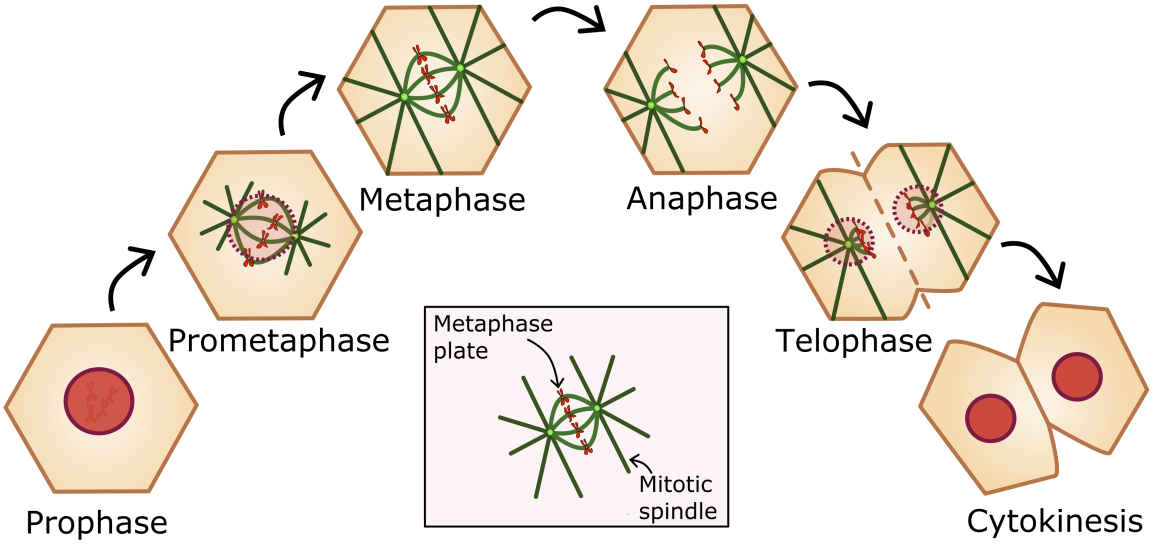

Figure 1.1. **Stages of mitosis**. Diagram of mitotis from prophase to cytokinesis. The mitotic spindle assembles at prometaphase. The chromosomes line up to create the metaphase plate for metaphase where the spindle aligns itself in the cell. The chromosomes are cleaved at anaphase and pulled to the spindle poles at telophase. Cytokinesis completes cell division by cleaving the cell in two.

ulation of APC/C to trigger anaphase depends on the spindle assembly checkpoint, which ensures that all kinetochore attachments are correctly captured by the spindle prior to the cleavage of the chromosomes [28]. This spindle-assembly checkpoint ensures that equal genetic material is allocated to the two daughter cells. Segregation of the chromosomes to the spindle poles in anaphase is followed by telophase, where the separated chromosomes decondense and the nuclear envelope reforms around them to create two nuclei on opposite ends of the mother cell. The cell is then cleaved in two by a contractile actin ring to create two daughter cells, each containing one nucleus (Figure 1.1). [28].

As the chromosomes are segregated to the spindle poles upon anaphase onset, which defines the locations of the daughter nuclei, the positioning of the mitotic spindle is paramount for determining the orientation and size of the resulting daughter cells. Cell division can either be defined as symmetric or asymmetric. Symmetric divisions produce two daughter cells of equal size, containing the same intracellular components (e.g. proteins, mRNA). Alternatively, asymmetric divisions result in daughter cells of either unequal size, unequal cellular components, or both. Both asymmetric and symmetric divisions are generally determined by the placement and orientation of the mitotic spindle [28]. We will next discuss the importance of cell division orientation.

1.1.2 Consequences of oriented cell divisions

The orientation in which cells divide has an important role in maintaining tissue organisation, as the position of the daughter cells can have implications for their fate [31]. The placement of cells can affect their exposure to extracellular environments [20], [32], [33]. For example, the neural progenitor cells in the spinal cord neuroepithelia of chicks divide such that one daughter cell is ejected and allowed to differentiate while the other remains

in the ventricular zone to continue dividing [34]. Disruption of this process, such that the progenitor cell is also ejected from the ventricular zone, results in the erroneous continued proliferation of the progenitor due to the lack of external signalling [35]. In the epidermis, cell divisions perpendicular to the plane of the tissue result in tissue stratification (Figure 1.2A) [32], [36].

Asymmetric divisions due to the asymmetric segregation of cellular material also affect cell fate [37]. In the *C. elegans* zygote, asymmetric divisions are mediated by polarity proteins PAR-1 and PAR-2 at the cell posterior, and proteins PAR-3, PAR-6 and PKC-3 at the anterior which determine the postioning of pulling forces acting on the spindle [37]. During angiogenesis, the asymmetric division of tip cells has been shown to promote cell migration and correct tip/stalk selection of the resulting daughter cells [38].

Alternatively, symmetric in-plane divisions are important for tissue elongation and spreading, particularly in epithelia [39]–[41] (Figure 1.2A). In epithelia, polarity protein Par-3 apically localises aPKC, which restricts the spindle movements to the plane of the epithelium by excluding LGN, a component of the spindle-orientation machinery [37]. In these tissues, the orientation of the mitotic spindle within the tissue plane can also have an impact on tissue structure. Germ band extension of *Drosophila* is driven by neighbour-neighbour switching (e.g. T1 transitions), but oriented divisions are needed as a supplement to this process for proper growth (Figure 1.2B)[39], while a mixture of oriented and random in-plane divisions in the mouse lung epithelium are required for maintaining the correct tissue architecture [8], likely due to randomly oriented divisions facilitating tissue spreading (Figure 1.2C).

The choice of division orientation is historically attributed to Hertwig's long axis rule [42], whereby cells divide perpendicular to their axis of largest elongation. Indeed, the long axis of the cell has been identified in a number of studies as the best predictor for division orientation [15], [17], [18], [43], [44], although there are also many exceptions to the rule [8], [12], [13], [16], [19], [45]. Minc *et al.* (2011) measured spindle orientation in sea urchin zygotes placed in microfabricated chambers with unique geometries [19]. In contrast to the long-axis expectation, often cells divided such that the daughter cells were placed along the direction of greatest geometric symmetry, away from the strict long-axis [19]. Elsewhere, re-shaping of oval cells into circular cells by stretching resulted in reliable re-orientation of divisions along the stretch axis, where Hertwig's rule would assume random divisions orientations for circular cells with no defined long axis [13].

Thus the orientation of divisions has important implications for the daughter cells as well as the architecture of the tissues they occupy. Further, the orientation of cell division is not easily explained by cell shape alone. To explore the factors which determine cell division orientation, we present the structure and function of the mitotic spindle whose function during cell division is vital for determining division orientation.

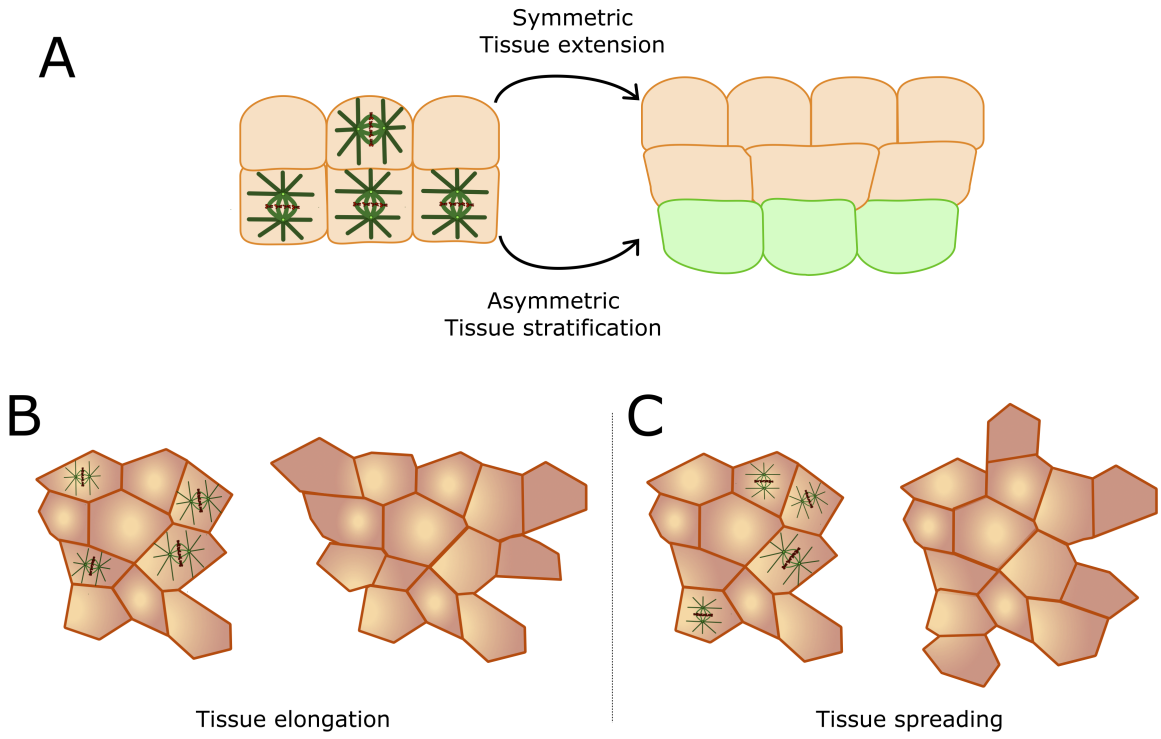

Figure 1.2. **The orientation of division has implications for tissue architecture.** A) Symmetric divisions in epithelia lead to tissue extension, while asymmetric divisions lead to tissue stratification and cells of different cell fates (green vs cream). B) Cell divisions within the epithelial plane aligned along the same axis leads to tissue elongation. C) Cell divisions within the epithelial plane with a random distribution of orientations leads to tissue spreading.

1.2 Mitotic spindle structure and interactions

1.2.1 Structure of the mitotic spindle

The mitotic spindle is a large microtubule (MT)-based structure which forms during mitosis and is instrumental to generating two daughter cells of equal genetic components [47], [48]. There are three types of MTs which make up the spindle structure: the kinetochore MTs, the interpolar MTs, and the astral MTs (Figure 1.3A). All three emerge from two spindle poles, with the interpolar MTs forming an anti-parallel overlap at the spindle centre, while the kinetochore MTs interact with and bind to the chromosomes to form the metaphase plate [28], [47], [49]. In order to pass through the mitotic checkpoint to anaphase, each chromosome must be correctly aligned at the equator with one attachment to each spindle pole via the kinetochore MTs [28]. The characteristic fusiform shape of the spindle achieved by the kinetochore and interpolar MTs is flanked by the astral MTs which extend away from the overlapping area to contact the cell cortex (Figure 1.3).

The microtubules themselves are rigid, hollow tubes assembled from α- and β-tubulin heterodimers, which stack together to create long polarised protofilaments which are then folded into a tube formation [28]. Ring-shaped structures of γ-tubulin reside at the centrosome and promote nucleation of microtubules by association with $\alpha\beta$-tubulin dimers [50]. Both α- and β- tubulin bind to guanosine triphosphate (GTP), which is stable in α-tubulin but open to hydrolysis to guanosine diphosphate (GDP) in β-tubulin. GDP promotes the dis-

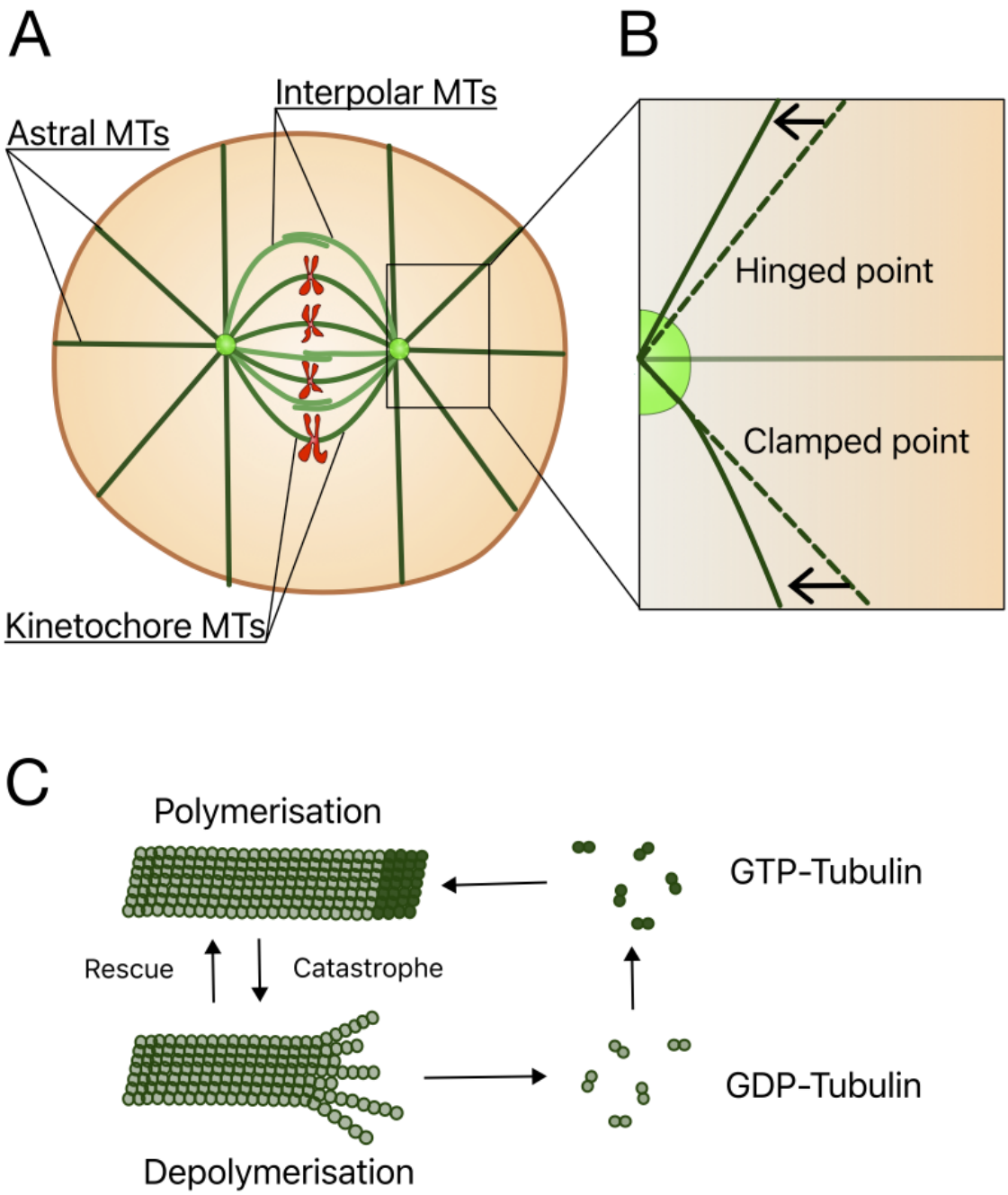

Figure 1.3. **Microtubules in the mitotic spindle** A) A schematic of the mitotic spindle, with labelled interpolar, kinetochore and astral microtubules. The chromosomes (red) are held central to the spindle by interactions with kinetochore microtubules. Interpolar microtubules overlap in this central region and stabilise the fusiform shape. Astral microtubules extend outward and contact the cell cortex. All three populations of microtubules nucleate from the spindle poles (the centrosomes) from their minus ends. B) The difference between hinged and clamped nucleation points for microtubules which are moved along the direction indicated by the arrows. A hinged microtubule can change its angle at the nucleation site, while clamped microtubules are held at a constant angle of nucleation. Dotted microtubules indicate the position of the microtubule prior to movement. C) (Adapted from [46]) The dynamic instability of microtubules, comprising of phases of polymerisation (growing) and depolymerisation (shrinking). Transitions between these phases are termed 'catastrophe' (growing $\rightarrow$ shrinking) and 'rescue' (shrinking $\rightarrow$ growing). Polymerisation is stabilised by the GTP-tubulin cap which allows the addition of more GTP-tubulin. Without the GTP-tubulin cap, the GDP-tubulin lattice rapidly disassociates.

association of β-tubulin from the microtubule lattice resulting in depolymerisation of the microtubule [46], [51], [52]. Alternatively, GTP-bound tubulin dimers are stable and promote microtubule growth. A GTP 'cap' at the plus end of microtubules stabilises microtubule growth until the rate of addition of new GTP-tubulin dimers drops below the rate of hydrolysis, resulting in the loss of the cap and an entry into the depolymerisation phase. This switching between growing and shrinking is called 'catastrophe' while switching from shrinking to growing is called 'rescue' (Figure 1.3C). The dynamic switching between the two phases is called dynamic instability and facilitates MT-based force generation [18], [53], [54], the modelling of which we will discuss in section 1.5.2. With reference to cell division in particular, it has been shown in HeLa cells that a reduction of dynamic instability delays anaphase onset [18], highlighting its importance for cell division.

1.2.2 Interactions of the mitotic spindle

The mitotic spindle structure is maintained by interactions between MTs and associated proteins. The kinetochore microtubules are highly bundled at their plus ends into K-fibres by association with short lengths of anti-parallel MTs and MT-associated proteins such as PRC1 which binds overlapping MTs [49], [55]. Motor proteins dynein and kinesin associate with MTs and 'walk' along them with directed motion due to the microtubule polarity [28]. Kinesins are plus-end directed motors (toward the quickly polymerising or depolymerising MT end), such that overlapping microtubules, both associating with kinesins, will slide away from one another [56], [57], a mechanism which is thought to aid in the association of anti-parallel interpolar MTs at the spindle cortex [57]. Dyneins are minus-end directed (toward the spindle pole) [51] and have been implicated in spindle pole focusing and balancing of kinesin-mediated outward pushing of the spindle poles to maintain a stabilised spindle shape [58]–[60]. Dynein has been shown to have slip-bond behaviour with the MT, whereby increased load on dynein will increase its unbinding rate [61]. However, further studies have indicated that this slip-bond behaviour may be directional, with unbinding under load toward the plus end of microtubules being more resistant to unbinding [62]. This directional differential unbinding could assist minus-end directed motion by providing resistance against net forces away from the minus end [62].

Dynein's function as a motor protein is modulated by its association with activator dynactin and cargo proteins [63]. At the spindle pole this cargo is NuMA, which is required for proper spindle focusing and stabilisation (Figure 1.4A) [25]. Dynein also interacts with astral microtubules at their plus-ends [64]–[66]. Dynein/dynactin is held at the cortex by association with the Gαi/LGN/NuMA tertiary complex (Figure 1.4B) [64], [67]–[69], whose anchoring to the cell edge allows dynein's minus-end directed motion to result in a net pulling force on the spindle [64]–[66]. Dynein in the cytoplasm is also thought to contribute to spindle pole positioning, due to the drag forces created in the cytoplasm as dynein moves its cargo along the microtubule length [70], [71]. This cytoplasmic pulling is thought to be the main driving force for spindle positioning in oocytes, where the cell is too large for astral microtubule-cortex interactions [70]. The association of dynein at the cortex with as-

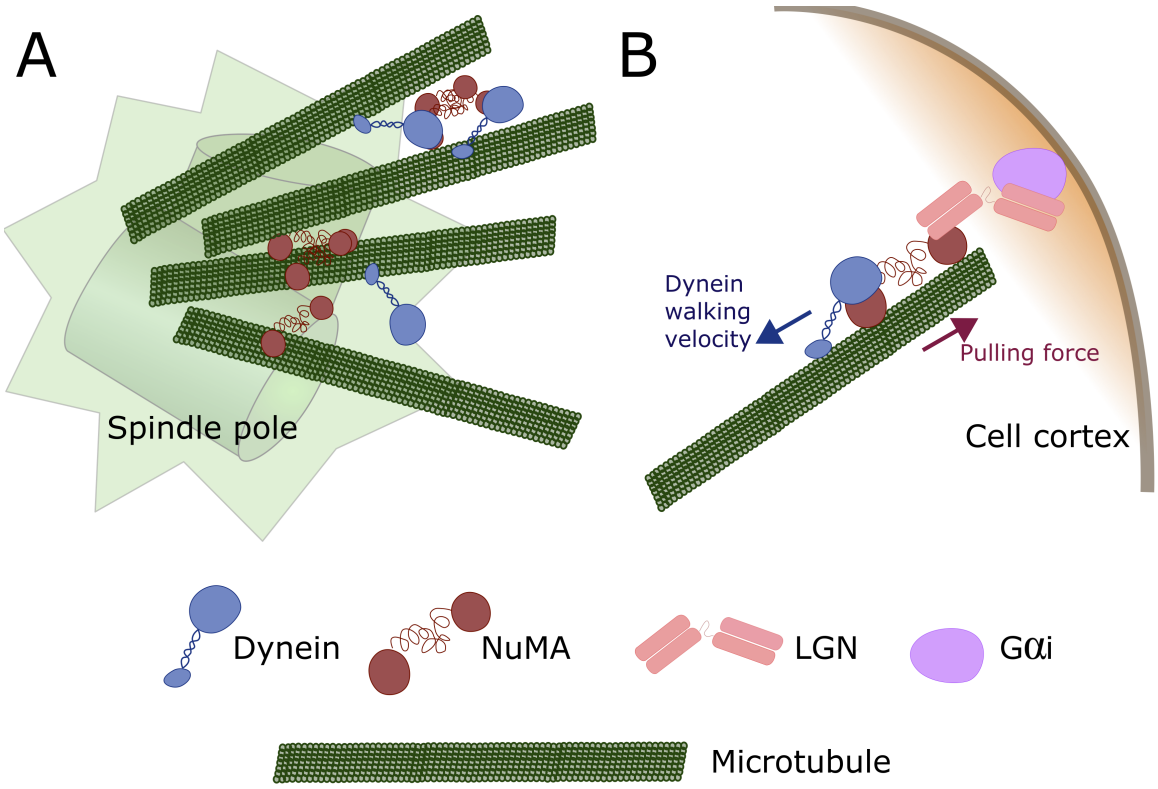

Figure 1.4. **The microtubules of the spindle interact with dynein and NuMA at the spindle poles and the cell cortex**. A) NuMA binds to microtubules and dynein at the spindle poles to facilitate spindle focusing and maintain the bipolar spindle structure. B) Dynein is held at the cortex by association with the Gαi/LGN/NuMA complex. Dynein's minus-end directed motion along the microtubule exerts a pulling force on the microtubule towards the cell cortex.

tral microtubule plus ends is one of the main driving forces for this project. In particular, NuMA's role in spindle formation and positioning is of particular interest. We will further discuss NuMA in section 1.4.

Non-motor proteins are also involved with spindle assembly and dynamics. The kinases, Polo-like kinase 1 (Plk1) and Aurora-A, are vital at the spindle poles to maintain spindle integrity [72], [73]. Plk1 also affects spindle dynamics by its ability to phosphorylate cortical NuMA [74], causing delocalisation of dynein from the cortex upon close proximity of the spindle pole [26]. A chromosome-derived RanGTP gradient is also involved in maintaining spindle structure [72], [75] and spindle positioning due to its ability to exclude cortical LGN [26], [75], [76].

1.2.3 Spindle dynamics

The mitotic spindle is a dynamic structure, the movements of which have been attributed to the spindle finding the approriate division axis in the cell before division, either along the long axis [18], [77], or due to polarity proteins [37]. This makes understanding these movements crucial for understanding how its positioning is controlled to determine the ultimate orientation.

The dynamics of spindles can be broadly divided into translational movements, rotational

movements, and oscillatory movements. Most often, spindles will exhibit combinations of these within a single division. Biphasic dynamics have been reported in multiple systems involving rotational phases and maintenance phases [18], [77]. In HeLa cells the rotational phase was described as a rotation from spindle assembly to the cell long axis, followed by a maintenance phase where the orientation toward the long axis was held [18]. These same two phases were observed in the epithelium of *Xenopus* embryos, though within the maintenance phase the spindle was revealed to oscillate about the division axis [77]. It is unclear whether the same oscillations existed but were undetected in the HeLa cells studied in [18], as these cells were imaged at a temporal resolution of 4 minutes per frame as opposed to the 5 s per frame resolution employed in [77]. Interestingly, Corrigan *et al.* (2013) reported translational oscillations of the spindle pole along the pole-pole axis, and these oscillations ceased upon depletion of LGN [18].

The dynamics of the posterior mitotic spindle pole in the single cell *C. elegans* embryo have been well characterised [78], [79]. As metaphase proceeds, the spindle is displaced towards the posterior of the cell and this displacement coincides with highly conserved oscillations of the posterior pole as a result of increased force generation by cortical dynein [78], [80]. Interestingly, the posterior pole experiences a build-up of oscillations before they die back down, suggesting that the mechanisms by which the posterior pole oscillates change upon the approach of anaphase [78]. Pécréaux *et al.* (2006) attribute this amplification and cessation of oscillations to the activity of dynein, which they suggest increases as metaphase proceeds [78]. The mechanism which could modulate dynein's activity is unclear but is potentially attributed to LIN-5, the *C. elegans* equivalent of NuMA [67], [81].

Analysis of monopolar spindles has also shown that the localisation of LGN, NuMA's cortical binding partner, is dynamic due to its exclusion from the vicinity of the chromosomes, a result of a chromatin-derived RanGTP gradient [76]. The monopolar spindles were shown to 'chase' regions of high LGN intensity, while the constant relocation of LGN upon nearing of the chromosomes kept the spindle pole in motion. In particularly elongated cells, this resulted in a spindle pole which oscillated along the length of the cell [76]. This study highlights that spindle positioning is a dynamic process, with monitoring of the current cell state a crucial component in orienting the spindle. Indeed, the dynamic action depends upon presence of the astral microtubules [76]. Astral microtubules are key for spindle dynamics, as depletion of them by treatment with low dose nocodazole results in erroneous spindle centring and orientations, as well as reduced spindle velocity [13], [19], [26], [44], [64], [79], [82]–[84]. Thus the mitotic spindle requires the interaction of astral microtubules with cortical elements for proper spindle orientation and dynamic movements.

Interestingly, in the developing airway epithelium of mouse, two distinct spindle dynamic behaviours have been observed. Cells were identified within a single population to have either 'fixed' spindles (spindles which rotate to their final orientation within 6 minutes of metaphase and cease movements after this), or 'rotating' spindles (spindles which continue to move and dynamically change their angle throughout metaphase). The fixed spindles tended to result in divisions along the longitudinal axis of the airway, while rotating spin-

dles divided with a random orientation [8]. Thus the two populations of cells have separate functions in tissue growth, with rotating spindles contributing to tissue spreading and fixed spindles contributing to tissue elongation. Upregulation of ERK signalling in these tissues resulted in more 'rotating' spindle phenotypes even in more elongated cells [8]. ERK-signalling is upregulated in stretched cells [85] and produces a contractile response within the cell [86], thus the increase in ERK-signalling creating a spindle response suggests that mechanical tension may have an effect on measurable spindle dynamics, especially in a tissue context.

1.3 Cellular responses to mechanical tension

1.3.1 Transduction of forces in tissues

In order to understand how cells divide in response to tension, it is useful to first consider how cells, and specifically epithelial cells, experience force.

Epithelial tissues are cell layers of tissue which define the structure of organs and compartments within organisms and act as barriers between the 'inside' and 'outside' [10]. Cells in an epithelial tissue are connected to neighbouring cells via cell-cell junctions to form a cohesive barrier [28]. A number of different types of junctions exist within the epithelial cells for cell-cell communication and barrier maintenance. One such junction is the adherens junction, which connects cytoskeletal components of neighbouring cells, allowing mechanical stress to be communicated between cells in the tissue [10], [28]. A core component of the adherens junction is E-cadherin, a transmembrane protein which clusters at junctions to knit with the E-cadherin molecules of the neighbouring cell [10]. E-cadherin associates with p120-catenin and β-catenin, which in turn mediate binding with α-catenin and the actin cytoskeleton [28]. In the absence of force, α-catenin exists in a closed confirmation such that it associates only with β-catenin and F-actin. However, upon the application of an external force by the neighbouring cell, α-catenin is stretched into an open conformation which exposes a vinculin-binding domain [87]–[89]. The binding of vinculin further promotes the recruitment of more actin to stabilise the junction and increase actomyosin contractility [28], [89], [90].

Actomyosin contractility generates forces inside the cell. Actomyosin, a complex of actin and the motor proten myosin, is capable of both responding to and creating mechanical tension [91]. In particular myosin II is required for generating tension and resisting mechanical stress in tissues by inducing a sliding motion of antiparallel F-actin leading to a contraction force [92]–[95]. Actomyosin contractility can be upregulated by the tension-activated Rho GTP-ase RhoA [96]. Active RhoA activates ROCK1 to increase myosin II acivity, as well as promoting actin polymerisation via formins [83], [97]. It has been shown that optogenetic activation of RhoA in HeLa cells can cause measurable cell shape deformities due to asymmetric tension created by localised actomyosin contractility [83]. Also, the aforementioned connection of the contracting actin cytoskeleton to E-cadherin provides a means

of transferring intracellular forces to the neighbouring cells through the adhesion site [98], [99]. Thus cells are capable of generating tension intrinsically through actomyosin contractility, as well as responding to forces through adhesions.

As well as cell-cell communication through connections of the actin cytoskeleton, mechanical stretch can also alter cell behaviour by activating specific mechanosensitive ion channels in the membrane [100], [101]. Stretch-activated ion channels such as Piezo1 cause influx of Ca^{2+} ions which upregulate ERK signalling to activate cyclin-B and cause the cell to enter mitosis [100]. Mechanical stretch has been shown to increase division rate in the epithelial tissue of the *Xenopus laevis* animal cap [15]. However, ERK is also an upregulator in the pathway to promoting actomyosin contractility [86]. Thus mechanosensitive ion channels can also induce cell contractile behaviour in response to stress.

1.3.2 Cell division under mechanical tension

As cells have been shown to be able to both generate and respond to tension [28], [40], [90], and tension has been implicated in affecting spindle dynamics [8], we next introduce specific examples of the impact of tension on cell division orientation. Cell shape changes are linked to the direction of applied tension [4], [12], [13], [15], [17], [21], [43], so determining the important factor is difficult and the topic of much debate. As such we also introduce examples of division orientations determined to arise from cell shape factors.

Cell divisions attributed to cell tension

In individual HeLa cells, optogenetic cortical recruitment of RhoA to increase localised actomyosn contractility was shown to induce a spindle response, whereby mitotic spindles actively rotated away from regions of high cortical contractility [83]. To reduce the impact of shape-effects, the analysis was limited to cells showing only a very small augmentation in shape due to the contractility, thus the dramatic change in spindle orientation was attributed to cell tension effects [83].

In tissues, sites of adhesion are important for directed cell divisions, in particular the E-cadherin at adherens junctions has been shown to be vital for maintaining in-plane divisions in the epithelia of MDCK cells [102]. Thus cortical cues are likely to play a role in determining division orientation in tissue cells. Indeed, cortical cues have also been shown to determine division orientation even in single HeLa cells plated on fibronectin-coated micropatterns [45]. Adhesive retraction fibres connect the cell to the micropatterns to reshape the cell, and maintain a memory of this shape as the cell rounds up during mitosis [45]. These retraction fibres were shown to act as a spindle guide to orient the mitotic spindle and resulting cell division, and laser ablation of the fibres has been shown to create a spindle re-orientation response away from the ablation site [13] suggesting that the tension propagating through the fibres is the important factor for controlling spindle orientation. Further, the behaviour of the mitotic cells to round up further highlights the importance of

the adhesive cortical cues, as without them the spindle would otherwise have oriented itself randomly if the shape of the cell during mitosis were the important factor [45]. Similarly, adhesion of cells onto oval-shaped micropatterns which could be stretched into a circle showed an orientation response of cells along the direction of stretch, rather than the expected random distribution for shape-based effects (Figure 1.5A) [13], highlighting that tension can also impact cell division orientation in single cells.

In tissues, disentangling shape and force is more difficult as neighbour-neighbour interactions and actomyosin contractility could impact local mechanical tensions [15], [21]. The detailed complexity added by neighbour-neighbour interactions makes the application of a global stretch on tissues an interesting experimental method for exploring the impact of tension on cells [12], [15], [17]. Hart *et al.* (2017) use a uniaxial stretch system on confluent MDCK monolayers to show that cell divisions re-orient along the stretch axis independently of cell shape when monolayers are subject to a 12% stretch [12]. The low percentage of stretch (measured by displacement of nuclei upon application of the stretch) was used to decrease the shape-change effect they might impart on the cells, as they determined that a 12% stretch was not sufficient to create a significant change in cell shape [12]. However, this level of tension was sufficient to create a myosin II response, which was recruited to and amplified at the cortical regions perpendicular to the application of stretch indicating an actomyosin response through E-cadherin mediated force transduction (Figure 1.5B) [12], [89]. Divisions perpendicular to actomyosin cables were also described by Scarpa *et al.* (2018) at compartmental boundaries of the *Drosophila* embryo during segmentation [14]. These divisions aligned perpendicular to the compartmental boundaries unless the shape was significantly elongated, an observation which was also reported by Hart *et al.* (2017).

The impact of tension on cell division has also been investigated without the application of an artificial stretch. The *Drosophila* wing pouch has both regions of stretch at the tissue periphery and compression at the tissue centre [4]. Interestingly, in this tissue, myosin II was polarised tangent, rather than perpendicular, to the stretch [4]. The divisions in the *Drosophila* wing pouch occurred parallel to the actomyosin cables [4]. This was similar to what was seen in the *Drosophila* notum, where the extensile peripheral cells also aligned their divisions with the axis of stretch [16]. Importantly, in the crowded midline of the notum, cells were unable to orient their divisions with their long axis, which implicates tension as the important factor for determining division orientation [16].

Thus, while tension has been implicated as an important factor for determining cell division orientation, the cellular mechanisms remains unclear. The contrasting observations of the regions of accumulated myosin II combined with the relative spindle orientation suggests that myosin II does not directly contribute to cell division orientation, but it may instead be working indirectly through internal changes to the cell. Interestingly, significantly elongated cells showed division orientations along the long axis of the cell not aligned with global tension [12], [14], suggesting that cell shape is an important factor.

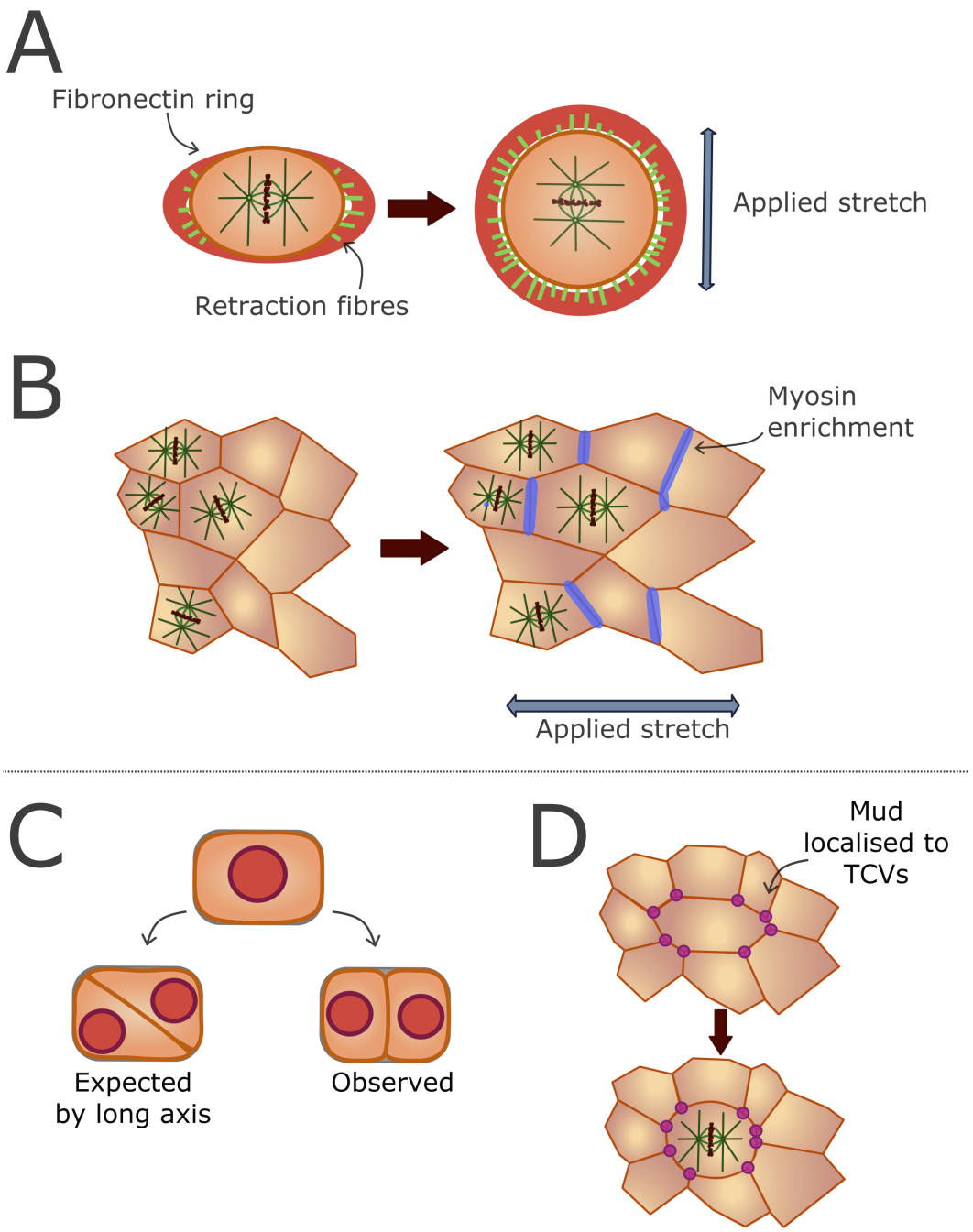

Figure 1.5. **Cell divisions according to external tension and cell shape**. A) Reorientation of the mitotic spindle in a cell plated on an oval adhesive surface and stretched into a circle. The spindle reorients according to the stretch axis [13]. B) Alignment of divisions with the axis of tissue stretch, perpendicular to regions of accumulated myosin II [12]. C) Observed cell division orientation in a sea urchin zygote confined to a rectangular well. The expected orientation by Hertwig's long axis rule is in contrast to the symmetric orientation observed [19]. D) Localised Mud (NuMA's homolog) in the *Drosophila* pupal notum tissue. Mud localisation provides a spatial landmark for the cell shape according to the TCV position upon cell rounding [43].

Cell divisions attributed to cell shape

A similar cell-stretch experiment to that described in [12] but with a much greater stretch of 30% showed that when cells were elongated away from the applied stretch they continued to divide along their long axis, seemingly unaffected by the global tension of the tissue [17]. Interestingly, using a vertex-based model to infer local stresses of tissue-bound cells, it has been shown that the local stress axis of individual cells within a tissue are aligned with the elongation of the cell shape, if the cell shape is defined in terms of the tricellular vertices (TCVs, the points where three or more cells meet) [21]. Analysis of division orientations in the *Xenopus laevis* animal cap epithelial tissue shows an alignment with the shape of the cell when defined in this way, with the presence of the protein LGN at the TCVs appearing to be important for this orientation [15]. The alignment of division with the TCVs is perturbed upon the overexpression of cadherin, which results in the relocation of LGN to the cell edges, upon which cell division aligned best with cell shape as determined by the cell perimeter rather than TCVs [15]. This again highlights the importance of cell-cell adhesions to neighbours in generating a spindle response, and thus the shape-based cues may arise from neighbour-neighbour interactions [15].

The positions of the TCVs have also been implicated as key regions for proper spindle alignment in *Drosophila* tissues [43]. Mud, the *Drosophila* homolog of NuMA, is key for spindle alignment and is localised to the TCVs of cells in this tissue. Upon entry into mitosis the cells round up and the static Mud localisation provides spatial landmarks which allow the spindle to align with the long axis of the cell (Figure 1.5D). Computational modelling was used to indicate that the position of Mud at the TCVs could provide a cell-shape based mechanism to explain how cell divisions align with tissue stretch [43].

In single cells, the sea urchin zygote was shown to orient its divisions away from the cell long axis as determined using the Hertwig long axis rule (Figure 1.5C) [19]. However, this new division orientation could be described by a MT-length minimising function, which places the spindle at the orientation of maximum symmetry with minimised MT lengths extending from the spindle poles, revealing a new way of measuring cell shape [19].

A recent PhD thesis from the Woolner lab has shown that an applied cell tension aids cell division orientation along the cell long axis, and that this alignment with cell shape under tension requires NuMA at the cell cortex [27]. Importantly, upon depletion of NuMA protein levels, spindle align less well with cell shape, but only in stretched, not in unstretched, tissues. Thus shape-based and force-based effects may be more subtle than previously thought, with an external tension creating an additional cell-based response which allows the spindle to align with the cell's long axis [27].

We previously described how the mitotic spindle is positioned due to the interactions of the astral microtubule with elements at the cell cortex (Section 1.2.2), and spindle positioning has been shown to be a dynamic process which depends upon these interactions (Section 1.2.3). Importantly, the resulting cell division orientation is shown to be tension-sensitive,

though whether or not this sensitivity is due to force-based or shape-based effects is unclear (Section 1.3.2). A key player in spindle orientation is NuMA, which has roles both at the spindle poles [25] and at the cell cortex [64], [103].

1.4 Nuclear mitotic apparatus (NuMA) protein

The large (≈ 240 kD) protein NuMA is important for the spindle orienting mechanism [32], [36], [64], [65], [69], [104], [105] and is instrumental as a spindle-pole focusing protein [24], [106], [107]. This section aims to explore some of the basic properties of NuMA with regard to its structure and function. In doing so, NuMA will be highlighted as a key player in the spindle orienting mechanism with an argument for its potential function in translating extrinsic mechanical cues to intrinsic effects in the form of spindle movements.

1.4.1 NuMA functions at the cortex and the spindle poles

Following the breakdown of the nuclear envelope at prometaphase, NuMA localises to the spindle poles in a characteristic crescent shape [107] as a result of its association with both dynein and microtubules [108]. Here, the association of NuMA with dynein, dynactin, microtubules and its ability to form dimers focuses the microtubule bundles to create the fusiform shape of the bipolar spindle (Figure 1.4A).

The spindle also interacts with NuMA at the cell cortex, where it is found in conjunction with LGN and Gαi (Figure 1.4B) [4], [64], [69]. This ternary complex provides a tether for dynein which can transfer pulling forces to the spindle through association with astral microtubules. It is NuMA's recruitment to the cortex and subsequent recruitment of dynein that is important for spindle positioning, with LGN and Gαi acting as cues for precise localisation [36], [64].

1.4.2 Binding domains and interactions

NuMA contains two globular head and tail domains separated by an unusually long coiled-coil of approximately 210 nm (Figure 1.6A) [106], [109]–[112]. NuMA resides mainly in the nucleus when cells are not undergoing mitosis [106], [108], [110], in contrast to Mud, which doesn't localise to the nucleus and is localised to the cell cortex prior to prophase [43]. The presence of dynein [4], microtubule [113], [114], and LGN [113], [115] binding domains give function to NuMA at both the spindle poles and the cell cortex.

At the spindle poles, NuMA interacts with both dynein and microtubules to form a rigid spindle pole architecture [24], [25], [110], [112]. While at the poles, NuMA may also dimerise with other NuMA molecules due to hydrodynamic interactions between neighbouring coiled-coil regions, which aids in NuMA's function as a pole focusing factor [116], [117]. NuMA at the spindle pole may be phosphorylated by kinase Aurora-A, which results in increased

mobility of NuMA at the spindle poles and relocation of NuMA to the cell cortex [118]. LGN binding has also been shown to result in the translocation of NuMA from the spindle poles, likely due to the overlapping LGN and MT binding domains which disrupt NuMA's association with microtubules at the spindle pole [113], [115], [119].

NuMA's localisation to the cortex is spatially coincident with the localisation of LGN [32], [120] and stabilised by interactions of NuMA with F-actin through a 4.1-binding domain [103]. This localisation is independent of microtubule binding [32], [120]. What's more, the depletion of NuMA-microtubule interactions results in misalignment between spindle orientation and NuMA/LGN localisation [120]. Therefore, while NuMA's cortical localisation is microtubule-independent, NuMA-MT interactions are important for spindle positioning. Interestingly, NuMA-MT interactions should be abolished when bound to LGN [113], [115]. The presence of a second microtubule binding domain has been suggested which could explain how NuMA at the cortex can associate with both LGN and microtubules [118]. Although as the LGN-MT binding domain overlap has been implicated in the dynamic exchange of NuMA at the spindle poles when cytoplasmic LGN competes NuMA away from the microtubules [113], [115], [119], the mechanism of the second binding domain is unclear. Interestingly, it has also been observed that NuMA can localise to the cell periphery without LGN/Gαi through a direct membrane binding domain, although this action is inhibited by CDK1-mediated phosphorylation until chromosome segregation events occur at anaphase [121].

NuMA-phosphorylation by spindle-pole residing Polo-like kinase (Plk1) results in the exclusion of NuMA from the cortex [26], [74], while the RanGTP gradient from the chromosomes disrupts the association of LGN-NuMA with the cortex, increasing the complexity of the dynamic localisation of NuMA [26], [76].

1.4.3 Structure and the coiled-coil

The coiled-coil domain of NuMA is largely unexplored in terms of function. This section of the protein is unusually long, arranged in an α-helix [106], [109]–[112] with two parallel strands. The presence of discontinuities in the phasing of the heptad structure are likely to affect the propensity of the conformation to kink, bend or deform [109], [111]. The coiled-coil can also give rise to NuMA dimerisation through hydrophobic interactions [116], [117], and this dimerisation is thought to aid in the spindle-pole focusing function [116].

Dynein binds to the N-terminal end of the coiled-coil, overlapping with the coiled-coil region (Figure 1.6A) [4]. Computational studies into the mechanical responses of coiled-coils have suggested that the binding of molecules to coiled-coils can introduce a displacement in one of the helices, which results in an amplified bending displacement of the coil. The helical structures respond to local perturbations with amplified bending responses, where the magnitude of amplification increases with coiled-coil length [122]. It is thus possible that dynein binding to NuMA induces a conformational change to its structure, or that mechanical perturbations as a result of cortical tension can be amplified down the coil to affect its

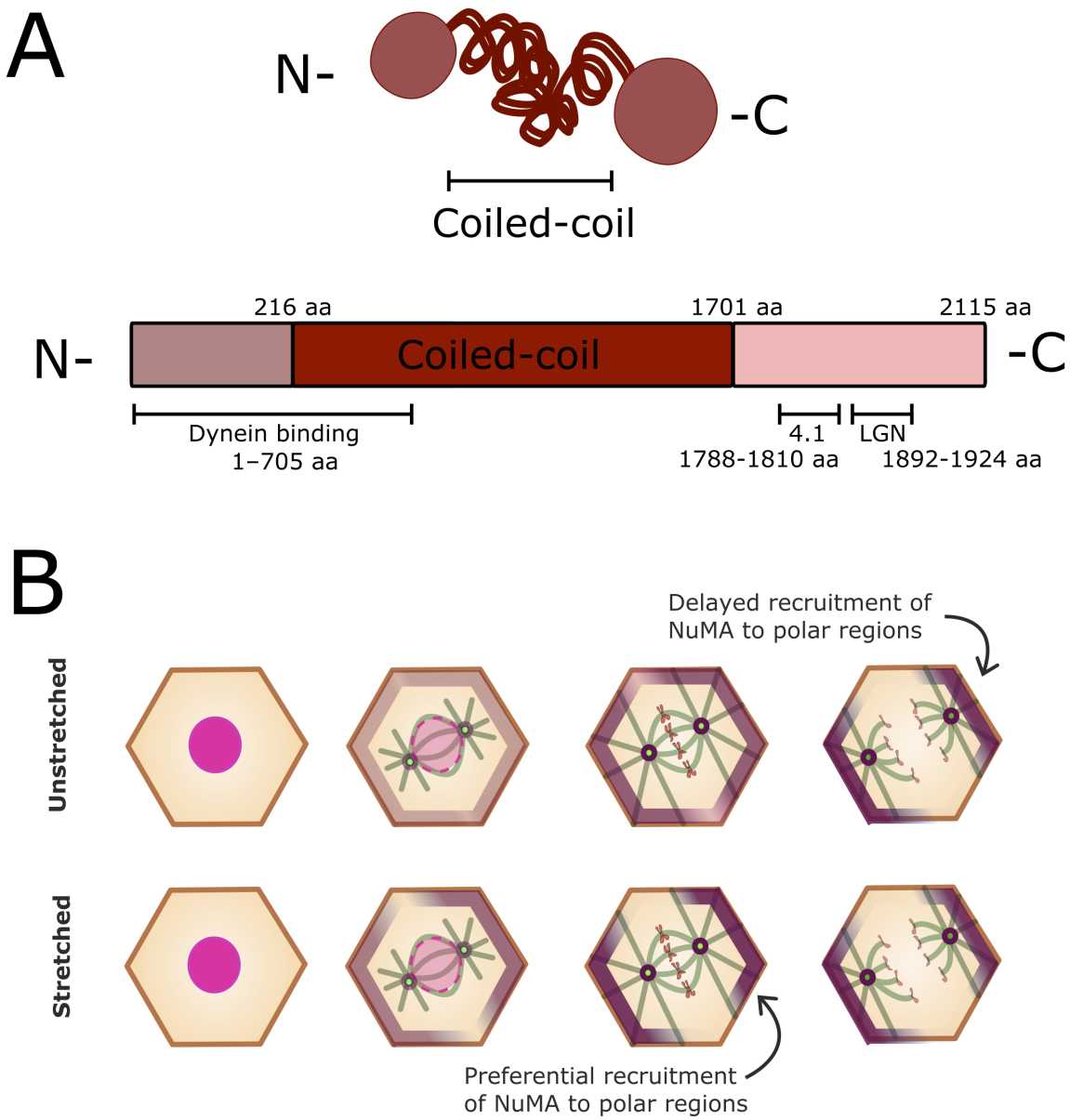

Figure 1.6. **NuMA's key binding domains and cortical localisation**. A) The structure of NuMA showing two golobular N- and C- terminals and a large central coiled-coil region. The dynein, 4.1 and LGN binding domain locations along NuMA. aa - amino acids. B) The temporal recruitment of NuMA to the cell cortex in unstretched and stretched cells, as seen in unpublished work from the Woolner lab [27].

binding affinity.

1.4.4 Implications in tension-sensitive spindle orientation

NuMA clearly has a central role in spindle orientation, as disruption of the NuMA-dynein-MT interactions reliably result in spindle orientation defects [12], [16], [26], [43], [64], [103]. What is less clear is NuMA's role in tension-sensitive spindle orientation.

Bosveld *et al.* (2016) observe NuMA's *Drosophila* homolog Mud at the TCVs of the pupal notum epithelium. At the TCVs, Mud colocalises with tricellular junction proteins, which connect neighbouring cells lie at the TCVs in this tissue, and are thus locations likely to contribute to neighbour-neighbour force communication [43]. Laser ablation of the micro-

tubules of the mitotic spindles showed that pulling forces towards the TCVs were reduced upon depletion of Mud, as characterised by the recoil velocity of the centrosome connected to the ablated microtubules. This increased pulling force towards the TCVs was simulated mathematically, showing that amplification of pulling forces at the sites of Mud localisation are sufficient to orient the mitotic spindle according to TCV anisotropy [43]. However, unlike Mud, which localises to the cortex at the TCVs throughout mitosis, NuMA is only localised to the cell cortex during metaphase [27], [81]. In the Woolner lab, recent unpublished quantitative analysis of the localisation of GFP-NuMA in *Xenopus laevis* shows that NuMA localises preferentially to the cell edge rather than the TCVs, with an accumulation that builds through metaphase until anaphase [27]. Thus NuMA's dynamic localisation increases the complexity of spindle positioning in vertebrate tissue. Further, the temporal accumulation of NuMA to the polar cortex (aligned with the spindle pole-pole axis) was found to be tension-sensitive, showing an earlier relocation from the equatorial cortex (aligned with the metaphase plate) to the polar cortex in stretched tissues compared to unstretched tissues (Figure 1.6B) [27]. Thus NuMA's localisation is not only dynamic but linked to applied tensions.

Keratinocytes also showed a NuMA-mediated spindle reorientation response which was required to reorient spindles under a uniaxial stretch [103]. The application of stretch resulted in NuMA localisation perpendicular to the axis of stretch [103], a phenotype which has also been observed in stretched MDCK monolayers [12]. Knockdown of NuMA resulted in a loss of reorientation of the spindle along the stretch axis [103], indicating that NuMA may be important for stretch-induced cell division orientation. The localisation of NuMA was shown to depend upon its 4.1-binding domain, which stabilises NuMA's interaction to the cortex when associated with LGN. This stabilisation function was shown by deletion of the 4.1 binding domain, which resulted in an increased mobility of NuMA at the cortex and impaired spindle orientation. Thus it is suggested that NuMA requries association with both LGN and F-actin through the 4.1 binding domain to function correctly [103].

Interestingly, Kelkar *et al.* (2022) show that an induced localised cortical contraction is sufficient to displace the mitotic spindle without affecting the localisation of NuMA [83]. NuMA was depleted in these cells by application of the chemical inhibitor MLN8237 which targets Aurora-A kinase activity [83], [123]. As Aurora-A is required to phosphorylate NuMA at the spindle poles, leading to its relocation to the cell cortex, MLN8237 reduces cortical localisation by inhibiting sequestering from the poles [118]. Interestingly, while the localisation of NuMA in these cells was not a predictor for spindle orientation, depletion of cortical NuMA resulted in a cessation of spindle rotation. Rotations were considered to be a result of pulling forces which were reduced upon cortical contraction [83]. Actomyosin contractility has been shown to not affect NuMA localisation [103], thus this suggests that contractile forces may decrease NuMA's function without affecting its localisation.

Recent unpublished work from the Woolner lab shows that NuMA may respond specifically to anisotropic tension [27]. Tarannum (2022) showed in their recently submitted thesis that cell division orientation with the cell long axis is improved in *Xenopus laevis* animal cap

tissue subject to a uniaxial stretch, and that this improvement depends on NuMA. Depletion of NuMA, using a morpholino knockdown approach, disrupted division orientation alignment with cell shape. By analysing division orientation in stretched and unstretched tissues subject to a NuMA knockdown (KD), it was shown that NuMA-mediated spindle orientation was most important for stretched tissues to align their divisions with cell shape. Depletion of NuMA caused spindles to align less well with cell shape, but only in stretched, and not unstretched, tissues [27]. However, analysis of the spindle translational velocities showed that spindles moved more slowly in the absence of NuMA, and this effect was independent of the applied tension [27]. Interestingly, the NuMA-mediated spindle reorientation specifically responded to anisotropic tension rather than isotropic tension, further complicating our ideas for NuMA's functioning mechanism [27].

While NuMA is a key player in tension-sensitive spindle orientation, its specific response to anisotropic rather than isotropic tension, combined with the spindle velocity response both with and without stretch, raises questions about the mechanisms by which NuMA may be functioning. We wish to explore NuMA's function as a spindle orientation factor by using mathematical modelling to elucidate the factors which may be perturbed under stretch.

1.5 Mathematical modelling of the mitotic spindle

To help determine NuMA's precise role in tension-sensitive spindle orientation and to understand how tissue stretch regulates spindle dynamics more generally, we turn to mathematical modelling. Mathematics allows for the disentanglement of correlative and causative effects in systems where the decoupling of processes or mechanisms is difficult. By building a model based on current assumptions and testing this model in experimentally replicable conditions, the model — and the initial assumptions on which the model was built — are put to the test. A number of mathematical models of spindle orientation have thus been developed and explored in various ways and the many mechanisms suggested for correct cell division orientation make for a rich literature of the various methods used to test these mechanisms [124]–[126]. However, NuMA's role in this process has not yet been fully explored. Here we introduce a number of the mathematical models that have been used to describe the components of the mitotic spindle and its positioning in the cell.

1.5.1 Cell division orientation due to geometry of the cell

Cell division orientation has been studied in terms of the cell and tissue geometry [15], [127]. In the epithelial layer of *Xenopus laevis*, the cells form a polygonal lattice due to their close packing. Shape tensors may be defined to describe the cell shapes in terms of the cell area, the cell perimeter, and the tricellular vertices (TCVs, the points where 3 or more cells meet). These tensors allow the principal axes of the shape to be determined (the short and long axes of the cell), from which the cell circularity may be extracted as the ratio of their corresponding eigenvalues. By using these shape measures, it was shown that

the cell division orientation aligned well with the long axis of the cell determined from the TCV shape tensor [15]. Interestingly, over-expression of adhesion-protein cadherin resulted in cell division orientations which aligned best with the long axis of the cell determined from the perimeter shape tensor instead. Cadherin over-expression also led to a redistribution of cortical LGN from the TCVs to the entire cell edge [15], suggesting that the shape tensors may be used to describe the distribution of spindle-orienting machinery within the cell in order to predict the resulting cell division orientation. This model may therefore be used to determine which spatial localisation of spindle-orienting components dominates in cells, though the details of the components and how they act to produce a spindle effect are omitted. Thus a more intricate model is needed to describe the mechanical processes happening inside the cell.

1.5.2 Modelling the microtubules

The microtubules (MTs) are the structures which make up the mitotic spindle. They nucleate from the spindle poles (the centrosomes) at their minus ends, and grow at their plus ends towards either the cell cortex (astral MTs) or the spindle equator. At the spindle equator they interact with the chromosomes (kinetochore MTs) or MTs from the opposite pole (interpolar MTs) (Figure 1.3A) (see section 1.2). As MTs are a core component in the cell division machinery, their correct mathematical description is vital to be able to create a working model of the movements of the mitotic spindle. Here we introduce some of the ways MTs have been modelled. Many more studies have been done outside of the direct mitotic spindle context due to their role in positioning other cellular components, such as the nucleus prior to nuclear envelope breakdown and the formation of the spindle pole [19], [71], [128]–[130]. These studies provide insights which may be applied to the action of MTs during cell division because the processes are similar. The formation of the bipolar spindle and the various forces involved are well studied [124], particularly with reference to the stabilisation of the chromosomes and the subsequent entry into the spindle-assembly checkpoint [131], [132]. However this aspect of microtubule function is not the subject of this study, thus we instead focus on the modelling of microtubules in a force-generation context.

MTs are long, thin filaments with a high flexural rigidity and thus may be considered to be relatively rigid structures over the length scale of an average cell [133]–[135]. It has been shown experimentally that a MT of length L will buckle under an applied load if the load exceeds a critical value f_E [133], [136], given by

$$f_E = a\frac{\kappa}{L^2}, \tag{1.1}$$

for flexural rigidity κ (units Nm^2) and constant a. The value of a varies based on the MT nucleation point (a smaller value if hinged, where the MT may rotate freely about its end, or a larger value if clamped, where the angle of the MT end is held constant (Figure 1.3B)) [137]. Then the maximum resistive force a MT may supply is f_E, and this is increased for

short, rigid, clamped MTs. The high flexural rigidity then gives MTs the ability to provide pushing forces against approaching surfaces and boundaries.

In a mathematical study into the elasticity of interpolar and kinetochore MTs, the flexural rigidity was cited as being elevated due to the bundling of MTs in these populations by crosslinking proteins, with further elevation of rigidity if the bundling interactions were strong [135]. The elastic stiffness K can be predicted *in silico* by solving for the shape of a filament with flexural rigidity κ being acted on by a range of tangentially applied forces F. Then by Hooke's law

$$K = -\frac{\Delta F}{\Delta l} \tag{1.2}$$

for ΔF the difference in force magnitude required to produce a difference Δl in inward displacement between the ends of the MT [135]. This elastic stiffness is shown to decrease for: i) bundles of fewer MTs, ii) weaker cross-linking between MTs within the bundle, iii) hinging at the nucleation point, and iv) buckling [135]. Results i) and ii) arise due to their effect in decreasing the flexural rigidity of the MT bundle, while iii) was described above in its augmentation of the critical force leading to buckling.

The length-dependence of the buckling force is additionally complicated by the dynamic nature of MTs. They go through phases of growing and shrinking, termed 'dynamic instability' [51], [52]. Dynamic instability (described in section 1.2) is driven by GTP, which is incorporated into the MT plus end via binding to tubulin dimers, and eventually hydrolysed within the micotubule lattice into GDP. The structure of the MT lattice is stable for GTP-tubulin subunits, promoting growth, and unstable for GDP-tubulin subunits, promoting shrinkage [46], [51], [52]. Microtubules are considered to have a GTP-cap, a sequence of tubulin dimers at the growing tip which are bound to GTP and which stabilise the MTs growth. Loss of the GTP-cap, by reduced binding of new tubulin subunits or by hydrolysis of the cap into GDP, results in rapid depolymerisation of the microtubule (Figure 1.3C) [46], [51], [52]. Monte Carlo kinetic simulations based on the binding affinities and disassembly rates of GTP and GDP sub-units show that biologically-relevant rate constants result in slow growth of microtubules with GTP-caps, and the rapid disassembly of microtubules whose caps have been hydrolysed into GDP [138]. Both of these phases were shown to exist in a wide range of tubulin concentrations and highlighted that the biphasic behaviour could be explained entirely by the binding affinities of the component sub-units.

Mogilner and Oster (1999) described the growth-related pushing forces using a Brownian Ratchet theory, such that thermal fluctuations between the barrier and the end of the growing microtubule allow for the addition of tubulin sub-units which create a force on the barrier [139]. The stall force, the maximum force a growing microtubule may exert on a barrier in this way, has been predicted to depend upon the number of filaments which make up the microtubule [139]–[141] as well as the strength of the lateral interactions between the filaments [141]. This mirrors the dependence of the flexural rigidity of a MT bundle on the number of MTs and the strength of the cross-linking proteins [135]. The predicted force-velocity relationship due to tubulin addition matched those measured experimentally [136].

Together, these stall forces may create pushing forces against cellular components in order to orient the mitotic spindle, and stochastic mathematical models may be used to describe the pushing effect.

While the growth of a microtubule may be modelled mathematically to as fine a scale as the stochastic addition of individual tubulin sub-units, when more macroscale properties of the structure are considered, individually modelling each microtubule becomes laborious and computationally expensive. This is especially true when considering the interactions between whole microtubules and other cellular components. As such, cellular-level models often take the main results of the molecular-level models and represent them in more simple forms which capture the most important characteristics. The dynamic instability of microtubules can be described alternatively by considering the relative rates of catastrophe (the growing→shrinking transition) and polymerisation (the shrinking→growing transition), combined with experimentally-derived growing and shrinking velocities [137], [142], [143].

Dynamic instability [137], [143] has been implicated in displacement mechanisms for the MT organising centre (MTOC) from which the MTs nucleate (e.g. the centrosomes). The MTs in the growing phase are considered to grow against a barrier and supply a force equal to their stall force, before undergoing catastrophe and entering their shrinking phase [137], [143]. The dynamic catastrophe and recovery ensures that a central stable point exists for the spindle, because as long as nucleation and MT growth rates are constant in all directions, then at the centre of a cell there will be equal probability for pushing events to occur from all directions. In the case of an off-centre spindle, then the side closest to the cell membrane will have a larger chance of experiencing pushing events as more MTs can grow and contact the cortex in a given time [137]. This dynamic MT array effect can be thought of as a spring, where the spring constant is inversely proportional to the distance of the spindle from the cortex such that smaller MTs act as stiffer springs that can thus provide more force. The simplification of modelling MTs as restoring springs has been used previously [78]–[80]. However, the ‘spring system’ described in [80] reads similarly to a force from a potential energy: the further away from the centre of the range of motion the MT-attached spindle pole moves, the greater the restoring force provided. As cell edge locations are not specified in this 1D model of spindle pole motion, the restoring force could perhaps best be described as a pulled, extended spring from the centre of cell, rather than a pushing spring from the compressed microtubules.

In all, it has been determined by the use of stochastic simulations [139], [141], [142] as well as deterministic models [137], [139] that dynamic instability is an intrinsic behaviour of MTs that emerges as a result of the binding and hydrolysis of GTP-tubulin at the growing plus ends of microtubules. This dynamic instability is required to produce pushing forces against stationary barriers and can be used to calculate an effective spring constant for the MT array. Additionally, external forces may bend MTs, which have also been shown to respond elastically [133], [135]–[137] Taken together, the dynamic instability and elasticity of microtubules gives them an overall centring mechanism within the cell due to their abil-

ity to push against rigid obstacles, acting as a restoring spring which could be incorporated into a model as a general centring force.

1.5.3 Modelling motor proteins

Motor proteins are also a source of forcing on the mitotic spindle. The motor proteins dynein and kinesin interact with the MTs of the spindle and produce forces based on their direction of motion. Dynein, a minus-end directed protein, has motion toward the centrosome, while kinesin is a plus-end directed protein and thus has motion away from the centrosome. The simultaneous binding of dynein and kinesin to MTs and other structures within the cell (such as the cell cortex or cargos within the cytoplasm) creates a force on the microtubule which can then be transferred to the centrosome [47]. Indeed, the magnitude of these forces and the resulting effect on spindle orientation are significant, such that in large cells where the MTs are too small to contact the cell edge, motor proteins are determined to be responsible for spindle centring [70]. As kinesins are generally thought to have more of an impact on the establishment of the spindle shape rather than its position, they will be largely omitted from the future discussion: we will focus instead on the impact of dynein and the different ways it has been modelled.

Many mathematical models of cell division are based solely upon the pulling action of dynein [19], [43], [45], [144], while others consider dynein to be just one contribution in a balance of pulling and pushing forces [129], [137], [143], [145]–[147]. We again note that some of the models introduced are concerned with the positioning of the nucleus or single centrosomes as opposed to mitotic spindles, as the mechanisms are considered to be similar. We will introduce how pulling forces by motor proteins have been described and implemented in other mathematical models.

One incorporation of dynein-related forces is by way of a force that is proportional to MT length [19], [130], [143], [148]. This length-dependence fits well with a cytoplasmic pulling description, where dynein transporting cargo along an MT creates a force directed away from the centrosome due to drag (opposite to the direction of dynein motion). The length-dependence comes in here as more dyneins may load onto a longer MT. Kimura and Onami (2005) studied the positioning of the pronuclear complex (PNC) by comparing pushing by microtubules and pulling by cytoplasmic dynein [130]. They show that the models of pulling best replicated the distance-time graphs of the PNC obtained through experiment [130]. Cytoplasmic pulling could lead to centring as a spindle perturbed Δx to the right from the centre of a symmetric cell will have MTs up to $2\Delta x$ longer on the left than the right. Thus more dyneins will be able to load onto the left and create a net pulling force to the left, back to the centre of the cell. Pulling by cytoplasmic dynein has been shown to lead to the centring of centrosomes in the *C. elegans* embryo [71].

Alternatively, pulling by dynein has also been described in terms of concentrations. Increasing the concentration of ‘force generation’ at experimentally-identified sites of mo-

tor protein activity [43], [45], [148] best describes cortical force generation by cortically-located dynein (by interactions with LGN/NuMA or Pins/Mud).

Describing cortical and cytoplasmic pulling in these ways simulates the net effect of the pulling force without detailed concern for the biological processes which create the forces. More detailed models incorporate pulling by considering the stall force of dynein as a parameter in the determination of the force it exerts along the microtubule [128], [129], [144]–[146]. That is, in general

$$f_{\text{dyn}} = f_0 \left(1 - \frac{v}{v_0}\right) \quad (0 \leq v \leq v_0) \tag{1.3}$$

for some stall force f_0, unloaded dynein walking velocity v_0 and the magnitude of the loaded velocity of dynein v, loaded with a force f_{dyn}. The stall force is the applied force at which a motor protein will cease its motion, thus when $f_{\text{dyn}} = f_0$, then $v = 0$. This force determination may be used for cortical dynein [144]–[146] and cytoplasmic dynein [128]–[130], [145], [146]. A similar formulation for dynein pulling in *C. elegans* describes the velocity of cortical dynein along a microtubule as

$$v = v_0 - \frac{kv_0}{f_0} y - \frac{\mathrm{d}z}{\mathrm{d}t} \tag{1.4}$$

for k the stiffness of the elastic linker with extension y which binds dynein to the cortex, with $\frac{\mathrm{d}z}{\mathrm{d}t}$ describing the velocity of approaching spindle pole (and thus the velocity of the microtubule) (Figure 1.7) [80]. This can be compared to (1.3) by writing the force $f = ky$, then

$$f = f_0 \left(1 - \frac{v}{v_0} - \frac{1}{v_0}\frac{\mathrm{d}z}{\mathrm{d}t}\right). \tag{1.5}$$

This force is different to f_{dyn} alone as it incorporates pulling from dynein's walking velocity as well as dynein's strength of binding to the cortex via GPR-1/2/LIN-5, which is here taken to have an elastic response. We will explore the model in [80] in more detail in Chapter 4.

The affinity for dynein's binding and unbinding is incorporated explicitly in few models [80], [128], [145], [146]. It has been shown that dynein forms a slip bond with microtubules [61], therefore increased loads should also increase the unbinding rate. This can be accounted for with an unbinding rate with an exponential dependence on load

$$\omega_{\text{off}} \propto e^{f/f_{\text{off}}}, \tag{1.6}$$

where ω_{off} is the unbinding rate and f_{off} is the characteristic force which controls the sensitivity of unbinding to load [80], [145], [146]. The affinity for binding has also been included in some studies, where binding is increased in previously-identified regions of high localisation of LGN/NuMA/Dynein (or their homologues) [145]. This is similar to the description of pulling by way of concentrations, by allowing the concentration of pulling motors to accumulate as a result of the higher binding affinity rather than by an artificial pulling

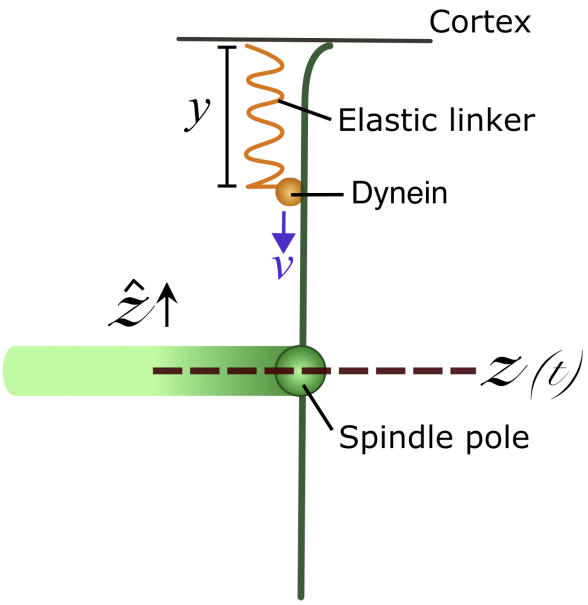

Figure 1.7. **Modelling dynein attachment to the cortex with an elastic linker**. Diagram showing how dynein is modelled as an motor protein head attached to the cell cortex via an elastic linker with extension length y. Dynein binds with microtubules (green line) extended from the spindle pole, which lies at position $z(t)$. The velocity of the microtubule-bound dynein away from the cortex, v, depends on the relative velocity of the spindle pole and on the restoring force provided by the elastic linker [80].

from those identified regions.

As the description of force generators become more complex, the methods by which the resulting force acts on the spindle are calculated will become more complex to accommodate, in particular when variable binding and unbinding affinities are of concern. Simpler descriptions in the form of length-dependent or concentration-based forces lend themselves to being solved analytically in order to determine the states of lowest energy for the system to reside in, while complex dynamic interactions between motors travelling along microtubules with velocities require numerical and time-dependent approaches to solving the resulting spindle dynamics.

Following this introduction into methods of describing both microtubules and force generators, we introduce how combinations of pushing through microtubules and pulling through motor proteins have been incorporated studies into the correct positioning of cellular components such as the PNC, centrosomes, and mitotic spindle.

1.5.4 Modelling positioning due to pushing and pulling

The above sections have highlighted cortical pushing (by MTs), cortical pulling (by cortical dynein) and cytoplasmic pulling (by cytoplasmic dynein) as the main mechanisms by which the stable orientation and positioning of the mitotic spindle within the cell may be achieved. Indeed, it could be argued that all three play an important role, though often only one or two are considered to dominate in particular circumstances. For example, in very large cells

such as the *Xenopus laevis* or zebrafish single cells, the astral MTs may be unable to contact the cortex [70] and thus unable to produce or be subject to any cortical forces. Thus cytoplasmic pulling is expected to dominate in this regime.

Nazockadast *et al.* (2017) study the hydrodynamic interactions between MTs while positioning the PNC, comparing the resulting cytoplasmic flows from purely pushing, purely cortical pulling and purely cytoplasmic pulling regimes [128]. This model includes: i) pushing from microtubules by treating them as hinged linear springs; ii) cortical pulling by dynein with constant unbinding rates and spatially-varying binding rates based on previous observations of locations of increased binding of dynein, and a force as in (1.3); and iii) cytoplasmic dynein with constant binding and unbinding rates and a force as in (1.3), with an additional viscous term to account for the transport of a cargo through a viscous fluid. The resulting flows were similar for both cortical forcing methods (pushing and pulling) but markedly different for the cytoplasmic pulling model. Experimentally, the cytoplasmic flow has not been fully investigated, although if all three play a part in the positioning of the PNC then likely a flow field combining features from all three regimes would be observed. However, other studies suggest that microtubule pushing and cytoplasmic pulling are the dominant forces in the centring of the PNC [129]. As the flow fields for cortical pushing and pulling were very similar, it is likely that the observed flow fields in a combined pulling and pushing mechanism would look similarly. The positioning of the PNC is a smooth centring process with a translation and a rotation to the final position, and this is recapitulated in these models [128], [129]. However the movements of the mitotic spindle in *Xenopus laevis* tissue cells have been shown to be dynamic, particularly toward anaphase [77], thus it may not be appropriate to directly apply the models of the PNC to the spindle.

To determine the cell division orientation, some studies calculated the torque incident on the spindle due to pulling forces [19], [43], [45]. In these studies, the pulling forces were assumed to come from either MT length-dependent forces [19], or concentration-based forces [43], [45]. Common to all three is that the pulling forces were assumed to be static, and that the probability distribution of spindle orientations, $P(\alpha)$ were of the form

$$P(\alpha) \sim e^{w/d} \tag{1.7}$$

for spindle orientations α, w the energy due to torque, and d a noise parameter. From this the most likely spindle orientation could be determined on a cell-by-cell basis from an energy minimisation perspective. While these models were successful in determining the cell division orientation for a variety of interesting geometries, we highlight that due to the omission of explicit force sources, it is still unclear whether pulling alone is responsible for the movement of the spindle. In particular, the length-dependent force employed by Minc *et al.* (2011) may be a combination of pushing and pulling, where pushing is increased in shorter microtubules and thus the balance of pushing and pulling is such that there is a net decrease in pulling force. Alternatively, length-dependent forces may be describing cytoplasmic pulling alone [19]. The precise mechanism behind this length-dependent force is thus unclear. Interestingly, increasing pulling forces based on the intensity of GFP-Mud,

a NuMA homologue, at the tricellular vertices of the cells in *Drosophila* tissues resulted in division orientations which closely matched experiment. Alternatively, cells cultured on adhesive micropatterns such that they took the shape of interesting geometries also divided in orientations that matched closely with simulated cells when pulling forces were enhanced at regions of high retraction fibre density [45]. Together, these confirm that increased pulling forces at locations of known dynein accumulation may orient the spindle. Though again, the mechanistic detail is lost in the simplification of the forces, as explicitly MT-based forces are not described. Further, the dynamic detail of the spindle positioning is lost. Interestingly, Corrigan *et al.* (2005) use a similar method of force amplification at discrete cortical locations in rounded cells to produce noisy rotational spindle dynamics [149]. Their stochastic description of cortical cue activation and de-activation simulates noisy rotation toward the long axis as defined by the anisotropy in the placement of the cortical cues [149], highlighting the importance of cortical pulling elements in creating dynamic movements of the spindle. However the time-resolution of these dynamic movements is low, reflecting well the dynamics of spindles imaged at frame intervals of 3 minutes. Interestingly, despite the stochastic model timestep being orders of magnitude smaller than this (0.2 s), the model matched these dynamics well [18], [149]. This is interesting as dynamic spindle oscillations have been observed at finer timescales of imaging in other systems [77]–[79], suggesting that cortical cues alone cannot account for the dynamic spindle oscillations at finer time resolution.

Akiyama *et al.* (2018) propose a model which includes both length-dependent and concentration-based forces on the spindle [148]. This model accurately reproduces cell division orientations leading to cyst and early embryo development, while also having a temporal element to the determination of the spindle pole positioning [148]. The orientations of the spindle were determined by describing the concentration of active cortical force generators (dynein) by a function G which varies according the locations of adhesive regions of the cell, while also incorporating a MT-length dependence on the strength of the pulling force from contributions of cytoplasmic dynein [148], [150]. By describing the central spindle array (centrosome→centrosome) as a spring, both 2D and 3D motion of the spindle is determined and its stable end-position taken as the orientation of the cell division. The relative simplicity of this model highlights that detailed descriptions of the mechanisms involved in positioning the spindle are not required to successfully determine the final orientation of cell division. However, once again the spindle dynamics which have been observed experimentally elsewhere [8], [18], [79] may require a more detailed mathematical description.

Li and Jiang (2017) use a stochastic model to explicitly describe the interactions of MTs with chromosomes, motor proteins and boundaries to create self-assembled spindles within cells [146]. This model has been used and adapted to investigate spindle orientation. Using band domains of adhesion where the binding rate of dynein is increased, MTs and chromosomes self-assemble into a mitotic spindle and orient within the simulated cells as a result of a combination of pushing forces and dynein-mediated pulling forces at both the cortex

and the cytoplasmic domain. Dynein was considered to unbind with a load dependence (1.6), and produce a force as in (1.3). This resulted in spindles which aligned with the adhesion sites [145] similarly to what has been shown in simpler models [43], [45]. However, the spindle was shown to align with the cell long axis instead if the cell was particularly elongated, with the adhesion sites located away from the long axis [145]. We suggest this competition between cell shape and cell adhesion arises due to the adhesion-independent pushing of the microtubules, which will try to align the spindle along the long axis of the cell, vs. the pulling by dynein which is elevated at sites of increased adhesion. Then for very elongated cells the microtubule pushing will 'win' against the pulling from dynein. Interestingly, the simulated spindles were shown to form already in line with their final division axis, with no characteristic movements of the spindle once assembled. This is in contrast to what has been observed of spindle dynamics experimentally [8], [77], [78] which leads to the question of what is different between the assumed interactions of the component structures used in [145] and in these cases where prolonged spindle dynamics are observed. The large-scale stochastic model described in [145], [146] has a great number of variables which may be adjusted to account for experimentally observed spindle dynamics, but elucidating exactly which parameter is the most important would be difficult. We thus turn to the model described by [80], which looks specifically at the balance between pushing and pulling forces at the cell cortex, such that we might determine if it is this balance that is the most important for creating dynamic spindle movements.

The Grill *et al.* (2005) model [80] is a one-dimensional model which describes the oscillation of the posterior pole of the spindle in the first cell division of *C. elegans*. The oscillation arises due to the interactions of the force generators (dynein) attached to the cortex by an elastic linker (GRP-1/2/LIN-5), with a constant binding rate and a load-dependent unbinding rate similar to (1.6), though it is instead implemented as an extension-sensitive unbinding rate, as the loading force is due to the load provided by the bound elastic linker $f = ky$, with extension y and elastic stiffness k. Dynein does not provide the force on the mitotic spindle alone, but works together with the elastic linker to pull on the spindle with a force given by (1.5). By considering separate populations of dynein-linker complexes (termed 'force generators') which exist above and below the spindle pole, Grill *et al.* (2005) describe how the probabilities of force generators binding and unbinding with extensions y evolve in time using a system of Fokker-Planck equations. The spindle pole is positioned by a combination of pulling from the populations of force generators and a restoring force which is considered to arise from the bending elasticity of MTs [80]. However, as the restoring term to the spindle pole position z is given as $-Kz$, for MT bending elasticity K, we note that rather than a bending elasticity of compressed MTs, this best describes the situation of a spring extending from the cell centre line at $z = 0$, as the MT length and subsequent compression is not explicitly considered. Despite this, the model produces oscillations of the mitotic spindle pole with amplitudes and periods which match experimentally observed oscillations, though the experimental oscillations were much noisier. The implementation of a stochastic simulation also seemed to produce similar oscillations, though the details of this stochastic simulation were omitted from the paper and so cannot be prop-

erly assessed. Further, an approximation to the Fokker-Planck equations in the form of an ODE model was introduced and used to determine the presence of a Hopf bifurcation at a critical number of force generators, which is in line with experimental observations of a cessation of oscillations upon the depletion of dynein [78]. The reduction of the PDEs to the ODEs however is very briefly described, and the full behaviour of the models for different parameters were not explored. Schwietert and Kierfield (2020) use Fokker-Planck equations to describe emergent lateral oscillations of the chromsomes at the spindle equator due to kinetochore-microtubule attachment [151]. Using similar equations, the action of a population of kinesins in displacing a microtubule from a harmonic trap has been described, with the emergence of interesting dynamics such as relaxation oscillations [152]. Indeed, the single population of force generators interacting with a harmonic trap can give rise to sub-harmonic oscillations due to the complex coupling between the MT position and the collection motion of the motors [153]. The addition of an opposing populations of force generators to generate collective motions is likely to have similarly interesting dynamics which we wish to explore.

As the model introduced by Grill *et al.* (2005) describes dynamic movements of the spindle well, and also incorporates the slip-bond behaviour of dynein as well as a restoring force to denote the presence of MTs, we aim to fully explore this system in order to determine whether or not it may be used to describe the dynamics of the mitotic spindle in *Xenopus laevis* tissue cells. We believe that this model includes sufficient detail about the action of the sources of the forces acting on the mitotic spindle to create a dynamic response such that it can be used to direct us to the parameters which are most important to elicit dynamic spindle movements.

1.6 The early gastrula *Xenopus laevis* animal cap as a model system

Xenopus laevis is a widely used model organism for cell and developmental biology [154], whose presence in the lab has led historically to understanding key processes such as nuclear envelope breakdown and spindle formation [155]. It has been utilised in a number of studies into cell division and mechanical stress during development [156]. The genome of *Xenopus* has been sequenced and shown to have structural similarities to the human genome [157], [158], making *Xenopus* a choice for the study of human diseases. A number of studies highlighted in this thesis are based upon HeLa cell lines [13], [18], [45], [64], [76], [84], which are robust, highly proliferative, and well studied [159]. However HeLa cells are genetically abnormal, containing a hyper-triploid chromosome number as well as being abnormally invasive [160]. Additionally, HeLa cells have been shown to produce multipolar spindles and demonstrate chromosome fragmentation upon division, even prior to perturbation by miRNA-targetted knockdown microtubule-associated proteins [161]. As we wish to explore the dynamics of the mitotic spindle, a system with a mitotic spindle and cell division process more representative of a ‘regular’ system is preferable. It is important to note also that the HeLa cell line is derived from a cancer cell [162], then the results of these studies

may be applicable to cancerous, but not healthy, cells. To fully understand the processes underpinning cell division *in vivo*, animal models must be utilised.

A female *Xenopus* may be induced by hormone injection to lay eggs, and a single clutch may contain upwards of thousands of eggs which are fertilised and develop externally and synchronously [157]. This large brood size, combined with highly regulated developmental timings, facilitates the study of early embryo development by providing a large number of test subjects to observe. The *Xenopus* egg has a clear animal-vegetal axis prior to fertilisation [28], and this axis coincides an externally-observable pigment distribution which is maintained through early development [163]. For imaging purposes, albino strains of *Xenopus* may be used. The transparency of albino embryos lend themselves to direct imaging, for example, neuronal growth in the developing brain can be easily imaged *in vivo* for studies into developmental seizures [164], [165].

Both *in vitro* and *in vivo* analysis can be done by utilising *Xenopus*. Egg extracts can be produced by centrifuging *Xenopus* eggs, which contain an abundance of proteins which are important for driving early cell divisions and are even capable of performing DNA repair outside of the cell [166]. Of particular use is the ability to arrest the fertilised *Xenopus* eggs at a particular stage of the cell cycle before centrifuging [167], while chemical addition of ions such as calcium may be selectively introduced to the extract to push the system into later stages of the cell cycle for controlled progression through the various stages of the cell cycle [168]. Egg extracts have been used to study a range of processes, including but not limited to, DNA repair [166], nuclear envelope assembly [169], mitotic spindle assembly [167], [170], and the formation and regulation of mitotic checkpoints [171].

The information gathered from *Xenopus* extracts is powerful, as *Xenopus*-specific findings can be taken inside the dynamic, developing tissues of the embryo. Indeed, for studies into morphogenesis and mechanobiology, *Xenopus* has proven to be an invaluable tool and its morphogenetic processes are well defined. For example, the large-scale cell movements which occur during gastrulation are well defined within the *Xenopus* embryo, where a population of cells at the involuting marginal zone (IMZ) move inwards and back toward the blastocoel roof as a result of apical constriction of neighbouring bottle cells (Figure 1.8A-C) [3]. Convergent extension occurs by thinning of the IMZ radially and extension of the IMZ along the animal-vegetal pole, leading to an elongated body axis [3]. Thus, mechanobiological processes are key during embryonic development. The forces produced during convergent extension have been probed by using *Xenopus* explants adhered to a fibronectin-coated 'sled' attached to a fibre-optic probe, whose deflection can be used to measure the pulling forces produced by the converging cells [172]. This tractor pull assay is just one form of mechanical measurement which the *Xenopus* embryo is amenable to. Mechanical stresses may be measured by wounding via blade or laser ablation, where the recoil velocity magnitude and direction provides a measure and map of the forces acting on the damaged site [173]–[175]. Indeed, laser ablation has been used to show that cells expressing the $kRas^{V12}$ oncogene are hyper-contractile and generate anisotropic strain to surrounding tissue cells in *Xenopus laevis* embryos [175].

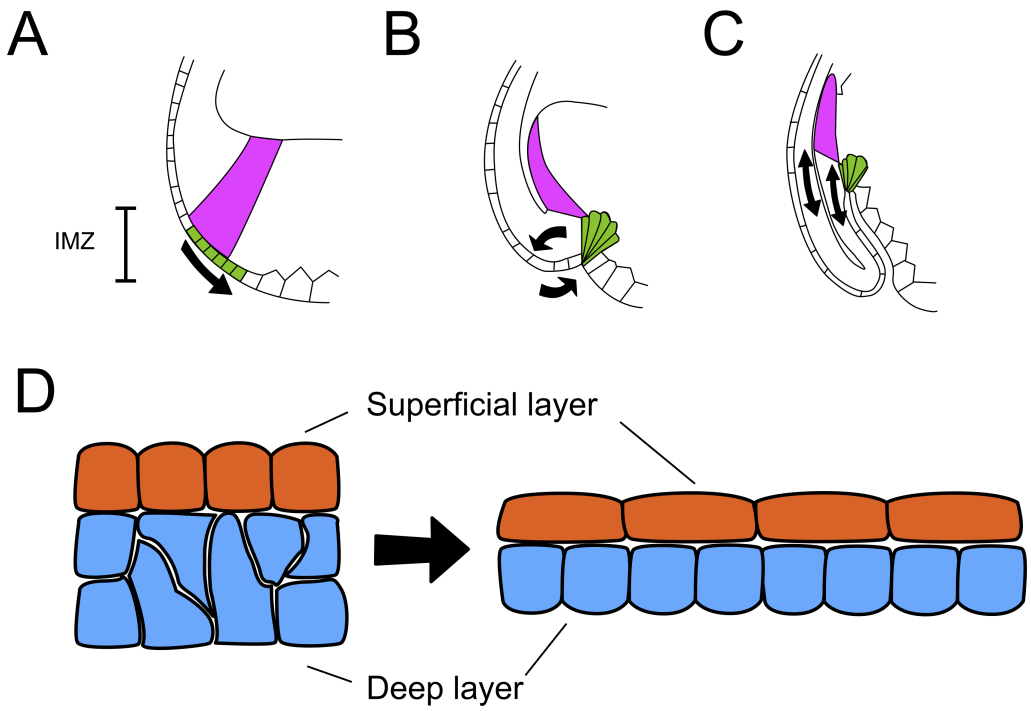

Figure 1.8. **Large scale movements in the *Xenopus laevis* embryo**. A-C) Movements of the involuting marginal zone (IMZ) during gastrulation due to apical constriction of the bottle cells (green) leading to involution of the leading edge mesendoderm (pink). A) Bottle cells contract, and B) involution is initiated, leading to C) spreading of the mesendoderm along the blastocoel roof and convergent extension of the IMZ. D) During epiboly, intercalation of the deep layers of the animal cap (blue) leads to stretching of the tightly adhered superficial cell layer (orange). Figures adapted from [3].

Increasingly, non-destructive techniques have been used to probe the mechanical environment of *Xenopus* cells. Cantilever deflection by growing tissues can be used to provide quantitative measurements of tissue stiffness and contractile forces, a method used to probe the forces present in blastopore closure [176]. Strain mapping by analysis of cell shape and movements can be used to infer relative forces acting in different stages of development qualitatively [176]. The vertex model also provides a non-invasive method of inferring local forces present in a tissue by analysis of the shape and size of tissue-bound cells [15], [21]. The vertex model has been used specifically in the *Xenopus* system to study cell division orientation in the epithelial layer of the animal cap tissue, relative to the local and global forces experienced by the dividing tissue cells [15], [175]. The cells in this epithelial tissue do not round upon during mitosis and tend to divide symmetrically [3], [15], then a two-dimensional vertex model is an acceptable description of this system without substantial loss of accuracy in predictions [15], [21], [175].

As well as probing the mechanical environment present within *Xenopus*, it is possible to perturb the mechanical environment externally and observe the effects on various processes, including cell division [15]. Explants of tissue from the animal pole of an early gastrula embryo can be adhered to a fibronectin-coated PDMS membrane and will continue to divide at room temperature [177]. While useful for probing the internal forces (e.g. measurements of forces during convergent extension [172], above), these explants are also amenable to application of external forces. Using a stretching device, the PDMS membrane can be

stretched externally which in turn stretches the mounted explant. This system can then be imaged by a confocal microscope. Here we focus on the outer epithelial cells of the animal cap explant.

For the work in this thesis, the use of *Xenopus laevis* as a model organism in which to study cell divisions specifically has many advantages [156]. The *Xenopus* embryos develop at room temperature, which lends itself to live imaging without the need to externally incubate the embryo. Varying the temperature of the embryo effects the timing of development, with lower temperatures slowing the periods of time between divisions [157]. What's more, the relatively large size of the cells make microinjection and live imaging of subcellular processes easier [178], [179]. The combination of the size of the embryo and the temperature sensitivity makes the embryo amenable to studies such as that conducted by Anderson *et al.* (2017) [180], where cell divisions across the embryo were desynchronised by using a temperature gradient. Interestingly, the development of *Xenopus* is robust enough that the desynchronisation of cell division events across the embryo does not lead to a decrease in embryo viability [180]. Combined with the ease of applying global forces to excised tissue from the embryo, the robustness, size, and temperature-controlled developmental timings make the *Xenopus* embryo an excellent system in which to study spindle dynamics of dividing cells under tension.

The application of a reproducible external force to the animal cap tissue is also biologically relevant. During epiboly of the *Xenopus laevis* embryo through blastulation and gastrulation, the overlying cells in the outer epithelial layer are stretched by the intercalation of the deep layers, increasing the area on which the upper cells sit (Figure 1.8D) [3]. The magnitude of this *in vivo* strain, as measured by cell aspect ratio, is analogous to the approximately 20% strain experienced by the epithelial cells in our *ex vivo* stretch (resulting from a 30% strain of the PDMS) [15], [181]. Thus, applying an external stretch to the animal cap tissue in this way places the cells in an environment not too dissimilar to the environment that the cells would be experiencing *in vivo*. The technique by which we apply an external stretch has been optimised for use in the Woolner lab [182].

The animal cap explant is composed of three cell layers: apical/superficial, intermediate, and basal, with the intermediate and basal cells together making the deep layer. The apical layer is comprised of tightly adhered epithelial cells with approximately polygonal shapes due to the dense cell packing [183], [184] while the deep layer cells are loosely connected to their neighbours to allow the fluid exchange of neighbours during intercalation of the deep cell layers during epiboly [184]. This system is powerful as the apical divisions are unlikely to be directly affected by adhesion to the PDMS membrane, as the layer under observation retains its natural adhesions to the cells below it. Thus the cells under observation experience the applied strain through their connections with other cells rather than direct connection with the PDMS. This confers an advantage over cell culture monolayers, which must be grown directly on a substrate and thus create cell-matrix adhesions [185]. This may affect the resulting cell behaviour as the adhesion to the substrate may create additional cues for the cell to respond to. While cell-matrix adhesions are still present in the animal

cap explant system, the imaged superficial cells retain their natural adhesions to the deep layer cells. Thus, we expect that there are fewer alterations to the behaviour of the cells due to the basal adhesions, as the deep layer cells act as a 'buffer' between the superficial cells and the substrate.

To assess the impact of a partial NuMA knockdown on cell division, we employ the morpholino-targetted knockdown protocol optimised within the lab to create a spindle movement response without perturbing the integrity of the spindle pole such that it fractured into multipolar spindles [27]. As *Xenopus* is an allotetraploid organism, with genes on short (S) and long (L) chromosomes, the morpholino-targetted knockdown of NuMA was done in two stages to target both *numa1.L* and *numa1.S* [186].

1.7 Project aims

Using this model system, we aim to shed light on the mechanisms governing spindle positioning and dynamics by:

1. characterising spindle dynamics in stretched and unstretched epithelia in terms of translational and rotational movements such as oscillations;
2. developing a mathematical model of spindle movements due to contributions from microtubule pushing forces and motor protein pulling forces and exploring the parameters which may affect spindle dynamics; and
3. using the mathematical model to shed light on the effect of a partial NuMA knockdown on spindle dynamics in stretched tissue.

To address these aims, we investigate spindle movements in unstretched and stretched epithelia by using the movements of the metaphase plate as a proxy for the movements of the mitotic spindle (Chapter 3). We investigate spindle dynamics in terms of translational movements, exploring the shape path followed by the spindle over the course of metaphase, as well as investigating the rotational movements of the mitotic spindle and the emergence of oscillations in the spindle angle. These dynamics are also investigated in stretched tissues subject to a partial NuMA knockdown.

We also build upon a model of spindle pole displacements due to cortical pulling forces and microtubule-based restoring forces introduced by Grill *et al.* (2005). We develop stochastic simulations and Fokker-planck equations to explore the model and identify parameters which impact spindle dynamics (Chapter 4). We then perform systematic asymptotic analysis to produce a system of ODEs, and subsequently an algebraic formulation which more simply describe the model (Chapter 5), building a direct link between highly coupled stochastic simulations and a single algebraic equation to describe dynamic spindle movements.

Chapter 2

Materials and methods

Due to the interdiscplinary nature of this project the methods are split into the methods used to acquire and analyse biological data [Chapter 3], and the methods used to analyse the mathematical models [Chapter 4]. The computational method for each mathematical model introduced is included in depth in Chapter 4, whereas in this chapter we instead highlight specifically the methods used to analyse the mathematical solutions.

2.1 Methods for Chapter 3

2.1.1 Acquisition of embryos for tissue explants

The model organism used to collect data was *Xenopus laevis* (African clawed frogs). Both pigmented and albino frogs were used in this work. Male and female frogs were both housed within the animal facility at the University of Manchester.

Natural mating was used to acquire embryos as follows:

1. **4-7 days ahead of egg collection:** Female frogs were pre-primed by injection with 50 units of pregnant mare's serum gonadotrophin (PMSG) (*Intervet UK*) into the dorsal lymph sac.
2. **1 day ahead of egg collection:** Male and pre-primed female frogs were primed by injection of 100 units (male) and 200 units (female) of human chorionic gonadotrophin (HCG) (Chorulon: *MSD*) into the dorsal lymph sac.
3. **2-5 hours ahead of egg collection:** Primed male and female frogs were transferred into the same tank (one tank per male/female pair) for amplexus.
4. **1 hour ahead of egg collection:** Frog pairs were transferred into fresh aquarium water, such that all collected eggs were fertilised within the same 1 hour window.

All work with *Xenopus laevis* was performed using protocols approved by the UK Government Home Office under the Home Office Project Licence PFDA14F2D (Holder: Professor Enrique Amaya) and Home Office Personal Licences held by Sarah Woolner, Georgina Goddard, Dionn Hargreaves and Nawseen Tarannum.

2.1.2 RNA synthesis and preparation

Proteins BFP-CAAX and mCherry-histone2B were used to visualise the cell membranes and chromosomes respectively. The preparation of the capped mRNA was as follows:

1. **Plasmid linearisation:** pCS2 plasmids were linearised with Not1 (5 μg of plasmid, 10 μl of NEB buffer 3.1, 1 μl of BSA (*NEB, B9000S*), 8 units of Not1, made up to 100 μl with water) at 37°C for 1 hour. Not1 (2 units) was added and incubated for 1 hour at 37°C. Following linearisation, residual RNAses and proteins were digested by the addition of 5 μl of 10% SDS and 5 μl of proteinase K (*Ambion, AM2546*) at 50°C for 30 minutes.

2. **DNA extraction:** The sample was diluted with 100 μl of water. DNA as extracted with phenol-chloroform (pH 7.9) (*Ambion, AM9730*) and precipitated with 40 μl of NH_4Ac and 800 μl of 100% ethanol overnight (-20°C). The DNA was then pelleted and washed with 800 μl of 70% ethanol. Once dry, the pellet was resuspended in 10 μl of water.

3. **Capped mRNA synthesis:** An *in vitro* transcription reaction was set up using 1 μg of the resuspended DNA. (mMESSAGE mMACHINE SP6 transcription kit [2 μl of 10X reaction buffer, 10 μl of 2X NTP/CAP, 2 μl of enzyme mix, up to 20 μl with water]. Incubated at 37°C for 3 hours. The reaction was terminated by the addition of 115 μl water and 15 μl NH_4Ac stop solution.

4. **mRNA extraction:** The RNA was extracted with 150 μl of phenol-chloroform (pH 6.6) and then 200 μl of chloroform. This RNA was then precipitated with 200 μl of isopropanol at -80°C overnight. The precipitated RNA was pelleted and washed with 200 μl of 70% ethanol before air-drying at room temperature. The dried pellet was resuspended in 10 μl of water and quantified using spectrophotometry. The mRNA was diluted to 1 g/l and stored at -80°C until use.

2.1.3 Morpholino preparation

Custom-made NuMA1.S (5' to 3' sequence: GTCATTATGCTTCAGCACTTCTCCC) and NuMA1.L (5' to 3' sequence: GCCATTTTGTTTCACTACTTTTCCC) morpholinos (MOs) (*Gene Tools, LLC (USA)*) were resuspended in water at a stock concentration of 1 mM and stored at -80°C until use. Prior to microinjection, MOs were incubated for 5 minutes at 65°C and then incubated at 37°C until microinjection.

2.1.4 Preparation of *Xenopus laevis* embryos for imaging

The embryos collected from the natural matings of the frogs were prepared for imaging as follows:

Experiment	Stage microinjected	Injected substance	Needle concentration
Unstretched	2-cell	mRNA: BFPCAAX mRNA: mCherry-Histone2B	0.1 g/l 0.1 g/l
Stretched	2-cell	mRNA: BFPCAAX mRNA: mCherry-Histone2B	0.1 g/l 0.1 g/l
Stretched NuMA knockdown	2-cell	mRNA: BFPCAAX mRNA: mCherry-Histone2B MO: NuMA1.S	0.1 g/l 0.1 g/l 1 mM
	4-cell	MO: NuMA1.L	1 mM

Table 2.1. List of mRNAs and MOs microinjected in each experimental condition.

1. **De-jellying:** Collected embryos were de-jellied using 50 ml of 2% L-cysteine solution [1 g of L-cysteine (*Sigma, 168149*) in 50 ml of 0.1% Marc's modified Ringer's solution (MMR), NaOH added until a pH 7.9-8.0 achieved]. The 0.1% MMR solution was diluted from 10X MMR [1 M NaCl, 20 mM KCl, 10 mM $MgCl_2$, 20 mM $CaCl_2$, 1 mM EDTA, 50 mM HEPES, up to 5 L with distilled water, pH 7.8]. The eggs were swirled in the L-cysteine solution until the jelly coat of the embryos was removed. The L-cysteine solution was then discarded and the embryos washed six times in a total of 200 ml of 0.1% MMR before being incubated at room temperature in fresh 0.1% MMR.

2. **Microinjections:** Healthy embryos were transferred into a dish containing 0.1% MMR and 5% Ficoll (*Merck, F4375*) and microinjected with mRNAs and/or morpholinos as described in Table 2.1 using a Picospritzer III Intracel injector (*Parker instrumentation*) (Figure 3.11A, mRNA injection indicated). Microinjection with mRNAs was done by Dionn Hargreaves, microinjection of morpholinos were done by Nawseen Tarannum. Injected embryos were washed in 0.1% MMR and incubated in fresh 0.1% MMR overnight at 16°C.

3. **Animal cap dissection for unstretched and stretched tissues:** Animal cap explants were prepared from the injected embryos at the early gastrula stage (stage 10) (Figure 3.11B). The embryos were transferred to Danilchik's for Amy explant culture media (DFA) [53 mM NaCl, 5 mM Na_2CO_3, 4.5 mM Potassium gluconate, 32 mM Sodium gluconate, 1 mM $CaCl_2$, 1 mM $MgSO_4$, up to 1 L with MilliQ water, pH 8.3 with Bicine] in 0.1% BSA (*Sigma, A7906*). The vitelline membranes were removed from the embryos using forceps, and the explant removed by incisions with the forceps around the animal pole resulting in separation of the animal cap tissue from the embryo [187]. The animal caps were then transferred onto a fibronectin-coated PDMS membrane with the basal side in contact with the membrane to prevent balling up and held in place with a coverslip. The caps were then left to recover for 2 hours at 18°C before imaging (Figure 3.11C) [182].

2.1.5 Preparation of PDMS membranes

The PDMS membranes were prepared as described previously [182]. In summary:

1. **Making the mixture:** The Silicone Sylgard 184 kit (*SLS, 63416.5S*) [40 g Sylgard liquid and 4 g curing agent] was mixed continuously in a plastic cup for 5 minutes and placed in a vacuum chamber for 1 hour to remove air bubbles.
2. **Creating the membranes:** The de-bubbled sylgard mixture was slowly poured into 8 membrane moulds. Bubbles from pouring were removed by popping them with a sharp implement. The filled moulds were incubated at 65°C for 2.5 hours.
3. **Membrane storage:** Following an overnight cooling at room temperature, the membranes were manually removed from the moulds and washed in 1X Phosphate buffered saline (PBS) and stored at room temperature until use.
4. **Preparation for membrane adhesion:** A day prior to the animal cap excision, the membranes were incubated under UV for 30 minutes and then coated in 1 ml of 10 μg/ml fibronectin (*Sigma, F1141*) in 1X PBS. The membranes were incubated at 4°C overnight and washed the following day (3 washes with 1X PBS, one wash with DFA in 0.1% BSA (*Sigma, A7906*). The membranes were then refilled with DFA with 0.1% BSA.

2.1.6 Stretch protocol and imaging

The PDMS membrane was mounted onto a stretch apparatus (*custom made by Deben UK 722 Limited*) and subjected to a uniaxial stretch of either 0% for the 'unstretched' condition (0.5 mm displacement to ensure that the membrane remained taut under gravity and the weight of the animal cap) or 35% for the 'stretched' condition (8.6 mm displacement) [21]. Images were acquired every 5 seconds on a Leica TCS SP8 AOBS upright confocal using a 20X dipping objective at 2X confocal zoom (Figure 3.11D, E)

The confocal settings were as follows: pinhole 1.9 airy unit, 600 Hz bidirectional scanning, format 1024 x 1024. Images were collected using hybrid detectors with the detection mirror settings for red and blue at 600-690 nm, and 415-516 nm respectively, using the white light laser with excitation at 586 nm, and 405 nm laser lines. The images were collected non-sequentially with a z-spacing of 10 μm between sections. Images were taken continuously without resetting for drifting in order to ensure no missing data points for dividing cells. The maximum imaging duration per animal cap was 2 hours.

2.1.7 Image analysis

All images were processed and analysed on `ImageJ` [188]. All measurements were taken from maximum intensity projections of the z-stack images. Source code for data analysis and plotting is available at github.com/dionn-hargreaves/Data_plotting_Utils.

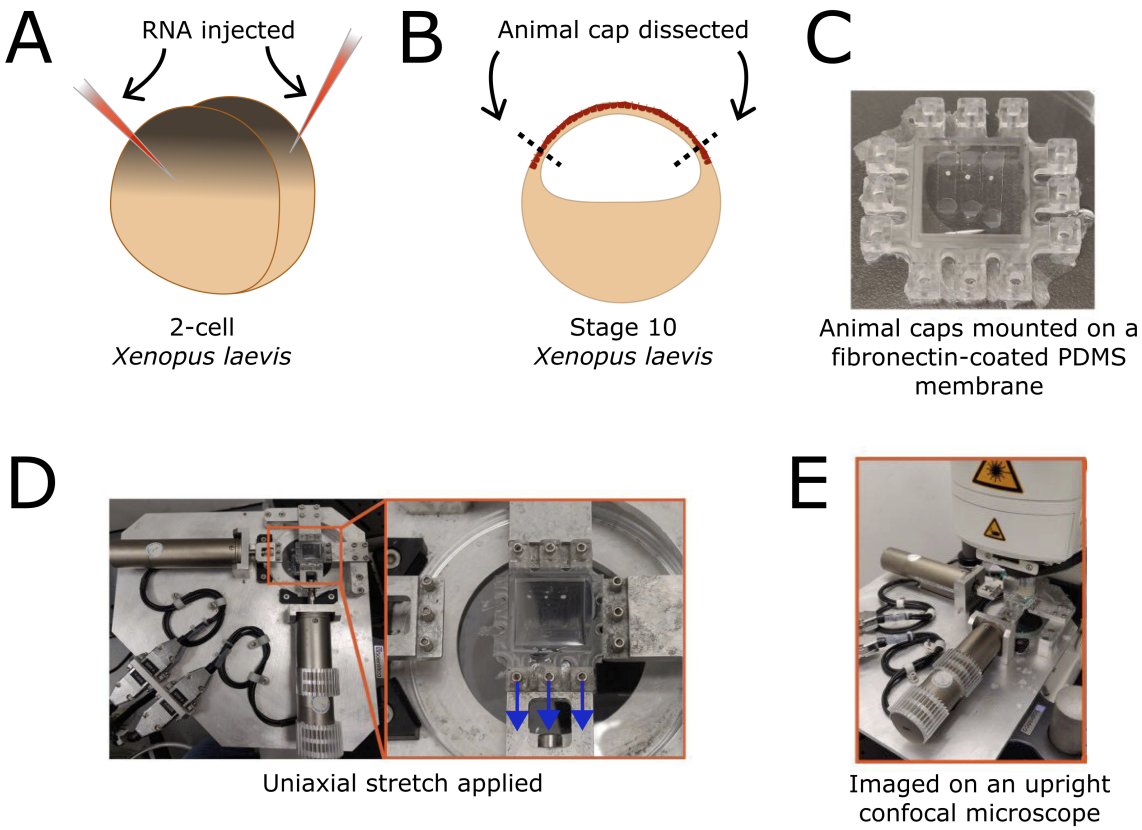

Figure 2.1. **Experimental set up.** A) *Xenopus laevis* embryos injected at the 2-cell stage with RNA(s) encoding fluorescently-labelled proteins. B) Animal cap dissected at stage 10. Epithelial tissue of the animal cap is indicated in red. C) Animal cap explants are adhered to a fibronectin-coated PDMS membrane. D) A uniaxial mechanical stretch device is used to provide a stretch of 0% (unstretched) or 35% (stretched). E) Epithelial cells are imaged using an upright confocal microscope.

Analysis of the mitotic spindle

To confirm that the metaphase plate could be used a proxy for spindle movements, movies of whole embryos with the chromosomes (mCherry-Histone2B) and the mitotic spindle (GFP α-tubulin) tagged were analysed [179]. Each spindle pole was manually tracked in each frame using the `ImageJ` multi-point tool, returning an x and y coordinate for each pole. These positions were then used to determine the centre of the spindle and the angle between the spindle and horizontal axis using a `Julia` script. The centre of the spindle was taken to be the point halfway between the measured poles, $(x_c, y_c) = \frac{1}{2}(x_1 + x_2, y_1 + y_2)$. The angle of the spindle was determined in each frame by $\theta = \arctan(\frac{y_2 - y_1}{x_2 - x_1})$.

Analysis of the metaphase plate

To track translational and rotational dynamics of the spindle through metaphase, the metaphase plate (visualised with mCherry-histone2B) was used as a proxy. Each end of the metaphase plate was tracked in each frame using the `ImageJ` multi-point tool, returning an x and y coordinate for each point. These positions were then used to determine the centre of the metaphase plate and the angle between the plate and horizontal axis using a `Julia` script. The centre of the metaphase plate was taken to be the point halfway between the measured

ends, $(x_c, y_c) = \frac{1}{2}(x_1 + x_2, y_1 + y_2)$. In the unstretched, stretched and NuMA KD tissues, to correct against drift of the tissue, the centre of the cell at the beginning of metaphase, $\mathbf{R}_1$, and the end of metaphase, $\mathbf{R}_2$, were used to create a linear correction to the metaphase plate position across metaphase time. Determination of the cell centre is described in Section 2.1.7. The drift-corrected centre was thus defined as

$$\mathbf{R}(t) = \mathbf{R}_1 + \frac{t}{t_{\text{met}}}(\mathbf{R}_2 - \mathbf{R}_1). \tag{2.1}$$

This 'corrected' centre was used to determine the metaphase plate position about the cell centre of mass. The angle of the metaphase plate in each frame was determined by $\theta = \arctan(\frac{y_2 - y_1}{x_2 - x_1})$.

The track traced by the centre of the metaphase plate was used to define a gyration tensor, S, as

$$S = \frac{1}{N}\begin{bmatrix} \sum_{i=1}^{N}(x^i - \langle x\rangle)^2 & \sum_{i=1}^{N}(x^i - \langle x\rangle)(y^i - \langle y\rangle) \\ \sum_{i=1}^{N}(x^i - \langle x\rangle)(y^i - \langle y\rangle) & \sum_{i=1}^{N}(y^i - \langle y\rangle)^2 \end{bmatrix}, \tag{2.2}$$

for $\langle x\rangle$ and $\langle y\rangle$ the mean x and y positions of the metaphase plate centre, which is at position (x^i, y^i) at a time t^i. This tensor is a measure of rotational inertia of the hypothetical rigid object made up of individual particles lying at positions (x^i, y^i) for all i [189]. The principal axes of the track were extracted by determining the eigenvectors and eigenvalues (λ_1, λ_2) of the gyration tensor (2.2). The orientations of the major and minor axes were determined from the eigenvectors. The circularity of the tracks, C_T were determined by

$$C_T = \frac{\lambda_1}{\lambda_2} \tag{2.3}$$

which takes a value between 0 and 1 (a track is more elongated toward $C_T = 0$, a track is more circular toward $C_T = 1$).

Analysis of cell shape and division orientation

Cell shapes were analysed to determine the cell centre, $\mathbf{R}$, cell area, A, the cell circularity, C, and the orientation of the cell major axis, θ_c. Cell edges and tricellular vertices were manually traced at the beginning and end of metaphase using the `ImageJ` 'Paintbrush tool' (brush width = 1 pixel). Manual traces were used rather than automated cell segmentation algorithms such as Cellpose, as this algorithm had not yet been refined or trained for the images produced in this thesis [190]. The manual traces were processed using in-house `Python` scripts to return measures of the cell area, cell circularity, and cell major axis [15], [21]. The measurements were made based on the polygonised cell according to the positions of the TCVs.

Cell shapes were described by their circularity, C, the ratio of the principal eigenvalues of the cell shape tensor. The circularity has a value between 0 and 1, with 1 representing a circular cell [15], [21], [175]. The cells were partitioned into 'elongated' and 'circular' based

on the threshold value of 0.6 (circular if $C > 0.6$, elongated if $C \leq 0.6$). This threshold value was chosen based on methods used elsewhere, where are choice of $C = 0.65$ at the threshold was used [15], [27]. Here, the value was decreased from 0.65 in order to partition the data such that sufficient numbers of cell divisions existed within each group. Indeed, the threshold of 0.6 lies halfway between $C = 0.2$ and $C = 1$, which we argue are the biologically-relevant observable extremes (no cells below $C = 0.2$ were recorded, and $C = 0$ corresponds to a completely 1D cell).

The cell major axis orientation, θ_{c}, was determined as the angle of the major axis as determined from the cell shape tensor [15], [21].

The division orientation, θ_{D} was measured using the `ImageJ` 'straight line' tool by drawing a line between the two separating daughter nuclei of a dividing cell at late anaphase. The angle of division relative to the horizontal was calculated from this line within `ImageJ`.

2.1.8 Correlating spindle to chromosome movements

To confirm the correlation between spindle movements and the metaphase plate movements [Section 3.2.1], live images of developing *Xenopus* embryos provided by Sarah Woolner were analysed. The experimental method for the acquisition of this data by Sarah Woolner is as follows.

For live imaging of mitotic spindles in *Xenopus* embryos, both cells of two-cell embryos were microinjected with 5 nl of mRNA for GFP–α-tubulin (needle concentration of 0.5 mg/ml) and Cherry–H2B (0.1 mg/ml). Embryos were incubated for 20 hours post fertilization at 16°C and then mounted for live imaging in 0.1X Marks Modified Ringers (MMR) [10X solution: 1 M NaCl, 20 mM KCl, 10 mM $MgCl_2.6H_2O$, 20 mM $CaCl_2.2H_2O$, 1 mM EDTA disodium salt, 50 mM Hepes, up to 5 L with distilled water], using a ring of vacuum grease to contain the embryos and support a glass coverslip [179]. Imaging took place at developmental stages 10–11. Single focal plane live-cell images of spindles were collected at room temperature (21°C) every 20 seconds using a confocal microscope (FluoView FV1000; Olympus) with FluoView acquisition software (Olympus) and a 60X, 1.35 NA U Plan S Apochromat objective. Time-lapse videos were constructed from the single focal plane images using `ImageJ` [60].

2.1.9 Statistical analysis

Statistical analysis was performed using GraphPad Prism 9. All samples were tested for normality using the Shapiro-Wilk and D'Agostino-Pearson normality tests. The normality test was then used to decide between parameteric or non-parametic statistical tests for all samples. For two samples: Welch's t-test was used to compare the fraction of major axis movement in elongated and circular cells as the distributions were normal but with different variances and sample sizes; the Wilcoxon matched-pairs signed rank test was used

to analyse the distributions of cell and track circularities as the data was paired and non-Gaussian according to the normality test; the Mann-Whitney U Test was used to analyse the distribution of i) periods of oscillation between elongated and circular cells, ii) periods of oscillation between the 1st and 2nd halves of metaphase, and iii) the goodness measure of the oscillations in the 1st and 2nd halves of metaphase, due to these samples being non-Gaussian according to the normality test. We note that for the periods and goodness measures of oscillations in the 1st and 2nd halves of metaphase, a small percentage of cells showed oscillations in both halves and thus were paired. In this case `Prism` reported an exact p-value. Relationships between parameters were determined using the Spearman rank correlation test, in particular, i) bounding area of spindle movement vs metaphase time, ii) goodness measure of oscillation vs period of oscillation, iii) goodness measure of oscillation vs metaphase time, iv) period of oscillation vs metaphase time, and v) goodness measure of oscillation vs cell circularity, as these data failed the normality test. For three or more samples: the Kruskal-Wallis test and post hoc Dunn's multiple comparisons test were used to analyse the distributions of i) the normalised net displacement, ii) the normalised maximum displacement from the cell centre, iii) metaphase time, iv) effective spindle speed, v) the alignment of cell and track major/minor axes orientations with division orientation, vi) period of oscillation, and vii) goodness of oscillation. All of these data failed the normality test and were unpaired thus the choice of a non-parametric, unpaired statistical test. Count data (fraction of oscillating spindles) was compared using Fisher's exact test and represented as a fraction of the population for clarity of visualisation. For all tests, p values below 0.05 were considered statistically significant. All statistical tests are indicated in figure legends and also within the main text for significant differences.

2.2 Methods for Chapter 4

2.2.1 Computational modelling

All computational modelling was done using `Julia`. Stochastic simulations were run using The Computational Shared Facility 3 at the University of Manchester. All other simulations and codes were capable of being run on a personal laptop (2.2 GHz 6-Core Intel Core i7 processor).

2.3 General methods

2.3.1 Detection of oscillations and period of oscillations

Oscillations were detected from signals (e.g. angles of metaphase plates, the position of the mathematically modelled spindle pole) by analysis of the periodogram produced using `Julia` package `QuantEcon.jl`. The input data is pre-whitened (transformed such that it resembled white noise), analysed (periodogram created) and then re-coloured (reversing

the initial transformation) such that the resulting periodogram is closer to the true spectral density of the data without noise. A threshold value was determined from the interquartile range (IQR) of the spectrum data on a cell-by-cell basis, above which the spectrum peaks were determined to be weak outliers of the data [191]. Peaks below the threshold were assumed to be random noise in the measured signals. Then values above

$$\text{Threshold} = \text{Q3} + 1.5\text{IQR} \tag{2.4}$$

are weak outliers of the data and considered to correspond to an oscillation, for Q3 the upper quartile. Frequencies, f of the outliers were determined from the periodogram, from which the periods of oscillation were determined by

$$T = 1/f. \tag{2.5}$$

Periods corresponding to 95% of the metaphase time were discarded as artefacts resulting from the general trend of the input data. For the presence of multiple peaks of the periodogram, only the dominant peak was reported (the peak with the largest amplitude).

In this thesis, a measure we call 'Goodness of fit' was calculated for each oscillatory spindle, to further probe the strength of the outlier frequency. The measure was defined as the ratio of the weak outlier threshold (2.4) to the amplitude of the peak,

$$\text{Goodness measure} = 1 - \frac{\text{Threshold}}{\text{Peak amplitude}}. \tag{2.6}$$

The goodness measure is close to 1 for peaks far exceeding the threshold and closer to 0 for peaks close to the threshold. This measure was chosen to reflect how far above the weak outlier threshold the periodogram peak lies, assuming that peaks elevated further away from the threshold level are more likely to reflect a 'true' dominant oscillation in the signal. Source code for data analysis and plotting is available at github.com/dionn-hargreaves/Data_plotting_Utils.

2.3.2 Figure assembly and illustration

Figures were assembled and illustrated using illustration software `Vectornator`. Images of tissues were opened using `ImageJ` and annotated in `Vectornator`. Raw data of chromosome position (Figure 3.4Cii), angle, and the accompanying periodograms (Figure 3.9) were produced using the `Plots` package in `Julia`. The graphs of the biological data were produced using `GraphPad Prism`. The solutions of the mathematical models were produced using the `Plots` package in `Julia`.

Chapter 3

Characterising spindle dynamics in response to external stretch and depletion of NuMA

3.1 Introduction

Division orientation in cells is governed by the positioning mechanisms of the mitotic spindle. The final direction of division orientation has been attributed to both cell shape [19], [43], [44] and cell tension [6], [12], [13]. However, the direction of local mechanical cell stress has been shown to align with cell shape in tissues, which makes disentangling shape-based effects from force-based effects difficult [15]. Increasing tissue tension mechanically has been shown to result in divisions which are orientated along the stretch axis [12], [15]. Division orientation is determined by the orientation of the mitotic spindle which is positioned in the cell through interactions of its astral microtubules with the cortical network and associated proteins [192]. In particular, spindle positioning has been attributed to microtubule pushing [54], [78], [137], [143], [193] and pulling of astral microtubules at the cell cortex through interactions with the motor protein dynein. The Gαi/LGN/NuMA complex resides at the cortex and anchors dynein to create a spindle-pulling response [43], [64], [79]. As a core component of the spindle orientation machinery, disruption of NuMA has been shown to affect the ability of cells to align their spindles effectively [12], [27], [64], [83], [103]. In *Drosophila*, NuMA's homolog Mud is constitutively located to the TCVs of epithelial cells and has been shown to be important for orientation of the mitotic spindle with cell shape [43]. This was demonstrated using a mathematical model of spindle positioning, whereby forces acting on the spindle were amplified at the TCVs and resulted in spindle alignments which matched well with experiment [43]. This matched geometrical determinations of cell division orientation, as the locations of the TCVs were also shown to be good predictors for division orientation in *Xenopus* animal cap epithelia [15]. However, in recent unpublished work from the Woolner lab, NuMA has been shown to have both a tension-sensitive dynamic localisation to the cell cortex over the course of metaphase and a specific spindle-orientation response to anisotropic force rather than isotropic force [27]. This localisation was specifically not enriched at the TCVs, suggesting that NuMAs func-

tion may be more complex that Muds function in *Drosophila*. The exact mechanism by which NuMA functions in tension-sensitive division orientation still remains unclear.

The morpholino-induced partial knockdown of NuMA in the *Xenopus laevis* animal cap system has been shown to affect division orientation with respect to stretch and mitotic spindle dynamics [27], where the inability of the spindle to align with the cell long axis coincided with a reduction in the translational speed of the mitotic spindle [27]. However, this analysis was based on time lapse movies with a coarse time resolution (30 s). It has been shown at a higher time resolution (5 s) in whole *Xenopus laevis* embryos that the mitotic spindle oscillates toward the end of metaphase, prior to anaphase onset [77]. This type of complex dynamic behaviour was not seen at the lower time resolution of 30 s, thus it was unclear whether or not these dynamics also existed in the animal cap tissue, or further how they might be perturbed by the knockdown of NuMA. In this chapter, we aim to characterise the dynamics of the mitotic spindle in both unstretched and stretched animal cap tissue in order to investigate the mechanical effect of stretch on spindle positioning within the cell. Using the same morpholino knockdown method as in [27], we also aim to characterise the effect that reducing the levels of NuMA has on the mitotic spindle dynamics, specifically in stretched tissue. The work presented in this chapter will be further analysed by a mathematical model which will be developed in chapters 4 and 5.

3.2 Results

3.2.1 Spindle movements are correlated with chromosome movements

In order to investigate spindle dynamics in response to mechanical forces and cell shape changes, it was important to have a robust method of tracking the spindle movements. Overlaying spindle movement tracking, we also needed a method to simultaneously monitor cell shape and to investigate key proteins which may be involved (for example, NuMA). To combat over-saturation of the cells with fluorescent tags, which would not only make imaging more difficult but also decrease the health of the embryos, we sought to minimise the number of structures being imaged. To this end, we used BFP-CAAX to image the cell membranes and mCherry-histoneH2B (cherry-H2B) to tag the chromosomes. We note also that cherry-H2B is often brighter than GFP-α-tubulin, and less prone to moving out of the plane of view of the $z-$slices, properties which are particularly of use when imaging at high frame rates. The formation of the metaphase plate was used to identify entry into metaphase, and the movements of the metaphase plate were used as a proxy for spindle movements.

To confirm that metaphase plate dynamics could be used to infer spindle dynamics, *Xenopus laevis* whole embryos expressing both GFP-α-tubulin and cherry-H2B were live imaged by confocal microscopy and the resulting time lapse movies analysed (Figure 3.1A,B).

The angles of the spindle and metaphase plate about their respective mean angle were extracted from the movies (Figure 3.1C-D). In keeping with the assumption that the spindle

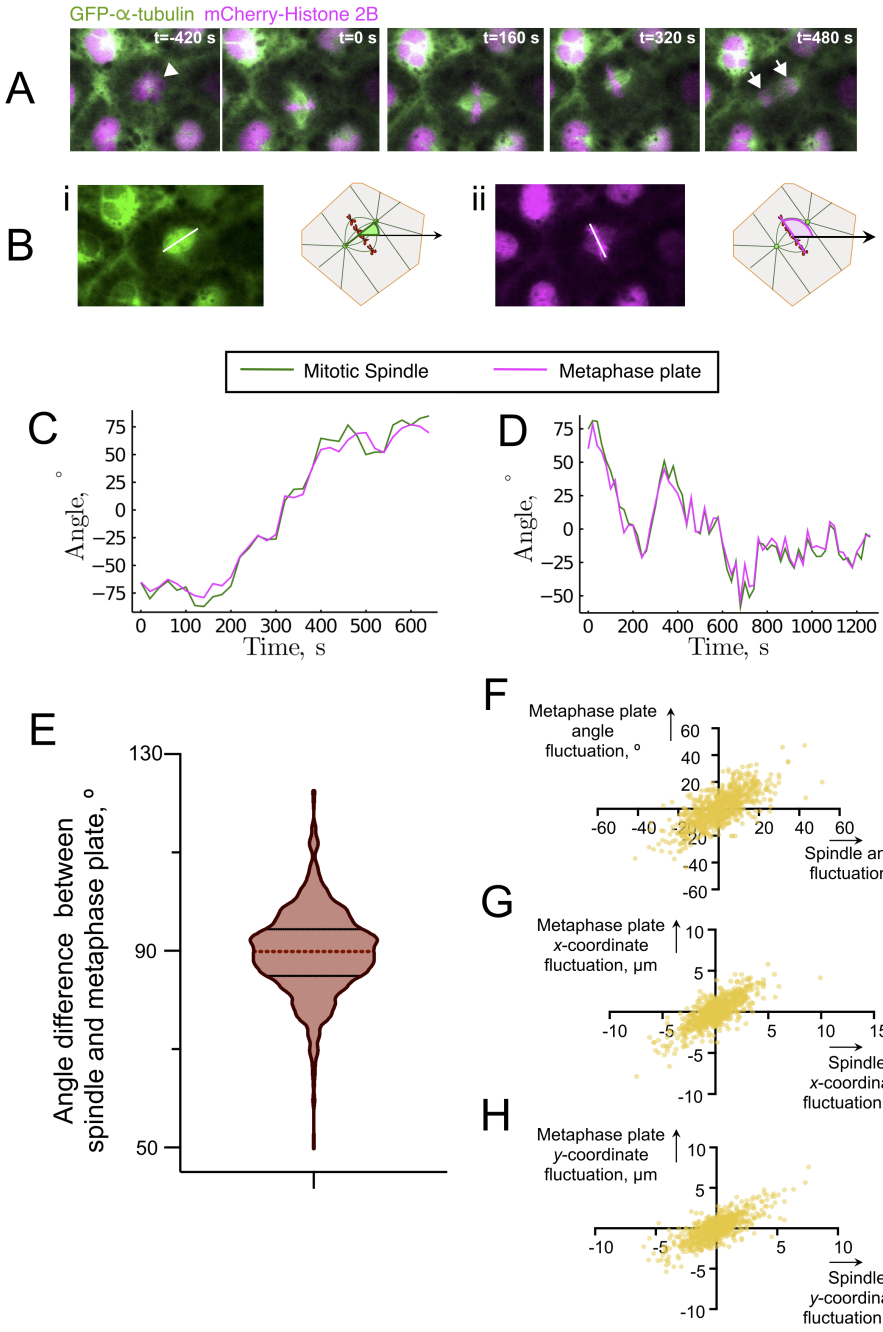

Figure 3.1. **Spindle movements are correlated with metaphase plate movements.** A) Time-lapse images of example cells showing the positions of the spindle and metaphase plate from interphase to anaphase. Arrowheads in the first frames indicate the nucleus of the cell of interest. Arrows in the final frames indicate the separation of chromosomes at anaphase. Time is chosen such that $t = 0$ coincides with the formation of the metaphase plate. B) Schematics of the angle measurements for i) the mitotic spindle and ii) the metaphase plate. White lines overlayed on the confocal images connect the measured spindle pole positions and metaphase plate end-points. C) and D) The orientation of the spindle and metaphase plate, normalised about their mean angle, for two example cells. E) A violin plot of the angle between the spindle and metaphase plate using data from all cells at all timepoints. Median and interquartile range indicated. Analysed using the Wilcoxon Signed Rank Test against a hypothetical median of 90°. H) F) G) Comparison of the fluctuations of the F) angle, G) x-coordinate of the centre of mass, and H) y-coordinate of the centre of mass of the spindle and metaphase plate. 'Fluctuations' are defined as the difference between two consecutive frames. Samples were analysed using the Spearman rank correlation test.

and metaphase plate are perpendicular, the mean angle difference measured was $90 \pm 9°$ (mean$\pm$SD) (Figure 3.1E). Comparison of this distribution with the hypothetical median of $90°$ showed no statistical significance.

Comparisons of the inter-frame angle displacements show a strong correlation between

the metaphase plate and spindles (Figure 3.1F) (p<0.0001. Analysed using the Spearman rank correlation test), with a strong correlation between the centre of mass of the metaphase plate and the spindle in both the x and y directions (Figure 3.1G,H) (p<0.0001. Analysed using the Spearman rank correlation test). Thus we conclude that the relative movements of the mitotic spindle can be inferred from the metaphase plate, and from this point onwards we use the metaphase plate dynamics as a proxy for spindle dynamics.

3.2.2 The mitotic spindle undergoes translation movements during metaphase

In order to characterise spindle dynamics, we separated the translational movements of the spindle from the rotational movements of the spindle. Often, studies into spindle dynamics focus on the spindle undergoing a rotation to its final orientation, without measuring translational dynamics [8], [18], [19], [43], [149]. We studied the translational dynamics by tracking the centre point of the metaphase plate through metaphase, defined as the point mid-way between the metaphase plate ends. Tracks cease at the onset of anaphase, where the chromosomes begin to separate from one another. We note that we didn't observe significant spindle movement following the onset of anaphase (data not shown), and this cessation of movement upon anaphase onset has also been reported previously [194]. The distances travelled are normalised here by a length scale defined by the cell size, such that a cell of area A_{c} has a length scale given by the diameter of a circular cell with the same area. A cell size normalisation was used in order to quantify the relative fraction of the cell explored by the mitotic spindle. Then spindles which travelled the entire length of a small cell would be measured similarly to spindles which travelled the entire length of a large cell. Then $d = \sqrt{\frac{4A_{\mathrm{c}}}{\pi}}$ is the length scale used to normalise the following displacements.

The final displacement of the spindles, immediately prior to anaphase onset, were compared across the unstretched, stretched and NuMA KD conditions (Figure 3.2A). The cells entered anaphase with the spindles on average within 10% of the cell centre (fractions: 0.07 ± 0.05 unstretched, 0.07 ± 0.04 stretched, 0.08 ± 0.04 stretched NuMA KD tissue, mean$\pm$SD). No significant difference was identified between the three conditions.

Comparison of the magnitude of the total displacement of the spindle (the distance between the final position and the initial position) shows that for each condition (unstretched, stretched, and stretched + NuMA KD), the spindle undergoes a net translation over the course of metaphase, though there is no significant difference between the three conditions. The net displacement of the spindle over metaphase is approximately equal regardless of whether the cells are stretched or under a NuMA knockdown (Figure 3.2B).

We next consider the centring ability of the spindles, whereby spindles which are being centred are positioned closer to the cell centre at the end of metaphase than they are at the beginning. That is, the distance between the initial spindle position and the cell centre, d_1, is larger than the distance between the final spindle position and the centre, d_2. Thus $d_1 - d_2 > 0$ if a spindle is more centred at the end of the metaphase. A population with no directed centring mechanism is expected to be distributed with a median of 0, either because

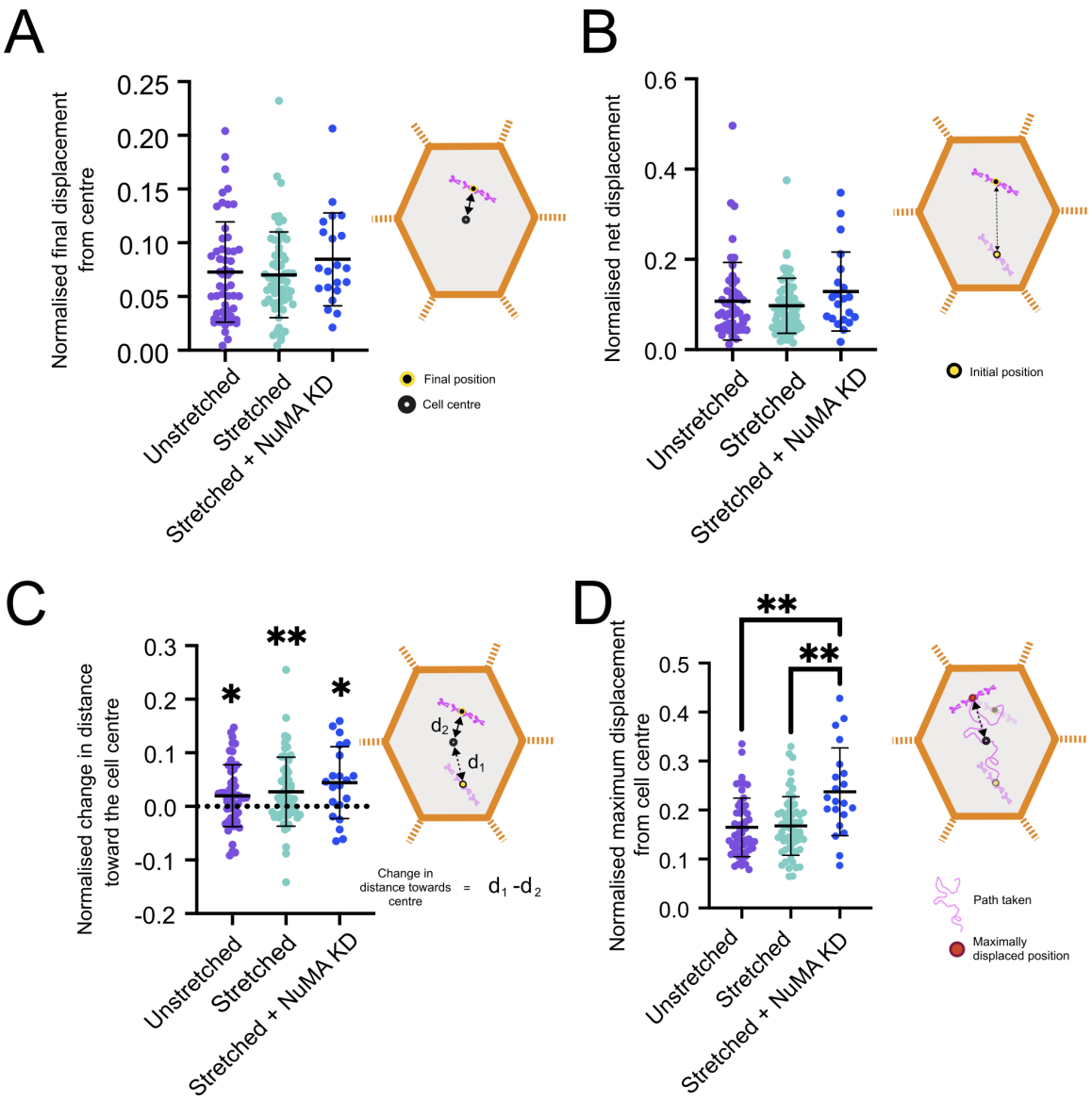

Figure 3.2. **The mitotic spindle centre is not static with respect to the cell.**. A) The final distance from the cell centre, immediately prior to anaphase onset, normalised to each individual cell length scale. The cell length scale is defined as the diameter of a circular cell whose area equals the area of the measured cell, $d = \sqrt{\frac{4A_c}{\pi}}$. Data analysed using the Kruskal-Wallis test and post hoc Dunn's multiple comparisons test. Error bars represent the standard deviation B) The total displacement of spindle centres normalised to each individual cell length scale. Analysed using the Kruskal-Wallis test and post hoc Dunn's multiple comparisons test. Error bars represent the standard deviation. C) The change in distance toward the cell centre, normalised to individual cell length scales. Analysed using the Wilcoxon test compared with 0 change. Error bars represent the standard deviation. Statistical significance represented by p=0.0027** (stretched); 0.0368* (unstretched); 0.0142* (stretched + NuMA KD). D) The maximum absolute displacement a spindle moves from the cell centre, normalised to each individual cell length scale. Analysed with the Kruskal-Wallis test and post hoc Dunn's multiple comparisons test. Error bars represent the standard deviation. Statistical significance represented by p=0.0011**(unstretched compared with stretched + NuMA KD); p=0.0028**(stretched compared with stretched + NuMA KD). KD - knockdown. Indicators for non-statistically significant results are omitted. Unstretched: n=53 cells from 8 embryos; Stretched: n=62 cells from 7 embryos; Stretched + NuMA KD: n=21 cells from 3 embryos.

they will each undergo no net displacement either toward or away from the cell centre, or more likely because there will be equal numbers of spindles moving toward and away from the cell centre over the whole population. The stretched condition showed a significant bias toward centring (Figure 3.2C) (p=0.0027. Wilcoxon Signed Rank Test, compared with a theoretical median of 0), as did the unstretched condition (p = 0.0368. Wilcoxon Signed Rank Test, compared with a theoretical median of 0). Further, knockdown of NuMA did not affect the centring ability of the spindle (Figure 3.2C) which remained significantly biased toward a centring regime (p = 0.0142. Wilcoxon Signed Rank Test, compared with a theoretical median of 0). The Wilcoxon Signed Rank non-parametric test was chosen as the stretched condition data was not normally distributed. Comparison of the three conditions with one another showed that they are not statistically different to one another (Kruskal-Wallis test and post hoc Dunn's multiple comparisons test), suggesting that all three conditions show the same overall centring behaviour. However, due to the small elevation above zero and the large spread of the data, more in-depth analysis on the centring behaviour would be beneficial moving forward.

We went on to measure the maximum displacement of the spindle from the cell centre, in order to determine whether the spindles in any of the conditions were more centred in general over the course of metaphase. We found that the spindles of the cells in the unstretched and stretched tissues remained closer to the centre of the cell than the stretched NuMA KD tissue (Figure 3.2D) (p=0.0011 comparison to unstretched; p=0.0028 comparison to stretched. Kruskal-Wallis test and post hoc Dunn's multiple comparisons test). Moreover, there was no significant difference between the unstretched and stretched conditions.

We conclude that the mitotic spindle undergoes translational movements within the cell, with the cells of the stretched NuMA knockdown tissues having spindles which deviate from the cell centre more than in unstretched and stretched conditions (Figure 3.2D). Despite this increased deviation, the net displacement between the final and initial positions of the spindle are consistent across the three conditions (Figure 3.2B), suggesting either that the path taken between the start and end points is not direct, or that the spindles of NuMA knockdown tissue are less clustered toward the centre. However, the movement of the spindle has an overall bias toward the cell centre across all three conditions (Figure 3.2C).

3.2.3 Perturbation by mechanical stretch or NuMA knock down affects both metaphase time and the area explored by the spindle, but not the spindle velocity

We next investigated whether the increased deviation from the cell centre in the NuMA KD tissue was a result of the spindle having more time to explore the cell. Stretched tissue was shown to have a significant reduction in metaphase time compared with the unstretched tissue cells (p=0.0015. Kruskal-Wallis test and post hoc Dunn's multiple comparisons test). Interestingly, inducing knockdown of NuMA in stretched tissues increased the metaphase time significantly (p=0.0388, unstretched compared with stretched + NuMA KD; p<0.0001, stretched compared with stretched + NuMA KD) (Figure 3.3A).

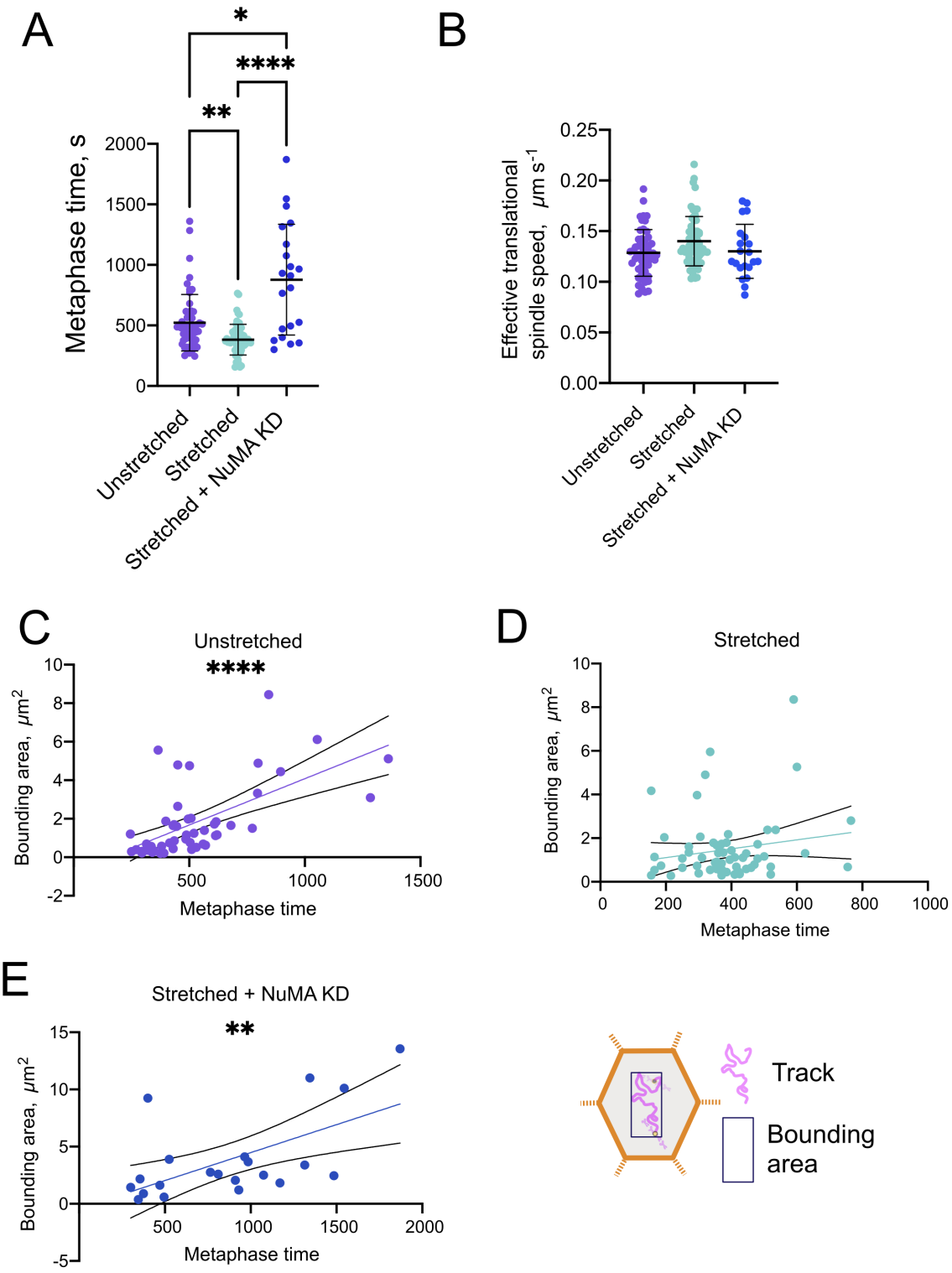

Figure 3.3. **The impact of metaphase time**. A) Metaphase time for each cell division in unstretched, stretched and stretched NuMA KD tissues. Error bars represent the standard deviation. Statistical significance represented by p=0.0388*,0.0015** and p<0.0001***. Analysed using the Kruskal-Wallis test and post hoc Dunn's multiple comparisons test. B) The total distance travelled per metaphase time, defining an overall speed of the spindle, over the unstretched, stretched and stretched NuMA KD conditions. Error bars represent the standard deviation. Analysed using the Kruskal-Wallis test and post hoc Dunn's multiple comparisons test. C), D) and E) Scatter graphs of the area bounding the spindle centre within the cell as function of metaphase time. Error bands represent the 95% confidence interval. p=0.0039** and p<0.0001****. Samples were analysed using the Spearman rank correlation test. KD - knockdown. Indicators for non-statistically significant results are omitted. Unstretched: n=53 cells from 8 embryos; Stretched: n=62 cells from 7 embryos; Stretched + NuMA KD: n=21 cells from 3 embryos.

This pointed to the potential for the difference in maximum displacement from the centre to be a result of the mitotic spindle having more time to explore the cell. Indeed, normalising the total distance travelled by each spindle by its total time in metaphase defines an approximate spindle speed, which is not significantly different across the three conditions (Figure 3.3B). This is contrast to what we expected by looking at the maximum displacements alone, and suggests that the spindles of the stretched NuMA KD tissue cells are able to become maximally displaced from the spindle centre because of their longer metaphase time rather than a change in their velocity.

In order to determine whether the larger displacements from the cell centre were likely to be a result of the increased metaphase time, we approximated the size of the space that the movements occupied by the maximum displacements of the x and y coordinates across metaphase and analysed this bounding area's correlation with metaphase time (Figure 3.3C). The bounding area was shown to be positively correlated with metaphase time for unstretched and stretched + NuMA KD tissues ($p<0.0001$, unstretched; $p=0.0039$, stretched+NuMA KD. Spearman rank correlation test), though interestingly in stretched tissues without perturbation of NuMA there was no significant correlation.

We conclude that there is no significant difference in spindle velocity across either the unstretched, stretched or stretched NuMA KD conditions. However, due to the size of the explored area being dependent on metaphase time, we look from here on at the shape of the area, rather than its absolute size.

3.2.4 Inducing a NuMA KD in stretched tissue biases spindle movements along the major axis of circular cells

In order to reduce the effect of long metaphase time, we turned to investigate the path of the spindle positioning with respect to the major and minor axes of the cell as calculated from the positions of the tricellular vertices (TCVs), the points where three or more cells meet. The TCVs have previously been identified as being positions which are good predictors for the ultimate cell division orientation [15]. Further, the elongation of the cell has been shown to effect the ability of the cell to orient its division with shape, with more elongated cells orienting their divisions with the long axis better than circular cells [15], [18], [19], [43], [45]. By defining the cell circularity, C as the ratio between the magnitude of the minor and major cell axes, we have a measure of how circular or elongated a cell is. We therefore investigate the motion of the spindle with reference to the axes defined by the positions of the TCVs in elongated ($C \leq 0.6$) and circular cells ($C>0.6$) (Figure 3.4A).

The track followed by the spindle through metaphase was separated into components along the major and minor axes of the cell shape (Figure 3.4B). The mean and standard deviation of each axis was calculated and used to define the bounds of the track which we used to determine the fraction of major axis movement. A fraction greater than 0.5 suggests the track bounds are a rectangle elongated along the major cell axis, while a fraction less than

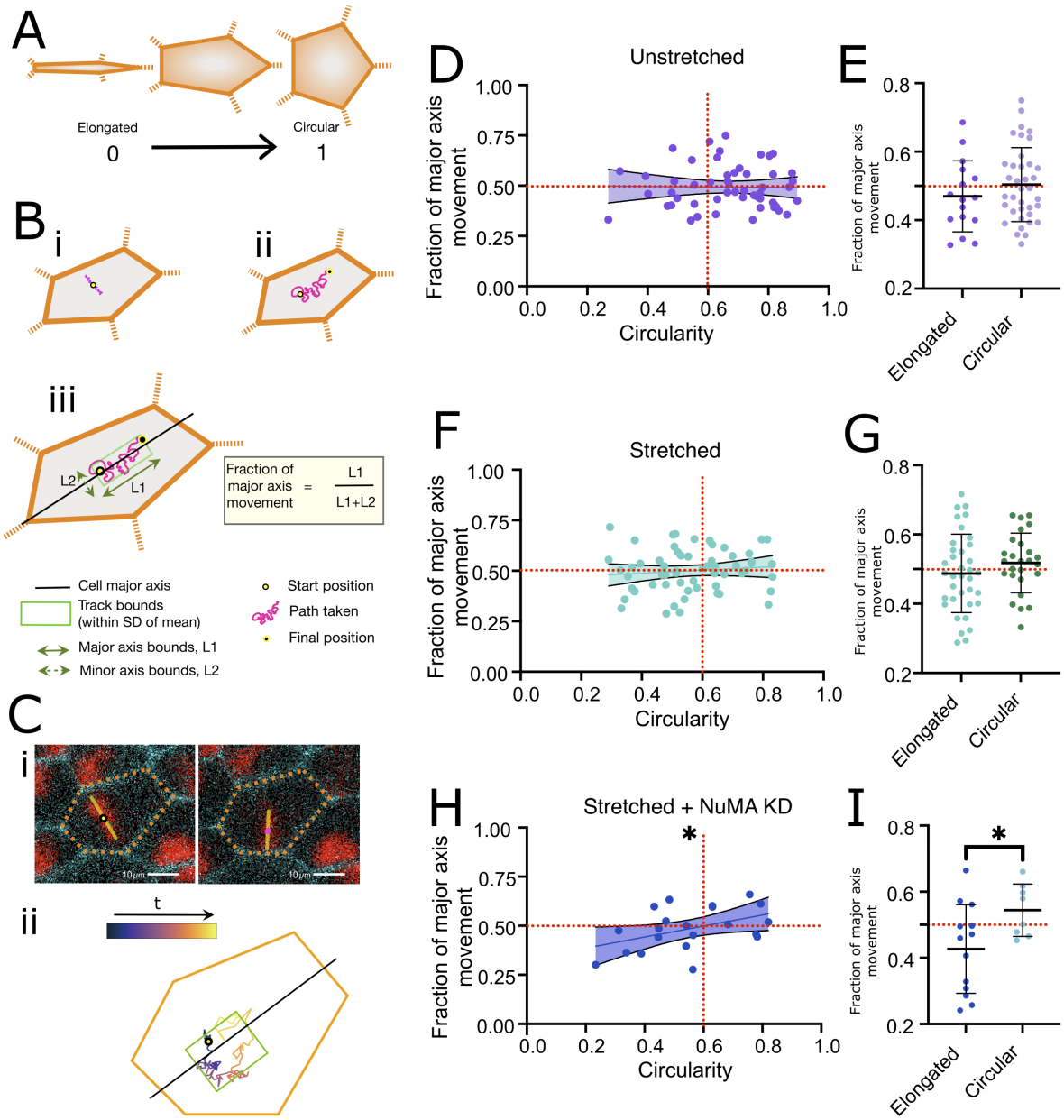

Figure 3.4. **Spindle movements with respect to cell shape.** A) Cell circularity is measured, where more circular cells have a value of 1. B) i) The centre of the metaphase plate is ii) tracked and used as a proxy for spindle movements. iii) The track is defined by the bounding box aligned with the cell major axis, whose lengths are equal to the standard deviation of the track about the mean, along the major (L1) and minor (L2) axes. These are used to define the fraction of movement along the major axis. C) i) An example cell during metaphase, showing the defined metaphase plate (yellow line) and the metaphase plate centre (dot) at two time-points, with ii) the resulting track through time. D,F,H) Scatter plots of individual cells in D) unstretched, F) stretched and H) stretched NuMA KD tissues, showing the relationship between cell circularity and the fraction of movement along the cell major axis. Red dotted lines indicate the chosen divide between elongated and circular cells, and the divide between a track more elongated toward the major axis (>0.5) and the minor axis (<0.5). Shaded regions indicate the 95% confidence interval. p=0.0430*. Samples were analysed using the Pearson R correlation test. Unstretched: n=53 cells from 8 embryos; Stretched: n=62 cells from 7 embryos; Stretched + NuMA KD: n=21 cells from 3 embryos. E,G,I) The same data as D,F,H) grouped into elongated and circular cells. Error bars represent standard deviation. Analysed using Welch's t test. p=0.0207*. KD - knockdown. Indicators for non-statistically significant results are omitted. Unstretched, elongated: n=16 cells from 6 embryos; Unstretched, circular: n=37 cells from 7 embryos; Stretched, elongated: n=36 cells from 7 embryos; Stretched, circular: n=26 cells from 4 embryos; Stretched + NuMA KD, elongated: n=13 cells from 3 embryos; Stretched + NuMA KD, circular: n=8 cells from 2 embryos.

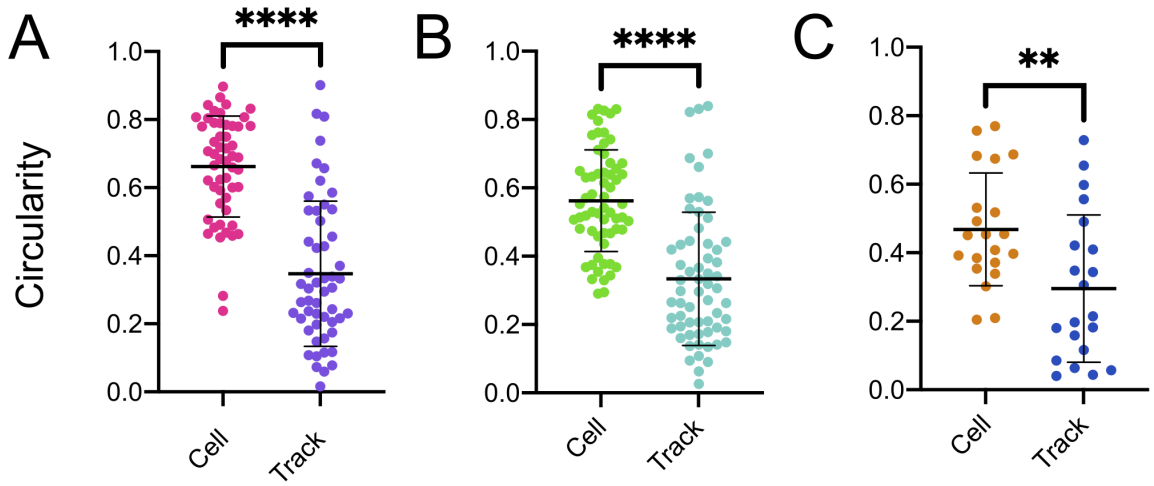

Figure 3.5. **The spindle track is more anisotropic than cell shape**. Circularities of cells and spindle centre track shapes, as determined from the gyration tensor of the track, in A) unstretched, B) stretched and C) stretched NuMA KD conditions. Error bars represent the standard deviation. Analysed using the Wilcoxon test. p<0.0001****, 0.0038**. KD - knockdown. Unstretched: n=53 cells from 8 embryos; Stretched: n=62 cells from 7 embryos; Stretched + NuMA KD: n=21 cells from 3 embryos.

0.5 suggests the track bounds are a rectangle elongated along the minor cell axis. An example cell track is shown in Figure 3.4C, with the major axis of the cell indicated by the black line. The major axis of the cell determined by the TCV position is likely to be more prone to geometric error than the major axis determined by cell perimeter or area, as the shape is described by fewer data points [15], and this error is likely to increase for more circular cells where the long axis of the cell is less well defined.

The fraction of movement along the major axis was investigated with respect to the cell circularity (Figure 3.4D,F,H). For unstretched and stretched tissues the fraction of movement along the major axis was not significantly different between elongated and circular cells (Figure 3.4E,G), indeed both cells show means around 0.5 suggesting there is no population bias of path elongation along either the major or minor axes of the cell. However, for stretched NuMA KD tissues, a significant difference emerges between the elongated and circular cells, with circular cells tending to have a bias toward movement along the major cell axis, and elongated cells having a bias toward the minor cell axis (Figure 3.4I).

3.2.5 Defining the track gyration tensor reveals that the overall track shapes are more anisotropic than the cell shapes

Following the general movement of the spindle along the major cell axis, we sought to investigate the elongation and overall orientation of the tracks by using the gyration tensor defined by

$$S = \frac{1}{N}\begin{bmatrix} \sum_{i=1}^{N}\left(x^i - \langle x\rangle\right)^2 & \sum_{i=1}^{N}\left(x^i - \langle x\rangle\right)\left(y^i - \langle y\rangle\right) \\ \sum_{i=1}^{N}\left(x^i - \langle x\rangle\right)\left(y^i - \langle y\rangle\right) & \sum_{i=1}^{N}\left(y^i - \langle y\rangle\right)^2 \end{bmatrix} \tag{3.1}$$

to determine the major and minor track axes. Here $\langle x \rangle$ and $\langle y \rangle$ represent the mean positions of the track, which is at position (x^i, y^i) at time t^i. Determination of the eigenvectors $\mathbf{v}_1, \mathbf{v}_2$ and corresponding eigenvalues (λ_1, λ_2) allows us to calculate the track circularity C_{T} by

$$C_{\mathrm{T}} = \frac{\lambda_1}{\lambda_2} \tag{3.2}$$

which, as with the cell circularity, is 1 for circular tracks and 0 for one-dimensional tracks. This method of describing the track circularity and major and minor axes is the same employed to describe cell shape by the positions of the TCVs [15], [21]. Interestingly, the circularity of the tracks in all three conditions were significantly less than the circularity of the cells (Figure 3.5) ($p<0.0001$ in unstretched and stretched tissues, $p=0.0038$ in stretched NuMA KD tissues. Wilcoxon matched-pairs signed rank test). The striking difference between the elongation of the tracks with the approximately square box of the bounds along the major and minor cell axes (Figure 3.4E,G,I, means around movement fraction 0.5), suggested that the tracks were not well aligned with the cell axes. Thus, the cell elongation axes were considered to be insufficient for predicting the shape of translational spindle movement tracks in unstretched and stretched tissues. However, we expect that the track major axis is more aligned with the cell major axis in circular stretched NuMA KD cells, as we saw a bias in spindle movements along the cell long axis when analysing movements specifically along and away from the cell shape axis (Figure 3.4I).

3.2.6 Spindles in circular cells have more translational movements perpendicular to the direction of cell division.

The alignment of cell orientation with division orientation has been observed previously [6], [15], [17], [27], [43], thus we sought to investigate the relationship between track orientation along the track major and minor axes with cell division. The orientation of the major and minor track axes can be determined as the orientation of the eigenvectors $\mathbf{v}_1, \mathbf{v}_2$. We compared the difference between the division orientation θ_{D}, measured from the horizontal (the stretch direction in stretched tissues) and the orientations of the tracks major (+) and minor (-) axes ($\theta_{\pm}$ measured from the horizontal) as well as the cell major axis (θ_{c}, measured from the horizontal). Thus $|\theta_{\mathrm{D}} - \theta_i|$=0 when perfectly aligned for $i \in (\pm, \mathrm{C})$ (Figure 3.6).

We find that in more circular cells, the minor track axis orientation is significantly closer to the cell division orientation than the major track axis orientation for all three conditions (Figure 3.6Aii,Bii, Cii) ($p=0.0019$, unstretched; $p=0.0072$, stretched; $p=0.0486$, stretched NuMA KD. Kruskal-Wallis test and Dunn's multiple comparisons test). This significance is lost in stretched and stretched NuMA KD elongated cells (Figure 3.6Bi,Ci), but maintained in the elongated unstretched cells ($p=0.0199$. Kruskal-Wallis test and Dunn's multiple comparisons test). We speculate that this may be because the degree of elongation of cells in stretched tissues are on average higher than the elongation of cells in unstretched tissues (can be seen in Figure 3.5) leading to a reduced effect across the elongation boundary.

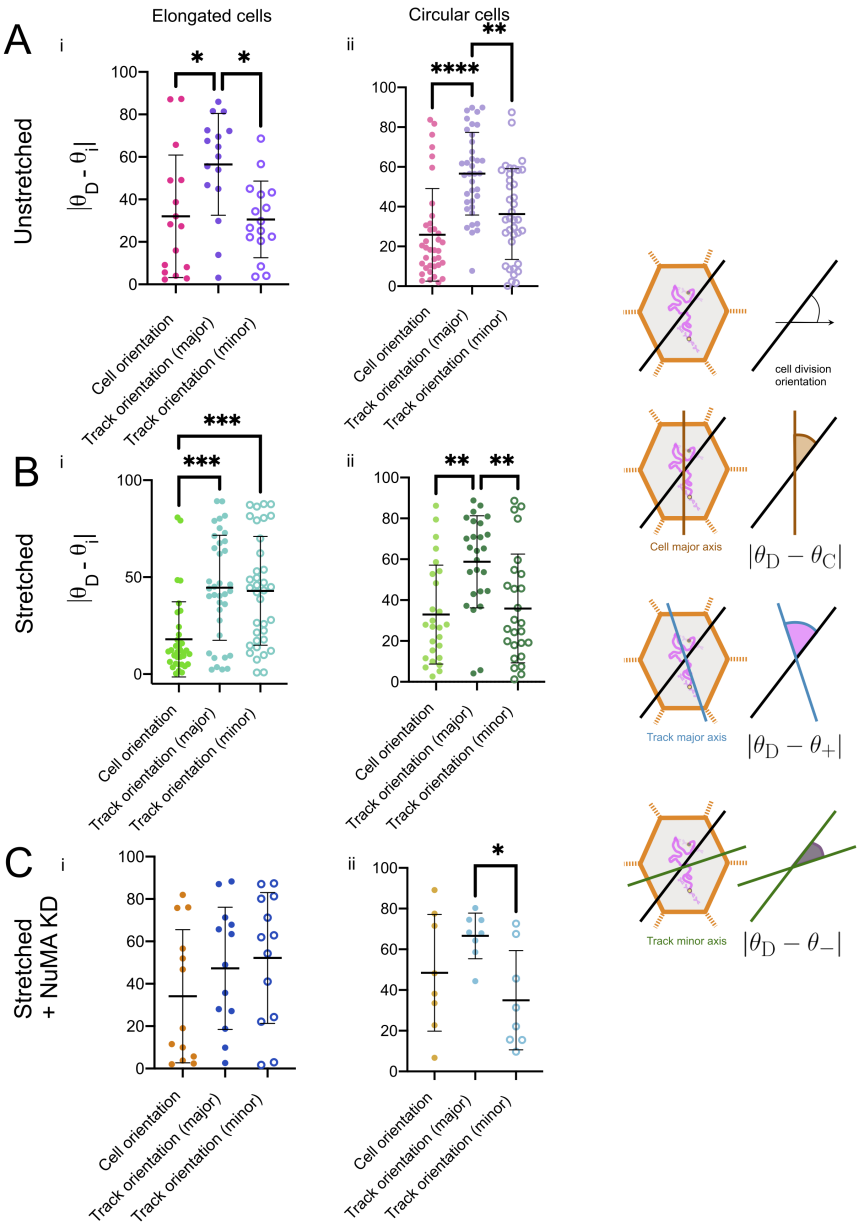

Figure 3.6. **Alignment of track major and minor axes with division.** Alignment of cell orientation, orientation of track major axis and orientation of track minor axis with the cell divsion orientation in A) unstretched, B) stretched, and C) stretched NuMA KD tissues, in i) elongated and ii) circular cells. Error bars represent the standard deviation. Samples analysed using the Kruskal-Wallis test and post hoc Dunn's test. Statistical significance represented by Ai) p=0.0259* (cell orientation compared with major axis orientation), 0.0199* (major axis orientation compared with minor axis orientation). Aii)p<0.0001****,0.0019**. Bi) p=0.0003*** (cell orientation compared with major axis orientation),0.0002*** (major axis orientation compared with minor axis orientation). Bii) p=0.0018** (cell orientation compared with major axis orientation),0.0072** (major axis orientation compared with minor axis orientation). Cii)p=0.0486*. KD - knockdown. Indicators for non-statistically significant results are omitted. Unstretched, elongated: n=16 cells from 6 embryos; Unstretched, circular: n=37 cells from 7 embryos; Stretched, elongated: n=36 cells from 7 embryos; Stretched, circular: n=26 cells from 4 embryos; Stretched + NuMA KD, elongated: n=13 cells from 3 embryos; Stretched + NuMA KD, circular: n=8 cells from 2 embryos.

In elongated cells the cell shape orientation is a better predictor of cell division orientation than the track major axis orientation (Figure 3.6Ai,Bi) (p=0.0259, unstretched; p=0.0003, stretched. Kruskal-Wallis test and Dunn's multiple comparisons test), though not significantly in the stretched NuMA KD tissue (Figure 3.6Ci).

We conclude that the track minor axis aligns closer with the cell division axis in circular cells than the track major axis, though this orientation bias is lost in elongated cells. We speculate whether this is because the major axis of spindle movement cannot be aligned with the minor axis of cell shape in very elongated cells as it is more restricted in motion along the minor cell axis.

3.2.7 The mitotic spindle undergoes rotational movements during metaphase

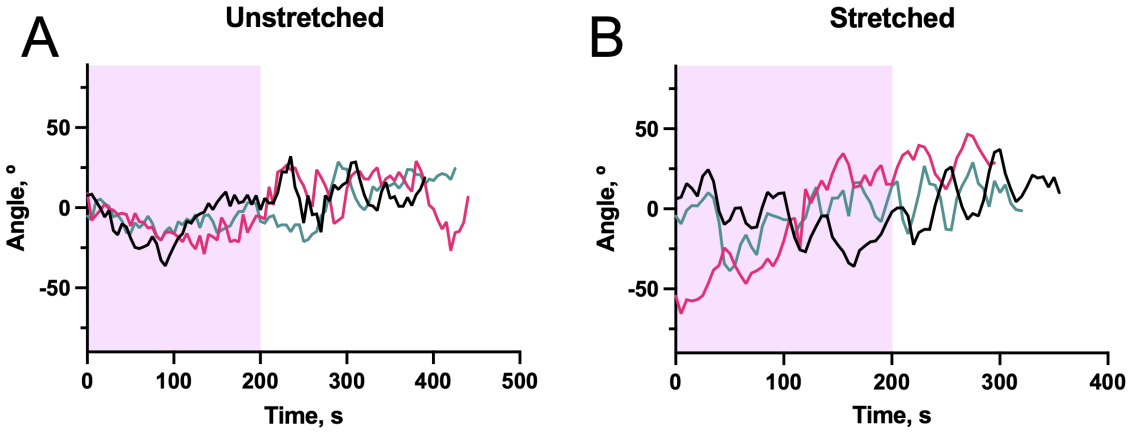

Figure 3.7. **Preliminary data of spindle angles in stretched and unstretched tissues.** Example spindle angles through metaphase from preliminary data collection in A) unstretched tissue cells; and B) stretched tissue cells. The first 200 s of metaphase is highlighted as an approximate indicator of first and second half of metaphase (inexact - for illustrative purposes across the examples).

Following investigation into the translational movements of the spindle, we next turned to the rotational movements of the spindle. The spindle orientation at anaphase is the important factor for determining cell division orientation [192], and the rotation towards this axis is driven by pulling forces [18], [43], [44], [83]. Preliminary data looking at the spindle angle through metaphase for unstretched and stretched tissues showed that the spindles were rotationally dynamic (Figure 3.7). In particular, the spindles in the stretched tissue appeared to have an oscillatory nature (Figure 3.7B) which was in contrast to the spindles of the unstretched tissue (Figure 3.7A), especially if we compared the first half of metaphase between the two conditions (pink shaded region). The spindles of the stretched tissues appeared to undergo large scale movements much earlier in metaphase, as opposed to the unstretched condition which appeared to have more noisy movements rather than defined coordinated movements. Following these qualitative observations of the preliminary data, we chose to quantitatively investigate the rotational dynamics of the mitotic spindle.

To first define the general rotational dynamics of the spindle, we investigated the angular displacement between the initial spindle orientation and the cell division orientation (the

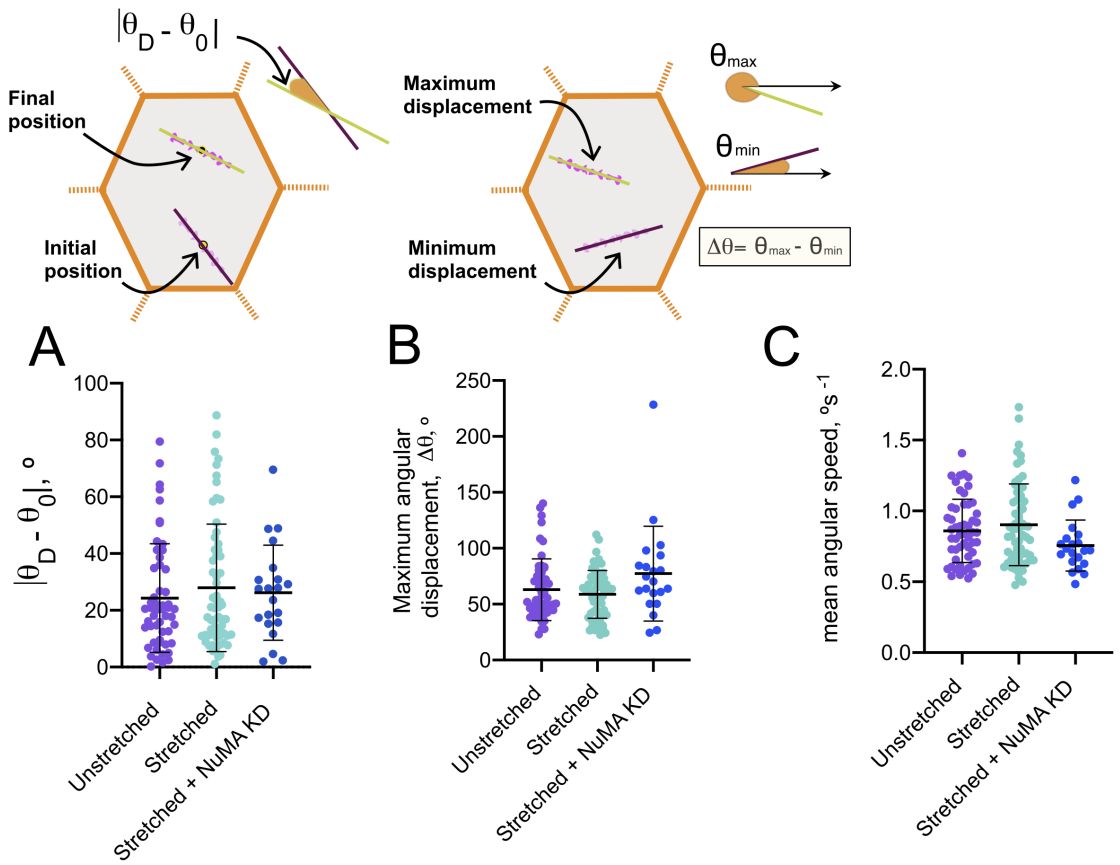

Figure 3.8. **General rotational movements of the spindle**. A) Alignment of the initial spindle orientation θ_0 with the cell division orientation θ_D. Error bars represent the standard deviation. Samples analysed using the Kruskal-Wallis test and post hoc Dunn's multiple comparisons test. B) The maximum angular displacement between the maximum angle and the minimum angle achieved for each spindle through metaphase. Error bars represent the standard deviation. Samples analysed using the Kruskal-Wallis test and post hoc Dunn's multiple comparisons test. B) The mean angular speed of each spindle through metaphase. Error bars represent the standard deviation. Samples analysed using the Kruskal-Wallis test and post hoc Dunn's multiple comparisons test. KD - knockdown. Indicators for non-statistically significant results are omitted. Unstretched: n=53 cells from 8 embryos; Stretched: n=62 cells from 7 embryos; Stretched + NuMA KD: n=21 cells from 3 embryos.

ultimate spindle orientation) (Figure 3.8A). Analysis of this data showed (with a Kruskal-Wallis test and post hoc Dunn's multiple comparisons test) no significant difference between the populations of spindles in each of the three conditions. On average, the initial spindles were formed within 30° of the ultimate division angle (unstretched: $24\pm3°$, stretched: $28 \pm 3°$, stretched NuMA KD: $26 \pm 4°$. Mean$\pm$SEM), though a sub-population of spindles did form initially much more displaced from the ultimate division angle in all three populations (Figure 3.8A). However, the maximum angular displacement of the spindle, defined as the displacement between the maximum and minimum angles achieved, was elevated from displacement between initial and final spindle position (Figure 3.8B), which highlights that the spindle does not rotate towards its final orientation along the shortest path. However, no statistical significance was seen between unstretched, stretched or stretched NuMA KD maximum displacements. The mean angular speed of the spindles in the three conditions were also not statistically significantly different.

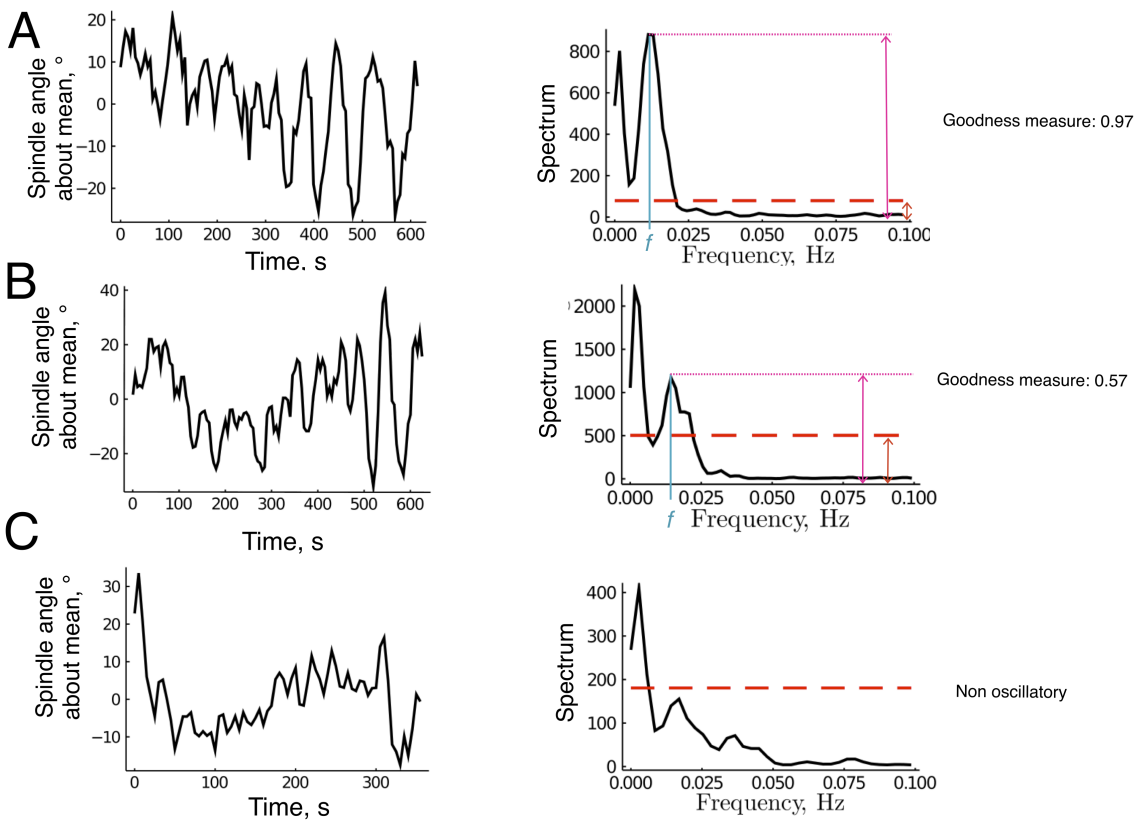

Figure 3.9. **Examples of angle tracks**. Examples of tracks deemed to be A) and B) oscillatory, and C) non-oscillatory by analysis of the associated periodograms. Thresholds above which periodogram spectrum peaks are considered significant are denoted by the red dotted line. The identified frequency of oscillation is indicated by f. The threshold height (red double-headed arrow) and peak amplitude (magenta double headed arrow) are used to define the goodness measure of the identified oscillation. Peaks corresponding to frequencies which result in periods within 95% of the track duration were discarded as trend artefacts.

3.2.8 The mitotic spindle oscillates as it is positioned during metaphase

We next investigated rotational spindle movements by seeking oscillations using a periodogram to determine the dominant frequencies present in the 'signal tracks' (the angles of the spindle through time) (Figure 3.9). The peaks of the periodogram were determined to be significant and thus correspond to an oscillatory frequency if they surpassed a defined outlier threshold (Section 2.3.1). The periods within 95% of the total duration were also determined to be trend lines and were thus omitted from the analysis (Figure 3.9C). We assigned each oscillation a 'goodness measure', which we defined based on the ratio of the outlier threshold to the periodogram peak amplitude. Thus,

$$\text{Goodness measure} = 1 - \frac{\text{Threshold}}{\text{Peak amplitude}}, \tag{3.3}$$

and the goodness measure is close to 1 for peaks far exceeding the threshold and closer to 0 for peaks close to the threshold (Figure 3.9A,B). We note that this goodness measure was created for this work explicitly to distinguish between oscillations which are less defined (just passing the threshold) and more defined (far surpassing the threshold).

The fraction of oscillatory spindles decreased in stretched tissue cells by comparison with unstretched tissue cells (p=0.0312, Fisher's exact test), though all of the stretched NuMA

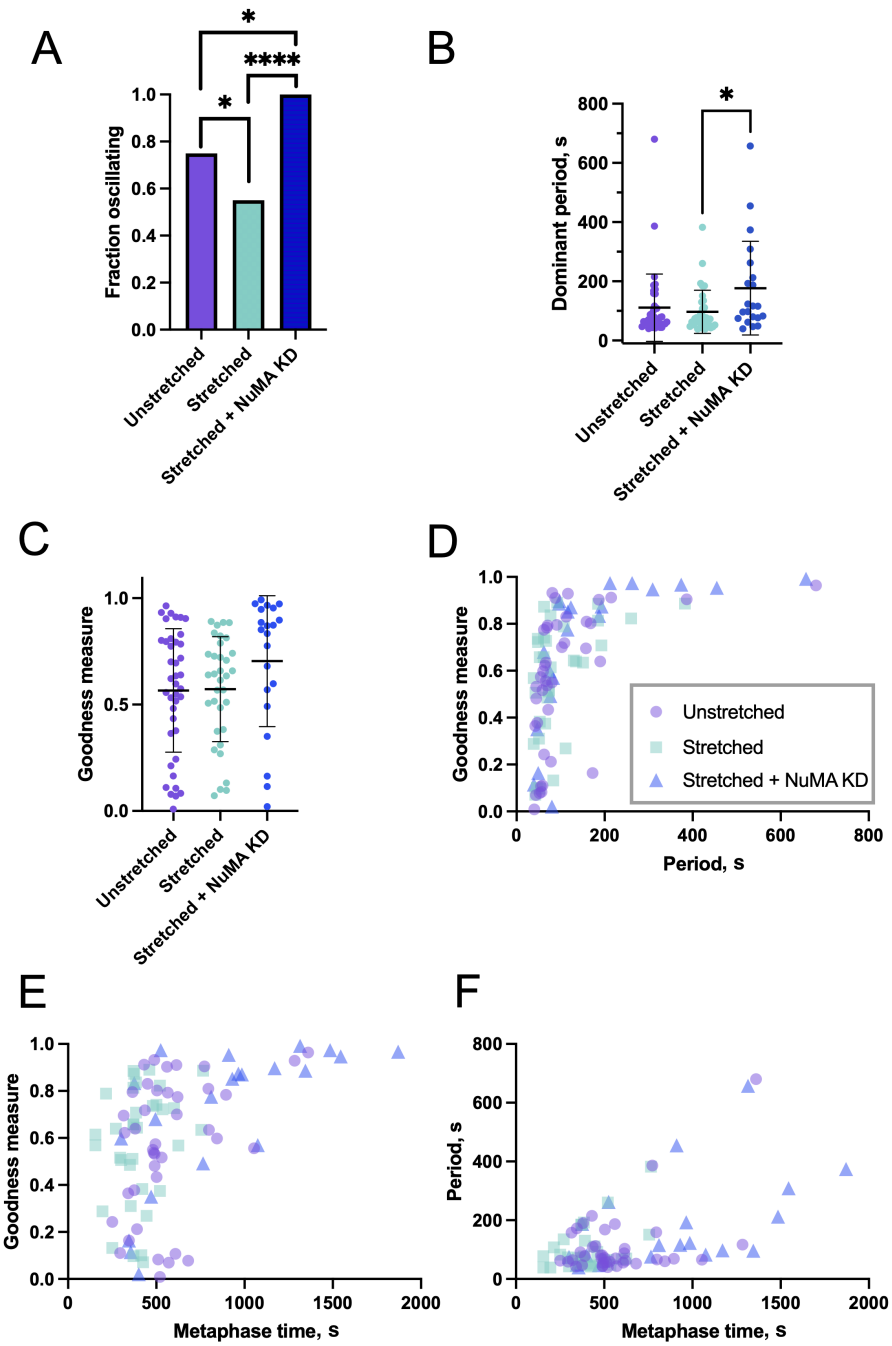

Figure 3.10. **Oscillations of the mitotic spindle through metaphase**. A) The fraction of spindles which oscillate in the unstretched, stretched, and stretched NuMA KD tissues. Sample count data analysed using Fisher's exact test. Unstretched: n=53 cells from 8 embryos; Stretched: n=62 cells from 7 embryos; Stretched + NuMA KD: n=21 cells from 3 embryos. B) Comparison of the dominant periods of the oscillating spindles in each condition. Error bars represent the standard deviation. Samples analysed using the Kruskal-Wallis test and post hoc Dunn's multiple comparisons test. C) Comparison of the goodness of the oscillations detected across the three conditions. Error bars represent the standard deviation. Samples analysed using the Kruskal-Wallis test and post hoc Dunn's multiple comparisons test. D) A scatterplot comparing the goodness measure of oscillations against the period of the oscillations. All three conditions present on the same plot. E) Comparison of the goodness measure of oscillations against the corresponding cell's metaphase time. F) Comparison of the period of oscillation with metaphase time. D,E,F) all use the same legend. Data analysed using the Spearman rank correlation test. Statistical significance represented by A) p=<0.0001****, 0.0312* (unstretched compared with stretched),0.0145* (unstretched compared with stretched NuMA KD). B) p=0.0387*. KD - knockdown. Indicators for non-statistically significant results are omitted. B), C), D), E) and F) from Unstretched: n=40 cells from 8 embryos; Stretched: n=34 cells from 6 embryos; Stretched + NuMA KD: n=21 cells from 3 embryos.

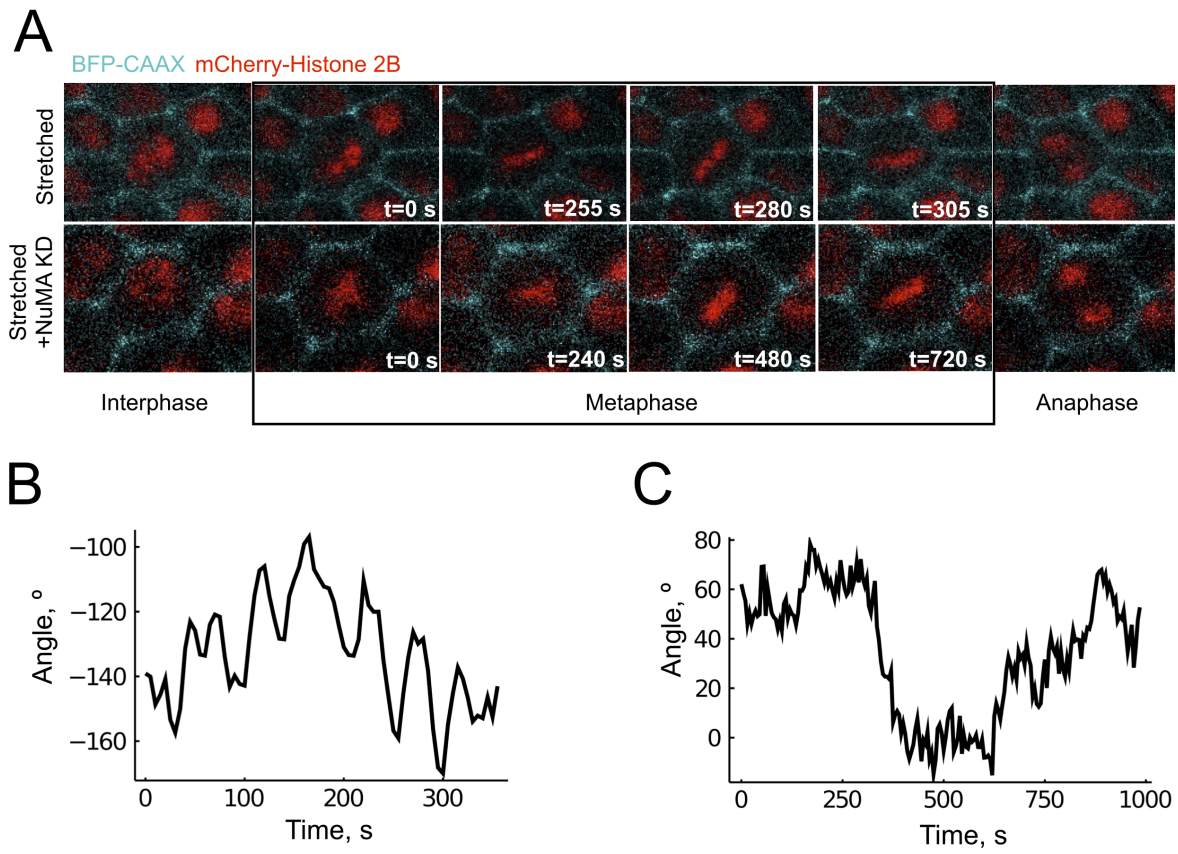

Figure 3.11. **Microscope images of oscillations in stretched tissues**. A) Time lapse images of oscillations of the metaphase plate (red - mCherry-Histone2B) during metaphase in stretched tissue and stretched NuMA KD tissue. A single oscillation is shown in each case. The cell membrane is tagged with BFP-CAAX. The resulting spindle angle signals from these cells are shown for the B) stretched tissue cell, and C) stretched NuMA KD tissue cell. KD - knockdown

KD cells were characterised as oscillatory, increased from both the stretched ($p<0.0001$, Fisher's exact test) and unstretched ($p=0.0145$, Fisher's exact test) (Figure 3.10A). The stretch regime had no effect on the dominant period of oscillation of the spindles (unstretched 111 ± 18 s, stretched 97 ± 13 s; mean$\pm$SD) (Figure 3.10B), though the NuMA KD stretched cells had spindles whose oscillations had periods significantly longer than the periods in stretched tissues ($p=0.0387$, Kruskal-Wallis test and post hoc Dunn's multiple comparisons test) (Figure 3.10B and Figure 3.11). Due to the asymmetry of the distributions of the periods, we also note here the median values for each condition, unstretched 70 s; stretched 70 s; stretched NuMA KD 116 s. We note that the periods above 600 s are unlikely to be present in stretched tissues due to the decreased metaphase time.

Statistical analysis of the goodness measures over the three conditions reveals no significant difference (Figure 3.10C). Analysis of the correlation of goodness measure with period shows a positive correlation (Figure 3.10D) ($p<0.0001$ for unstretched, $p=0.0032$ for stretched, $p<0.0001$ for stretched + NuMA KD. Spearman rank correlation test). In order to determine whether or not the goodness measure was sensitive to track duration we also analysed the correlation of the goodness measure with metaphase time and determined that there was no correlation in unstretched and stretched conditions. However, the stretched NuMA KD condition showed a positive correlation with metaphase time ($p = 0.0002$. Spearman rank correlation test). Longer metaphase times are correlated with longer periods for

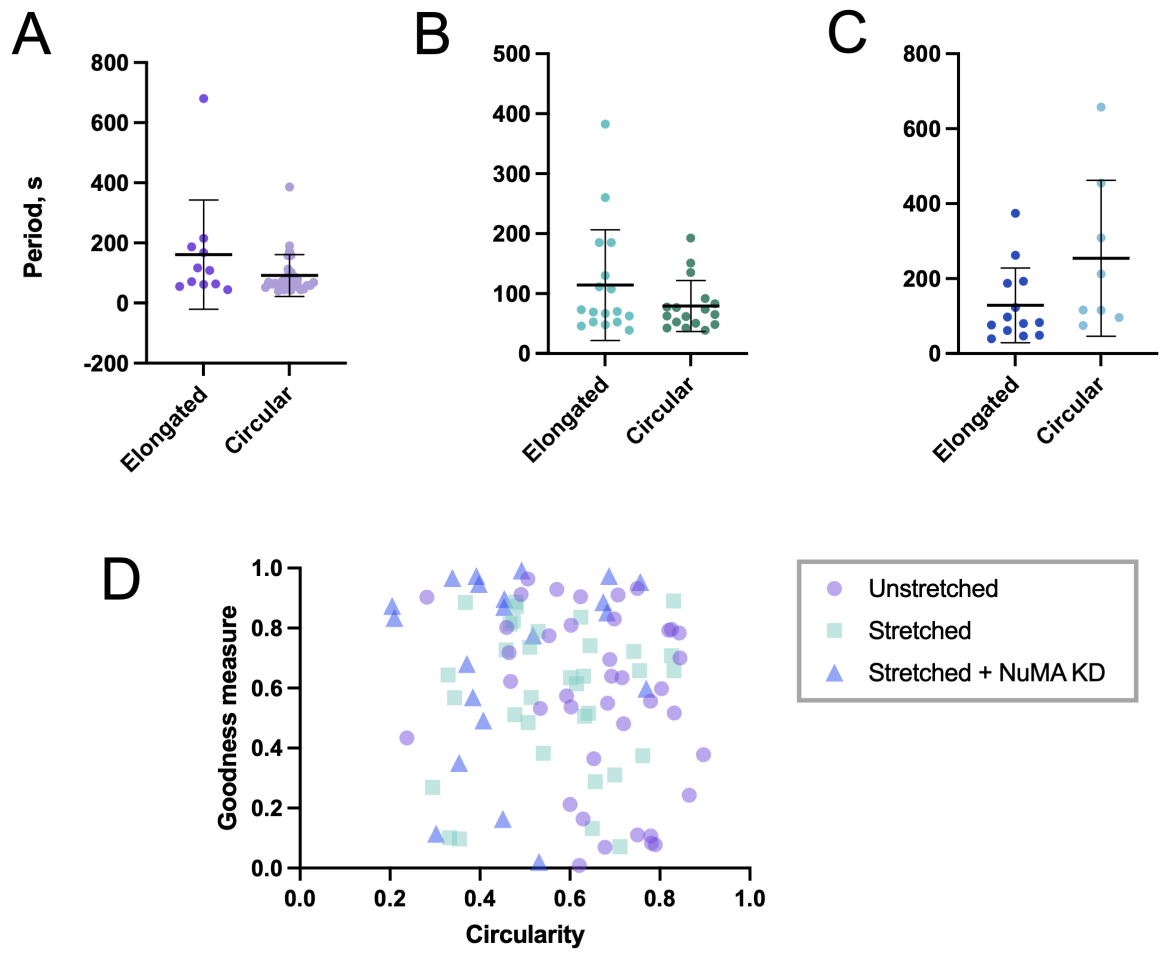

Figure 3.12. **The effect of circularity on oscillations**. Comparison of periods of oscillation in elongated and circular cells in A) unstretched, B) stretched, and C) stretched NuMA KD conditions. Error bars represent the standard deviation. Data analysed using the Mann-Whitney test. D) Scatter graph of the goodness of oscillation compared with cell circularity for unstretched, stretched and stretched NuMA KD tissues. Data analysed using the Spearman rank correlation test. KD - knockdown. Indicators for non-statistically significant results are omitted. Unstretched, elongated: n=11 cells from 7 embryos; Unstretched, circular: n=29 cells from 7 embryos; Stretched, elongated: n=17 cells from 4 embryos; Stretched, circular: n=17 cells from 6 embryos; Stretched + NuMA KD, elongated: n=8 cells from 2 embryos; Stretched + NuMA KD: n=13 cells from 3 embryos.

the stretched NuMA KD tissue (p=0.0012. Spearman rank correlation test) but not for unstretched or stretched tissues (Figure 3.10F). We also acknowledge that longer metaphase times allow for the presence of longer periods to become established sufficiently that they may be picked out by the periodogram in a noisy signal, but more data would be needed in order to determine whether or not this has a significant effect on the data. By visual confirmation of the oscillations within the signals, we observed that the spindle oscillations present in stretched tissue cells (Figure 3.11B) were less noisy than the longer oscillations seen in NuMA KD tissues (Figure 3.11C), suggesting that they may be arising from different mechanisms.

3.2.9 Cell circularity has no effect on the period or quality of oscillation

As in the analysis of the translational movements, we split the data into oscillations within elongated and circular cells. We saw no significant difference between the mean period be-

tween the two populations (Figure 3.12A,B,C). There was also no correlation between the circularity and the goodness of oscillation (Figure 3.12D) (Spearman rank correlation test). We conclude that cell circularity has no effect on the quality of the oscillation, nor does it have a significant effect on the period of oscillation.

3.2.10 Oscillation period is independent of when the oscillations happen during metaphase

Our preliminary data suggested that spindles may show different rotational dynamics between early and late metaphase, in particular in unstretched tissues (Figure 3.7A), whereas stretched tissues seemed to have less of a difference in behaviour between the two halves (Figure 3.7B). Additional to this data, a previous study looking at spindle dynamics in *Xenopus leavis* embryos described early metaphase as a rotation to the final orientation, while oscillations built up toward the onset of anaphase [77]. We thus sought to determine whether or not this difference was present in our full data sets, as well as in our stretched NuMA KD tissue. We saw a significant increase in the fraction of oscillating spindles between the first and second halves of metaphase in unstretched tissues (Figure 3.13A) ($p=0.01$. Fisher's exact test). This trend was lost in the stretched and stretched NuMA KD tissues (Figure 3.13A). The periods of the detected oscillations showed no significant difference between early and late metaphase across any of the three conditions (Figure 3.13B,C,D). Further, analysis of the goodness measure of the oscillations also showed no significant difference between early and late metaphase in either of the three conditions (Figure 3.13E,F,G).

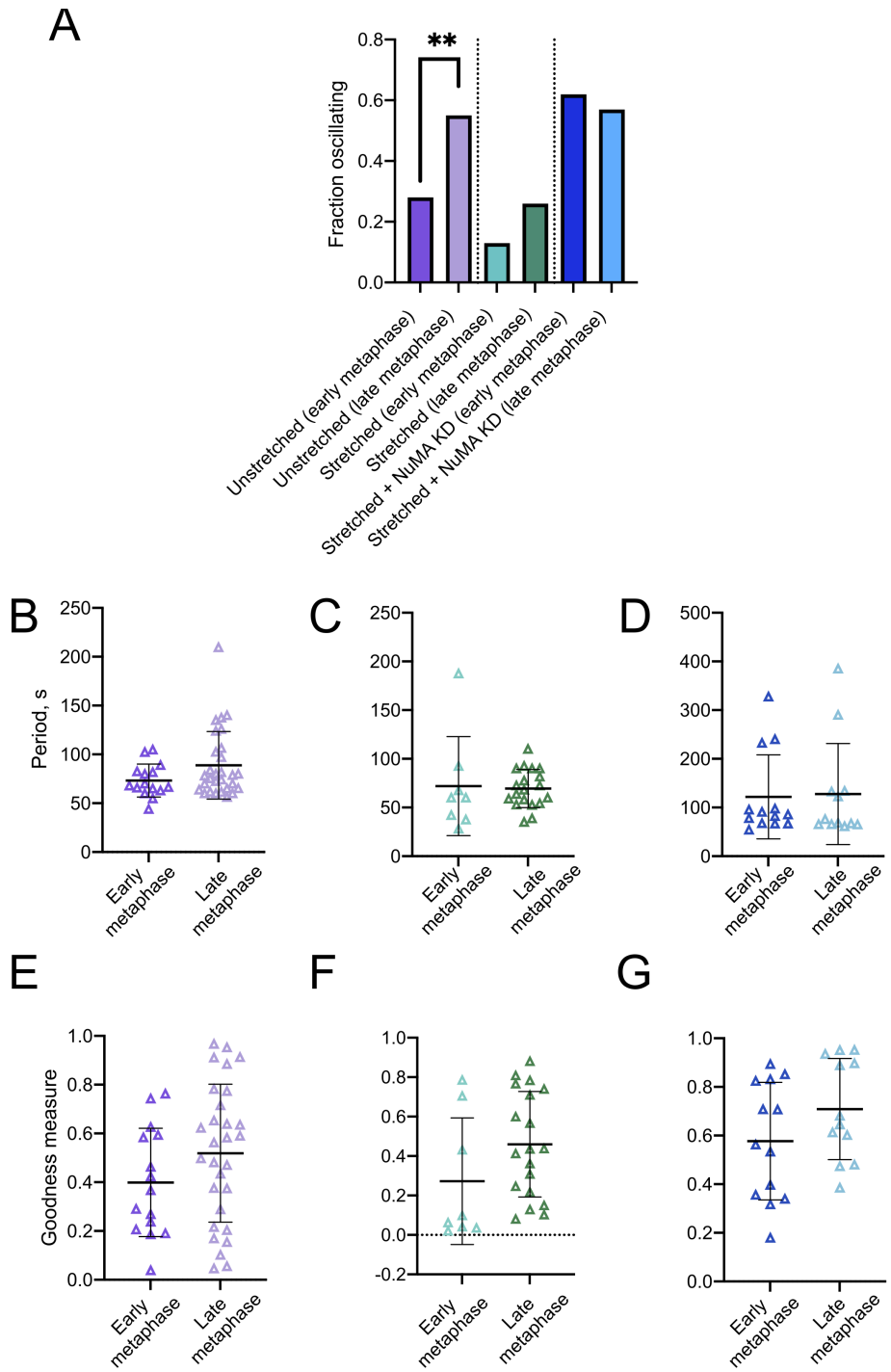

Figure 3.13. **Spindle oscillations in early and late metaphase**. A) A comparison of the fraction of oscillating spindles during early and late metaphase. Sample count data analysed using Fisher's exact test. Unstretched: n=53 cells from 8 embryos; Stretched: n=62 cells from 7 embryos; Stretched + NuMA KD: n=21 cells from 3 embryos. B) C) D) Comparison of periods of spindle oscillation detected in early and late metaphase in B) unstretched, C) stretched and D) stretched NuMA KD tissues. Error bars represent the standard deviation. Data analysed using the Mann-Whitney U test. E) F) G) The goodness of oscillation of the identified oscillations in early and late metaphase in E) unstretched, F) stretched, G) stretched NuMA KD tissues. Error bars represent the standard deviation. Data analysed using the Mann-Whitney U test. Statistical significance represented by p=0.01**. KD - knockdown. Indicators for non-statistically significant results are omiitted. Unstretched, early metaphase: n=15 cells from 8 embryos; Unstretched, late metaphase: n=29 cells from 8 embryos; Stretched, early metaphase: n=8 cells from 4 embryos; Stretched, late metaphase: n=16 cells from 7 embryos; Stretched + NuMA KD, early metaphase: n=13 cells from 2 embryos; Stretched + NuMA KD: n=12 cells from 2 embryos.

3.3 Discussion

Protein NuMA has been implicated in spindle positioning due to its interactions with motor protein dynein, which work together to pull the spindle into position [43], [64], [79]. Interestingly, division orientation has been attributed to both cell shape [19], [43], [44] and cell tension [6], [12], [13], though elucidating which is the responsible factor is difficult as applied tensions deform cell shapes [15]. Indeed, how NuMA and dynein function differently under tension to create a shape-based or force-based division orientation response in unclear. With an aim to understand more directly how tension regulates division orientation, here we have investigated in detail how the application of a known tensile force impacts mitotic spindle dynamics in a tissue context. In addition, we have compared spindle dynamics in control tissue with tissue in which the key spindle orientation protein, NuMA, has been knocked down. It has been shown in a recently submitted thesis from the Woolner lab that NuMA is required for orienting the spindle to tension and cell-shape [27], but the exact mechanism by which NuMA functions, especially in tension-sensitive spindle orientation, remains unclear. By examining spindle dynamics in detail, we aim to gather information to refine and improve mathematical models of spindle dynamics (Chapters 4, 5) with the ultimate goal of shedding new light on how the spindle responds to external force.

Prior to embarking upon our study of mitotic spindle dynamics, we confirmed that metaphase plate dynamics could be used as a proxy for spindle dynamics by analysing their angles and positions in *Xenopus laevis* embryos expressing cherry-H2B and GFP-α-tubulin [179] (Figure 3.1). This analysis was important to reduce the number of fluorescent tags present in the cell. mCherry-Histone2B was chosen to monitor the cell's progression through mitosis, while BFP-CAAX could be used to measure the cell shape. Only fluorescently tagging two proteins of interest was important for our initial hope to also image GFP-NuMA in order to monitor its dynamic localisation at the cell cortex. However, GFP-NuMA proved difficult to image with a significant intensity (data not shown), thus imaging it at such a dynamic timescale of 5 s per frame was infeasible. However, we continued to pursue imaging without GFP-NuMA in the hope that the imaging of NuMA could be optimised at a later date and subsequently re-introduced in rescue experiments. We showed that the metaphase plate and mitotic spindle lie perpendicular to one another (Figure 3.1E), with coordinated fluctuations in both their angles and respective centre of mass' (Figure 3.1F,G,H). Thus we conclude that the metaphase plate can be monitored and used to describe the accompanying dynamics of the mitotic spindle.

Using this imaging approach, we went on to explore the spindle dynamics in terms of its translational positioning within the cell. The spindle was shown to have an overall centring mechanism, by analysis of the proximity of the final positions to the cell centre (unstretched, and stretched within the central 0.07 ± 0.05 and 0.07 ± 0.04 fraction of the cell respectively, mean$\pm$SD) (Figure 3.2A) and the distance of the centre of mass of the metaphase plate from the cell centre between the start and end points of metaphase (Figure 3.2C). Further, the maximum displacement of the spindles from the cell centre in ei-

ther unstretched or stretched tissue cells showed no significant difference within the conditions (Figure 3.2D), suggesting that the application of a stretch does not affect the ability of spindles to maintain their position at the cell centre. This has important implications for the ability of cells in tissues to generate two daughter cells of equal size despite the mechanical environment, as an off-centre division will not evenly distribute cellular components [78], [195]. We suggest that the correct centring of the spindle despite the application of stretch aids in the maintenance of a population of cells of equal sizes and function.

Analysis of the effective speed, calculated by dividing the sum of the root mean squared displacement over metaphase time for each spindle, revealed that the spindle speed was unchanged between the unstretched and stretched tissues (Figure 3.3B). This suggests that the balance of forces acting on the spindle to position it within the unstretched and stretched tissues are unaffected by stretch, as a shift in the balance of forces on the spindle would result in spindles which moved at a different rate. For example, less pulling by cortical dynein would result in spindles which moved more slowly [18], [78], [80]. By defining the bounding area explored by the mitotic spindle in terms of its greatest displacements in the x and y coordinate space, we saw a correlation between the explored area and metaphase time in unstretched tissues but not in stretched tissues (Figure 3.3C), suggesting that the spindles in unstretched tissues explore the cell throughout metaphase until anaphase onset, while in stretched tissues they may undergo more directed motion toward their final position. The metaphase times in stretched tissue (6 ± 2 min) were also significantly shorter than in the unstretched tissues (8 ± 4 min, mean$\pm$SD). We speculate that cells with particularly long metaphase times may have internal cues which are preventing the cell from entering anaphase, possibly due to the spindle being unable to position itself correctly within the cell. This is similar to the conclusion drawn by O'Connell and Wang (2000) [44], whereby cells whose spindles were formed far away from the long axis of the cell were delayed in entering anaphase. While their suggestion of a mitotic checkpoint relating to spindle positioning was mostly based upon rotational positioning, the translational positioning of the spindle may also contribute to entry through the mitotic checkpoint before anaphase is able to proceed. This metaphase time effect could be due to either rotational or translational dynamics, however, the overall centring seen across both stretched and unstretched tissues suggests that the spindle is sufficiently positioned to enter anaphase and gives evidence to the existence of a spindle positioning-related mitotic checkpoint.

As the area of the cell explored by the spindles in the various conditions are linked to the metaphase time, we moved on to analyse the spindle movements in terms of ratios of the directions travelled instead, such that we might shed some light on the directionality and shape of the tracks traced by the spindle centres (Figure 3.4). The locations of the TCVs have been implicated as core components in the determination of the cell division orientation [15], [43]. In particular the orientation of the cell major axis, where the cell shape is defined in terms of the locations of the TCVs, has been shown to align well with the cell division orientation, particularly in elongated cells [15]. Oscillations of the mitotic spindle along the pole-pole axis (i.e., along the axis of spindle orientation) have been previously

described in HeLa cells, toward sites of cortical enrichment of dynein [18], [26], however, movements perpendicular to the spindle orientation have also been described [77]. To explore this in our tissue, we reframed the track taken by the spindle relative to the cell major axis, and used the standard deviation of the path along the cell major and minor axes to define a new bounding area. We defined a fraction of major axis movement, whose value is above 0.5 for spindles with movements biased along the cell major axis rather than along the cell minor axis. The standard deviation was chosen here in order to reduce the effect of outlier track positions on the analysis. The aim here was to determine whether the anisotropy of cell shapes had an effect on the spindle movements.

The work of Dimitracopoulos *et al* (2020) recently showed that monopolar spindles in elongated HeLa cells showed a broad range of movement similar to an oscillation along the length of the cell [76], due to the interactions of astral microtubules with cortical elements (dynein/NuMA/LGN, visualised by GFP-LGN). The presence of the chromosome-derived RanGTP gradient was shown to exclude LGN (and thus NuMA and dynein) from the cortex upon close proximity, reducing the pulling power acting on the spindle pole from the regions within 4 μm of the metaphase plate [76]. From this we would expect that the closer proximity of the metaphase plate to the cell cortex in elongated cells would result in a more polarised distribution of dynein/NuMA/LGN at the distant cell edges, and thus more pulling power resulting in movement along the major cell axis. Movements in this plane have been recorded for elongated cells previously [18]. Contrary to this, the experimentally measured spindle dynamics showed no bias towards movement along or against the cell major axis regardless of circularity or stretch condition (Figure 3.4E,G). This lack of bias suggests that either that a) movements of the spindle do not have a directional bias with regards to the spindle orientation, or b) the spindles in these cells are not well aligned with the cell long axis for a significant fraction of metaphase, leading to more random movements. While a strict analysis of the movements along the orientation of the mitotic spindle over the course of metaphase would have been beneficial here (as in [18]), this analysis could not be completed due to time constraints.

To further explore the precise shape of the tracks taken by the mitotic spindle, in particular to determine whether or not there was any directional bias in the movements not related to the cell shape, we defined the gyration tensor of the spindle positions over all of metaphase. The eigenvectors of the gyration tensor were used to define the major and minor track axes, while their associated eigenvalues were used to define a track circularity. Interestingly, both unstretched and stretched tissues had spindles whose centre of mass moved along a track which was more elongated than the cells they were in (Figure 3.5A,B). Thus the spindle movements do have a directional bias - they are just not correlated with the cell shape orientation (Figure 3.4E,G).

By defining the spindle track major and minor axes, we compared the spindle movements with the cell division orientation (Figure 3.6). Interestingly, the analysis showed that in unstretched tissues, the track major axis was significantly less oriented along the division axis than cell shape was, with the track minor axis better oriented with the division axis. This

significance was increased in the circular cells (Figure 3.6A). Then in unstretched tissues, the range of translational mitotic spindle movement is increased away from the division axis, rather than along it. The circular cells in the stretched tissues showed this same bias (Figure 3.6Bii), though in the elongated cells tissues both the major and minor axes of the track elongation were significantly further away from the division axis than cell shape was (Figure 3.6Bi). This suggests that in elongated cells the orientation of the track is randomly distributed with no clear bias. As we saw no clear bias between the fraction of movement along the cell major axis (Figure 3.4G), and we expect cell shape to be well aligned with division orientation in stretched, elongated cells [8], [15], [27], [175], this randomisation of the track orientation is consistent across Figures 3.4G and 3.6Bi. We suggest that the elongation of the cell is the reason for this - as the spindle would be expected to be more aligned with the cell long axis due to geometric constraints.

If the spindle orientation machinery is such that it tends to create more movements perpendicular to the plane of division, but the length of the cell is significantly decreased in that plane due to the cell elongation, then this places a geometric restriction on the spindle movements which may be redirected off-axis, creating the randomised distribution seen in Figure 3.6Bi. Lateral movements of the spindle toward the cell cortex would result in the close proximity of the metaphase plate to the cortex, which has been shown to exclude LGN (and thus NuMA and dynein) due to the chromosome-derived Ran-GTP gradient [76]. This creates localised regions of LGN/NuMA/dynein from which pulling forces could be acting, away from the lateral cell edges. The close proximity of the spindle to the cell cortex would also decrease the angle between the astral MTs and the cortex which has been shown to result in dynein-mediated 'sliding' of the spindle along the cortex as more dyneins can load onto a single MT to pull it along the cell edge [82]. We therefore suggest that due to the asymmetry in the localisation of dynein from the chromosome-derived Ran-GTP gradient and sliding effects, this redirects the lateral motion of the spindle into more randomised motion in the elongated cells of the stretched tissue, due to geometric constraints. We speculate that this effect is stronger in more elongated cells, thus the effect is not seen in the elongated cells in the unstretched tissue as the 'elongated' cells in this tissue are on average less elongated than those in the stretched tissue (see distribution of points below $C = 0.6$ in Figures 3.4D, F). We would ideally prefer to further divide the data into degrees of elongation, however more data would be required to have a sufficiently large number of data points in each category from which to draw conclusions. An alternative hypothesis for this effect is that sliding interactions of the MT with cortical elements may require tension to create a stable substrate to transfer forces effectively [16], thus the off-axis pulling due to microtubule sliding could be less effective in unstretched cells. Again, more data will be required to fully investigate this.

We next analysed the rotational movements of the mitotic spindle, which have been the subject of more studies than the translational movements, though often at a decreased frame rate [8], [16], [18], [44], [82], [83]. Preliminary data confirmed that the angle of the mitotic spindle was rotationally dynamic in both unstretched and stretched tissues, though the

data in stretched tissues suggested the presence of more coherent oscillations earlier on in metaphase (Figure 3.7). Despite our initial expectations for this data, we found that in general the number of oscillating spindles in stretched cells was reduced relative to in the unstretched conditions (Figure 3.10A) with no effect on the quality of the oscillations as determined by a defined 'goodness measure' (Figure 3.13C). Interestingly, the application of stretch had no effect on any of the rotational dynamics we measured, including the net angular displacement (Figure 3.8A), the mean angular speed (Figure 3.8C), nor the period of oscillation (Figure 3.10B). Further, the increased maximum angular displacement relative to the initial displacement from the division angle (Figure 3.8B compared with Figure 3.8A) suggests that spindles do not take the shortest path toward their final orientation.

The circularity had no effect on the period or quality of oscillations in either stretched nor unstretched tissues (Figure 3.12). This is in contrast with what was reported by Tang *et al.* (2018) when they investigated spindle dynamic behaviours in the mouse lung epithelium [8]. Their work showed that two populations of spindle dynamics existed within the tissue - 'rotating' spindles, which moved continuously through metaphase, and 'fixed' spindles, which rotated to their final orientation at the beginning of metaphase and maintain this position until anaphase. They attribute the existence of these two populations to the relative elongation of the cells - with elongated cells having fixed spindles rather than rotating spindles [8]. We would expect that more oscillatory spindles would be considered to be 'rotational' and thus correspond to more circular cells, while 'fixed' spindles would not oscillate. The invariance of the oscillation period and goodness of oscillation with circularity is in contrast to this expectation. Interestingly however, stretching the lung tissue on a silicon membrane caused a net elongation of the lung cells and also a greater number of fixed spindles - suggesting that an external mechanical stretch reduces movement dynamics, which matches our observation that fewer spindles oscillate in stretched tissue (Figure 3.10A and Figure 3.13A). However, due to the low temporal resolution of the data obtained by Tang *et al.* (2018) (3 minutes per image) [8], our expectations for how these spindles might look at a higher temporal resolution is entirely speculation. Interestingly, they also show that promoting ERK1/2 signalling by constitutive expression of activated BRAF resulted in more rotating spindles [8]. As ERK1/2 signalling is elevated in tissues experiencing tension [85] and has been shown to promote actomyosin contractility [196], we conclude that ERK1/2 signalling in unstretched tissues may function separately to an externally applied tension.

We separated metaphase time into two halves in order to determine whether or not the spindles build up to form oscillations in late metaphase. This behaviour was predicted from our preliminary data (Figure 3.7) and has also been previously observed in the epithelial tissue of *Xenopus laevis* embryos [77]. We saw a significant increase in the number of oscillating spindles in late metaphase in unstretched tissues, but this significance was lost in the stretched tissues (Figure 3.13A). Interestingly, the quality and period of oscillation were both unaffected by the timing of oscillation onset (Figures 3.13B, C, E, F). This suggests the existence of a barrier that needs to be overcome in order to promote oscillations, though once this barrier is surpassed then the resulting dynamics are invariant between conditions.

For example, in the first cell division of *C. elegans* the mitotic spindle is displaced towards the posterior of the embryo [197], [198], and this movement coincides with large oscillatory dynamics in the lateral position of the posterior pole [78]. This lateral oscillation depends upon a threshold number of cortical dyneins, below which oscillations cannot be sustained [79]. We suggest that a threshold may also exist in the *Xenopus laevis* animal cap tissue, and that threshold is more easily surpassed in unstretched tissues rather than stretched tissues, and in late rather than early metaphase. Interestingly, the lack of dependence on cell circularity suggests that this effect may be tension-regulated rather than geometric.

To determine whether or not the movements of the mitotic spindle were perturbed upon knockdown of NuMA, which localises to the cell cortex during metaphase and interacts with dynein to produce displacements of the spindle pole [26], [64], [103], we induced a partial NuMA knockdown by morpholinos, using a method described and used previously in the Woolner lab [27]. The partial knockdown of NuMA in this way has been shown to affect the ability of cells in stretched and unstretched *Xenopus laevis* animal cap tissue to orient their divisions with the cell long axis [27]. Analysis of NuMA's binding partner LGN shows a reduced cortical localisation signal under low tissue tension in dense MCDK monolayers [12], pointing to a potential tension-dependent localisation of NuMA at the cortx through its interactions with LGN. Tension-sensitive localisation of NuMA to the cell cortex was observed and quantified by Taranuum (2022), showing a preferential recruitment to the cell cortex proximal to the spindle poles earlier in mitosis in stretched tissues when compared with unstretched tissues. This temporal and tension dependent accumulation of NuMA is particularly interesting, as the *Drosophila* homolog (Mud) is static at the cell cortex and localises specifically to the TCVs of tissue cells [43]. We would expect that the dynamic recruitment of NuMA to the cell cortex would affect spindle dynamics, as the recruitment of dynein/dynactin to the cortex to position the spindle will also be dynamic. Indeed, Taranuum (2022) reported reduced translational speeds of spindles in NuMA KD tissues, though the temporal resolution of the live imaging was too large (30 s per frame) to determine whether this shift in speed was a result of less directed motion of the mitotic spindle or indeed a result of loss of cortical force generation [27]. Interestingly, our data showed no significant difference in the effective translational speed of the mitotic spindle in NuMA KD tissue (Figure 3.3B), highlighting the value of analysing the temporal dynamics of the spindles at a higher frame rate. Unfortunately, due to a decline in the health of the *Xenopus laevis* embryos and time constraints, large samples of NuMA KD data could not be collected. As such, we were unable to include data from unstretched NuMA KD tissues in our analysis, and the dataset for divisions in stretched NuMA KD tissues is also smaller than we would have preferred (n=21, compared with n=53 in the unstretched condition and n=62 in the stretched condition).

The net translational movements of the mitotic spindle in the stretched *Xenopus laevis* animal cap tissue were unaffected by the knockdown of NuMA (Figure 3.2A, B, C). The NuMA knockdown spindles ended metaphase within the central 0.08 ± 0.04 fraction of the cell (mean$\pm$SD) (Figure 3.2A), and displayed a net centring mechanism from its initial place-

ment in the cell upon metaphase onset (Figure 3.2C). This centring mechanism was invariant between stretched or NuMA knockdown conditions, suggesting that NuMA is not required for spindle centring. This is aligned with previous studies which implicate pulling forces by cortical dynein//NuMA/LGN as decentring forces [54], [78], [80], while microtubules pushing at the cortex have been implicated as a spindle centring mechanism [78], [137]. Thus, the result that a knockdown of NuMA has no effect on the centring mechanism suggests that the net result of the spindle position may be a result of microtubule-based pushing forces rather than cortical forcing by dynein.

Interestingly, the knockdown of NuMA also increased the normalised maximum displacement of the spindle from the cell centre, suggesting that while an overall centring mechanism may function normally, the spindle takes a more deviatoric path toward its final position. The increased metaphase time of NuMA KD cells (Figure 3.3A) combined with the final positioning of the spindle being at the cell centre suggests that NuMA KD impairs spindle positioning, but a mitotic checkpoint may exist which requires the spindle to be properly positioned in the cell before proceeding to anaphase [44]. This increased metaphase time was also observed in unstretched tissues, with a positive correlation between the deviation of the path from the cell centre (Figure 3.3C). Thus, due to NuMA's tension-sensitive function in spindle orientation [27], we suggest that NuMA operates at the cell cortex and aids correct spindle centring in stretched tissues, though the NuMA-mediated mechanism for spindle positioning works in conjunction with another NuMA-independent mechanism which results in the final spindle position. Interestingly, dynein-mediated pulling of the spindle has shown to increase centring in cultured BS-C-1 cells [193], thus it is not necessary that the presence of NuMA would de-centre the spindle as we previously thought.

Another suggestion for the increased deviation from the cell centre in NuMA KD tissues is that it may be due to the partial knockdown of NuMA within the cell. Rather than in a full knockout, small populations of force generating cortical complexes may remain in the cell which may impart asymmetric forces on the spindle leading to increased decentring for part of metaphase. NuMA has been shown to form clusters at the cell cortex due to interactions in the C-domain of neighbouring NuMAs [64]. Thus, small pools of NuMA could accumulate to one area of the cell cortex and provide sufficient force to pull the spindle out of the cell centre in some cases. This could also account for the lack of change in spindle velocity we observed in the NuMA KD tissue (Figure 3.3B), as occasional pulling on the spindle from an asymmetric distribution would increase spindle velocity in the direction of the localised NuMA, increasing the mean velocity over the course of metaphase. We would have expected a reduction in NuMA to instead reduce the spindle velocity and the spindle displacement, as this has been reported in other systems for knockout of NuMA's binding partner LGN [18], [26]. Thus it is possible that a NuMA-indepedent mode of spindle orientation may be at play such as microtubule pushing [54], [78], [137], [143], [193], cytoplasmic pulling by dynein [70], [71], or a NuMA-independent role for LGN, though there is no current evidence for this. In order to gain more insight into this deviatoric path taken by the spindles in the NuMA KD tissue cells, we went on to look more closely at the path of the

mitotic spindle.

Intriguingly, knockdown of NuMA in stretched tissues showed a significant separation of the mode of movement between more circular and more elongated cells, with elongated cells having a broader range of movement along the cell minor axis than the major axis, behaviour which is flipped for the circular cells (Figure 3.4I). This is in contrast to what was seen in the unstretched and stretched tissues, where no such bias with cell shape was observed in either elongated or circular cells (Figure 3.4E, G). The track taken by the spindle was also elongated relative to the cell shape (Figure 3.5C) and most interestingly, the track minor axis of orientation aligned better with the cell division orientation than the track major axis in circular cells (Figure 3.6Cii), though not in elongated cells (Figure 3.6Ci). If we consider the results that the spindles in the circular cells in the NuMA KD tissue have a greater fraction of movement along the major axis of the cell, and also that the track minor axis is better aligned with the cell division orientation than the track major axis, then this suggests that the cell division axis is not well aligned with the cell shape, as is indicated by the discrepancy between the cell shape orientation and the division orientation ($\|\theta_{\mathrm{D}} - \theta_{\mathrm{C}}\| = 50 \pm 30^{\circ}$, mean$\pm$SD), an effect that has been more completely described previously [27]. The effect of spindle translational movements primarily occurring perpendicular to the plane of division is consistent in circular cells across the unstretched, stretched and NuMA KD conditions, suggesting that the translational movements of the spindle are independent of NuMA and cell shape orientation in more circular cells. In elongated cells the track alignment is again randomised with respect to cell division angle, though primarily now aligned with the minor cell axis. We venture that this is a shape-based effect due to microtubule pushing forces, and hope that mathematical modelling will help to elucidate the mechanisms creating this effect.

We next sought to analysis the effect of a NuMA KD on rotational dynamics of the spindle pole. The rotational speed was unaffected by NuMA KD in the previous analysis by Taranuum (2022) [27]. Our analysis of spindle angular velocity at the higher frame rate also showed no significant difference in the rotational speed (Figure 3.8C), though analysis of the means of the populations showed a 1.2-fold decrease in rotational speed between the stretched and stretched KD conditions. This is expected from studies into LGN, NuMA and dynein knockouts which also showed a reduced rotational speed [16], [83]. We suggest that acquiring more data may make this fold change statistically significant. Additionally, we saw no change between the stretch or NuMA KD conditions in either the net angular displacement of the spindle (Figure 3.8A) or the maximum angular displacement achieved by the spindle throughout metaphase time (Figure 3.8B). When combined with the increased metaphase time in NuMA KD tissues (Figure 3.3A), we suggest that this decrease in angular velocity does not affect the maximum angular displacement achieved by the spindle as the spindle is moving for more time. However, the randomisation of the cell division angle with respect to cell shape (Figure 3.6C) suggests that the mechanisms which correctly orient the spindle with the cell shape are perturbed under NuMA KD, as has been shown in previous studies [12], [18], [26], [43], [64], [83], [103].

By analysis of the angle through metaphase time using a periodogram, it was shown that stretched NuMA KD tissues all had spindles which oscillated, and the mean period of oscillation was elevated significantly from the periods of the oscillations in stretched tissues (Figure 3.10B). However, we acknowledge that the spindle oscillations detected in the NuMA KD tissue were less coordinated than the clear oscillations observed by eye in the unstretched and stretched tissue spindles (Figure 3.11) Indeed, the oscillations detected with a period of $\approx$ 70 s in the unstretched and stretched tissues had fewer noisy sub-movements along their period, while the NuMA KD large scale oscillations were often obscured by noise. This suggests that our use of the 'goodness measure' calculation was not appropriate for measuring the quality of the oscillations between conditions, especially given the correlation between the goodness measure and increased metaphase times (Figure 3.10E). Moving forward, we intend to use a Gaussian process tool to extract oscillations from the signal data [199]. This tool has been developed for extracting oscillations from stochastic time series' and has been used to describe oscillatory dynamics in protein expression fluctuations [200]. The Gaussian processes method can also be used to return the amplitude of oscillation, a quantity which is not returned by periodogram analysis. Despite these shortcomings in the goodness measure of oscillation, we conclude that the modes of rotational dynamics between control and NuMA KD tissues are different, due to the marked difference in the oscillation period between the conditions and by visual analysis of the spindle angle through metaphase (Figure 3.11).

As with the stretched and unstretched conditions, we saw no significant difference between the oscillation period of elongated and circular cells in the NuMA KD tissue (Figure 3.12C), nor between the oscillation period in early and late metaphase (Figure 3.13D). Despite this, the trend of increasing the number of oscillating cells as metaphase progressed seen in unstretched tissues was lost in NuMA KD tissues (Figure 3.13A), again suggesting that the longer period oscillations in NuMA KD tissue are of a different form than those in the unstretched tissues with regular levels of NuMA. Indeed, if we consider that the partial knockdown of NuMA results in a small population of NuMA which clusters at the cell cortex [64], and this population is sufficient to create an asymmetric force on the mitotic spindle, we would expect a movement toward this population which would then be depleted upon close contact with the spindle pole due to the spindle pole-derived Plk gradient which phosphorylates cortical NuMA [26]. Then NuMA may be redistributed around the cortex far away from the spindle pole and re-clustered until it is again sufficient to displace the pole again, as was seen in monopolar spindles which were observed to 'chase' areas of high LGN concentration [76]. We speculate that this could cause long range noisy oscillations of the spindle pole due to less coordinated pulling forces acting upon the spindle, though given our current data we cannot confirm whether this mechanism exists. We suggest that a more complete reduction of cortical NuMA would help us to determine whether or not this happening. Application of chemical inhibitor MLN8237 onto cells has been shown to inhibit Aurora-A kinase [123] which in turn leads to the removal of NuMA from the cortex [118]. This occurs due to the inhibition of Aurora-A mediated phosphorylation of NuMA, which is required to displace NuMA from the spindle poles leading to its relocation to the

cell cortex [118]. Thus we would expect that the application of MLN8237 would lead to a cessation of long range spindle dynamics if they occur as a result of the partial NuMA knockdown.

The movements of the mitotic spindle are thus dynamic and complex. The translational path taken by the spindle is highly elongated in all conditions, though the orientation of this elongation is dependent upon cell circularity. Contrary to what was expected, the orientation of spindle movements were biased away from the division axis in circular cells, rather than along the cell elongation axis as was expected. Further, in elongated cells this bias was lost, though the orientation in this case was aligned with neither the cell axis nor the division orientation. Interestingly, in NuMA knockdown tissues the track orientation maintained the same biases with respect to division orientation, but these biases now had components along the cell long axis in more circular cells and along the cell short axis in elongated cells. These results combined with the invariance in the cell centring mechanisms suggested that NuMA is not required for the overall translational positioning of the mitotic spindle. In contrast, rotational oscillations of the spindle pole occur, likely produced by similar mechanisms in the unstretched and stretched tissues as indicated by the similarity in the periods of the oscillations. However, the number of oscillating spindles is reduced in stretched tissues, suggesting that the mechanism which defines the threshold at which oscillations occur may be more difficult to overcome under net tension. Indeed, the NuMA KD tissues all showed oscillations though of a longer period than those in the control tissue, suggested NuMA KD spindle oscillations arise from a different mechanism to in the control tissue. Thus if NuMAs operation is modulated by tension, it could be connected to the oscillation threshold. In order to explore how these dynamics could be explained, we intend to investigate the emergence of oscillations due to a balance of microtubule pushing forces and cortical pulling elements using a mathematical model (Chapters 4, 5), such that we may shed light on the processes which promote oscillations and dynamic spindle movements.

Chapter 4

One dimensional models of stochastic spindle movement reveal factors which promote oscillatory behaviour

4.1 Introduction

The aim of this work is to develop a model which can simulate movements of the mitotic spindle prior to anaphase, using information that is known (or speculated) about the mechanisms which govern the final orientation of cell division. A functioning mathematical model based on prior observations can be used to predict responses of a system in alternative conditions. These predictions can then be tested experimentally to validate the hypotheses on which the model is built. In the case of this work, we wish to create a mathematical model which can recapitulate the typical mitotic spindle movements that we have identified experimentally, in particular the oscillations of the mitotic spindle combined with its overall centring mechanism (Chapter 3), and shed light on the processes that may be occurring within the cell to create these movements. For example, parameters which we identify as having a measurable effect on spindle pole movements, such as varying the magnitude of pulling forces by depletion of cortical elements (such as NuMA), may be measured experimentally to confirm whether or not similar effects are seen *in vivo*.

In this chapter, one dimensional (1D) model descriptions are developed and explored. By beginning with a more complex 1D model and simplifying it (Chapter 5), it is possible to maintain the required level of detail to retain interesting features which may then be applied to develop a two dimensional (2D) model (Appendix A).

Here a description of 1D movements is introduced. The model we investigate was initially developed by Grill *et al.* (2005) [80] to describe the lateral oscillation of the *C. elegans* posterior spindle pole. The framework on which the mathematics in this section is developed has not previously been explored fully. The Grill model successfully captures the 1D oscillation that is characteristic to the first cell division of *C. elegans*. However, the interesting spindle pole dynamics we have seen experimentally in 2D (Chapter 3) are less well characterised. It is an open question whether or not they occur due to the shape of the di-

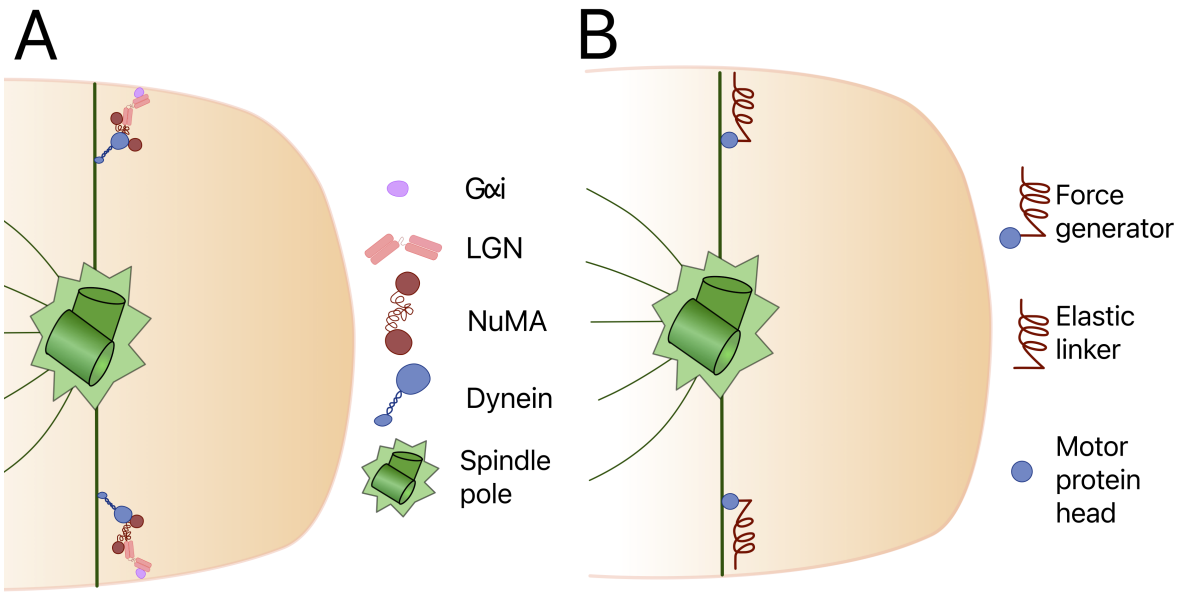

Figure 4.1. **Simplification of relevant protein complexes for modelling** A) Protein complexes Gαi/LGN/NuMA anchor motor protein dynein to the cell cortex. Dynein imparts a force on the spindle pole through interactions with astral microtubules which emanate from the spindle pole. B) The Gαi/LGN/NuMA complex is mathematically described as an elastic linker between motor protein head dynein and the cell cortex. The entire elastic linker/motor protein head assembly is referred to as a force generator.

viding cell or some intrinsic change in the spindle positioning mechanisms due to external tension. The 1D description used by Grill *et al.* (2005) focuses on the action of elastic force generators at the cell periphery, which can be linked to the action of motor proteins and their corresponding linker proteins at the cortex (Figure 4.1). We choose this framework as we also see oscillations in the spindle positioning (Chapter 3) which we believe to be a result of pulling from proteins at the cortex. Accordingly, the model explicitly simulates the stochastic shortening and lengthening of the elastic linkers, as well as their ability to bind and unbind with microtubules in order to influence movements of the spindle (Section 4.2). This model can also be expressed as a Fokker-Planck system of partial differential equations (Section 4.3) which mirror those used by Grill *et al.* (2005). We use this framework and subsequent PDE system to provide a solid base on which to perform systematic asymptotic analysis to produce a system of ODEs (Chapter 5) which can then be more easily extended to a 2D model.

All model formulations explored in this chapter and the next (Chapters 4 and 5) will consider the same setup (Figure 4.1) as described by Grill *et al.* (2005). The Gαi/LGN/NuMA complex is described as an elastic linker connecting the motor protein head (dynein) to the cell cortex. As a microtubule minus-end directed protein, dynein binds to and moves along microtubules toward the spindle pole creating a microtubule plus-end directed pulling force [60], [61], [64], [201]. This entire structure will henceforth be referred to as a 'force generator'. Force generators may exist in bound or unbound states, which correspond to whether or not they are bound to a microtubule. Microtubule binding implies that the force generator may impart a pulling force on the mitotic spindle pole, while unbound force generators have no effect on the spindle pole position. We consider here the one dimensional move-

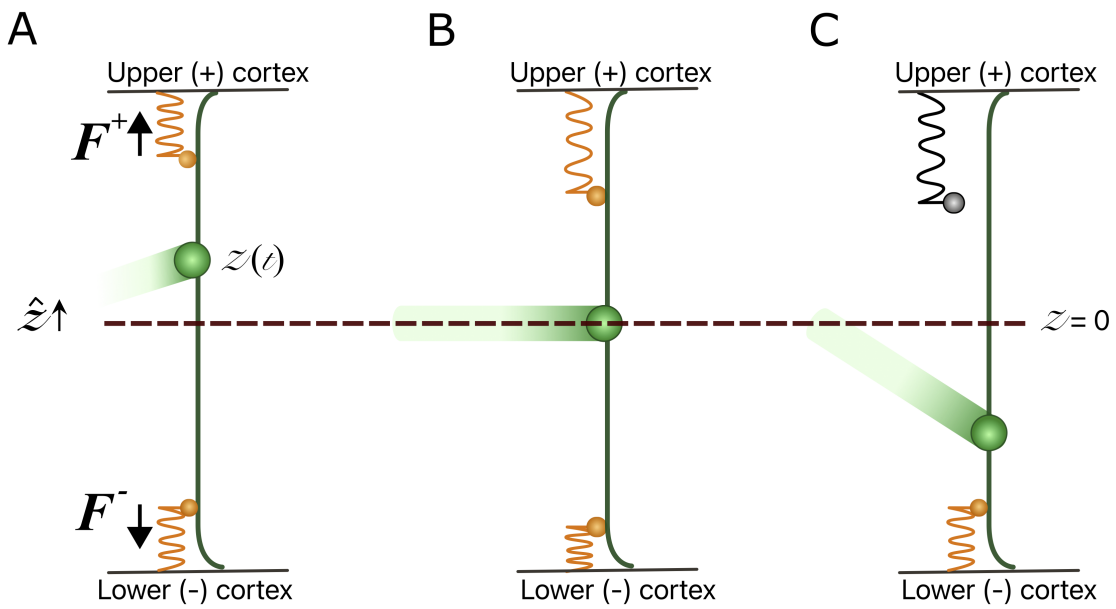

Figure 4.2. **Diagram of spindle pole in three conditions.** A) The spindle pole (green) lies between the upper and lower cortex at position $z(t)$. Force generators (orange) at each cortex comprise a motor protein head and an elastic linker which produce pulling forces $F^{\pm}$. B) The movement of the spindle pole will affect the linker extensions of the motor proteins. Movement away from the upper cortex will lengthen the linkers of the upper force generators while compressing the linkers of the lower force generators. C) Force generators with more extended linkers have an increased unbinding rate. Unbound generators cannot produce a pulling force (indicated by a grey force generator).

ments of a single spindle pole as a result of pulling by the populations of force generators which exist on either side of the pole central position $z\,(t)\,=\,0$. The two populations will be referred to as existing within the 'upper' and 'lower' cortex (Figure 4.2), in reference to whether they are assumed to be populating the region of the cell cortex above ($z\,>\,0$) or below ($z\,<\,0$) the central position. Force generators may switch their binding state, the details of which will be described more explicitly below.

4.2 Stochastic model: Simulations using the Gillespie algorithm

We first use stochastic simulations to investigate predictions of the Grill *et al.* (2005) model [80], postponing descriptions based on Fokker-Planck equations to later sections.

4.2.1 Theoretical description

The spindle pole position is influenced by pulling events acting on astral microtubules which emanate from the spindle pole and extend to the cell cortex. The pulling events are created stochastically by individual force generators which lie at the cell cortex and bind to microtubules. For simplicity the 1D model considers two opposing populations of force genera-

tors which sit in an 'upper' and 'lower' cortex, labelled $\pm$ hereafter. The force generators comprise a motor protein head connected to the cortex via an elastic linker of stiffness k_{g} (Figure 4.1A). The motor protein head can be considered to be dynein, which walks along the microtubules to the microtubule minus ends at the spindle pole. The populations of N force generators will exert pulling forces toward their respective cortex with a magnitude

$$F^{\pm} = k_{\mathrm{g}} \sum_{n=1}^{N} y_{\mathrm{b}}^{(n)\pm}, \tag{4.1}$$

where $y_{\mathrm{b}}^{(n)\pm}$ is the extension of the elastic linker of bound (b) force generator n (Figure 4.2). Only bound generators are considered as they are connected to the spindle pole via a microtubule and can thus produce a pulling force. By (4.1) a force generator with a more extended linker will provide a greater pulling force than a force generator with a more retracted elastic linker. Unbound force generators $\left(y_{\mathrm{u}}^{(n)\pm}\right)$ are not connected to the spindle pole and will thus be unable to provide any form of forcing (black force generator in Figure 4.2C). A restoring force opposes movements of the spindle pole, representing astral microtubules with stiffness k_{MT} arising from dynamic instability and bending effects [78]–[80], [135], [137]. A spindle pole at position $z\,(t)$ at a time t in a viscous fluid with an effective friction coefficient ξ will move along the $\hat{\mathbf{z}}$ direction. Its position will evolve in time according to

$$\xi \frac{\mathrm{d}z}{\mathrm{d}t} + k_{\mathrm{MT}} z\,(t) = F^{+} - F^{-}. \tag{4.2}$$

This is an ordinary differential equation (ODE) with stochastic forcing because the linkers bind and unbind randomly. The movements of the spindle pole are therefore tightly coupled to the individual extension lengths of the force generator linkers, as they define the magnitude of pulling force each force generator provides. The walking action of the motor protein heads, which have walking velocities

$$v_{\mathrm{b}}^{(n)\pm} = v_0 \left(1 - \frac{k_{\mathrm{g}} y_{\mathrm{b}}^{(n)\pm}}{f_0}\right) \mp \frac{\mathrm{d}z}{\mathrm{d}t}, \tag{4.3}$$

provides additional complexity to the system. This expression for $v_{\mathrm{b}}^{(n)\pm}$ combines the spontaneous, unloaded walking velocity v_0, which is reduced due to the effect of the tensile force acting upon the motor protein head by the elastic linker $\left(\frac{k_{\mathrm{g}} y_{\mathrm{b}}^{(n)\pm}}{f_0}\right)$, with the relative velocity of the spindle pole. Here, f_0 is the stall force of the force generator i.e., under no influence from the spindle pole; if an elastic linker was of an extension y_0 such that $k_{\mathrm{g}} y_0 = f_0$, then the net velocity of the motor protein head would be zero. The spindle pole velocity term $\mp \frac{\mathrm{d}z}{\mathrm{d}t}$ arises due to the force generator being connected to the moving spindle pole via the microtubules. As the spindle pole moves towards a bound force generator it will compress the elastic linker and thus reduce its relative walking velocity. Alternatively as the spindle pole moves away from the bound force generator it will extend the elastic linker and therefore increase its relative walking velocity (Figure 4.2B). This can be likened to walking along or against a moving walkway.

We aim to model the stochastic forcing on the mitotic spindle via the force generators, and

calculate the resulting spindle pole position. The pulling from the force generators due to the action of the walking motor protein heads will perturb the position of the spindle pole $z(t)$ and increase the extension of the elastic linkers $y_{\text{b}}^{(n)\pm}$. Perturbations to $z(t)$ will affect the relative velocity of the walking motor protein head by (4.3), while changes to $y_{\text{b}}^{(n)\pm}$ will affect the pulling power of the force generator by (4.1) and also the relative velocity of the walking motor protein head (4.3). In order to capture these coupled dynamics we explicitly consider the length changes of the elastic linkers by discretising $y_{\text{b}}^{(n)\pm}$ in increments of Δy and using a Gillespie algorithm to model the stochastic extensions and retractions via the relative motions of the walking motor protein heads. The Gillespie algorithm will also be used to capture stochastic changes of the binding state of the force generators, as they bind and unbind from microtubules.

The Gillespie algorithm describes a small number of force generators interacting with the spindle pole via microtubules, rather than bulk reactions of large numbers of force generators. It allows us to look explicitly at the direct consequences to individual force generators and the spindle pole of discrete stochastic interactions. The extension of an elastic linker is discretised into states $y_{\text{b(u)}}^{(n)\pm,i}$ with $i = 0, 1 \ldots M$, separated by a fixed distance measure Δy such that $y_{\text{b(u)}}^{(n)\pm,i+1} = y_{\text{b(u)}}^{(n)\pm,i} + \Delta y$ (Figure 4.3A). Each force generator n has identifiers which denote the associated cortex ($\pm$), the current extension state (i), and the binding state (u for unbound, b for bound). The binding state will be identified in the subscript and written as b(u), referring to how the subscript may be either b or u. At any time, a generator may

- retract: $y_{\text{b(u)}}^{(n)\pm,i} \rightarrow y_{\text{b(u)}}^{(n)\pm,i-1}$ with a probability $r_{\text{b(u)}}^{(n)\pm,i}$;
- extend: $y_{\text{b(u)}}^{(n)\pm,i} \rightarrow y_{\text{b(u)}}^{(n)\pm,i+1}$ with a probability $f_{\text{b(u)}}^{(n)\pm,i}$; or
- switch between bound and unbound: $y_{\text{b}}^{(n)\pm,i} \leftrightarrow y_{\text{u}}^{(n)\pm,i}$ with a probability $s_{\text{b(u)}}^{(n)\pm,i}$.

These state-changing events are illustrated graphically in Figure 4.3A.

Choosing values for $r_{\text{b(u)}}^{(n)\pm,i}$, $f_{\text{b(u)}}^{(n)\pm,i}$, and $s_{\text{b(u)}}^{(n)\pm,i}$ is non-trivial. To begin, the switching probabilities were chosen such that an unbound generator may switch to become a bound generator within a short time τ with a probability $s_{\text{u}}^{(n)\pm,i} = \tau\omega_{\text{on}}$ for a constant binding rate ω_{on}. This reflects the fact that a force generator is as likely to be in close enough proximity to a microtubule to bind with it when fully extended from the cortex ($y_{\text{u}}^{(n)\pm,i=M} = y_{\text{max}}$) as it would be if it were not extended at all $\left(y_{\text{u}}^{(n)\pm,i=0} = 0\right)$. Here, y_{max} is the maximum length an elastic linker may have. In a short time τ, a bound generator may unbind with probability $s_{\text{b}}^{(n)\pm,i} = \tau\omega_0 e^{\gamma^* y_{\text{b}}^{(n)\pm,i}}$. The dynein-microtubule binding has been shown to have a slip-bond behaviour [61], thus the unbinding of the force generator from the microtubule was chosen to be tension sensitive, where more tension acting on the force generator by the elastic linker increases its unbinding rate [80], [145], [146]. The constant parameter ω_0 sets the unbinding rate at zero extension, i.e. when there is no loading force on the motor protein head from the elastic linker. The scaling parameter γ^* defines the sensitivity of the unbinding to the elastic linker extension y.

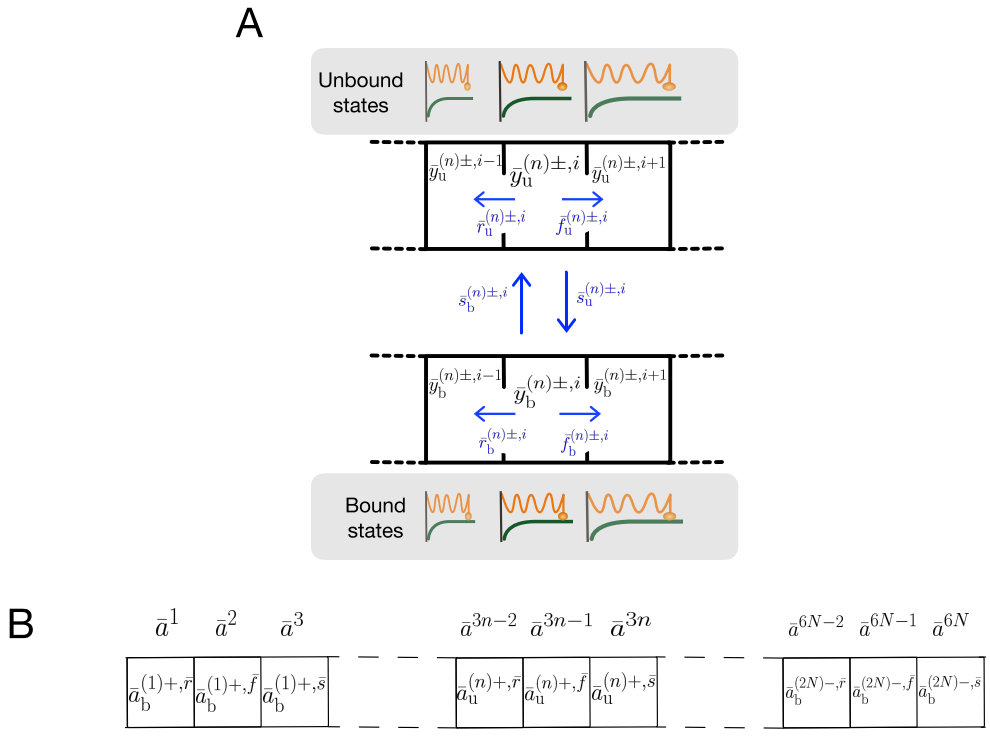

Figure 4.3. **Graphical map of extension states for unbound and bound force generators.** A) Unbound generators in state $\bar{y}_{\mathrm{u}}^{(n)\pm,i}$ may extend or retract with probabilities $\bar{f}_{\mathrm{u}}^{(n)\pm,i}$ and $\bar{r}_{\mathrm{u}}^{(n)\pm,i}$. Bound generators in state $\bar{y}_{\mathrm{b}}^{(n)\pm,i}$ may extend or retract with probabilities $\bar{f}_{\mathrm{b}}^{(n)\pm,i}$ and $\bar{r}_{\mathrm{b}}^{(n)\pm,i}$. Bound generators may unbind or vice-versa with rate constants $\bar{s}_{\mathrm{b}}^{(n)\pm,i}$ and $\bar{s}_{\mathrm{u}}^{(n)\pm,i}$ respectively. Diagrams of force generators show corresponding extension and binding states. Each individual force generator n exists within these states. B) Concatenated list of rate triplets to show numbering regime. Probabilities from $\bar{a}^1$ to $\bar{a}^{3N}$ correspond to force generators $1 \rightarrow N$ which exist in the upper cortex. Probabilities $\bar{a}^{3N+1}$ to $\bar{a}^{6N}$ correspond to force generators $N+1 \rightarrow 2N$ which exist in the lower cortex.

In order to obtain expressions for $r_{\mathrm{b(u)}}^{(n)\pm,i}$ and $f_{\mathrm{b(u)}}^{(n)\pm,i}$, consider

$$v_{\mathrm{b}(u)}^{(n)\pm,i} = \frac{\Delta y}{\tau}\left(f_{\mathrm{b(u)}}^{(n)\pm,i} - r_{\mathrm{b(u)}}^{(n)\pm,i}\right) \tag{4.4}$$

and

$$D_{\mathrm{b}(u)}^{(n)\pm} = \frac{(\Delta y)^2}{2\tau}\left(f_{\mathrm{b(u)}}^{(n)\pm,i} + r_{\mathrm{b(u)}}^{(n)\pm,i}\right) \tag{4.5}$$

as an effective drift speed and diffusion coefficient for force generators respectively. These facilitate comparison with the Fokker-Planck equations presented in Section 4.3 below, and arise from considering extension or contraction of each linker as a biased random walk. The bound velocity $v_{\mathrm{b}}^{(n)\pm,i}$ may be calculated for the current system state by modifying (4.3) for the discretised description to give

$$v_{\mathrm{b}}^{(n)\pm,i} = v_0 - \mu y_{\mathrm{b}}^{(n)\pm,i} \mp \frac{\mathrm{d}z}{\mathrm{d}t}. \tag{4.6}$$

The parameter $\mu = k_{\mathrm{g}} v_0 / f_0$ captures the velocity reduction under force due to the elastic linker, while the velocity of the spindle pole may be calculated using (4.2). The unbound

velocity ${v_{\mathrm{u}}}^{(n)\pm,i}$ arises due to the motor protein head being pulled back toward the cortex by the elastic linker through a viscous medium (the cytoplasm) and may be determined by equating the potential energy stored in the elastic linker with work done against drag. The forces in both processes must be equal and

$$\xi_{\mathrm{g}} {v_{\mathrm{u}}}^{(n)\pm,i} = -k_{\mathrm{g}} y_{\mathrm{u}}^{(n)\pm,i}. \tag{4.7}$$

The expression for $v_{\mathrm{u}}^{(n)\pm,i}$ may therefore be written

$$v_{\mathrm{u}}^{(n)\pm,i} = -\nu y_{\mathrm{u}}^{(n)\pm,i} \tag{4.8}$$

for relaxation parameter $\nu = k_{\mathrm{g}}/\xi_{\mathrm{g}}$. The drag coefficient ξ_{g} is determined by assuming a Stokes' law formulation for the viscous force. Using the largest proteins in the force generator complex (dynein, length approximately 50 nm [202], and NuMA, length approximately 210 nm [106]), we estimate that a force generator has a Stokes radius of order $\mathcal{O}\left(10^{-1}\right)$ smaller than the spindle pole, then $\xi_{\mathrm{g}} \approx \xi \times 10^{-1}$. Both (4.4) and (4.8) may be calculated from the current system state, while diffusive terms $D_{\mathrm{b(u)}}^{(n)\pm}$ in (4.5) are assumed to be constants and will henceforth be labelled $D_{\mathrm{b(u)}}$. Equations (4.4) and (4.5) may be rearranged to give probabilities $f_{\mathrm{b(u)}}^{(n)\pm,i}$ and $r_{\mathrm{b(u)}}^{(n)\pm,i}$, as summarised in Table 4.1. In order to prevent extension beyond y_{max} or retraction through the cortex ($y_{\mathrm{b(u)}}^{(n)\pm,i} < 0$), no flux conditions are enforced by setting $r_{\mathrm{b(u)}}^{(n)\pm,i=0} = 0$ and $f_{\mathrm{b(u)}}^{(n)\pm,i=M} = 0$.

The Gillespie algorithm [203] stipulates that the probability of a state-changing event (extension, retraction, or switch) happening within a short time τ is exponentially distributed with rates $r_{\mathrm{b(u)}}^{(n)\pm,i}/\tau$, $f_{\mathrm{b(u)}}^{(n)\pm,i}/\tau$, and $s_{\mathrm{b(u)}}^{(n)\pm,i}/\tau$, which sum together to give a total rate

$$R = \frac{1}{\tau} \sum_{n=1}^{2N} \left(r_{\mathrm{b(u)}}^{(n)\pm,i} + f_{\mathrm{b(u)}}^{(n)\pm,i} + s_{\mathrm{b(u)}}^{(n)\pm,i} \right). \tag{4.9}$$

Here $2N$ is the total number of force generators within the system (N per cortex), each of which is associated with either the upper (+) or lower (-) cortex, has an extension state i, and is either bound (b) or unbound (u). We assume that only one event for one force generator may occur, removing the possibility of simultaneous events. As $r_{\mathrm{b(u)}}^{(n)\pm,i}$, $f_{\mathrm{b(u)}}^{(n)\pm,i}$ and $s_{\mathrm{b(u)}}^{(n)\pm,i}$ are proportional to the short time τ (Table 4.1), the rates $r_{\mathrm{b(u)}}^{(n)\pm,i}/\tau$, $f_{\mathrm{b(u)}}^{(n)\pm,i}/\tau$, and $s_{\mathrm{b(u)}}^{(n)\pm,i}/\tau$ (and thus R) are independent of τ. A random variable ζ_1 is chosen from a uniformly random distribution between 0 and 1 ($\zeta_1 \sim \mathcal{U}[0,1]$) and the time to the next event is calculated using

$$\tau = \frac{1}{R} \log\left(1/\zeta_1\right). \tag{4.10}$$

The rescaled rates $a_{\mathrm{b(u)}}^{(n)\pm,r}(i) = \frac{1}{R} r_{\mathrm{b(u)}}^{(n)\pm,i}/\tau$, $a_{\mathrm{b(u)}}^{(n)\pm,f}(i) = \frac{1}{R} f_{\mathrm{b(u)}}^{(n)\pm,i}/\tau$ and $a_{\mathrm{b(u)}}^{(n)\pm,s}(i) = \frac{1}{R} s_{\mathrm{b(u)}}^{(n)\pm,i}/\tau$ are concatenated in triplets for each force generator n, giving a list of potential states a^j with $j \in [1, 6N]$ which sum together to give $\sum_{j=1}^{6N} a^j = 1$ (Figure 4.3B). Choosing an independent random variable from a uniformly random distribution, $\zeta_2 \sim \mathcal{U}[0,1]$, the

	Dimensional		Non-dimensional	
	Bound events	Unbound events	Bound events	Unbound events
$s^{(n)\pm,i}$	$\tau\omega_0 e^{\gamma^* y_{\mathrm{b}}^{(n)\pm,i}}$	$\tau\omega_{\mathrm{on}}$	$\bar{\tau}\bar{\omega}_0 e^{\gamma\bar{y}_{\mathrm{b}}^{(n)\pm,i}}$	$\bar{\tau}\bar{\omega}_{\mathrm{on}}$
$r^{(n)\pm,i}$	$\tau\left(\frac{D_{\mathrm{b}}}{(\Delta y)^2}-\frac{v_{\mathrm{b}}^{(n)\pm,i}}{2\Delta y}\right)$	$\tau\left(\frac{D_{\mathrm{u}}}{(\Delta y)^2}+\frac{\nu y_{\mathrm{u}}^{(n)\pm,i}}{2\Delta y}\right)$	$\bar{\tau}\left(\frac{\alpha}{(\Delta\bar{y})^2}-\frac{\bar{v}_{\mathrm{b}}^{(n)\pm,i}}{2\Delta\bar{y}}\right)$	$\bar{\tau}\Gamma\left(\frac{\beta}{(\Delta\bar{y})^2}+\frac{\bar{y}_{\mathrm{u}}^{(n)\pm,i}}{2\Delta\bar{y}}\right)$
$f^{(n)\pm,i}$	$\tau\left(\frac{D_{\mathrm{b}}}{(\Delta y)^2}+\frac{v_{\mathrm{b}}^{(n)\pm,i}}{2\Delta y}\right)$	$\tau\left(\frac{D_{\mathrm{u}}}{(\Delta y)^2}-\frac{\nu y_{\mathrm{u}}^{(n)\pm,i}}{2\Delta y}\right)$	$\bar{\tau}\left(\frac{\alpha}{(\Delta\bar{y})^2}+\frac{\bar{v}_{\mathrm{b}}^{(n)\pm,i}}{2\Delta\bar{y}}\right)$	$\bar{\tau}\Gamma\left(\frac{\beta}{(\Delta\bar{y})^2}-\frac{\bar{y}_{\mathrm{u}}^{(n)\pm,i}}{2\Delta\bar{y}}\right)$

Table 4.1. The probabilities for bound and unbound generators in spatial state i in terms of dimensional and non-dimensional quantities. Parameter Δy is the fixed distance between extension states.

next state-changing event is determined as the first j such that

$$\sum_{j'=1}^{j} a^{j'} > \zeta_2. \tag{4.11}$$

Force generators in the upper (n^+) and lower (n^-) cortex have corresponding events a^j where $j \in [1, 3N]$ and $j \in [3N+1, 6N]$ respectively.

In order to calculate the spindle pole position, we implement a forward Euler approximation of (4.2), as

$$\xi\frac{z(t+\tau)-z(t)}{\tau} + k_{\mathrm{MT}} z(t) = F^+ - F^- \tag{4.12}$$

which may be used to calculate the pole position at a time $t+\tau$

$$z(t+\tau) = \left(1-\frac{\tau k_{\mathrm{MT}}}{\xi}\right) z(t) + \frac{\tau k_{\mathrm{g}}}{\xi}\left(\sum_{n'=1}^{N'} y_{\mathrm{b}}^{(n')+,i}(t) - \sum_{n=1}^{N} y_{\mathrm{b}}^{(n)-,i}(t)\right). \tag{4.13}$$

Here n' and N' are the equivalent of n and N, introduced only so that we may separate the upper and lower cortex in this expression.

4.2.2 Non-dimensionalisation of the stochastic system

As this model is concerned with the action of force generators and their effect on the spindle pole position, it is appropriate that the problem should be scaled to time and length scales relevant to the movements of the force generators. We set y_0, the extension at which the velocity of the motor protein head is zero in the absence of connection to the spindle pole, as the natural length scale of the problem: $y_0 = f_0/k_{\mathrm{g}} = v_0/\mu$. Further, the timescale may be chosen to reflect the velocity reduction under the force of the elastic linker, $t_0 = \mu^{-1}$. Using this non-dimensionalisation we rewrite the system in terms of scaled parameters (Table 4.3). Using these parameters, the non-dimensionalised spindle pole velocity (4.2) becomes

$$\bar{\xi}\frac{\mathrm{d}\bar{z}}{\mathrm{d}\bar{t}} = -K\bar{z}(\bar{t}) + \left(\sum_{n'=1}^{N'} \bar{y}_{\mathrm{b}}^{(n')+,i}(\bar{t}) - \sum_{n=1}^{N} \bar{y}_{\mathrm{b}}^{(n)-,i}(\bar{t})\right), \tag{4.14}$$

Description	Parameter	Value	Reference	Notes
Drag coefficient	ξ	10^{-6} Nsm^{-1}	[80]	
Microtubule stiffness due to bending elasticity	k_{MT}	4×10^{-6} Nm^{-1}	[80], [135]	Baseline used, varied quantity
Elastic linker stiffness	k_{g}	8×10^{-5} Nm^{-1}	[80]	
Stall force	f_0	3×10^{-12} N	[61], [80], [204]	
Spontaneous velocity of force generators	v_0	1.8×10^{-6} ms^{-1}	[80], [205]	
Normalised spontaneous velocity of bound force generators	μ	50 s^{-1}	[80]	v_0 per length at stall force y_0
Relaxation (retraction) rate of unbound generators	ν	10^3 s^{-1}	([80], [111], [202])	Order of magnitude estimate relative to ξ using Stokes' law
Sensitivity of unbinding to linker extension	γ^*	5.6×10^7 m^{-1}	([80])	Calculated using expression in [80]
Diffusion coefficient of bound generators	D_{b}	5×10^{-15} m^{2}s^{-1}	[80]	
Diffusion coefficient of unbound generators	D_{u}	5×10^{-14} m^{2}s^{-1}	([80])	Order of magnitude estimate using $D_{\text{u}} = \nu \frac{k_{\text{b}} T}{k_{\text{g}}}$ with $T \approx 310$ K
Number of force generators per cortex	N	-		Varied quantity
Maximum linker extension	y_{max}	2.16×10^{-7} m	([80])	Calculated in reverse from $\bar{y}_{\text{max}} = 6$
Microtubule-generator binding rate	ω_{on}	0.15 s^{-1}		Baseline used, varied quantity
Microtubule-generator unbinding rate coefficient	ω_0	0.05 s^{-1}	[80]	

Table 4.2. Parameter values and descriptions. References in parenthesis contain information which was used in order to derive the parameter value rather than explicitly stating a value.

where dimensionless quantities are barred. The non-dimensionalised pole position update (4.13) becomes

$$\bar{z}\left(\bar{t}+\bar{\tau}\right) = \left(1 - \frac{\bar{\tau} K}{\bar{\xi}}\right) \bar{z}\left(\bar{t}\right) + \frac{\bar{\tau}}{\bar{\xi}} \left(\sum_{n'=1}^{N'} \bar{y}_{\text{b}}^{(n')+,i}\left(\bar{t}\right) - \sum_{n=1}^{N} \bar{y}_{\text{b}}^{(n)-,i}\left(\bar{t}\right) \right), \tag{4.15}$$

while the velocity of the bound generators (4.6) becomes

$$\bar{v}_{\text{b}}^{(n)\pm,i} = 1 - \bar{y}_{\text{b}}^{(n)\pm,i} \mp \frac{\mathrm{d}\bar{z}}{\mathrm{d}\bar{t}}. \tag{4.16}$$

All new probabilities are described in Table 4.1. The non-dimensional diffusive parameters α and β for bound and unbound generators respectively (Table 4.1) are determined from two different methods. For bound generators, parameter D_{b} characterises velocity fluctuations of the attached dynein molecule [80], and this coefficient is scaled by parameters relating to the unloaded motor protein and the length of the elastic linker at stall force to define α. However, for the unbound force generators, the Einstein relation $D_{\text{u}}/\nu = k_{\text{b}}T/k_{\text{g}}$ has been used to define velocity fluctuations of the unattached dynein molecule, as it is pulled back toward the cell cortex by the elastic linker. Parameter k_{b} is the Boltzmann constant and T is the temperature, taken here to be approximately 310 K. Then $\beta = \left(\frac{\mu}{v_0}\right)^2 \frac{k_{\text{b}}T}{k_{\text{g}}}$ is the non-dimensionalised equivalent of D_{b}.

The following observations may be made by considering this non-dimensionalised system.

Non-dimensional parameter	Components	Interpretation
$\bar{\xi}$	$\xi \frac{\mu}{k_{\text{g}}}$	Effective drag coefficient, ratio of spindle pole drag to the drag on a bound force generator.
K	$\frac{k_{\text{MT}}}{k_{\text{g}}}$	Relative stiffness of microtubules to elastic linkers.
$\bar{\omega}_{\text{on}}$	$\frac{1}{\mu}\omega_{\text{on}}$	Binding rate relative to normalised unloaded velocity of a bound force generator.
$\bar{\omega}_0$	$\frac{1}{\mu}\omega_0$	Unbinding rate relative to normalised unloaded velocity of a bound force generator.
$\bar{y}_{\text{max}}$	$\frac{\mu}{v_0} y_{\text{max}}$	Maximum elastic linker extension per extension at stall force.
γ	$\frac{\gamma^* v_0}{\mu}$	Ratio of extension at stall force to sensitivity length-scale $1/\gamma^*$.
α	$\frac{\mu}{v_0^2} D_{\text{b}}$	Diffusion coefficient for bound force generators, relative to unloaded motor protein velocity.
β	$\left(\frac{\mu}{v_0}\right)^2 \frac{k_{\text{b}}T}{k_{\text{g}}}$	Diffusion coefficient for unbound force generators relative to unloaded motor protein velocity.
Γ	$\frac{\nu}{\mu}$	Relaxation of unbound generators relative to normalised bound velocity.

Table 4.3. Parameters of the non-dimensionalised system in terms of the parameters from the dimensional system. All parameters now re-framed relative to the time and length scales set by the bound force generators under no external loading.

- Unbound probabilities are biased toward retraction events due to the reduction in extension probabilities $f_{\text{u}}^{(n)\pm,i}$ for any non-negative extension of the force generator elastic linker $\bar{y}_{\text{u}}^{(n)\pm,i}$.
- The bias toward retraction or extension for bound force generators depends upon the direction of the motor protein head velocity. If the velocity $\bar{v}_{\text{b}}^{(n)\pm,i}$ is negative then the retraction probability will dominate over extension, and vice-versa if the velocity is positive.
- If diffusive terms are much larger than drift terms, extension and retraction probabilities are approximately equal for both unbound and bound force generators ($r_{\text{b(u)}}^{(n)\pm,i} \approx f_{\text{b(u)}}^{(n)\pm,i}$).
- The probability of unbinding $s_{\text{b}}^{(n)\pm,i}$ increases exponentially for force generators with more extended elastic linkers. The sensitivity of unbinding depends upon the parameter γ, which measures the ratio of the stalling extension $y_0 = v_0/\mu = f_0/k_{\text{g}}$ with the sensitivity length-scale set by γ^*.
- The ratio of microtubule stiffness to elastic linker stiffness, K, determines the strength of centring forces vs pulling forces in (4.14). If $k_{\text{MT}} \ll k_{\text{g}}$, then $K \ll 1$ and the spindle pole dynamics will be dominated by the pulling effects from the populations

of force generators in either cortex, until the spindle pole is displaced sufficiently far from the cell centre $\bar{z} = 0$ such that the restoring force $-K\bar{z}$ may be of a similar order of magnitude to the pulling forces. Thus towards the centre of the cell, pulling forces are the main source of spindle dynamics, while towards the cell periphery restorative centring forces will dominate.

- Force generators whose elastic linkers are extended such that the force acting on the motor protein head is equal to the stall force ($\bar{y}_{\mathrm{b}}^{(n)\pm,i} = 1$) have a relative velocity which depends entirely upon the velocity of the spindle pole (4.16).

With these observations in mind we now present the implementation of the model.

4.2.3 Computational method

In order to implement this algorithm, the following simulation method was used.

1. The list `GeneratorList` was created which was $2N$ in length with 2 elements in each column. Element 1 corresponded to the extension of force generator n while element 2 corresponded to the binding state (1 for a bound generator, -1 for an unbound generator). Columns $1 \rightarrow N$ held the state information for force generators in the upper cortex while elements $N + 1 \rightarrow 2N$ corresponded to the state information of the force generators in the lower cortex.
2. The list of the scaled probabilities was constructed in triplets corresponding to retraction, extension and switching events for each force generator, resulting in a $6N$ length list of probabilities (Figure 4.3B).
3. The spindle pole velocity was calculated by (4.14).
4. A random number generator was used to produce pairs (ζ_1, ζ_2) between 0 and 1 from a uniformly random distribution in order to calculate time step $\bar{\tau}$ (4.10) and event j (4.11).
5. The chosen event was actioned inside `GeneratorList` and the simulation time updated.
6. The new spindle position at time $\bar{t} + \bar{\tau}$ was determined by (4.15).
7. The bound velocities $\bar{v}_{\mathrm{b}}^{(n)\pm,i}$ were recalculated and the probability values updated to reflect the new system state at time $\bar{t} + \bar{\tau}$.
8. Steps (3-7) above were cycled until a chosen end-point time was achieved.

Source code is available (at /github.com/dionn-hargreaves/StochasticSimulation_SpindleMovements. We note the following computational complications based on the form of the probabilities (Table 4.1)

1. The unbound probability for extension, $f_{\mathrm{u}}^{(n)\pm,i}$ (see Table 4.1) has the potential to become negative when $\bar{y}_{\mathrm{u}}^{(n)\pm,i} > 2\beta/\Delta\bar{y}$. As the maximum value that $\bar{y}_{\mathrm{u}}^{(n)\pm,i}$ may take is $\bar{y}_{\mathrm{max}}$, we choose $\Delta\bar{y} < 2\beta/\bar{y}_{\mathrm{max}}$.

2. The bound probabilities for extension and retraction, $f_{\mathrm{b}}^{(n)\pm,i}$ and $r_{\mathrm{b}}^{(n)\pm,i}$, have the potential to become negative when $\left|\bar{v}_{\mathrm{b}}^{(n)\pm,i}\right| > 2\alpha/\Delta\bar{y}$.

These 'negative probabilities' likely arise due to the combination of continuous dynamics (the velocity of the spindle pole) and discrete dynamics (the actions of the stochastic force generators). Hybrid Gillespie algorithm methods which combine deterministic and stochastic systems to describe reaction mechanisms have been shown to result in negative numbers of reaction species due to the balance of slow and fast dynamics being modelled [206]. In the case of negative retraction probabilities, this corresponds to a system state where the possibility for retraction is essentially impossible due to the connection of the force generator to the spindle pole. One way to circumvent this issue would be to impose an extra condition that probabilities which are calculated to be negative are set to zero. Another method, which is the method we have chosen in order to minimise external constraints on the system, is to ensure that our discretisation length $\Delta\bar{y}$ is small enough such that the conditions identified in complications 1. and 2. are addressed.

We note that complication 1 is easily implemented when choosing parameters due to its bounding condition being formed of pre-defined constants. However, as $\bar{v}_{\mathrm{b}}^{(n)\pm,i}$ is affected by both the elastic linker extension and the spindle pole velocity, complication 2 is more difficult to circumvent. To estimate an upper bound on $\bar{v}_{\mathrm{b}}^{(n)\pm,i}$ we consider

$$\bar{v}_{\mathrm{b}}^{(n)+,i}|_{\mathrm{max}} = 1 - \bar{y}_{\mathrm{max}} - \left.\frac{\mathrm{d}\bar{z}}{\mathrm{d}\bar{t}}\right|_{\mathrm{max}}, \tag{4.17}$$

with $\bar{y}_{\mathrm{max}} \gg 1$ and $\frac{\mathrm{d}\bar{z}}{\mathrm{d}\bar{t}}|_{\mathrm{max}} \gg 1$. To estimate $\frac{\mathrm{d}\bar{z}}{\mathrm{d}\bar{t}}|_{\mathrm{max}}$, we assume the extreme situation whereby $z = 0$ with all force generators in the lower cortex being either unbound or at zero extension, $\bar{y}_{\mathrm{b}}^{(n)-,i} = 0$, and all force generators in the upper cortex bound with maximum extension $\bar{y}_{\mathrm{b}}^{(n)+,i} = \bar{y}_{\mathrm{max}}$. Then by (4.14),

$$\frac{\mathrm{d}\bar{z}}{\mathrm{d}\bar{t}}|_{\mathrm{max}} \sim \frac{N}{\bar{\xi}}\bar{y}_{\mathrm{max}}, \tag{4.18}$$

where "$\sim$" denotes "scales as". Thus, as the number of force generators N increases, we expect also that the magnitude of the velocity of the spindle pole increases. Then,

$$\bar{v}_{\mathrm{b}}^{(n)\pm,i}|_{\mathrm{max}} \sim 1 - \bar{y}_{\mathrm{max}} - \frac{N}{\bar{\xi}}\bar{y}_{\mathrm{max}} \tag{4.19}$$

so that negative values of $f_{\mathrm{b}}^{(n)\pm,i}$ and $r_{\mathrm{b}}^{(n)\pm,i}$ can be avoided provided that

$$\Delta\bar{y} < 2\alpha/\left|1 - \left(1 + \frac{N}{\bar{\xi}}\right)\bar{y}_{\mathrm{max}}\right|. \tag{4.20}$$

As a result the computational cost is predicted to increase with the number of force generators N due to both increasing the number of available events the system may choose, and due to a necessary reduction in $\Delta\bar{y}$ in order to prevent negative values of the event probabilities.

4.2.4 Increasing computational efficiency

Gillespie algorithms are noted as being inefficient and computationally expensive due to their nature in tracking all individual events, with many studies exploring methods to increase the computational efficiency in various ways [207]–[211]. Of note are the τ-leaping method [208], the next reaction method [207] and an optimised direct method [210]. In particular, the τ-leaping method is a popular choice of optimisation and has been further expanded upon to become implicit [209]. Many studies combine various methods of tuning the time step size for scaleable simulations [211], [212].

Briefly, the τ-leaping method uses a Poisson approximation to 'leap' over many reaction events and can produce accurate results so long as the propensity functions, which we refer to as probabilities in this work, are slowly varying during time steps. That is, τ must satisfy the leap condition of being small enough such that the propensity functions do not change significantly in such a time [208], [209], [211], [212]. Plotting the probabilities over a period of time shows that indeed they are slowly varying, but discontinuous jumps occur occasionally in the backward and forward event parameters (Figure 4.4B). Here we have chosen $\bar{r}_{\mathrm{b}}^{(n)+,i=1}$ and $\bar{f}_{\mathrm{b}}^{(n)+,i=1}$ to illustrate this effect. The unbound probabilities remain constant along each i as they are uncoupled from the spindle pole. The large jumps in the forward and backward event probabilities coincide with large changes in the velocity of the spindle pole (Figure 4.4A). These discontinuities prevent us from using the τ-leaping method to increase the efficiency of this system.

The next reaction method [207] uses dependency graphs in order to update only the required propensity functions at each timestep. Instead of calculating only the time until the next event, all times for all possible events are calculated and stored chronologically. The first time is stepped to with its corresponding event triggered, and only the possible events (and their corresponding times) connected to this one according to the dependency graph are updated. This method has been shown to be more efficient than the standard method. A problem with this method is that it has been developed for loosely coupled systems as opposed to the highly coupled system we are considering. As the bound force generators are each heavily coupled to the dynamics of the mitotic spindle, and unbinding or binding will have an effect on these dynamics, this method is likely to not be effective.

In contrast to these adaptations to the simulation algorithm, the optimised direct method instead reorders the reactions in storage in order of decreasing firing frequency and combines this with selective updating of propensity functions according to dependencies, as in the next reaction method [207]. The firing frequency is the frequency of a particular event being triggered in the system and requires several tuning simulations to estimate. This method

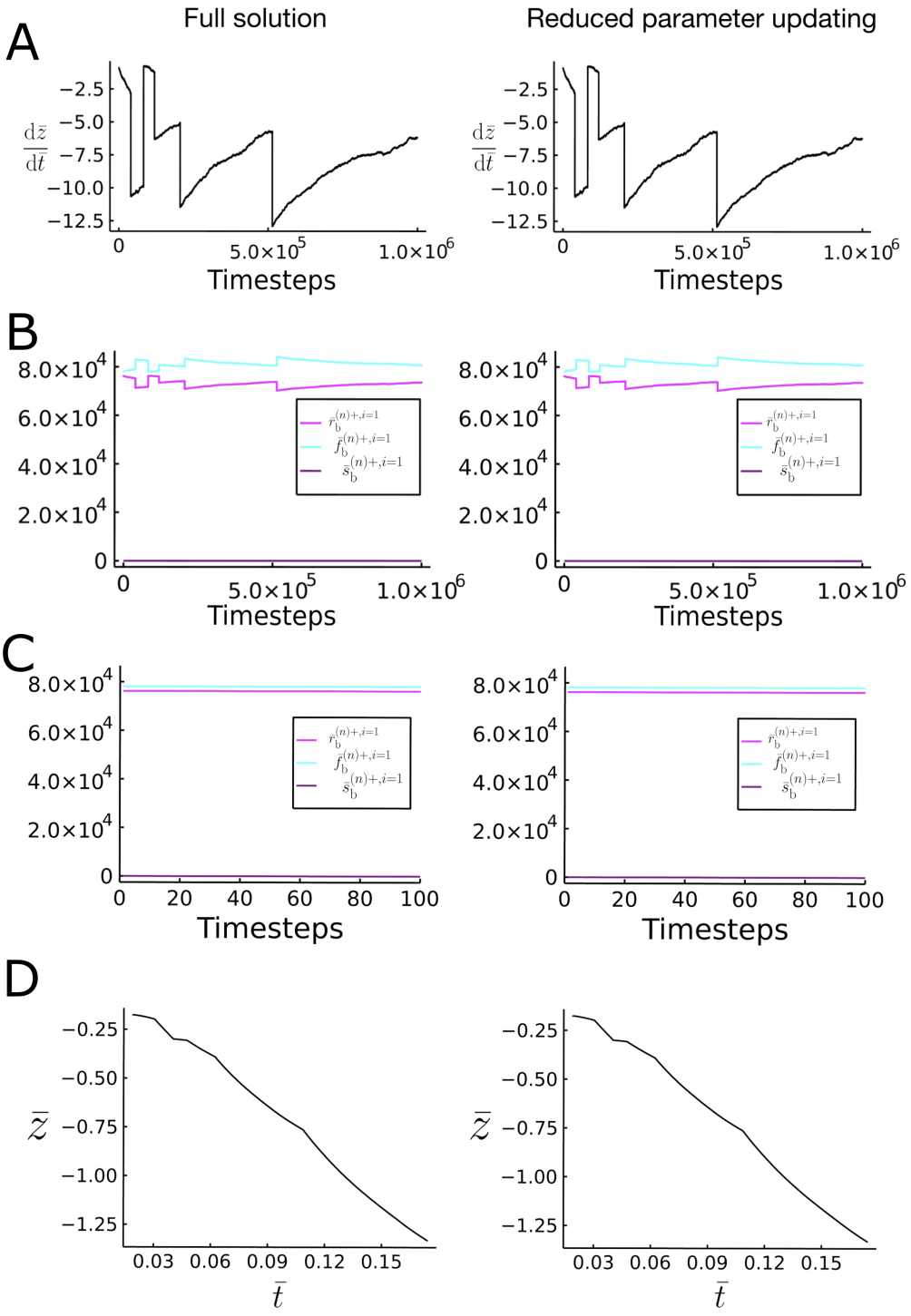

Figure 4.4. **Reducing the computational expense of the stochastic model**. Comparison between solutions of (left) the full solution and (right) the solution when rate coefficients are updated every $J^{\mathrm{w}} = 10$ timesteps and when $\bar{z}_{\bar{t}}^{\mathrm{Thld}} = 0.2$. A) A plot of the spindle pole velocity $\frac{\mathrm{d}\bar{z}}{\mathrm{d}\bar{t}}$ at each timestep taken by the stochastic model. B) Plots of the probabilities $\bar{r}_{\mathrm{b}}^{(n)+,i=1}$, $\bar{f}_{\mathrm{b}}^{(n)+,i=1}$ and $\bar{s}_{\mathrm{b}}^{(n)+,i=1}$ as a function of the number of steps taken by the stochastic simulation for a short test case. C) Graphs in (B) over a shorter time-frame, illustrating that the probabilities are slowly varying over short time. D) The resulting solutions of spindle pole position $\bar{z}\,(\bar{t})$. Parameters: $N = 15, \alpha = 0.08, \beta = 0.04, \Gamma = 20, \bar{\omega}_{\mathrm{on}} = 0.005, \bar{\omega}_0 = 0.001, \gamma = 2, K = 0.005$

is appropriate for multiscale systems which have events which are triggered very often as well as events which are very rare. It allows decreased 'search depths' to find the next reaction while also saving on the computation time in updating the parameters following an event triggering. However, due to the complexity of the system we consider, the firing frequency is less well defined. Indeed the events (switching, retracting, extending) have probabilities which are heavily dependent on the current binding and extension state of the individual force generators as well as the dynamics of the spindle pole position. It follows that the firing frequencies of particularly events in our model would also be dynamic, and a re-ordering of the event list for searching purposes would need to reflect this. As such, we combine some of the features exploited in the above optimisations and use them to produce a system-specific optimisation.

Considering that the average time of a single step in the stochastic model is on the scale of $(5\pm1)\times10^{-8}$ [in non-dimensional units], it was assumed that over a window of J^{w} timesteps, the rate coefficients may be considered to be constant, as illustrated in Figure 4.4C. However, plotting the rate coefficients in time revealed the presence of discontinuous jumps which correspond to significant changes in $\bar{z}_{\bar{t}} \equiv \frac{\mathrm{d}\bar{z}}{\mathrm{d}\bar{t}}$ (Figure 4.4A,B). In order to ensure that these 'jumps' weren't missed, we chose to update the rate coefficients in an *ad hoc* mannner if the spindle pole velocity at timestep j was determined to be above a threshold, $\bar{z}_{\bar{t}}^{\mathrm{Thld}}$, such that $|\bar{z}_{\bar{t}}\,(j) - \bar{z}_{\bar{t}}\,(j-1)\,| > \bar{z}_{\bar{t}}^{\mathrm{Thld}}$, as well as every J^{w} timesteps.

To test and tune the size of this window and threshold we used a known sequence of random variables to feed into short simulations to produce duplicate systems where the window and threshold were the only varying values. Solutions for the reduced updating method best matched the full solution when $\bar{z}_{\bar{t}}^{\mathrm{Thld}} = 0.2$ and $J^{\mathrm{w}} = 10$ (Figure 4.4C). Larger values of J^{w} did not incur a major loss of the solution shape but we opted to underestimate the size of the window needed in order to produce simulations which were as reliable as possible. These parameter values were chosen to produce the results described below. Simulations were run for either 10^{10} timesteps or 165 hours (real time), whichever came first.

4.2.5 Results of the stochastic model

Using the parameters shown in Table 4.2, with $N = 15$, the stochastic model shows the emergence of spontaneous oscillations, following some initial transients from the initial conditions (Figure 4.5A), as shown here in an example. The average extensions $\langle \bar{y}_{\mathrm{b(u)}}^{\pm} \rangle = \frac{\sum_{n=1}^{N} \bar{y}_{\mathrm{b(u)}}^{(n)\pm,i}}{n_{\mathrm{b(u)}}^{\pm}}$ were calculated at each timestep, with $n_{\mathrm{b(u)}}^{\pm}$ the number of bound (unbound) force generators at time $\bar{t}$. The average extensions of the bound force generators $\langle \bar{y}_{\mathrm{b}}^{+} \rangle$ and $\langle \bar{y}_{\mathrm{b}}^{-} \rangle$ oscillate in anti-phase to one another (Figure 4.5B). Further, the average extension of unbound force generators $\langle \bar{y}_{\mathrm{u}}^{\pm} \rangle$ appeared to remain close to 0 following the initial transients (Figure 4.5B). This action can be explained by considering the movement of the spindle pole through one cycle of oscillation (Figure 4.5C) and the average extension of the bound force generators as a function of this spindle position (Figure 4.3D). It is noted that 'gaps' in the $\langle \bar{y}_{\mathrm{b}}^{\pm} \rangle$ plots (Figure 4.5D) occur where there are no bound generators from which to

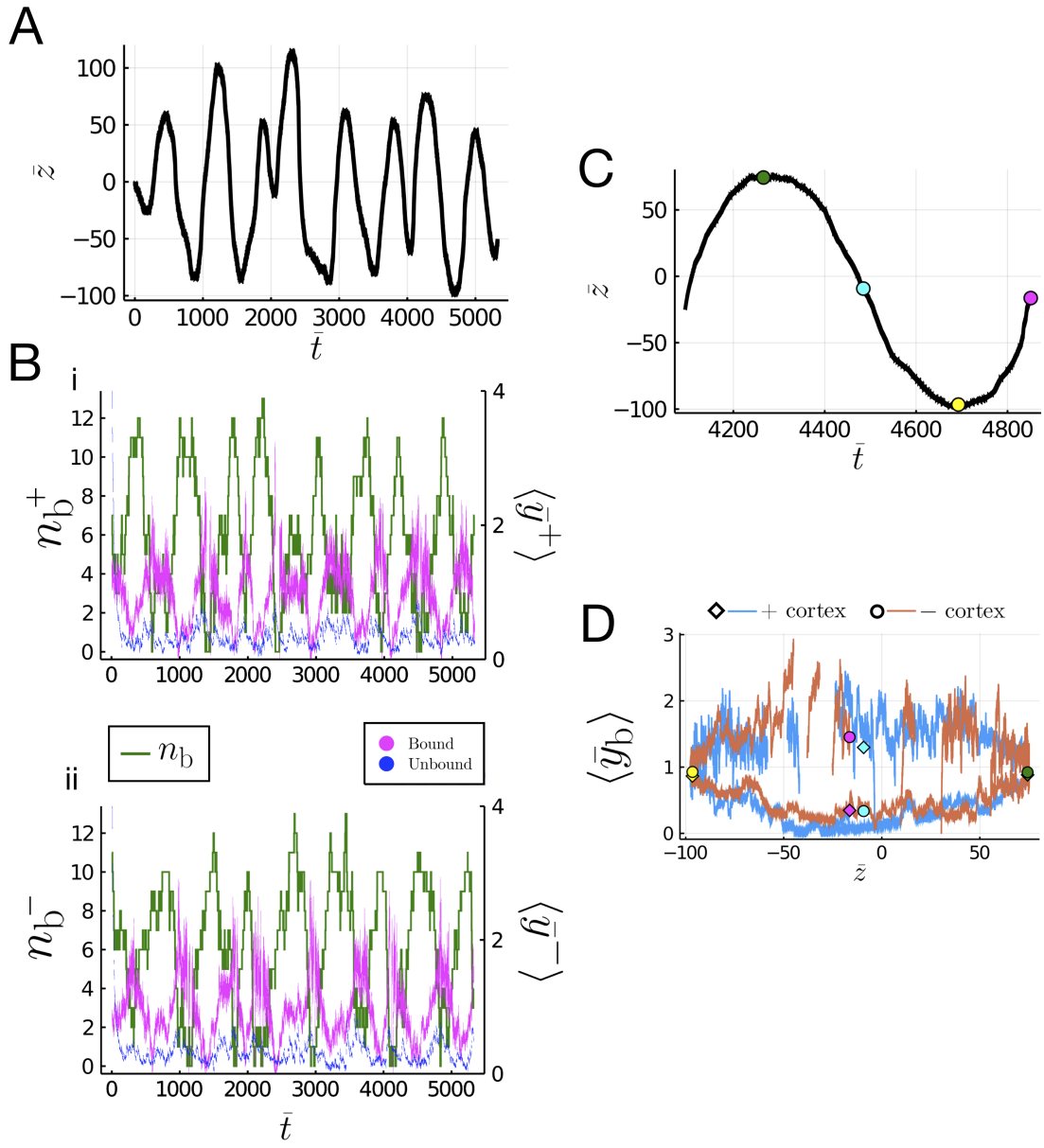

Figure 4.5. **A stochastic model results in spontaneous oscillations of the spindle pole position.** A) Evolution of the non-dimensionalised spindle pole position through time. B) The number of bound force generators in the i) upper (+) and ii) lower (-) cortex (left y-axis) through time. The average extensions of the bound (magenta) and unbound (blue) force generators in the i) upper (+) and ii) lower (-) cortex are also shown (right y-axis). C) A single period of oscillation of the spindle pole position. Dots correspond to moments in the cycle of interest and correspond colour-wise with the dots and diamonds plotted in D). D) Average extension of the bound generators in the upper and lower cortices as a function of pole position. Parameters: $N = 15, \alpha = 0.08, \beta = 0.04, \Gamma = 20, \bar{\omega}_{\text{on}} = 0.003, \bar{\omega}_0 = 0.001, \gamma = 2, K = 5 \times 10^{-2}$

extract an average (where n_b = 0 in Figure 4.5B).

Consider the following phases of movement identified by coloured symbols in Figure 4.5C, and D.

1. **Spindle moving away from the upper cortex (green to cyan)**. At the peak of the spindle pole oscillation, movement of the spindle is dominated by the microtubule restoring force. The bound generators are extended equally in the upper and lower cortices ($\langle \bar{y}_\mathrm{b}^+ \rangle \sim \langle \bar{y}_\mathrm{b}^- \rangle$ at the green timepoint (Figure 4.5D)) though there are a greater number bound in the upper cortex rather than the lower ($n_\mathrm{b}^+ > n_\mathrm{b}^-$, comparison in Figure 4.5Bi vs Bii). The restoring force ($-K\bar{z}$) is greater than the net upward pulling force provided by this unbalanced population ratio. As the spindle pole moves towards $\bar{z} = 0$ this restoring force decreases while the increasing spindle pole velocity results in a net compression of the elastic linkers on the lower cortex, due to a switch in the sign of $\bar{v}_\mathrm{b}^-$ ($\langle \bar{y}_\mathrm{b}^- \rangle$). Additionally, the spindle pole velocity increases the relative velocity of the force generators in the upper cortex, resulting in an extension of the elastic linkers at the upper cortex (Figures 4.5D; 4.2B), and shortening of the linkers at the lower cortex. Due to the tension-sensitive unbinding rate $\bar{\omega}_0 e^{\gamma \bar{y}_\mathrm{b}^+}$, this results in a gradual decrease in the number of upper bound force generators as $\langle \bar{\omega}_0 e^{\gamma \bar{y}_\mathrm{b}^+} \rangle$ increases in value, while the number of bound force generators in the lower cortex increases due to a constant binding rate and a decreased unbinding rate (Figure 4.5B).

2. **Spindle moving through the centre of its oscillating range, toward the lower cortex (cyan to yellow)**. As the spindle moves through $\bar{z} = 0$ the restoring force steadily increases from 0 to $-K\bar{z}$. This slows the movement of the spindle such that the velocity of the force generators in the lower cortex may become positive $\bar{v}_\mathrm{b}^-$ ($\langle \bar{y}_\mathrm{b}^- \rangle$) > 0 which allows these elastic linkers to extend (Figure 4.5D), decreasing the relative velocity of the remaining upper force generators, the average extension of which is also reduced due to the unbinding of those with larger extensions and binding of force generators with reduced extensions (Figure 4.5D). The number of bound generators in the lower cortex also begins to decline as they extend due to the increased unbinding rate (Figure 4.5Bii).

3. **Spindle moving away from the lower cortex (yellow to magenta)**. This phase replicates the first phase, but with the behaviours of upper and lower cortex reversed. The motion away from the cortex due to the restoring force results in a compression of the upper elastic linkers and an extension of the lower elastic linkers (Figure 4.5D), and a corresponding decrease in the absolute number of the bound force generators in the lower cortex as opposed to the increased binding observed in the upper cortex (Figure 4.5B).

The closed loops in $\langle \bar{y}_\mathrm{b}^\pm \rangle$-$\bar{z}$ space are traced anti-clockwise in the lower cortex and clockwise in the upper cortex (Figure 4.5D). At the stall force (when $\langle \bar{y}_\mathrm{b}^\pm \rangle \approx 1$), the direction of the solution loop is determined by the direction of acceleration of the spindle pole with

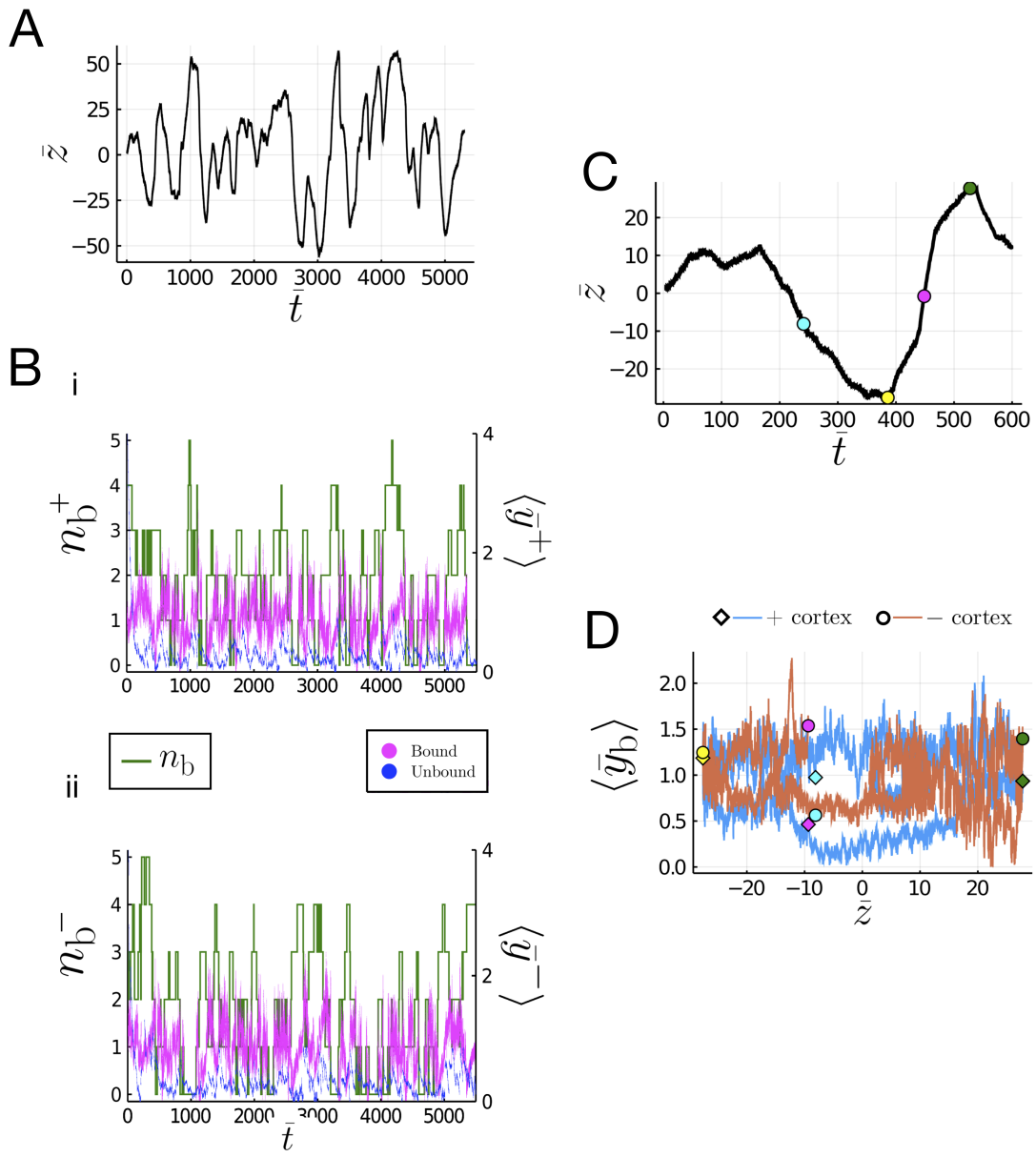

Figure 4.6. **Oscillations decrease in amplitude and regularity for fewer force generators.** A) Evolution of the non-dimensionalised spindle pole position through time. B) The number of bound force generators in the i) upper (+) and ii) lower (-) cortex (left y-axis) through time. The average extensions of the bound (magenta) and unbound (blue) force generators in the i) upper (+) and ii) lower (-) cortex are also shown (right y-axis). C) A single period of oscillation of the spindle pole position. Dots correspond to moments in the cycle of interest and correspond colour-wise with the dots and diamonds plotted in D). D) Average extension of the bound generators in the upper and lower cortices as a function of pole position. Parameters: $N = 5, \alpha = 0.08, \beta = 0.04, \Gamma = 20, \bar{\omega}_{\text{on}} = 0.003, \bar{\omega}_0 = 0.001, \gamma = 2, K = 5 \times 10^{-2}$.

respect to the cortex. That is, a force generator in the lower cortex whose elastic linker is at $\bar{y}_{\text{b}}^{(n)\pm,i} = 1$ will be decreasing its extension as the spindle pole accelerates toward it (negative acceleration, green point in Figure 4.5C, D) and increasing as the spindle pole accelerates away (positive acceleration, yellow point in Figure 4.5C, D). This was predicted by the form (4.16). Figure 4.5B shows, on average, that the number of bound force generators $n_{\text{b}}^{\pm}$ decreases as the linkers become more extended. This is expected by the form of $s_{\text{b}}^{(n)\pm,i} = \bar{\tau}\bar{\omega}_0 e^{\gamma \bar{y}_{\text{b}}^{(n)\pm,i}}$.

The same phases of movement are present in simulations with fewer force generators al-

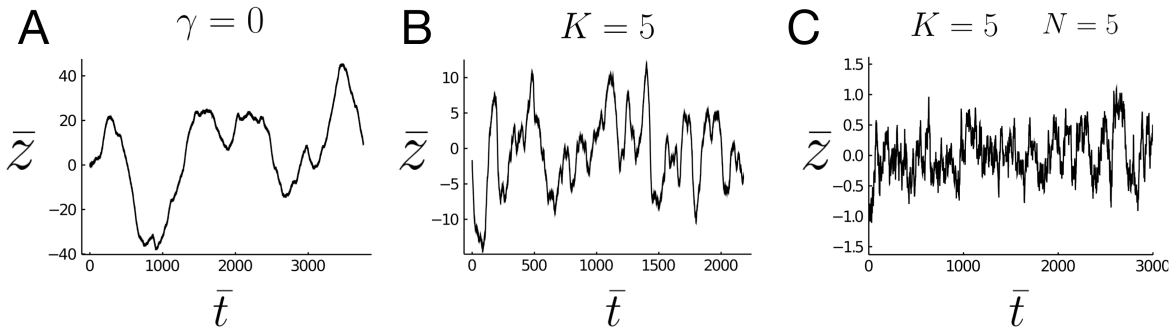

Figure 4.7. **Factors which affect the oscillatory dynamics of the spindle pole.** Evolution of the non-dimensionalised spindle pole position through time for different parameters. A) An example solution when the unbinding of the force generator is no longer tension-sensitive: $N = 15$, $K = 5 \times 10^{-2}$, $\gamma = 0$. B) An example solution when the restoring force is increased by a factor of 100: $N = 15$, $K = 5$, $\gamma = 2$. C) An example solution for reduced numbers of force generators and an increased restoring force: $N = 5$, $K = 5$, $\gamma = 2$. Remaining parameters: $\alpha = 0.08, \beta = 0.04, \bar{\omega}_{\text{on}} = 0.003, \bar{\omega}_0 = 0.001, \Gamma = 20$

though the clarity of the oscillations and coupled dynamics is reduced (Figure 4.6). The oscillations produced when $N = 5$ have a reduced amplitude (Figure 4.6A) and period ($T \approx 800$) compared with those produced in simulations with $N = 15$ force generators per cortex ($T \sim 900$). The period and approximate amplitude of oscillations observed when $N = 15$ are of a similar order of magnitude to those reported by Grill *et al.* (2005) in their stochastic simulation, though the details of the type of stochastic simulation used were omitted from the paper and so direct comparisons are difficult to make [80]. The presence of the closed loops in $\langle \bar{y}_{\text{b}}^{\pm} \rangle$-$\bar{z}$ space remains across both N values, as well as the anti-phase correlation between $\langle \bar{y}_{\text{b}}^{\pm} \rangle$ and $n_{\text{b}}^{\pm}$, though they are also much noisier when N is reduced (Figure 4.6B, D).

We now assess the impact of varying some of the parameters present in the model (Figure 4.7). Given the computational expense of the Gillespie algorithm, running a large number of simulations to properly explore the parameter space is infeasible. Additionally, the timespans achieved in these simulations are very short compared with the average metaphase time in *Xenopus* embryonic epithelial cells (Section 3.2.2) ($\bar{t} = 3000$ is equivalent to $t = 60$ s whereas metaphase time was approximately between 300-900 s). Despite this, we present the observations of the stochastic simulations for the few parameters we could vary.

Removing the tension sensitivity of unbinding by setting $\gamma = 0$ results in spindle pole movements which are less well defined (Figure 4.7A), with reduced deviation from the centre $\bar{z} = 0$ when compared with the "base" case shown in Figure 4.5A. Thus the tension sensitive unbinding rate is important for promoting coherent oscillations of the spindle pole, although noisier fluctuations of the pole may still exist due to the stochastic binding and unbinding. We would expect that running this simulation with more force generators would result in less dynamic behaviour, as individual binding and unbinding for small numbers of force generators is expected to have a significant effect on the spindle pole position. For a large population of force generators, an individual stochastically binding or unbinding event is likely to have a smaller overall effect.

The restoring force is modulated by the parameter K (Figure 4.7B). By increasing the restoring force we expect the spindle pole to remain more central in the cell, as the restoring force will outweigh the pulling forces by the cortical force generators. As expected, we observe a reduced deviation in the position of the spindle pole from the centre (Figure 4.7B). We also see a marked reduction in the clarity of the oscillations observed previously (Figure 4.5A). Further affecting the balance of restoring and pulling forces, by reducing the number of force generators to $N = 5$, results in a cessation of coherent movements (Figure 4.7C). Thus the correct balance of restoring and pulling forces is important for sustaining clear oscillations of the spindle pole.

4.2.6 Summary of the Gillespie simulations

The clear oscillations recovered from this model along with characteristic population dynamics in the upper and lower cortices reveal the emergence of collective motions and responses which we will investigate further using alternative formulations. This stochastic model has revealed that approximating the protein complex Gαi/LGN/NuMA at the cell periphery as a mechanical spring with a motor protein head (dynein), in conjunction with microtubule-based centring forces, is sufficient to create a significant dynamic movement of an otherwise untethered spindle pole. The resulting oscillation and force generator dynamics are noisy but with clear general trends, which become less noisy as N increases. This analysis suggests that only a small number of cortical force generators may be required to induce a dynamic mitotic spindle response. We have shown that the balance of restoring to pulling forces is an important factor in the outcome of the spindle pole movements, as increasing the restoring force or decreasing the pulling force reduces the clarity and amplitude of the movements of the spindle pole, resulting in much noisier oscillations. Further, the tension-sensitive unbinding rate of the motor proteins is required for promoting coherent oscillations. We highlight the qualitative similarity of the noisy oscillations produced using the Gillespie model and the oscillations of the mitotic spindle angles we measured experimentally (Figures 3.7 and 3.9). In particular, both the"good" experimentally measured oscillations (as quantified using the goodness measure) (Figure 3.9A compared with Figure 4.5A) and the less good (Figure 3.9B compared with Figures 4.6A, 4.7B) have qualitative similarities with the stochastic model results. We note however that the measured period of oscillations in the spindle angles were much longer than the periods of oscillations of the single spindle pole using the Gillespie model. This is likely due to our limited ability to increase N in these simulations due to computational expense, as the period of spindle pole oscillation increases with N. Additionally, we acknowledge that the angle of the two dimensional spindle measured experimentally is not directly comparable with the one dimensional movement of an individual spindle pole, as it is the relative motion of the two spindle poles which define the rotational dynamics of the entire mitotic spindle. As such, we continue with our analysis of the system by using a Fokker-Planck description. The Fokker-Planck description will allow us to explore the parameter space more completely at a reduced computational expense.

4.3 Stochastic model: a Fokker-Planck description

Simulating the system stochastically allows us to observe the emergence of spindle dynamics from a time series of discrete events. We have shown that oscillations of the spindle pole may occur spontaneously as a result of opposing pulling events and restorative microtubule-based centring forces. However, stochastic simulations are computationally expensive and this restricts our ability to fully explore the possibilities of the system efficiently. Further, as one aim is to produce a working two-dimensional model of spindle dynamics, a model which is computationally expensive in one dimension will become even more so in higher dimensions. Thus, we exploit a Fokker-Planck description of the system which mirrors that used previously to describe the oscillating spindle pole of early *C. elegans* [80]. Using this description, we hope to more rigorously explore the system by varying some of the many parameters, including the effects of diffusion (due to so-called 'demographic noise') and the relative magnitude of the centring force.

4.3.1 Theoretical description

To describe this model using a system of partial differential equations (PDEs), we consider $\bar{P}^{\pm}_{\text{b(u)}}\left(\bar{y}^{(n)\pm,i}_{\text{b(u)}},\bar{t}\right)$, the probability that the n$^{\text{th}}$ force generator is bound (or unbound) with an extension $\bar{y}^{(n)\pm,i}_{\text{b(u)}}$ at time $\bar{t}$. Using $\Delta\bar{t}=\bar{\tau}$, then

$$\begin{aligned}\bar{P}^{\pm}_{\text{b(u)}}\left(\bar{y}^{(n)\pm,i}_{\text{b(u)}},\bar{t}+\Delta\bar{t}\right)-\bar{P}^{\pm}_{\text{b(u)}}\left(\bar{y}^{(n)\pm,i}_{\text{b(u)}},\bar{t}\right)\\ =\bar{P}^{\pm}_{\text{b(u)}}\left(\bar{y}^{(n)\pm,i+1}_{\text{b(u)}},\bar{t}\right)r^{(n)\pm,i+1}_{\text{b(u)}}+\bar{P}^{\pm}_{\text{b(u)}}\left(\bar{y}^{(n)\pm,i-1}_{\text{b(u)}},\bar{t}\right)f^{(n)\pm,i-1}_{\text{b(u)}}+\bar{P}^{\pm}_{\text{u(b)}}\left(\bar{y}^{(n)\pm,i}_{\text{u(b)}},\bar{t}\right)s^{(n)\pm,i}_{\text{u(b)}}\\ -\bar{P}^{\pm}_{\text{b(u)}}\left(\bar{y}^{(n)\pm,i}_{\text{b(u)}},\bar{t}\right)\left(r^{(n)\pm,i}_{\text{b(u)}}+f^{(n)\pm,i}_{\text{b(u)}}+s^{(n)\pm,i}_{\text{b(u)}}\right).\end{aligned} \tag{4.21}$$

Equation (4.21) describes the probability of being in state $\bar{y}^{(n)\pm,i}_{\text{b(u)}}$ at time $\bar{t}+\Delta\bar{t}$ as a result of the system state at time $\bar{t}$. For example, the $\bar{P}^{\pm}_{\text{b(u)}}\left(\bar{y}^{(n)\pm,i+1}_{\text{b(u)}},\bar{t}\right)r^{(n)\pm,i+1}_{\text{b(u)}}$ term represents retraction from state $\bar{y}^{(n)\pm,i+1}_{\text{b(u)}}$ at a time $\bar{t}$. This can be rewritten using a Taylor expansion. In short, as $\bar{y}^{(n)\pm,i+1}_{\text{b(u)}}=\bar{y}^{(n)\pm,i}_{\text{b(u)}}+\Delta y$, then if $g^{\pm}\left(\bar{y}^{(n)\pm,i}_{\text{b(u)}},\bar{t}\right)\equiv\bar{P}^{\pm}_{\text{b(u)}}\left(\bar{y}^{(n)\pm,i}_{\text{b(u)}},\bar{t}\right)r^{(n)\pm,i}_{\text{b(u)}}$ we expand

$$g^{\pm}\left(\bar{y}^{(n)\pm,i+1}_{\text{b(u)}},\bar{t}\right)=g^{\pm}\left(\bar{y}^{(n)\pm,i}_{\text{b(u)}},\bar{t}\right)+\Delta\bar{y}g^{\pm}_{\bar{y}}\left(\bar{y}^{(n)\pm,i}_{\text{b(u)}},\bar{t}\right)+\frac{1}{2}\Delta\bar{y}^{2}g^{\pm}_{\bar{y}\bar{y}}\left(\bar{y}^{(n)\pm,i}_{\text{b(u)}},\bar{t}\right)+... \tag{4.22}$$

and similarly for $\bar{P}^{\pm}_{\text{b(u)}}\left(\bar{y}^{(n)\pm,i+1}_{\text{b(u)}},\bar{t}\right)f^{(n)\pm,i+1}_{\text{b(u)}}$, where subscripts $\bar{y}$ and $\bar{t}$ denote derivatives, giving

$$\begin{aligned}\Delta\bar{t}\bar{P}^{\pm}_{\text{b(u)},\bar{t}}=\Delta\bar{y}\left(\bar{P}^{\pm}_{\text{b(u)}}r^{\pm}_{\text{b(u)}}-\bar{P}^{\pm}_{\text{b(u)}}f^{\pm}_{\text{b(u)}}\right)_{\bar{y}}+\frac{1}{2}\left(\Delta\bar{y}\right)^{2}\left(\bar{P}^{\pm}_{\text{b(u)}}r^{\pm}_{\text{b(u)}}+\bar{P}^{\pm}_{\text{b(u)}}f^{\pm}_{\text{b(u)}}\right)_{\bar{y}\bar{y}}\\ -\bar{P}^{\pm}_{\text{b(u)}}s^{\pm}_{\text{b(u)}}+\bar{P}^{\pm}_{\text{u(b)}}s^{\pm}_{\text{u(b)}}+...,\end{aligned} \tag{4.23}$$

where all quantities are evaluated at extension $\bar{y}_{\mathrm{b(u)}}^{(n)\pm,i}$. Therefore, by (4.4-4.5) and recalling the non-dimensionalised parameters (Table 4.3), to leading order as $\Delta\bar{y} \to 0$ and $\Delta\bar{t} \to 0$ we may write

$$\bar{P}_{\mathrm{b},\bar{t}}^{\pm} = -\left(\bar{v}_{\mathrm{b}}^{\pm}\bar{P}_{\mathrm{b(u)}}^{\pm}\right)_{\bar{y}} + \left(\alpha\bar{P}_{\mathrm{b}}^{\pm}\right)_{\bar{y}\bar{y}} - \bar{\omega}_0 e^{\gamma\bar{y}}\bar{P}_{\mathrm{b}}^{\pm} + \bar{\omega}_{\mathrm{on}}\bar{P}_{\mathrm{u}}^{\pm}, \tag{4.24a}$$

$$\bar{P}_{\mathrm{u},\bar{t}}^{\pm} = -\left(\bar{v}_{\mathrm{u}}^{\pm}\bar{P}_{\mathrm{u}}^{\pm}\right)_{\bar{y}} + \left(\Gamma\beta\bar{P}_{\mathrm{u}}^{\pm}\right)_{\bar{y}\bar{y}} + \bar{\omega}_0 e^{\gamma\bar{y}}\bar{P}_{\mathrm{b}}^{\pm} - \bar{\omega}_{\mathrm{on}}\bar{P}_{\mathrm{u}}^{\pm}, \tag{4.24b}$$

and thus we have recovered the Fokker-Planck equations reported by Grill *et al.* (2005) [80]. These hold assuming that $\bar{v}_{\mathrm{b(u)}}^{\pm}$, α, $\Gamma\beta$, $\bar{\omega}_{\mathrm{on}}$ and $\bar{\omega}_0 e^{\gamma\bar{y}}$ of a similar magnitude. Using the parameter values explored in Section 4.2 these have a range of magnitudes between 10^{-3} and 10^{1}, as determined using a combination of experimental measurements, estimations and parameter fitting (many taken from the literature as used in [80]). While these may not be of strict identical order of magnitude, we argue that these terms are of similar enough magnitude that they should not be neglected from the analysis. Note we have used the non-dimensional expressions for $s_{\mathrm{b(u)}}^{\pm}$ in Table 4.1, with $\bar{\tau} = \Delta\bar{t}$. The elastic linker extension $\bar{y}$ is now considered as a continuous variable rather than one with discrete states, along with velocities $\bar{v}_{\mathrm{b(u)}}^{\pm}(\bar{y})$. The probability density functions $\bar{P}_{\mathrm{b(u)}}^{\pm}(\bar{y},\bar{t})$ may be rewritten as

$$\bar{P}_{\mathrm{b},\bar{t}}^{\pm} = \bar{\omega}_{\mathrm{on}}\bar{P}_{\mathrm{u}}^{\pm} - \bar{\omega}_0 e^{\gamma\bar{y}}\bar{P}_{\mathrm{b}}^{\pm} - \bar{J}_{\mathrm{b},\bar{y}}^{\pm}, \tag{4.25a}$$

$$\bar{P}_{\mathrm{u},\bar{t}}^{\pm} = -\bar{\omega}_{\mathrm{on}}\bar{P}_{\mathrm{u}}^{\pm} + \bar{\omega}_0 e^{\gamma\bar{y}}\bar{P}_{\mathrm{b}}^{\pm} - \bar{J}_{\mathrm{u},\bar{y}}^{\pm}, \tag{4.25b}$$

where probability fluxes $\bar{J}_{\mathrm{u}}^{\pm}(\bar{y},\bar{t})$ and $\bar{J}_{\mathrm{b}}^{\pm}(\bar{y},\bar{t})$ are of the form

$$\bar{J}_{\mathrm{b}}^{\pm} = \bar{v}_{\mathrm{b}}^{\pm}\bar{P}_{\mathrm{b}}^{\pm} - \alpha\bar{P}_{\mathrm{b},\bar{y}}^{\pm}, \tag{4.26a}$$

$$\bar{J}_{\mathrm{u}}^{\pm} = -\Gamma\left(\bar{y}\bar{P}_{\mathrm{u}}^{\pm} + \beta\bar{P}_{\mathrm{u},\bar{y}}^{\pm}\right), \tag{4.26b}$$

with boundary conditions

$$\bar{J}_{\mathrm{b}}^{\pm}(\bar{t},\bar{y}=0,\bar{y}_{\mathrm{max}}) = \bar{J}_{\mathrm{u}}^{\pm}(\bar{t},\bar{y}=0,\bar{y}_{\mathrm{max}}) = 0. \tag{4.27}$$

The expression for $\bar{v}_{\mathrm{u}}^{\pm} = -\Gamma\bar{y}$ has been inserted into (4.26b). Bound motor proteins have a relative velocity

$$\bar{v}_{\mathrm{b}}^{\pm} = 1 - \bar{y} \mp \frac{\mathrm{d}\bar{z}}{\mathrm{d}\bar{t}}, \tag{4.28}$$

as in (4.16). The Fokker-Planck equations (4.25a-4.25b) describe the evolution of the probability density functions of the bound and unbound generator elastic linker extensions as a result of their respective drift (velocity terms) and diffusion, and may be used to describe the force generator population dynamics.

Summation of (4.25a) and (4.25b) returns

$$\left(\bar{P}_{\mathrm{u}}^{\pm} + \bar{P}_{\mathrm{b}}^{\pm}\right)_{\bar{t}} + \left(\bar{J}_{\mathrm{u}}^{\pm} + \bar{J}_{\mathrm{b}}^{\pm}\right)_{\bar{y}} = 0 \tag{4.29}$$

where integration with respect to $\bar{y}$ and exploiting boundary conditions (4.26a) and (4.26b) ensures conservation of total probabilities

$$\int_0^{\bar{y}_{\max}} \left(\bar{P}_{\mathrm{b}}^{\pm} + \bar{P}_{\mathrm{u}}^{\pm}\right) \mathrm{d}\bar{y} = 1. \tag{4.30}$$

With these probability density functions, the pulling force toward each cortex (4.1) may instead be calculated as an average

$$\bar{F}^{\pm} = N \int_0^{\bar{y}_{\max}} \bar{y} \bar{P}_{\mathrm{b}}^{\pm}(\bar{y}, \bar{t}) \mathrm{d}\bar{y}, \tag{4.31}$$

which changes the forcing term of the spindle pole velocity (4.14) such that it reads

$$\bar{\xi}\bar{z}_{\bar{t}} = -K\bar{z} - N\left(\int_0^{\bar{y}_{\max}} \bar{y}\bar{P}_{\mathrm{b}}^{-}\mathrm{d}\bar{y} - \int_0^{\bar{y}_{\max}} \bar{y}\bar{P}_{\mathrm{b}}^{+}\mathrm{d}\bar{y}\right). \tag{4.32}$$

With supplemental initial conditions $\bar{P}_{\mathrm{b}}^{\pm}(\bar{y}, 0) = \bar{P}_{\mathrm{b0}}^{\pm}(\bar{y})$, $\bar{P}_{\mathrm{u}}^{\pm}(\bar{y}, 0) = \bar{P}_{\mathrm{u0}}^{\pm}(\bar{y})$, and $\bar{z}(0) = \bar{z}_0$, and boundary conditions (4.27), the coupled equations (4.25a), (4.25b), and (4.32) may be solved in time to return the dynamics of the spindle pole and the populations of cortical force generators, represented as probability densities over multiple realisations of the system.

By the form of (4.25a), (4.25b) and the fluxes (4.26a) and (4.26b), the following observations can be made.

- For large Γ in (4.26b), (4.25b) will be dominated by the advective term which will quickly 'sweep' any unbound force generators with a non-zero extension down toward $\bar{y} = 0$. As there is no flux through this boundary by (4.27), this will result in $\bar{P}_{\mathrm{u}}^{\pm}$ having a defined peak at $\bar{y} = 0$ which tapers away as $\bar{y}$ increases over a width given by the diffusive lengthscale $\beta^{\frac{1}{2}}$.
- The velocity term $\bar{v}_{\mathrm{b}}^{\pm}$ in (4.26a) is such that $\bar{P}_{\mathrm{b}}^{\pm}$ will similarly have a defined peak centred at $\bar{y}_{\mathrm{c}} = 1 \mp \bar{z}_{\bar{t}}$ (from (4.28)) if $\bar{y}_{\mathrm{c}} \ll \bar{y}_{\max}$. This peak will have a width of order $\alpha^{\frac{1}{2}}$.
- Varying the diffusive terms α and β will vary the width of the peaks described above. Large diffusive terms will result in wide flattened peaks while small diffusive terms will result in taller, narrower peaks. Relative height differences can be expected to occur due to the conservation of probabilities (4.29).
- The exponential unbinding rate $\bar{\omega}_0 e^{\gamma\bar{y}}$ will decrease the magnitude of $\bar{P}_{\mathrm{b}}^{\pm}(\bar{y})$ at higher values of $\bar{y}$. How 'large' $\bar{y}$ needs to be to induce this effect is modulated by the unbinding sensitivity γ.

4.3.2 Computational method

Equations (4.25a-4.25b) were solved by employing the method of lines, whereby spatial finite differences in $\bar{y}$ were used to create a system of ordinary differential equations which could be passed to an ODE solver in $\bar{t}$.

To discretise in $\bar{y}$, we consider discrete states $\bar{y}^i$ separated by a fixed distance measure $\Delta\bar{y}$. That is, $\bar{y}^{i+1} = \bar{y}^i + \Delta\bar{y}$ as in Section 4.2, with $\bar{y}^{i=0} = 0$ and $\bar{y}^{i=M} = \bar{y}_{\text{max}}$. Then using central finite differences on the spatial derivative, (4.25a) and (4.26a) become

$$\bar{P}^{\pm,i}_{\text{b},\bar{t}} = \bar{\omega}_{\text{on}}\bar{P}^{\pm,i}_{\text{u}} - \bar{\omega}_0 e^{\gamma\bar{y}^i}\bar{P}^{\pm,i}_{\text{b}} - \frac{1}{2\Delta\bar{y}}\left(\bar{J}^{\pm,i+1}_{\text{b}} - \bar{J}^{\pm,i-1}_{\text{b}}\right) \tag{4.33}$$

and

$$\bar{J}^{\pm,i}_{\text{b}} = \bar{v}^{\pm,i}_{\text{b}}\bar{P}^{\pm,i}_{\text{b}} - \frac{\alpha}{2\Delta\bar{y}}\left(\bar{P}^{\pm,i+1}_{\text{b}} - \bar{P}^{\pm,i-1}_{\text{b}}\right). \tag{4.34}$$

The velocity $\bar{v}^{\pm,i}_{\text{b}} = \bar{v}^{\pm}_{\text{b}}\left(\bar{y}^i\right)$ is given explicitly as

$$\bar{v}^{\pm,i}_{\text{b}} = 1 - \bar{y}^i \mp \bar{z}_{\bar{t}} \tag{4.35}$$

by insertion of $\bar{y}^i$ into (4.28).

By using central finite differences again, (4.25b) and (4.26b) are approximated as

$$\bar{P}^{\pm,i}_{\text{u},\bar{t}} = -\bar{\omega}_{\text{on}}\bar{P}^{\pm,i}_{\text{u}} + \bar{\omega}_0 e^{\gamma\bar{y}^i}\bar{P}^{\pm,i}_{\text{b}} - \frac{1}{2\Delta\bar{y}}\left(\bar{J}^{\pm,i+1}_{\text{u}} - \bar{J}^{\pm,i-1}_{\text{u}}\right) \tag{4.36}$$

and

$$\bar{J}^{\pm,i}_{\text{u}} = -\Gamma\bar{y}^i\bar{P}^{\pm,i}_{\text{u}} - \frac{\Gamma\beta}{2\Delta\bar{y}}\left(\bar{P}^{\pm,i+1}_{\text{u}} - \bar{P}^{\pm,i-1}_{\text{u}}\right). \tag{4.37}$$

These expressions hold for $i = 1, 2...M-1$.

At the $\bar{y}^{i=0}$ boundary we use a forward difference approximation of the spatial derivative to give

$$\bar{P}^{\pm,i=0}_{\text{u},\bar{t}} = -\bar{\omega}_{\text{on}}\bar{P}^{\pm,i=0}_{\text{u}} + \bar{\omega}_0 e^{\gamma\bar{y}^{i=0}}\bar{P}^{\pm,i=0}_{\text{b}} - \frac{1}{\Delta\bar{y}}\left(\bar{J}^{\pm,i=1}_{\text{u}} - \bar{J}^{\pm,i=0}_{\text{u}}\right), \tag{4.38a}$$

$$\bar{P}^{\pm,i=0}_{\text{b},\bar{t}} = \bar{\omega}_{\text{on}}\bar{P}^{\pm,i=0}_{\text{u}} - \bar{\omega}_0 e^{\gamma\bar{y}^{i=0}}\bar{P}^{\pm,i=0}_{\text{b}} - \frac{1}{\Delta\bar{y}}\left(\bar{J}^{\pm,i=1}_{\text{b}} - \bar{J}^{\pm,i=0}_{\text{b}}\right). \tag{4.38b}$$

Similarly, at the $\bar{y}^{i=M}$ boundary we use a backward difference approximation to give

$$\bar{P}^{\pm,i=M}_{\text{u},\bar{t}} = -\bar{\omega}_{\text{on}}\bar{P}^{\pm,i=M}_{\text{u}} + \bar{\omega}_0 e^{\gamma\bar{y}^{i=M}}\bar{P}^{\pm,i=M}_{\text{b}} - \frac{1}{\Delta\bar{y}}\left(\bar{J}^{\pm,i=M}_{\text{u}} - \bar{J}^{\pm,i=M-1}_{\text{u}}\right), \tag{4.39a}$$

$$\bar{P}^{\pm,i=M}_{\text{b},\bar{t}} = \bar{\omega}_{\text{on}}\bar{P}^{\pm,i=M}_{\text{u}} - \bar{\omega}_0 e^{\gamma\bar{y}^{i=M}}\bar{P}^{\pm,i=M}_{\text{b}} - \frac{1}{\Delta\bar{y}}\left(\bar{J}^{\pm,i=M}_{\text{b}} - \bar{J}^{\pm,i=M-1}_{\text{b}}\right). \tag{4.39b}$$

Recalling boundary conditions (4.27), then

$$\bar{J}^{\pm,i=0,M}_{\mathrm{b(u)}} = 0 \tag{4.40}$$

and (4.38a-4.39b) become

$$\bar{P}^{\pm,i=0}_{\mathrm{u},\bar{t}} = -\bar{\omega}_{\mathrm{on}}\bar{P}^{\pm,i=0}_{\mathrm{u}} + \bar{\omega}_0 e^{\gamma\bar{y}^{i=0}}\bar{P}^{\pm,i=0}_{\mathrm{b}} - \frac{1}{\Delta\bar{y}}\bar{J}^{\pm,i=1}_{\mathrm{u}}, \tag{4.41a}$$

$$\bar{P}^{\pm,i=0}_{\mathrm{b},\bar{t}} = \bar{\omega}_{\mathrm{on}}\bar{P}^{\pm,i=0}_{\mathrm{u}} - \bar{\omega}_0 e^{\gamma\bar{y}^{i=0}}\bar{P}^{\pm,i=0}_{\mathrm{b}} - \frac{1}{\Delta\bar{y}}\bar{J}^{\pm,i=1}_{\mathrm{b}}, \tag{4.41b}$$

$$\bar{P}^{\pm,i=M}_{\mathrm{u},\bar{t}} = -\bar{\omega}_{\mathrm{on}}\bar{P}^{\pm,i=M}_{\mathrm{u}} + \bar{\omega}_0 e^{\gamma\bar{y}^{i=M}}\bar{P}^{\pm,i=M}_{\mathrm{b}} + \frac{1}{\Delta\bar{y}}\bar{J}^{\pm,i=M-1}_{\mathrm{u}}, \tag{4.41c}$$

$$\bar{P}^{\pm,i=M}_{\mathrm{b},\bar{t}} = \bar{\omega}_{\mathrm{on}}\bar{P}^{\pm,i=M}_{\mathrm{u}} - \bar{\omega}_0 e^{\gamma\bar{y}^{i=M}}\bar{P}^{\pm,i=M}_{\mathrm{b}} + \frac{1}{\Delta\bar{y}}\bar{J}^{\pm,i=M-1}_{\mathrm{b}}. \tag{4.41d}$$

The expression for spindle pole velocity (4.32) is adapted such that the integral terms become summations. Then

$$\bar{\xi}\bar{z}_{\bar{t}} = -K\bar{z} - N\left(\sum_{i=0}^{i=M}\bar{y}^i\bar{P}^{-,i}_{\mathrm{b}} - \sum_{i=0}^{i=M}\bar{y}^i\bar{P}^{+,i}_{\mathrm{b}}\right). \tag{4.42}$$

The ODEs defined in (4.33),(4.36),(4.41a-4.41d) and (4.42) may be assembled into a matrix equation

$$\frac{\partial\mathbf{U}}{\partial\bar{t}} = \mathcal{A}\mathbf{f} \tag{4.43}$$

for a matrix $\mathcal{A}$, and a vector $\mathbf{U}$ whose components are the discretised $\bar{P}^{\pm,i}_{\mathrm{u}}$, $\bar{P}^{\pm,i}_{\mathrm{b}}$ and $\bar{z}$, concatenated together to give

$$\mathbf{U} = \begin{bmatrix}\bar{P}^{+,0}_{\mathrm{u}} & \dots & \bar{P}^{+,M}_{\mathrm{u}} & \bar{P}^{+,0}_{\mathrm{b}} & \dots & \bar{P}^{+,M}_{\mathrm{b}} & \bar{P}^{-,0}_{\mathrm{u}} & \dots & \bar{P}^{-,M}_{\mathrm{u}} & \bar{P}^{-,0}_{\mathrm{b}} & \dots & \bar{P}^{-,M}_{\mathrm{b}} & \bar{z}\end{bmatrix}^{\mathrm{T}}. \tag{4.44}$$

The vector $\mathbf{f}$ has flux terms interspersed between the probability terms

$$\mathbf{f} = \begin{bmatrix}\bar{J}^{+,i}_{\mathrm{u}} & \bar{P}^{+,i}_{\mathrm{u}} & \bar{J}^{+,i}_{\mathrm{b}} & \bar{P}^{+,i}_{\mathrm{b}} & \bar{J}^{-,i}_{\mathrm{u}} & \bar{P}^{-,i}_{\mathrm{u}} & \bar{J}^{-,i}_{\mathrm{b}} & \bar{P}^{-,i}_{\mathrm{b}} & \bar{z}\end{bmatrix}^{\mathrm{T}}, \tag{4.45}$$

where for brevity the terms $\bar{J}^{\pm,i}_{\mathrm{b(u)}}$ and $\bar{P}^{\pm,i}_{\mathrm{b(u)}}$ have been used to represent e.g. $\bar{J}^{+,i}_{\mathrm{u}} = \begin{bmatrix}\bar{J}^{+,0}_{\mathrm{u}} & \dots & \bar{J}^{+,M}_{\mathrm{u}}\end{bmatrix}$. In defining the problem in this way, the matrix $\mathcal{A}$ contains elements which remain constant. In particular if the flux terms were removed in order to define the entire system in terms of $\bar{P}^{\pm,i}_{\mathrm{b(u)}}$, such that $\frac{\mathrm{d}\mathbf{U}}{\mathrm{d}t} = \mathcal{A}^{\mathrm{Hyp}}\mathbf{U}$, the presence of $\bar{v}^{\pm,i}_{\mathrm{b}}$ in $\mathcal{A}^{\mathrm{Hyp}}$ would require a large number of elements of $\mathcal{A}^{\mathrm{Hyp}}$ to be updated. Having $\mathcal{A}$ remain a constant matrix increases the computational efficiency of the solver when $\bar{y}$ is discretised with small $\Delta\bar{y}$.

The following method was used to solve this system.

1. Initial conditions $\bar{P}^{\pm}_{\mathrm{b0}}\left(\bar{y}^i\right) = \left(\sqrt{0.08\pi}\right)^{-1} e^{-\left(\bar{y}^i-1\right)^2/0.08}$, $\bar{P}^{\pm}_{\mathrm{u0}}\left(\bar{y}^i\right) = \left(\sqrt{0.02\pi}\right)^{-1} e^{-\left(\bar{y}^i\right)^2/0.02}$ and $\bar{z}_0 = 10$ were defined.

2. The sparse matrix $\mathcal{A}$ was constructed using the Julia package `SparseArrays` which improves computational performance due to $\mathcal{A}$ containing a large number of zero values.

3. Initial conditions and the matrix $\mathcal{A}$ were passed to an ODE solver from the Julia package `DifferentialEquations` [213]. Within the solver, the following occurred at each timestep:

   (a) Velocity terms $\bar{v}_{\mathrm{b}}^{\pm,i}$ were calculated using (4.35).

   (b) Flux portions of $\mathbf{f}$ were defined using (4.34) and (4.37).

   (c) Equation (4.43) was defined and solved using a Tsitouras 5/4 Runge-Kutta method. This method is the recommended method for problems in Julia of moderate stiffness and utilises automatic step size selection based on the local error estimate [214].

4. The solver repeated steps 3(a)-3(c) until a pre-defined end-point in time.

Source code is available at github.com/dionn-hargreaves/FP_1DSpindle_methodoflines.

4.3.3 Results of the Fokker-Planck model

The solutions $\bar{z}$, $\bar{P}_{\mathrm{b}}^{\pm}$ and $\bar{P}_{\mathrm{u}}^{\pm}$ show an oscillating spindle displacement $\bar{z}$ (Figure 4.8) and an unbound probability density $\bar{P}_{\mathrm{u}}^{\pm}$ which remains maximal at $\bar{y} = 0$, while its amplitude varies in time as a consequence of (4.30). For the bound probability density functions $\bar{P}_{\mathrm{b}}^{\pm}$, the central positions $\bar{y}_{\mathrm{c}}^{\pm}$ (the positions around which the Gaussian curves are peaked), and amplitude $\bar{P}_{\mathrm{b}}^{\pm,\max}$ (the value of the peak of the Gaussian curves), oscillate concurrently with $\bar{z}$ (Figure 4.8C, G). Changing the locations of the Gaussian curve centres or widths in the initial conditions $\bar{P}_{\mathrm{b0}}^{\pm}$ and $\bar{P}_{\mathrm{u0}}^{\pm}$ had no effect on the final solutions following some initial transients (data not shown).

The behaviour of the peak position $\bar{y}_{\mathrm{c}}^{\pm}$ and amplitude $\bar{P}_{\mathrm{b}}^{\pm,\max}$ mirror the behaviour of the average extension $\langle \bar{y}_{\mathrm{b}}^{\pm} \rangle$ and number of bound force generators $n_{\mathrm{b}}^{\pm}$ in the stochastic simulation (Figure 4.5B). The general dynamics of $\bar{P}_{\mathrm{b}}^{\pm}$ are explained as follows, breaking an oscillation down into four phases (Figure 4.9).

1. **Spindle moving away from the upper cortex (1)**. Initially the bound generators in both the upper and lower cortex have the peaks of their Gaussian curves centred at the same extension, ($\bar{y}_{\mathrm{c}}^{+} = \bar{y}_{\mathrm{c}}^{-}$), but there is a higher probability that more generators are bound in the upper cortex than the lower ($\bar{P}_{\mathrm{b}}^{+,\max} > \bar{P}_{\mathrm{b}}^{-,\max}$). The upward pulling by the upper cortical generators is balanced by the microtubule resistance creating a restoring force ($-K\bar{z}$ term in (4.32)) and by downward pulling. As the spindle moves toward the centre, $\bar{P}_{\mathrm{b}}^{\pm,\max}$ decreases as $\bar{y}_{\mathrm{c}}$ increases due to the extension-dependent off

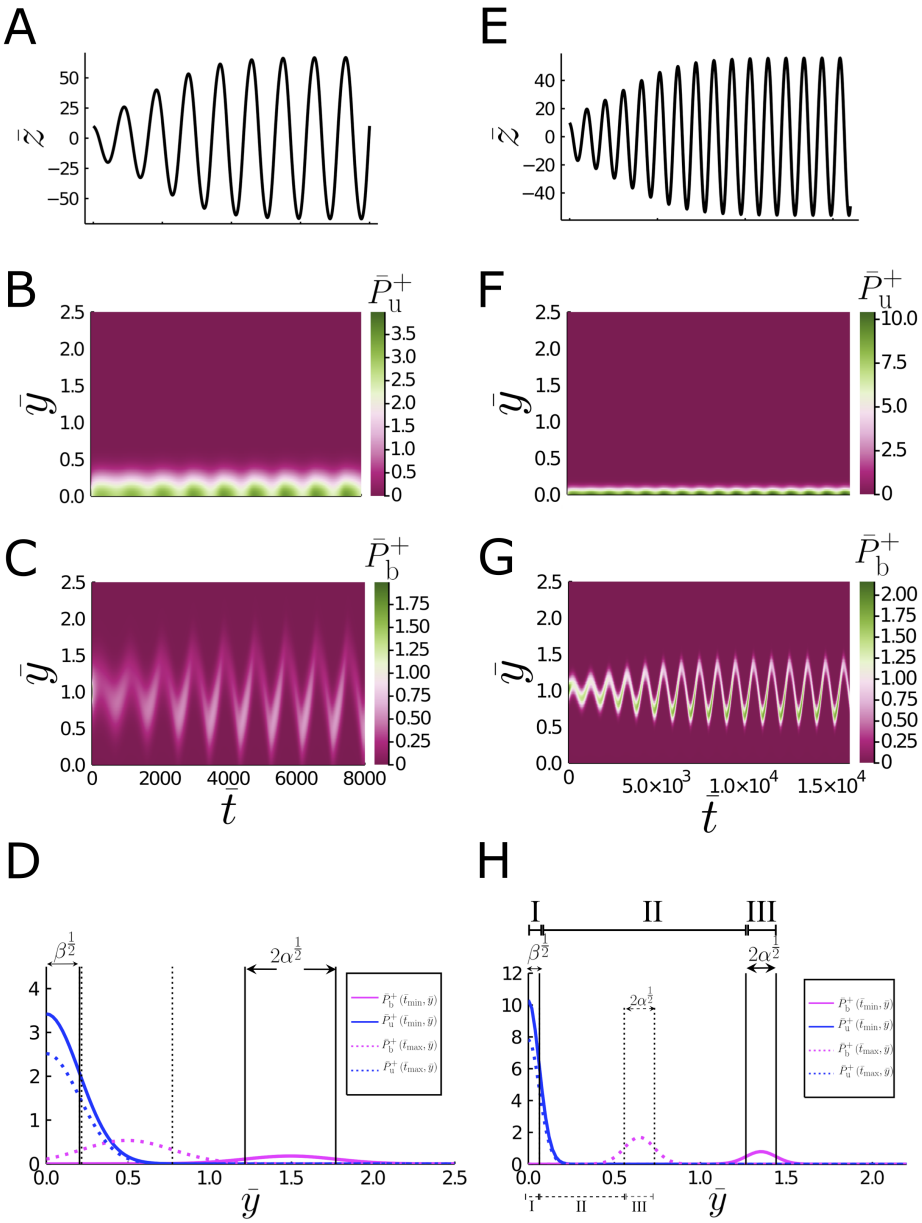

Figure 4.8. **The effect of varying the magnitude of diffusion in the PDE description**. A,E) Example solution to equations (4.25a),(4.25b),(4.32) using the method of lines, showing the pole position, $\bar{z}$ in time $\bar{t}$. Diffusion parameters α, β are a factor of 10 smaller in right column than in the left column. B,F) Heat map of $\bar{P}_{\mathrm{u}}^{+}$ in time. Colour indicates the amplitude of $\bar{P}_{\mathrm{u}}^{+}(\bar{y}, \bar{t})$. C,G) Heat map of $\bar{P}_{\mathrm{b}}^{+}$ in time. Colour indicates the amplitude of $\bar{P}_{\mathrm{b}}^{+}(\bar{y}, \bar{t})$. D,H) Probability density functions in the upper cortex at two instances of time. Solid line: $\bar{t} = \bar{t}_{\min}$, when the spindle pole is at $\bar{z} = 0$ and moving toward its minimum value ($\bar{z}_{\bar{t}} < 0$). Dotted line: $\bar{t} = \bar{t}_{\max}$, when the spindle pole is at $\bar{z} = 0$ and moving toward its maximum value ($\bar{z}_{\bar{t}} > 0$). The peak widths depend on the magnitude of the diffusion parameters $\beta^{\frac{1}{2}}$ and $\alpha^{\frac{1}{2}}$. H) The three regions used to reduce the system of ODEs to PDEs in Section 5.5 are indicated by roman numerals I, II, and III. The behaviour of the probability density functions in the lower cortex are in antiphase to the behaviour seen here. Solutions were obtained using parameters $K = 5 \times 10^{-2}$, $\bar{\omega}_{\mathrm{on}} = 3 \times 10^{-3}$, $N = 25$, $\gamma = 2$, $\bar{\omega}_0 = 1 \times 10^{-3}$, $\bar{\xi} = 6.25 \times 10^{-1}$. A-D) $\alpha = 8 \times 10^{-2}$ and $\beta = 4 \times 10^{-2}$, E-H) $\alpha = 8 \times 10^{-3}$ and $\beta = 4 \times 10^{-3}$.

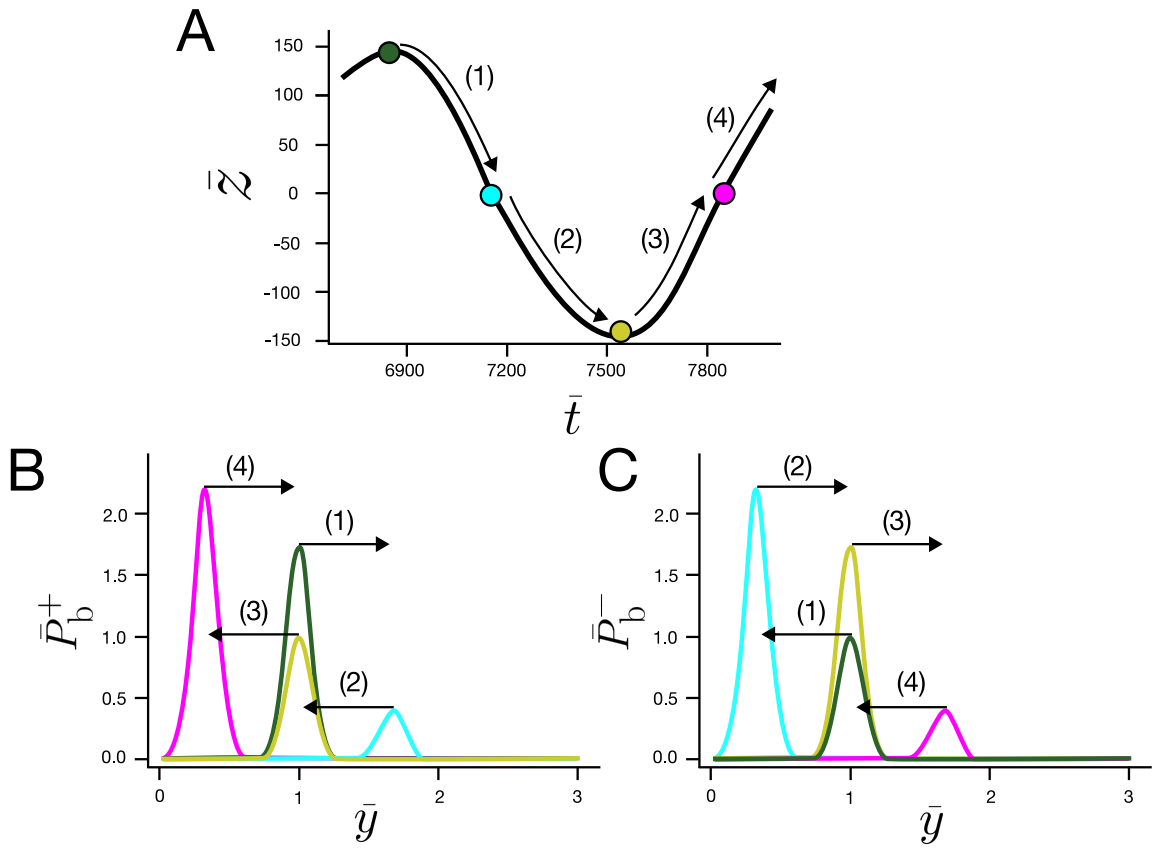

Figure 4.9. **Dynamics of bound probabilities in the upper and lower cortex ($\bar{P}_{\mathrm{b}}^{\pm}$) through one whole cycle of spindle pole oscillation.** A) Example oscillation of $\bar{z}$. Plotted points denote key time points used in the bound probabilities in the B) upper and C) lower cortex. Colours of lines in B) and C) correspond to time points indicated in A). Parameters: $K = 5 \times 10^{-2}$, $\bar{\omega}_{\mathrm{on}} = 3 \times 10^{-3}$, $N = 45$, $\gamma = 2$, $\bar{\omega}_0 = 1 \times 10^{-3}$, $\bar{\xi} = 6.25 \times 10^{-1}$. A-D) $\alpha = 8 \times 10^{-3}$ and $\beta = 4 \times 10^{-3}$

rate $\bar{\omega}_0 e^{\gamma \bar{y}}$. In the lower cortex, $\bar{y}_{\mathrm{c}}$ decreases as $\bar{v}_{\mathrm{b}}^{-}$ is decreased. More generators bind to the microtubule as $\bar{\omega}_0 e^{\gamma \bar{y}}$ has reduced relative to $\bar{\omega}_{\mathrm{on}}$. As the spindle pole passes through $\bar{z} = 0$, the only forces acting on the pole are the pulling forces by the cortical force generators, which are larger in the lower cortex due to the decreased unbinding.

2. **Spindle passing through its maximum velocity, toward the lower cortex (2)**. As the spindle passes through the fastest point of its oscillation $\bar{z}_{\bar{t}}^{\max}$, there is a greater probability of force generators in the lower cortex being bound to a microtubule than in the upper cortex ($\bar{P}_{\mathrm{b}}^{+,\max} < \bar{P}_{\mathrm{b}}^{-,\max}$). This is due to the increased unbinding rate when the generators are extended. Motion toward the lower cortex once the spindle passes $\bar{z} = 0$ is slowed by an increasing restoring force as the $-K\bar{z}$ term in (4.32) becomes positive. This in turn shifts $\bar{v}^{+}(\bar{y})$ such that $\bar{y}_{\mathrm{c}}^{+}$ is reduced toward $\bar{y}_{\mathrm{c}}^{+} = 1$, while $\bar{v}^{-}(\bar{y})$ is shifted such that $\bar{y}_{\mathrm{c}}^{-}$ is increased toward $\bar{y}_{\mathrm{c}}^{-} = 1$. The probability peak $\bar{P}_{\mathrm{b}}^{-}$ begins to decline as $\bar{y}_{\mathrm{c}}^{-}$ increases, due to the increase in $\bar{\omega}_0 e^{\gamma \bar{y}_{\mathrm{c}}^{-}}$. The upper cortex is likely to host more bound generators as $\bar{\omega}_0 e^{\gamma \bar{y}_{\mathrm{c}}^{+}}$ decreases relative to $\bar{\omega}_{\mathrm{on}}$.

3. **Spindle moving away from the lower cortex (3)**. Phase 3 mirrors Phase 1, with the behaviour of $\bar{P}_{\mathrm{b}}^{+}$ and $\bar{P}_{\mathrm{b}}^{-}$ reversed. The probability of bound generators in the lower cortex now decreases below that of the the upper cortex as the spindle approaches the centre of its oscillation.

4. **Spindle passing through the centre of its oscillating range, toward the upper cortex (4)**. This is as in Phase 2, again with the behaviour of $\bar{P}_{\mathrm{b}}^{+}$ and $\bar{P}_{\mathrm{b}}^{-}$ reversed.

In total, this can be described as a history-dependent effect on the amplitude of bound probability density $\bar{P}_{\mathrm{b}}^{\pm,\max}$. For example, if the spindle pole is passing through its fastest point of oscillation moving away from the upper cortex then the value of $\bar{P}_{\mathrm{b}}^{+,\max}$ is lower than it is when at its fastest point of oscillation moving towards the upper cortex. This is in contrast to the position of the Gaussian curve described by $\bar{y}_{\mathrm{c}}^{+}$, which is more extended when the spindle pole is moving away from the upper cortex and less extended when the spindle pole is moving towards the upper cortex. These behaviours are the same for $\bar{P}_{\mathrm{b}}^{-,\max}$ and $\bar{y}_{\mathrm{c}}^{-}$ if we consider movement away and then towards the lower cortex. This dependence on the history of the pole position is a result of the extension-sensitive unbinding rate $\bar{\omega}_0 e^{\gamma \bar{y}}$, which reduces $\bar{P}_{\mathrm{b}}^{\pm,\max}$ as $\bar{y}_{\mathrm{c}}^{\pm}$ increases, while the dynamics of the spindle pole directly affect $\bar{y}_{\mathrm{c}}^{\pm}$. This is the same as what we saw for the relationship between the number of bound force generators and their average extension in the stochastic formulation (Figures 4.5B, C, D).

As the general dynamics of the spindle pole have been retained by the Fokker-Planck description, we will now present the effects of varying different parameters in the model.

The effect of varying diffusivity

The diffusive terms α and β have been highlighted as modulators of the width of the peaks of the probability density functions $\bar{P}_{\mathrm{b(u)}}^{\pm}(\bar{y})$. Decreasing the values of α and β by a factor of 10 results in probability density functions which are taller and narrower than for larger values of α and β (Figure 4.8D,H).

In addition, the relative motion of the peaks is also altered. When diffusive terms are reduced, $\bar{P}_{\mathrm{b}}^{+}$ exists within a region of $\bar{y}$ which is spatially separated from $\bar{P}_{\mathrm{u}}^{+}$ at all times (Figure 4.8G, H). If we segment $\bar{y}$ into three distinct regions (I, II and III, where region I is of width $\mathcal{O}\left(\beta^{\frac{1}{2}}\right)$ and encompasses the peak of $\bar{P}_{\mathrm{u}}^{+}$, region III is of width $\mathcal{O}\left(\alpha^{\frac{1}{2}}\right)$ and encompasses the peak of $\bar{P}_{\mathrm{b}}^{+}$, and region II exists between them), then we see that the width of region II remains non-zero throughout the simulation (Figure 4.8H).

As well as modulating the probability density functions, the diffusive terms also affect the resulting dynamics of the spindle pole position. Decreasing α and β acts to increase the period, T, of oscillation (using a periodogram (Section 2.3.1), $T = 890$ increases to $T = 1000$ upon a decrease in α and β by a factor of 10) while decreasing the amplitude of the oscillation (Figure 4.8A, E). Additionally, the oscillations take more time and go through more oscillating cycles to build up to maximum amplitude when α and β are reduced (Figure 4.8A,E). Thus increasing diffusion has the effect of decreasing the period and increasing the amplitude of oscillation.

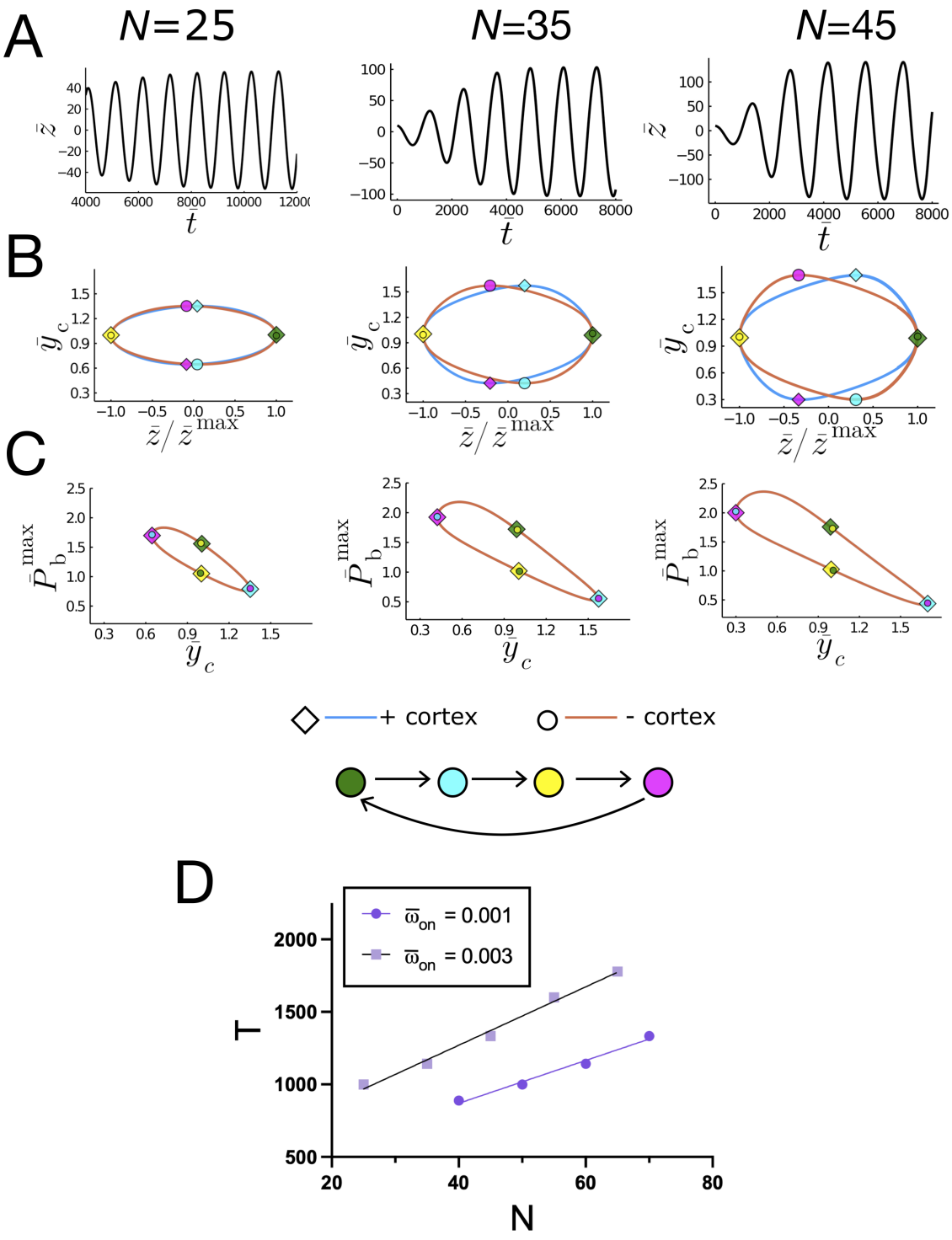

Figure 4.10. **Increasing the number of force generators N available to the system affects the magnitude, period and shape of the oscillations.** A) Spindle pole position $\bar{z}$ in time $\bar{t}$. B) $\bar{y}_c^{\pm}$ as a function of pole position $\bar{z}$. C) Peak $\bar{P}_b^{\pm,\max}$ as a function of $\bar{y}_c^{\pm}$. Line colours correspond to solutions in each cortex (blue = upper, orange = lower). The solution loops are taken from a segment of the solution where a maximum amplitude of spindle pole oscillation has been achieved. All solutions have been truncated to the time shown here for ease of comparison between different N values. D) Period of oscillation T as a function of N, shown for two different values of $\bar{\omega}_{\text{on}}$. Dots correspond to solutions, with the trend given by the line of best fit. Parameters: $K = 5 \times 10^{-2}$, $\bar{\omega}_{\text{on}} = 3 \times 10^{-3}$, $\gamma = 2$, $\bar{\omega}_0 = 1 \times 10^{-3}$, $\bar{\xi} = 6.25 \times 10^{-1}$, $\alpha = 8 \times 10^{-3}$ and $\beta = 4 \times 10^{-3}$

Varying the number of available force generators, N

The number of available force generators, N was shown in Figures 4.5 and 4.6 to impact the quality of the spindle pole oscillations predicted by the stochastic model, with fewer force generators producing noisier oscillations with shorter periods. Varying N in the PDE model also affects the oscillatory dynamics.

Increasing N produces spindle pole oscillations with a larger amplitude and an increased period (Figures 4.10A, D). Decreasing N below a threshold level leads to decaying oscillations (Figure 4.13A below). Interestingly, increasing the binding rate $\bar{\omega}_{\text{on}}$ also increases the period of oscillation for a given N (Figure 4.10D), possibly due to the increase in likelihood that a larger proportion of the force generator population will bind to create a pulling force on the spindle pole when $\bar{\omega}_{\text{on}}$ is increased, resulting in a similar response to increasing N. The period also increases less rapidly as N increases for $\bar{\omega}_{\text{on}} = 0.001$ than $\bar{\omega}_{\text{on}} = 0.003$.

Increasing N also increases the non-linearity of the oscillation, making the structure less sinusoidal, as indicated by the skewed $(\bar{y}_{\text{c}}, \bar{z}/\bar{z}^{\max})$ loops of the upper and lower cortex (Figure 4.10B). As $\bar{y}_{\text{c}}^{\pm} = 1 \mp \bar{z}_{\bar{t}}$, we expect that for $\bar{z}$ a sinusoidal curve in $\bar{t}$, then $(\bar{y}_{\text{c}}, \bar{z}/\bar{z}^{\max})$ would be a symmetric loop centred at $(\bar{z}/\bar{z}^{\max}) = 0$, $\bar{y}_{\text{c}}^{\pm} = 1$. Thus the upper and lower cortex solution loops would overlap perfectly. The skewing of the loops as N increases shows that increasing the number of force generators creates oscillations which tend toward a relaxation oscillation structure. This may be due to the pulling forces becoming the dominant factor in (4.32) for a greater range of the oscillatory path. The spindle pole must be displaced sufficiently far from the centre before $-K\bar{z}$ is large enough to overcome the pulling forces to slow and eventually reverse the spindle pole velocity, resulting in a quick reversal of the spindle pole velocity (fast dynamics) while the path toward the opposite cortex varies more slowly.

The magnitude of the bound probability peaks $\bar{P}_{\text{b}}^{\pm,\max}$ span a wider range as N increases (Figure 4.10C), as do the positions of the peaks $\bar{y}_{\text{c}}^{\pm}$ (Figure 4.10B, C). The positions $\bar{y}_{\text{c}}^{\pm}$ begin to vary quicker at the apices of the spindle oscillation, likely due to the changing $\bar{z}_{\bar{t}}$ term as $\bar{y}_{\text{c}}^{\pm} = 1 \mp \bar{z}_{\bar{t}}$. Then $\bar{P}_{\text{b}}^{\pm,\max}$ also changes due to the relative size of the tension-sensitive off rate compared with the constant on-rate. That is, if the spindle pole is at its maximum displacement near the lower cortex (yellow marker) the changing pole velocity from $\bar{z}_{\bar{t}} < 0$ to $\bar{z}_{\bar{t}} > 0$ will create a net positive motor protein velocity $\bar{v}_{\text{b}}^{-}$ which will increase the extension of the bound force generators, shifting $\bar{y}_{\text{c}}^{-} > 1$ and thus increasing the unbinding rate causing a decrease in $\bar{P}_{\text{b}}^{-,\max}$. On the opposing cortex, the change in direction of the spindle pole will serve to decrease the extensions of the bound force generators due to $\bar{v}_{\text{b}}^{+}$ becoming negative. This will decrease the relative size of the off rate as the force generators are less extended and thus there will be an increase in $\bar{P}_{\text{b}}^{+,\max}$.

Reducing the restoring force results in relaxation oscillations

On the presumption that the emergence of potential relaxation oscillations as the number of force generators N increases is due to the changing ratio of pulling to pushing (centring) forces, we reduce the restoring force ($-K\bar{z}$) in order to shift this balance without increasing pulling forces (Figure 4.11). Decreasing K by two orders of magnitude results in the emergence of relaxation oscillations, characterised by the approximately linear sections of $\bar{z}$ (Figure 4.11A). These linear sections correspond in time with slow phases in the time-evolution of $\bar{P}_{\mathrm{b}}^{\pm}$ (Figure 4.11B) and $\bar{y}_{\mathrm{c}}^{\pm}$ (Figure 4.11C), while the rapid change in the direction of motion of the spindle pole coincides with fast changes in the extension of the force generator bound probability centre $\bar{y}_{\mathrm{c}}^{\pm}$ and amplitude $\bar{P}_{\mathrm{b}}^{\pm}$. $\bar{P}_{\mathrm{b}}^{\pm}$ and $\bar{y}_{\mathrm{c}}^{\pm}$ are reminiscent of the structure of Van der Pol oscillators [215]. Van der Pol oscillations arise from non-linear damping acting upon non-conservative oscillators [216], though the exact combination of terms in the system used in this chapter which create this effect is unclear without further analysis. Non-linear damping works by forcing large amplitude oscillations to decay while amplifying small amplitude oscillations [216]. In this case, large amplitudes in $\bar{P}_{\mathrm{b}}^{\pm}$ and $\bar{y}_{\mathrm{c}}^{\pm}$ are self-limiting by the tension-sensitive on rate, while small amplitude oscillations are amplified by the relative motion of the spindle pole, which can create sharp changes in the dynamics of $\bar{P}_{\mathrm{b}}^{\pm}$ and $\bar{y}_{\mathrm{c}}^{\pm}$ due to the restoring force and coupling to $\bar{y}_{\mathrm{c}}^{\pm}$ by the $\bar{z}_{\bar{t}}$ term in (4.28). We will return to address the origins of relaxation oscillations in Chapter 5.

Recovery of oscillations when N is reduced below the threshold value

Numerically solving the PDE system for a range of values of N and $\bar{\omega}_{\mathrm{on}}$, at a fixed value of $K = 5 \times 10^{-2}$, results in a boundary in (N, $\bar{\omega}_{\mathrm{on}}$) space between oscillatory and non-oscillatory solutions (Figure 4.12). Reduction of the number of force generators, leading to a decrease in pulling forces, results in a cessation of oscillations (Figure 4.12, blue points, and Figure 4.13A). A similar threshold also exists for $\bar{\omega}_{\mathrm{on}}$, with the oscillatory section of parameter space forming a wedge shape bounded by non-oscillatory solutions (Figure 4.12). The lower edge of this boundary can be explained as for large N, smaller binding rates can result in oscillations as there is a sufficiently large number of force generators that may be bound at any given time. As N decreases, the binding rate must also increase to maintain a population of bound force generators sufficiently large to maintain oscillations. Below a threshold value of N (between $N = 20$ and $N = 25$ for this set of parameters), increasing the value of $\bar{\omega}_{\mathrm{on}}$ has no effect as there is insufficient pulling by the force generators available. The upper threshold arises due to the saturation of bound force generators on either side of the spindle pole. This wedge-shaped parameter space has been described previously [80], and the presence of this threshold has been experimentally validated in *C. elegans* embryos [78].

Interestingly, a solution in this parameter space which is shown to be non-oscillatory due to the number of force generators being below threshold (Figure 4.13A) can be pushed back into an oscillatory regime by either increasing the values of the diffusive terms α and β

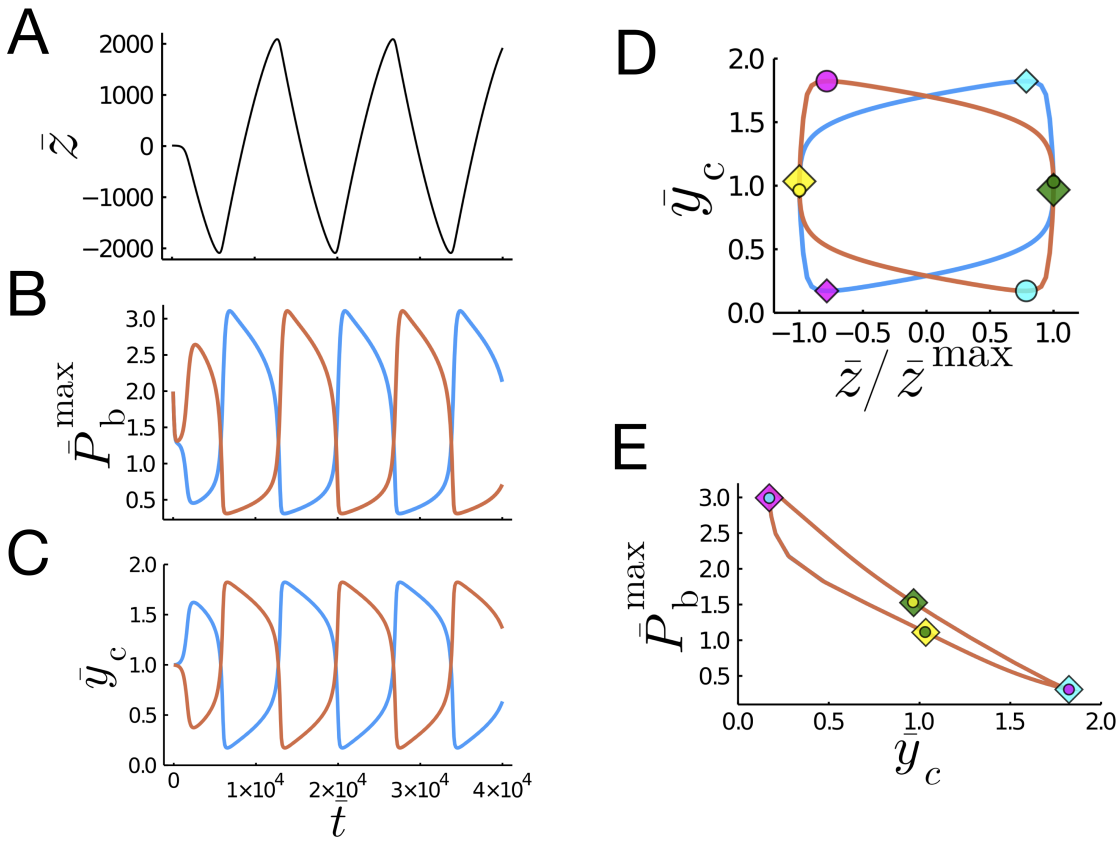

Figure 4.11. **Relaxation oscillations emerge when the restoring force is reduced.** A) Spindle pole position $\bar{z}$ in time $\bar{t}$. B) Peak of the probability density function for bound force generators $\bar{P}_{\mathrm{b}}^{\pm}$ in time $\bar{t}$. C) Central position of the $\bar{P}_{\mathrm{b}}^{\pm}$ peak $\bar{y}_{\mathrm{c}}$ in time $\bar{t}$. D) $\bar{y}_{\mathrm{c}}$ as a function of pole position $\bar{z}$. E) Peak $\bar{P}_{\mathrm{b}}^{\pm,\mathrm{max}}$ as a function of $\bar{y}_{\mathrm{c}}$. Figures A-C) share a time axis. Line colours correspond to solutions in each cortex (blue = upper, orange = lower) Parameters: $K = 5 \times 10^{-4}$,$N = 15$, $\bar{\omega}_{\mathrm{on}} = 3 \times 10^{-3}$, $\gamma = 2$, $\bar{\omega}_0 = 1 \times 10^{-3}$, $\bar{\xi} = 6.25 \times 10^{-1}$, $\alpha = 8 \times 10^{-3}$ and $\beta = 4 \times 10^{-3}$

(Figure 4.13B-D) or decreasing the strength of the restoring force K (Figure 4.13E-G). Increasing the diffusion results in oscillations with a reduced period when compared with the period of the decaying oscillations at the same number of force generators (Figure 4.13A, B). We suggest that the oscillations occurring when diffusion is increased arise from noise in the number of force generators with longer extensions due to the flattening of the bound probability density functions (Figure 4.8D). That is, variability in the extension of the populations of force generators creates enough noise in the system to continuously pull the spindle pole out of the central position, and the restoring force corrects this perturbation such that an oscillation is maintained. This is similar to what we observed in the stochastic model for small values of N (Figure 4.6). If we consider decreasing the restoring force, this allows the pulling forces created by smaller populations of force generators to be sufficiently large to induce spindle pole displacements from the cell centre before the restoring force can begin to act on the spindle pole to re-centre it.

4.3.4 Summary of the Fokker-Planck analysis

The Fokker-Planck system described in this section was used to explore the effects of varying parameters in this model description of spindle pole positioning. The populations of

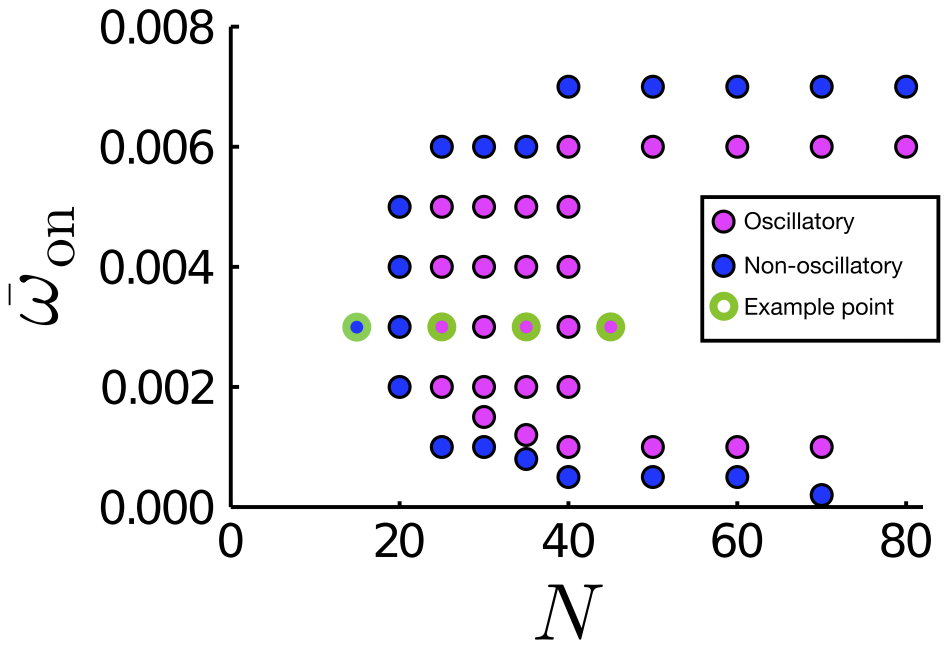

Figure 4.12. **Stability boundary between oscillatory and non-oscillatory solutions.** Numerically solving the Fokker-Planck system reveals the boundary in $(N, \bar{\omega}_{\text{on}})$ space which separates oscillatory from non-oscillatory solutions. Each scatter point represents a numerical solution, labelled in magenta if the spindle pole has sustained oscillations and blue if the spindle pole position decayed to $z = 0$ (non-oscillatory). The points with green boundaries are the example solutions used throughout this chapter. Parameters: $K = 5 \times 10^{-2}$, $\gamma = 2$, $\bar{\omega}_0 = 1 \times 10^{-3}$, $\bar{\xi} = 6.25 \times 10^{-1}$, $\alpha = 8 \times 10^{-3}$ and $\beta = 4 \times 10^{-3}$.

force generators were described in terms of their probability density functions of binding and unbinding at varying extensions of their elastic linkers. This description showed oscillatory dynamics in the amplitude of the peaks of the probability distributions, coupled with their most likely linker extension. Both the peak value $\bar{P}_{\text{b}}^{\pm}$ and central extension value $\bar{y}_{\text{c}}^{\pm}$ showed a hysteresis effect due to the extension-sensitive unbinding rate $\bar{\omega}_0 e^{\gamma \bar{y}}$ which matched what was seen in the stochastic model. Decreasing the diffusive terms reduced the width of the peaks of the probability density functions but increased the period of oscillation and decreased the amplitude of oscillation. Perturbing the balance of restoring to pulling forces by either increasing N or decreasing K resulted in oscillations with increased periods and amplitudes. Significantly increasing N and reducing K both lead to relaxation oscillations, characterised by slow phases where pulling forces dominate the movement of the spindle pole, and fast phases where the restoring forces become sufficiently large to change the direction of motion of the spindle pole. Increasing diffusive terms and reducing the restoring force are both sufficient to restore oscillations for small N, moving the threshold of N required to induce oscillations.

4.4 Discussion of Chapter 4

In this chapter we characterised the 1D system of pulling and pushing forces acting on the spindle pole to create a dynamic spindle pole response. Our aim was to establish a base

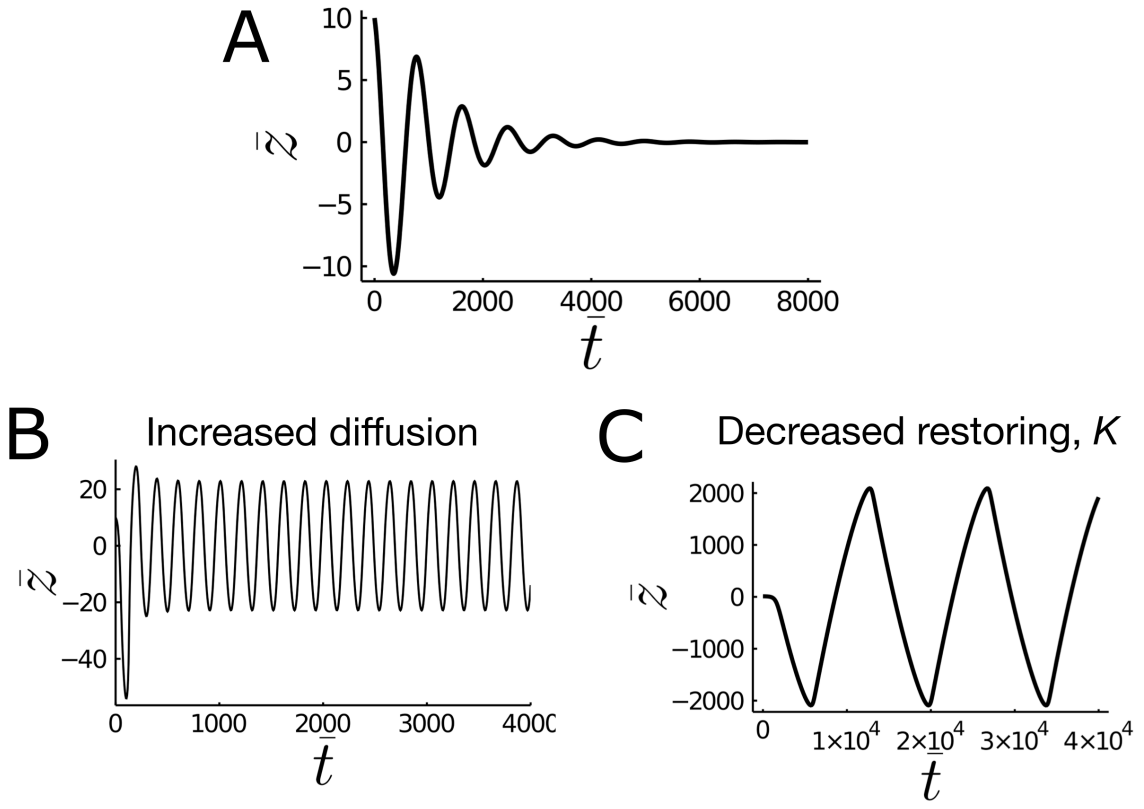

Figure 4.13. **Non-oscillating spindles may become oscillatory for higher diffusion and lower restoring forces.** Spindle pole position $\bar{z}$ in time $\bar{t}$ for $N = 15$ A) $\alpha = 8 \times 10^{-3}$, $\beta = 4 \times 10^{-3}$ and $K = 5 \times 10^{-2}$; B) $\alpha = 8 \times 10^{-1}$, $\beta = 4 \times 10^{-1}$ and $K = 5 \times 10^{-2}$; C) $\alpha = 8 \times 10^{-3}$, $\beta = 4 \times 10^{-3}$ and $K = 5 \times 10^{-4}$. Constant parameters: $\bar{\omega}_{\text{on}} = 3 \times 10^{-3}$, $\gamma = 2$, $\bar{\omega}_0 = 1 \times 10^{-3}$, and $\bar{\xi} = 6.25 \times 10^{-1}$.

system from which we could explore the factors affecting spindle positioning, with the ultimate goal of being able to recapitulate the spindle dynamics seen *in vivo*. In particular, we aimed to determine the main factors promoting the emergence of oscillations in the angle of the mitotic spindle, and the dynamic repositioning of the spindle toward the cell centre seen experimentally (Chapter 3). In this summary we will recap the features of the mathematical systems we have explored and also justify the model choice with respect to the literature. We postpone direct discussion of the implications of the model with respect to our experimental results until Chapter 6, after we have more fully investigated the mathematical system using a lower-order mathematical model (Chapter 5).

The system this chapter explores is that developed by Grill *et al.* (2005) to describe the oscillations of the posterior pole of the dividing single cell *C. elegans* embryo [80]. The Grill *at al.* (2005) system was chosen as it describes dynamic movements of the spindle pole, while incorporating slip-bond behaviour of dynein [61] as well as restoring forces by microtubules [133], [137]. We described the system using a stochastic model which we implemented using a Gillespie algorithm and a Fokker-Planck description. While Grill *et al.* (2005) show a result from a stochastic simulation, the simulation detail is ommitted from their description [80]. Further, the Fokker-Planck description in [80] was simplified by assuming that the probability distribution relaxed instantaneously to $P_{\text{u}}^{\pm} = A\,(t)\,e^{-y^2}$, where $A\,(t)$ is the amplitude of the Gaussian curve centred about $y = 0$. While our analysis of the full Fokker-Planck equations confirmed that $\bar{P}_{\text{u}}^{\pm}$ relaxed to $\bar{y} = 0$ (Figure 4.8B,G,D,H),

this result was not obvious. Indeed, our initial solutions of the problem showed a $\bar{P}_{\mathrm{u}}^{\pm}$ which was dynamic in $\bar{y}$ (data not shown), though a more careful estimation of ν using Stokes' law eradicated these dynamics. In general, the results presented in [80] were restricted to a very narrow set of parameters, thus exploration of the dynamics of the system from stochastic simulations through to the Fokker-Planck equations was required for proper analysis of the system.

The Gillespie algorithm chosen has both advantages and disadvantages. Notably, a large amount of computational power is needed to run different realisations of the model, and the scale of the model and the number of autonomous agents within it provide further burden to the cost of computation. In the case of this work, the problems highlighted in Section 4.2.3 limited our ability to fully explore the parameter landscape in a timely manner. A number of methods of increasing efficiency were explored (Section 4.2.4) but the highly coupled nature of the problem prevented a straightforward implementation of a known algorithm. Instead, we created a system-specific optimisation that allowed us to produce simulations of a sensible duration, though the scope of our parameter exploration was limited. We were restricted to simulations with small numbers of force generators N, while diffusive terms α, β could not be decreased significantly. We used the stochastic model to confirm the behaviours we expected from the simulations before describing the system using a PDE formulation. We then used the PDE Fokker-Planck description to more fully explore the impact of varying parameters.

Both the Gillespie and the Fokker-Planck formulations of this system resulted in oscillations in the position of the spindle pole, with coordinated dynamics between the spindle position and the populations of force generators in the upper and lower cortices. The number of bound force generators oscillates with the average extension of the elastic linker due to the effect of tension-sensitive unbinding, where more elongated linkers are under more net tension and thus the motor protein head dissociates from the microtubule. This oscillation is in anti-phase to the oscillation of the opposing population due to their coupling through the connection to the spindle pole (Figure 4.5D and Figure 4.2). Here the comparison with the PDEs has been drawn by describing the number of bound force generators with extended elastic linkers as a probability density function of a force generator being bound with elastic linker length $\bar{y}^{\pm}$.

The stochastic simulations show that coherent oscillations are reduced for increased restoring forces (by the increase of K) and decreasing pulling forces (by the reduction of N). Using values of N=15 and N=5 force generators per cortex produced simulations which displayed collective population dynamics from which spontaneous oscillations of the spindle pole emerged. As the number of force generators was decreased, the amplitude and period of the oscillations also decreased. By re-dimensionalising the data by $t = \bar{t}/\mu$ and $z = \bar{z}v_0/\mu$, with $v_0 = 1.8 \times 10^{-6}$ ms^{-1} and $\mu = 50$ s^{-1}, a period of $T(N = 15) \approx 18$ s was returned with a range of $z^{\max} - z^{\min} \approx 7$ μm. This oscillatory range and period is similar to the oscillatory range seen in the *C. elegans* first cell division spindle oscillation *in vivo*, where an oscillatory period of the posterior pole of 19.6 ± 3.0 s has been measured

[78]. This period is much shorter than what was measured experimentally in the cells of the *Xenopus laevis* animal cap (Figure 3.10B). The parameters we used were chosen to be those used by Grill *et al.* (2005) in their development of this mathematical system, as we were unable to confidently obtain estimations for all parameters specific to *Xenopus*. As our initial aim was to explore the system described by Grill *et al.* (2005), we prioritised creating a working model which we could directly compare to the results they reported, such that we could confirm that our interpretation aligned with theirs [80]. As such, the quantitative results presented here are tuned to *C. elegans* rather than the *Xenopus* system specifically, but we expect the behaviour of the model to remain the same. Indeed, by exploring the model in different regions of parameter space, we are well placed to estimate where in parameter space our experimental system may lie.

Removal of the tension sensitivity of the unbinding rate γ also leads to a loss of oscillations (Figure 4.7A). Altering these same factors in the Fokker-Planck description results in similar effects, where decreasing restoring forces promotes oscillations (Figure 4.13) and decreasing the number of force generators results in the cessation of oscillations (Figure 4.13). Numerically solving the PDE system for a range of values in $(N, \bar{\omega}_{\text{on}})$ space reveals a boundary between oscillatory and non-oscillatory solutions, as was reported by Grill *et al.* (2005) [80]. Our analysis of the PDEs suggests that this boundary is dependent on the diffusivity of the force generators as they try to walk along the microtubule, with diffusion promoting oscillations (Figure 4.13B), and on the restoring force provided by the microtubules (Figure 4.13C).

It was highlighted by the PDE model that altering the diffusion terms α and β had an effect on the resulting dynamics of the spindle pole. Increasing the diffusion parameters both decreased the period of oscillation of the spindle pole and increased the amplitude of the resulting oscillations. The promotion of oscillations as the diffusive terms α and β are increased is of interest to us due to the inherent noise in biological processes [217]. The diffusive terms represent noise in the random walk of dynein along microtubules, so that increased values of α and β represent an increase in deviation from the directed movement of the bound force generator. That is, we expect a bound force generator under no external loading to have a positive velocity along the microtubule leading to an extension of the elastic linker, but increasing α increases the likelihood of this bound generator to erroneously slip backwards along the microtubule or stay in the same place rather than move forward. Increasing α represents an imperfect system due to variations in the environment of the force generators that we cannot account for explicitly. This dependence of oscillation on the diffusivity parameters could explain why oscillations were still present in the stochastic simulations as N was decreased below the threshold for oscillation identified using the Fokker-Planck equations (where α and β were reduced) (Figure 4.5 shows oscillations at $N = 15$ in the stochastic simulations, despite being outside of the oscillatory solution region in Figure 4.12). However, we note that the oscillatory region determined was for a value of α and β a factor of 10 smaller than what was used in the stochastic simulations, as smaller values of α, β decreased the value of $\Delta\bar{y}$ required to produce stochastic simula-

tions thus making computation too expensive to generate simulations of sufficient timespan.

Comparison of the Fokker-Planck solutions with the stochastic simulations for the same choice of parameters, though with α and β an order of 10 smaller for the Fokker-Planck system, showed periods of $T^{\mathrm{FP}} \approx 16$ s vs $T^{\mathrm{G}} \approx 18$ s. Thus a 1.1-fold increase in the oscillation period using the Fokker-Planck equations. However, this comparison is not perfect, as the oscillations of the Fokker-Planck model were decaying (Figure 4.13A), though stochastic simulations with larger numbers of force generators for a more direct comparison were not feasible.

The range of the centre peak extension $\bar{y}_{\mathrm{c}}^{\pm}$ was narrower when compared with $\langle \bar{y}_{\mathrm{b}}^{\pm} \rangle$. The stochastic simulations show an average extension $0 \lesssim \langle \bar{y}_{\mathrm{b}}^{\pm} \rangle \lesssim 2$ when $N = 15$, while the Fokker-Planck equations required $N = 45$ before showing a similar range at small α, β. Thus we conclude that the Fokker-Planck description maintains characteristics of the solutions to the stochastic simulations, such as appropriately shaped limit cycles and dynamics of the bound force generators vs their extension lengths, however oscillations are promoted more readily and with a greater amplitude in Gillespie simulations. As we saw more similar results between the two descriptions when α, β were reduced in the Fokker-Planck formulation, we conclude that increased demographic noise at small values of N promote oscillatory dynamics.

By using the Fokker-Planck description to explore the system in regions of parameter space where simulations were computationally expensive, we discovered the emergence of relaxation oscillations as the restoring force parameter K was reduced (Figure 4.11). The resulting linear sections of the spindle pole oscillation correspond in time with slow phases in the time-evolution of $\bar{P}_{\mathrm{b}}^{\pm}$ and $\bar{y}_{\mathrm{c}}^{\pm}$ (Figure 4.11B, C), until the spindle pole is sufficiently displaced from the centre for the restoring force to create a rapid reversal in the spindle pole velocity $\bar{z}_{\mathrm{t}}$. This change in the spindle pole velocity results in a rapid increase in the value of $\bar{y}_{\mathrm{c}}$ on the opposite cortex, which in turn creates a rapid decrease in the value of $\bar{P}_{\mathrm{b}}^{\pm}$ due to the tension-sensitivity of the unbinding rate. The fast and slow phases of $\bar{P}_{\mathrm{b}}^{\pm}$ and $\bar{y}_{\mathrm{c}}$ in time give them the structure of Van der Pol oscillators, where their amplitudes are self-limited by the tension-sensitive unbinding and amplified by their connection to the motion of the spindle pole.

The stiffness of the microtubule, k_{MT} affects the parameter K linearly, thus changing K by two orders of magnitude is equivalent to changing the microtubule stiffness by two orders of magnitude. Alternatively, K may be decreased by increasing the stiffness of the elastic linker connecting the force generator to the cell cortex, k_{g}. We first focus on the stiffness due to the properties of the microtubule array. Here that force comes from the microtubule pressing against the cortex as the spindle moves towards it, due to bending and also due to dynamic instability of the microtubule array. Microtubules have a high flexural rigidity and may be considered as relatively rigid structures over the length-scale of a typical cell [133]–[135]. The baseline microtubule stiffness $k_{\mathrm{MT}} = 4 \times 10^{-6}$ Nm^{-1} was chosen to match that used previously [80] and was also corroborated as an appropriate order of magnitude in a

study into microtubule elasticity [135]. However, the mathematical model in [135] calculated the effective elastic stiffness by considering interpolar and kinetochore microtubules which make up the main body of the spindle (Figure 1.3A). These microtubules are bundled together by crosslinking proteins [218] where strong crosslinking increases the flexural rigidity of the bundle like N_{MT}^2, where N_{MT} is the number of microtubules which make up the bundle. In the calculation for the bending stiffness the bundles are assumed to be highly crosslinked sets of N_{MT}=10. The flexural rigidity of weakly crosslinked bundles are assumed to scale like N_{MT}, which would decrease the estimation of flexural rigidity and thus the elastic stiffness by a factor of $\mathcal{O}(10)$. Similarly, decreasing the number of microtubules present in the bundle would decrease the elastic stiffness due to the dependence upon N_{MT}. If astral microtubules are less bundled than the interpolar and kinetochore microtubules it follows that the microtubule stiffness chosen here could be an overestimation of a factor of 10-100. Additionally, the behaviour of the microtubule at the spindle pole can affect the restoring force [135], [137]. If the microtubule is allowed to hinge at the spindle pole, then the resulting effect on the critical buckling force results in a decreased restoring force provided by the microtubule [135], [137]. As such we expect perturbations to the scaffolding of the spindle pole by depletion of NuMA to reduce the restoring force provided by the microtubules.

The analysis in this chapter has confirmed that this model system may be used to describe dynamic movements of the spindle pole, and the main characteristics promoting oscillation are maintained when moving from stochastic simulations to a Fokker-Planck description of the model. We will now further reduce the Fokker-Planck equations into a lower order model to further probe the behaviour of the system without incurring the cost of numerous numerical simulations. This lower order model also has the advantage that it will be more readily expanded into 2D.

Chapter 5

Lower order models of spindle pole movements estimate amplitudes and periods of spindle pole oscillation

5.1 Introduction

The model of spindle movements as a result of cortical pulling and restoring forces has now been described using stochastic simulations (Section 4.2) and the Fokker-Planck equations (Section 4.3). Both methods reveal the emergence of established oscillations as the number of force generators increases, with the balance of restoring and pulling forces also being key players in the resulting spindle dynamics. The Fokker-Planck description suggests areas of parameter space where oscillations exist, and also areas where oscillations cannot be sustained. In this chapter, features of the model in different regions of parameter space will be explored and assumptions on the scale of various parameters will be made in order to reduce the PDEs to a smaller system of ordinary differential equations (ODEs), while keeping the main features of the full description intact.

When diffusivity terms are small, the PDEs reveal distinct regions of $\bar{y}$ space where the probability density functions $\bar{P}_{\mathrm{u}}^{\pm}$ and $\bar{P}_{\mathrm{b}}^{\pm}$ have most of their mass (Figure 4.8H). While varying the diffusive terms also has an impact on the oscillations, with larger diffusive terms promoting oscillations (Figure 4.13B), the amplitudes and periods of the more and less diffusive solutions are still of a similar order. As such, we now pursue the behaviour of the model with lower diffusivity to create a system of ODEs. In contrast to the *ad hoc* model reduction proposed by Grill *et al.* (2005), [80], here the Fokker-Planck system is reduced to ODEs using systematic asymptotic analysis. The model reduction implemented by Grill *et al.* (2005) is only very briefly described, with the bound probability density function replaced with an estimated typical linker length. The two populations of force generators are also lost from the discussion, described only in terms of a single population [80]. As the path from the Fokker-Planck description of the system to the ODEs is unclear, the coupling between the two populations of force generators and the spindle pole also becomes unclear. As such, our rigorous reduction to ODEs provides us with a solid basis from which to build upon and extend to 2D (Appendix A), as the results in terms of spindle pole dynamics and

individual force generator population dynamics are retained throughout the stochastic and deterministic descriptions.

Stability analysis is used to determine the factors which promote oscillations, while a further simplification of the system in the limit of small restoring forces reveals the structure of relaxation oscillations and provides an estimate of oscillation amplitude.

5.2 Systematically reducing the Fokker-Planck equations into ODEs

To reduce the Fokker-Planck model to a system of ODEs, it helps to rescale using the motor protein to microtubule binding rate, writing $\bar{t} = \tilde{t}/\bar{\omega}_{\text{on}}$ and $\bar{z} = \tilde{z}/\bar{\omega}_{\text{on}}$. Then (4.32) becomes

$$\bar{\xi}\tilde{z}_{\tilde{t}} = -\frac{K}{\bar{\omega}_{\text{on}}}\tilde{z} - N\left(\int_0^{\bar{y}_{\max}} \bar{y}\bar{P}_{\text{b}}^{-}\,\mathrm{d}\bar{y} - \int_0^{\bar{y}_{\max}} \bar{y}\bar{P}_{\text{b}}^{+}\,\mathrm{d}\bar{y}\right) \tag{5.1}$$

and (4.25a), (4.25b) similarly become

$$\bar{\omega}_{\text{on}}\bar{P}^{\pm}_{\text{b},\tilde{t}} + \bar{J}^{\pm}_{\text{b},\bar{y}} = \bar{\omega}_{\text{on}}\bar{P}^{\pm}_{\text{u}} - \bar{\omega}_0 e^{\gamma\bar{y}}\bar{P}^{\pm}_{\text{b}} \tag{5.2}$$

$$\bar{\omega}_{\text{on}}\bar{P}^{\pm}_{\text{u},\tilde{t}} + \bar{J}^{\pm}_{\text{u},\bar{y}} = -\bar{\omega}_{\text{on}}\bar{P}^{\pm}_{\text{u}} + \bar{\omega}_0 e^{\gamma\bar{y}}\bar{P}^{\pm}_{\text{b}}. \tag{5.3}$$

The intention is to develop an approximation to the oscillating spindle system for which $\bar{\omega}_{\text{on}} \sim \bar{\omega}_0 \sim \alpha^{1/2} \sim \beta^{1/2} \ll 1$. To minimise the introduction of further notation, we expand our solutions in terms of the small order parameter $\bar{\omega}_{\text{on}}$ and remain mindful moving forward that these parameters are of similar order. Consider the range of extension values $\bar{y}$ as being split into three regions (Figure 4.8H): region I over which $\bar{P}^{\pm}_{\text{u}}$ is peaked around $\bar{y} = 0$ with a width $\beta^{1/2}$; region III over which $\bar{P}^{\pm}_{\text{b}}$ is peaked with a width of $\alpha^{1/2}$ but whose centre moves as $\bar{y}_{\text{c}} = 1 \mp \tilde{z}_{\tilde{t}}$; and region II where advective terms dominate and the asymptotic limits of I and III are matched.

Solutions for $\bar{P}^{\pm}_{\text{u}}$ and $\bar{P}^{\pm}_{\text{b}}$ will be determined in regions I and III respectively, followed by matching their asymptotic limits in region II to reveal the ODE system which governs the time evolution of the parameters.

5.2.1 Region I

In Region I, we seek solutions $\bar{P}^{\pm}_{\text{u}} \sim \bar{P}^{\pm}_{\text{u0}} + \bar{\omega}_{\text{on}}\bar{P}^{\pm}_{\text{u1}} + ...$ where $\bar{P}^{\pm}_{\text{u0}}$ is a quasi-static solution whose shape is static but whose amplitude varies slowly in time, and $\bar{\omega}_{\text{on}}$ is a small parameter. Assume further that $\bar{P}^{\pm}_{\text{b}} \sim \bar{\omega}_{\text{on}}$ in this region (Figure 4.8H). Here, it is observed that $\bar{P}^{\pm}_{\text{u}}$ is sharply peaked about $\bar{y} = 0$ over a diffusive length-scale $\beta^{\frac{1}{2}}$ (Figure 4.8H). Thus, setting $\bar{y} = \beta^{\frac{1}{2}}Y$ in (5.3) gives

$$\bar{\omega}_{\text{on}}\bar{P}^{\pm}_{\text{u},\tilde{t}} - \Gamma\left(Y\bar{P}^{\pm}_{\text{u}} + \bar{P}^{\pm}_{\text{u},Y}\right)_Y = -\bar{\omega}_{\text{on}}\bar{P}^{\pm}_{\text{u}} + \bar{\omega}_0 e^{\left(\gamma\beta^{1/2}Y\right)}\bar{P}^{\pm}_{\text{b}} \tag{5.4}$$

with the boundary condition $\bar{J}_{\mathrm{u}}^{\pm}\left(\tilde{t},0\right)=0$. This boundary condition therefore becomes

$$\bar{J}_{\mathrm{u0}}^{\pm}\left(\tilde{t},0\right)+\bar{\omega}_{\mathrm{on}}\bar{J}_{\mathrm{u1}}^{\pm}\left(\tilde{t},0\right)=0 \tag{5.5}$$

where

$$\bar{J}_{\mathrm{u0}}^{\pm}=-\beta^{1/2}\Gamma\left(Y\bar{P}_{\mathrm{u0}}^{\pm}+\bar{P}_{\mathrm{u0},Y}^{\pm}\right), \tag{5.6a}$$
$$\bar{J}_{\mathrm{u1}}^{\pm}=-\beta^{1/2}\Gamma\left(Y\bar{P}_{\mathrm{u1}}^{\pm}+\bar{P}_{\mathrm{u1},Y}^{\pm}\right), \tag{5.6b}$$

which are both individually zero at $Y=0$ due to (5.5). To leading order in $\bar{\omega}_{\mathrm{on}}$, (5.4) becomes

$$\Gamma\left(Y\bar{P}_{\mathrm{u0}}^{\pm}+\bar{P}_{\mathrm{u0},Y}^{\pm}\right)_{Y}=0 \tag{5.7}$$

which may be integrated to give

$$\Gamma\left[Y\bar{P}_{\mathrm{u0}}^{\pm}+\bar{P}_{\mathrm{u0},Y}^{\pm}\right]_{0}^{Y}=0. \tag{5.8}$$

Thus, due to boundary condition (5.5),

$$Y\bar{P}_{\mathrm{u0}}^{\pm}+\bar{P}_{\mathrm{u0},Y}^{\pm}=0, \tag{5.9}$$

(5.8) gives

$$\bar{P}_{\mathrm{u0}}^{\pm}=A^{\pm}(\tilde{t})e^{-\frac{1}{2}Y^{2}} \tag{5.10}$$

as a solution, with $A^{\pm}\left(\tilde{t}\right)$ an amplitude which varies slowly in time.

At $\mathcal{O}\left(\bar{\omega}_{\mathrm{on}}\right)$, equation (5.4) becomes

$$\Gamma\left(Y\bar{P}_{\mathrm{u1}}^{\pm}+\bar{P}_{\mathrm{u1},Y}^{\pm}\right)_{Y}=\bar{P}_{\mathrm{u0},\tilde{t}}^{\pm}+\bar{P}_{\mathrm{u0}}^{\pm}. \tag{5.11}$$

We highlight here the absence of the $\bar{\omega}_{0}e^{\gamma\bar{y}}\bar{P}_{\mathrm{b}}^{\pm}$ term as we have assumed that $\bar{P}_{\mathrm{b}}^{\pm}\sim\bar{\omega}_{\mathrm{on}}$ in this region. Then (5.11) may be integrated to

$$\Gamma\left[Y\bar{P}_{\mathrm{u1}}^{\pm}+\bar{P}_{\mathrm{u1},Y}^{\pm}\right]_{0}^{Y}=\int_{0}^{Y}\left(A_{\tilde{t}}^{\pm}+A^{\pm}\right)e^{-\frac{1}{2}Y^{2}}\mathrm{d}Y \tag{5.12}$$

using the boundary conditions on flux (5.5) at $Y=0$. As the $Y\bar{P}_{\mathrm{u1}}^{\pm}$ term will dominate the left-hand side as $Y\to\infty$, we may write

$$\begin{aligned}\Gamma Y\bar{P}_{\mathrm{u1}}^{\pm}&\approx\int_{0}^{\infty}\left(\left(A_{\tilde{t}}^{\pm}+A^{\pm}\right)e^{-\frac{1}{2}Y^{2}}\right)\mathrm{d}Y\\&=\left(A_{\tilde{t}}^{\pm}+A^{\pm}\right)\sqrt{\frac{\pi}{2}}.\end{aligned} \tag{5.13}$$

Then,

$$\bar{P}_{\mathrm{u1}}^{\pm}\approx\frac{1}{\Gamma Y}\left(A_{\tilde{t}}^{\pm}+A^{\pm}\right)\sqrt{\frac{\pi}{2}},\qquad\left(Y\gg1\right). \tag{5.14}$$

Re-substitution of $Y = \beta^{-\frac{1}{2}}\bar{y}$ gives

$$\bar{P}^{\pm}_{\mathrm{u1}} \approx \frac{1}{\Gamma\bar{y}}\left(A^{\pm}_{\tilde{t}} + A^{\pm}\right)\sqrt{\frac{\pi\beta}{2}} \tag{5.15}$$

when $\beta^{1/2} \ll \bar{y}$.

Now that we have an expression for how the shape of the unbound force generator probability density function varies in time in region I, we go on to seek similar solutions for the bound generator probability density function in region III.

5.2.2 Region III

In region III we seek solutions of the form $\bar{P}^{\pm}_{\mathrm{b}} \sim \bar{P}^{\pm}_{\mathrm{b0}} + \bar{\omega}_{\mathrm{on}}\bar{P}^{\pm}_{\mathrm{b1}} + ...$ Here, the probability density function $\bar{P}^{\pm}_{\mathrm{b}}$ is sharply peaked about $\bar{y}_{\mathrm{c}} = 1 \mp \tilde{z}_{\tilde{t}}$ over a diffusive length-scale $\alpha^{\frac{1}{2}}$ (Figure 4.8H). Both $\alpha^{1/2}$ and $\bar{\omega}_{\mathrm{on}}$ are assumed to be small parameters of similar order. Thus, in this region about the peak of $\bar{P}^{\pm}_{\mathrm{b}}$, we set $\bar{y} = 1 \mp \tilde{z}_{\tilde{t}} + \alpha^{\frac{1}{2}}\hat{Y}$. By the chain rule, $\frac{\partial G\left(\hat{Y},\tilde{t}\right)}{\partial\tilde{t}} = \frac{\mathrm{d}\hat{Y}}{\mathrm{d}\tilde{t}}\frac{\partial G}{\partial\hat{Y}} + \frac{\mathrm{d}\tilde{t}}{\mathrm{d}\tilde{t}}\frac{\partial G}{\partial\tilde{t}}$ for any function of the two variables $\left(\hat{Y},\tilde{t}\right)$, and so

$$\frac{\partial}{\partial\tilde{t}} \to \pm\alpha^{-\frac{1}{2}}\tilde{z}_{\tilde{t}\tilde{t}}\frac{\partial}{\partial\hat{Y}} + \frac{\partial}{\partial\tilde{t}} \tag{5.16}$$

while also

$$\frac{\partial}{\partial\bar{y}} \to \alpha^{-1/2}\frac{\partial}{\partial\hat{Y}} \tag{5.17}$$

and equation (5.2) then becomes

$$\bar{\omega}_{\mathrm{on}}\left(\bar{P}^{\pm}_{\mathrm{b},\tilde{t}} \pm \alpha^{-\frac{1}{2}}\tilde{z}_{\tilde{t}\tilde{t}}\bar{P}^{\pm}_{\mathrm{b},\hat{Y}}\right) + \left(\alpha^{-1/2}\bar{v}^{\pm}_{\mathrm{b}}\bar{P}^{\pm}_{\mathrm{b}} - \bar{P}^{\pm}_{\mathrm{b},\hat{Y}}\right)_{\hat{Y}} = \bar{\omega}_{\mathrm{on}}\bar{P}^{\pm}_{\mathrm{u}} - \bar{\omega}_0 e^{\gamma(1\mp\tilde{z}_{\tilde{t}})}\bar{P}^{\pm}_{\mathrm{b}}. \tag{5.18}$$

Here, the off-rate $\bar{\omega}_{\mathrm{off}} = \bar{\omega}_0 e^{\gamma\left(1\mp\tilde{z}_{\tilde{t}}+\alpha^{1/2}Y\right)} = \bar{\omega}_0 e^{\gamma(1\mp\tilde{z}_{\tilde{t}})}e^{\gamma\alpha^{1/2}Y} \approx \bar{\omega}_0 e^{\gamma(1\mp\tilde{z}_{\tilde{t}})}$ because $\alpha^{1/2}$ is a small parameter. Recalling the expression for $\bar{v}^{\pm}_{\mathrm{b}}$ as given in (4.28) and inputting our expression for $\bar{y}$ in this region, (5.18) may be further simplified to

$$\bar{\omega}_{\mathrm{on}}\left(\bar{P}^{\pm}_{\mathrm{b},\tilde{t}} \pm \alpha^{-\frac{1}{2}}\tilde{z}_{\tilde{t}\tilde{t}}\bar{P}^{\pm}_{\mathrm{b},\hat{Y}}\right) - \left(\hat{Y}\bar{P}^{\pm}_{\mathrm{b}} - \bar{P}^{\pm}_{\mathrm{b},\hat{Y}}\right)_{\hat{Y}} = \bar{\omega}_{\mathrm{on}}\bar{P}^{\pm}_{\mathrm{u}} - \bar{\omega}_0 e^{\gamma(1\mp\tilde{z}_{\tilde{t}})}\bar{P}^{\pm}_{\mathrm{b}}. \tag{5.19}$$

Substituting the expansion $\bar{P}^{\pm}_{\mathrm{b}} \approx \bar{P}^{\pm}_{\mathrm{b0}} + \bar{\omega}_{\mathrm{on}}\bar{P}^{\pm}_{\mathrm{b1}} + ...$, then to first order (5.19) becomes

$$\left(\left(\hat{Y} \mp \bar{\omega}_{\mathrm{on}}\alpha^{-\frac{1}{2}}\tilde{z}_{\tilde{t}\tilde{t}}\right)\bar{P}^{\pm}_{\mathrm{b0}} - \bar{P}^{\pm}_{\mathrm{b0},\hat{Y}}\right)_{\bar{Y}} = 0 \tag{5.20}$$

where $\frac{\bar{\omega}_{\mathrm{on}}}{\alpha^{1/2}} = \mathcal{O}(1)$ has been used. By integration,

$$\left(\bar{Y} \mp \bar{\omega}_{\mathrm{on}}\alpha^{-\frac{1}{2}}\tilde{z}_{\tilde{t}\tilde{t}}\right)\bar{P}^{\pm}_{\mathrm{b0}} - \bar{P}^{\pm}_{\mathrm{b0},\bar{Y}} = C\left(\tilde{t}\right) \tag{5.21}$$

for $C\left(\tilde{t}\right)$ some constant of integration. The boundary condition $\bar{J}^{\pm}_{\mathrm{b}}\left(\tilde{t},\bar{y}=\bar{y}_{\max}\right) = 0$ becomes $\bar{J}^{\pm}_{\mathrm{b}}\left(\tilde{t},\hat{Y}\to\infty\right) \to 0$, while $\bar{J}^{\pm}_{\mathrm{b}}\left(\tilde{t},\bar{y}=0\right) = 0$ becomes

$\bar{J}^{\pm}_{\mathrm{b}}\left(\tilde{t},\hat{Y}\to-\infty\right)\to 0$. Then

$$\bar{J}^{\pm}_{\mathrm{b0}}\left(\tilde{t},\hat{Y}\to-\infty\right)+\bar{\omega}_{\mathrm{on}}\bar{J}^{\pm}_{\mathrm{b1}}\left(\tilde{t},\hat{Y}\to-\infty\right)\to 0 \tag{5.22}$$

where

$$\bar{J}^{\pm}_{\mathrm{b0}}=\alpha^{1/2}\left(\hat{Y}\bar{P}^{\pm}_{\mathrm{b0}}-\bar{P}^{\pm}_{\mathrm{b0},\hat{Y}}\right) \tag{5.23}$$

and

$$\bar{J}^{\pm}_{\mathrm{b1}}=\alpha^{1/2}\left(\hat{Y}\bar{P}^{\pm}_{\mathrm{b1}}-\bar{P}^{\pm}_{\mathrm{b1},\hat{Y}}\right) \tag{5.24}$$

which must both separately also tend to zero as $\hat{Y}\to-\infty$. Using this, (5.21) may be rewritten as

$$\alpha^{-1/2}\bar{J}^{\pm}_{\mathrm{b0}}\mp\bar{\omega}_{\mathrm{on}}\alpha^{-1/2}\tilde{z}_{\tilde{t}\tilde{t}}\bar{P}^{\pm}_{\mathrm{b0}}=C\left(\tilde{t}\right). \tag{5.25}$$

Making the assumption that $\bar{P}^{\pm}_{\mathrm{b0}}\to 0$ as $\hat{Y}\to-\infty$, which enforces (5.22) at leading order, then $C\left(\tilde{t}\right)=0$ and

$$\bar{P}^{\pm}_{\mathrm{b0},\hat{Y}}=-\left(\hat{Y}\mp\bar{\omega}_{\mathrm{on}}\alpha^{-\frac{1}{2}}\tilde{z}_{\tilde{t}\tilde{t}}\right)\bar{P}^{\pm}_{\mathrm{b0}}. \tag{5.26}$$

Integrating (5.26) gives the solution

$$\bar{P}^{\pm}_{\mathrm{b0}}=\tilde{B}^{\pm}\left(\tilde{t}\right)e^{\left(-\frac{1}{2}\hat{Y}^2\pm\bar{\omega}_{\mathrm{on}}\alpha^{-\frac{1}{2}}\tilde{z}_{\tilde{t}\tilde{t}}\hat{Y}\right)}=B^{\pm}\left(\tilde{t}\right)e^{\left(-\frac{1}{2}\left(\hat{Y}\mp\bar{\omega}_{\mathrm{on}}\alpha^{-\frac{1}{2}}\tilde{z}_{\tilde{t}\tilde{t}}\right)^2\right)} \tag{5.27}$$

for some $\tilde{B}^{\pm}\left(\tilde{t}\right)$ and $B^{\pm}\left(\tilde{t}\right)$, where $B^{\pm}\left(\tilde{t}\right)$ describes the amplitude of the peak of the probability density function (subject to smaller corrections) which varies in time. Returning to (5.19), with $\bar{P}^{\pm}_{\mathrm{u}}\ll\bar{P}^{\pm}_{\mathrm{b}}$, then to $\mathcal{O}\left(\bar{\omega}_{\mathrm{on}}\right)$

$$\left(\left(\hat{Y}\mp\bar{\omega}_{\mathrm{on}}\alpha^{-\frac{1}{2}}\tilde{z}_{\tilde{t}\tilde{t}}\right)\bar{P}^{\pm}_{\mathrm{b1}}+\bar{P}^{\pm}_{\mathrm{b1},\hat{Y}}\right)_{\hat{Y}}=\bar{P}^{\pm}_{\mathrm{b0},\tilde{t}}+\frac{\bar{\omega}_0 e^{\gamma(1\mp\tilde{z}_{\tilde{t}})}}{\bar{\omega}_{\mathrm{on}}}\bar{P}^{\pm}_{\mathrm{b0}}, \tag{5.28}$$

which may be rewritten as

$$\left(\alpha^{-1/2}\bar{J}^{\pm}_{\mathrm{b1}}\mp\bar{\omega}_{\mathrm{on}}\alpha^{-1/2}\tilde{z}_{\tilde{t}\tilde{t}}\bar{P}^{\pm}_{\mathrm{b1}}\right)_{\hat{Y}}=\bar{P}^{\pm}_{\mathrm{b0},\tilde{t}}+\frac{\bar{\omega}_0 e^{\gamma(1\mp\tilde{z}_{\tilde{t}})}}{\bar{\omega}_{\mathrm{on}}}\bar{P}^{\pm}_{\mathrm{b0}}. \tag{5.29}$$

Thus using (5.27) in (5.29) and integrating gives

$$\begin{aligned}\left[\alpha^{-1/2}\bar{J}^{\pm}_{\mathrm{b1}}\mp\bar{\omega}_{\mathrm{on}}\alpha^{-1/2}\tilde{z}_{\tilde{t}\tilde{t}}\bar{P}^{\pm}_{\mathrm{b1}}\right]^{\infty}_{\bar{Y}}=&\int_{\bar{Y}}^{\infty}\left(B^{\pm}_{\tilde{t}}\pm\bar{\omega}_{\mathrm{on}}\alpha^{-\frac{1}{2}}\tilde{z}_{\tilde{t}\tilde{t}\tilde{t}}\left(\bar{Y}\mp\bar{\omega}_{\mathrm{on}}\alpha^{-\frac{1}{2}}\tilde{z}_{\tilde{t}\tilde{t}}\right)\right)e^{\left(-\frac{1}{2}\left(\bar{Y}\mp\bar{\omega}_{\mathrm{on}}\alpha^{-\frac{1}{2}}\tilde{z}_{\tilde{t}\tilde{t}}\right)^2\right)}\\&+\left(\frac{\bar{\omega}_0 e^{\gamma(1\mp\tilde{z}_{\tilde{t}})}}{\bar{\omega}_{\mathrm{on}}}B^{\pm}\right)e^{\left(-\frac{1}{2}\left(\bar{Y}\mp\bar{\omega}_{\mathrm{on}}\alpha^{-\frac{1}{2}}\tilde{z}_{\tilde{t}\tilde{t}}\right)^2\right)}\mathrm{d}\bar{Y}.\end{aligned} \tag{5.30}$$

By assuming that $\bar{P}^{\pm}_{\mathrm{b1}}\to 0$ as $\hat{Y}\to\infty$, which enforces boundary condition $\bar{J}^{\pm}_{\mathrm{b1}}\to 0$ as

$\hat{Y} \to \infty$, then

$$-\alpha^{-1/2}\bar{J}^{\pm}_{\mathrm{b1}} \pm \bar{\omega}_{\mathrm{on}}\alpha^{-1/2}\tilde{z}_{\tilde{t}\tilde{t}}\bar{P}^{\pm}_{\mathrm{b1}} = \int_{\hat{Y}}^{\infty} \left(B^{\pm}_{\tilde{t}} \pm \bar{\omega}_{\mathrm{on}}\alpha^{-\frac{1}{2}}\tilde{z}_{\tilde{t}\tilde{t}\tilde{t}}\left(\hat{Y} \mp \bar{\omega}_{\mathrm{on}}\alpha^{-\frac{1}{2}}\tilde{z}_{\tilde{t}\tilde{t}}\right)\right) e^{\left(-\frac{1}{2}\left(\hat{Y}\mp\bar{\omega}_{\mathrm{on}}\alpha^{-\frac{1}{2}}\tilde{z}_{\tilde{t}\tilde{t}}\right)^2\right)} + \left(\frac{\bar{\omega}_0 e^{\gamma(1\mp\tilde{z}_{\tilde{t}})}}{\bar{\omega}_{\mathrm{on}}}B^{\pm}\right) e^{\left(-\frac{1}{2}\left(\hat{Y}\mp\bar{\omega}_{\mathrm{on}}\alpha^{-\frac{1}{2}}\tilde{z}_{\tilde{t}\tilde{t}}\right)^2\right)}\mathrm{d}\hat{Y}. \quad (5.31)$$

The left hand side (LHS) of (5.31) may be rewritten

$$\mathrm{LHS} = -\left(\hat{Y} \mp \alpha^{-1/2}\bar{\omega}_{\mathrm{on}}\tilde{z}_{\tilde{t}\tilde{t}}\right)\bar{P}^{\pm}_{\mathrm{b1}} + \bar{P}^{\pm}_{\mathrm{b1},\hat{Y}} \quad (5.32)$$

and so in the limit $\hat{Y} \to -\infty$, (5.32) is dominated by the $\hat{Y}\bar{P}^{\pm}_{\mathrm{b1}}$ term. Rearranging the right hand side gives, in this limit,

$$-\hat{Y}\bar{P}^{\pm}_{\mathrm{b1}} \sim \left(B^{\pm}_{\tilde{t}} + \frac{\bar{\omega}_0 e^{\gamma\left(\hat{Y}\mp\tilde{z}_{\tilde{t}}\right)}}{\bar{\omega}_{\mathrm{on}}}B^{\pm}\right)\int_{-\infty}^{\infty} e^{\left(-\frac{1}{2}\left(\hat{Y}\mp\bar{\omega}_{\mathrm{on}}\alpha^{-\frac{1}{2}}\tilde{z}_{\tilde{t}\tilde{t}}\right)^2\right)}\mathrm{d}\hat{Y} \pm \bar{\omega}_{\mathrm{on}}\alpha^{-\frac{1}{2}}\tilde{z}_{\tilde{t}\tilde{t}\tilde{t}}B^{\pm}\int_{-\infty}^{\infty}\left(\hat{Y} \mp \bar{\omega}_{\mathrm{on}}\alpha^{-\frac{1}{2}}\tilde{z}_{\tilde{t}\tilde{t}}\right)e^{\left(-\frac{1}{2}\left(\hat{Y}\mp\bar{\omega}_{\mathrm{on}}\alpha^{-\frac{1}{2}}\tilde{z}_{\tilde{t}\tilde{t}}\right)^2\right)}\mathrm{d}\hat{Y}.$$

The second integral vanishes, while the first integral can be evaluated and thus, as $\hat{Y} \to -\infty$,

$$\bar{P}^{\pm}_{\mathrm{b1}} \sim -\frac{\sqrt{2\pi}}{\hat{Y}}\left(B^{\pm}_{\tilde{t}} + \frac{\bar{\omega}_0 e^{\gamma(1\mp\tilde{z}_{\tilde{t}})}}{\bar{\omega}_{\mathrm{on}}}B^{\pm}\right) = \frac{\sqrt{2\pi\alpha}}{1-\bar{y}\mp\tilde{z}_{\tilde{t}}}\left(B^{\pm}_{\tilde{t}} + \frac{\bar{\omega}_0 e^{\gamma(1\mp\tilde{z}_{\tilde{t}})}}{\bar{\omega}_{\mathrm{on}}}B^{\pm}\right). \quad (5.33)$$

The asymptotic limits (5.15) and (5.33) as $Y \to \infty$ and $\hat{Y} \to -\infty$ respectively will now be matched inside region II.

5.2.3 Region II

In region II, advection terms dominate. These 'sweep' the bound force generators toward the peak of $\bar{P}^{\pm}_{\mathrm{b}}$ such that bound force generators will tend to have elastic linkers with an extension $\bar{y}_{\mathrm{c}} = 1 \mp \tilde{z}_{\tilde{t}}$, and the unbound force generators toward the peak of $\bar{P}^{\pm}_{\mathrm{u}}$ such that unbound force generators will tend to have an elastic linker with zero extension. Given that the probability density functions are peaked in regions I and II, $\bar{P}^{\pm}_{\mathrm{b},\bar{y}}$ and $\bar{P}^{\pm}_{\mathrm{u},\bar{y}}$ are both relatively small in region II, being given by the small correction terms $\bar{\omega}_{\mathrm{on}}\bar{P}^{\pm}_{\mathrm{u1}}$ and $\bar{\omega}_{\mathrm{on}}\bar{P}^{\pm}_{\mathrm{b1}}$, expressions for which we have determined in the limits $Y \to \infty$ and $\hat{Y} \to -\infty$ respectively. Then together, using (4.26a),

$$\bar{J}^{\pm}_{\mathrm{b}} = \bar{v}^{\pm}_{\mathrm{b}}\bar{P}^{\pm}_{\mathrm{b}} - \alpha\bar{P}^{\pm}_{\mathrm{b},\bar{y}} \approx \bar{v}^{\pm}_{\mathrm{b}}\bar{P}^{\pm}_{\mathrm{b}} \quad (5.34)$$

and so substitution of $\bar{P}^{\pm}_{\mathrm{b}} \approx \bar{\omega}_{\mathrm{on}}\bar{P}^{\pm}_{\mathrm{b1}}$ when $\hat{Y} \to -\infty$ and (4.28) returns

$$\bar{J}^{\pm}_{\mathrm{b}} \approx \sqrt{2\pi\alpha}\left(\bar{\omega}_0 e^{\gamma(1\mp\tilde{z}_{\tilde{t}})}B^{\pm} + \bar{\omega}_{\mathrm{on}}B^{\pm}_{\tilde{t}}\right). \quad (5.35)$$

Continuing, using (4.26b),

$$\bar{J}_{\mathrm{u}}^{\pm} = -\Gamma\left(\bar{y}\bar{P}_{\mathrm{u}}^{\pm} + \beta\bar{P}_{\mathrm{u},\bar{y}}^{\pm}\right) \approx -\Gamma\bar{y}\bar{P}_{\mathrm{u}}^{\pm} \tag{5.36}$$

and so substitution of $\bar{P}_{\mathrm{u}}^{\pm} \approx \bar{\omega}_{\mathrm{on}}\bar{P}_{\mathrm{u1}}^{\pm}$ when $Y \to \infty$ returns

$$\bar{J}_{\mathrm{u}}^{\pm} \approx -\bar{\omega}_{\mathrm{on}}\sqrt{\frac{\pi\beta}{2}}\left(A^{\pm} + A_{\tilde{t}}^{\pm}\right). \tag{5.37}$$

Then by the form of (5.35) and (5.37), to leading order $\bar{J}_{\mathrm{b},\bar{y}}^{\pm} = 0$ and $\bar{J}_{\mathrm{u},\bar{y}}^{\pm} = 0$ and therefore (5.35) and (5.37) are valid across the whole of region II. Further, since $\bar{J}_{\mathrm{b}}^{\pm}$ and $\bar{J}_{\mathrm{u}}^{\pm}$ are 0 at the boundaries (4.27), $\bar{J}_{\mathrm{b}}^{\pm} + \bar{J}_{\mathrm{u}}^{\pm} = 0$, a form of 'detailed balance', and thus

$$\sqrt{2\pi\alpha}\left(\bar{\omega}_0 e^{\gamma(1\mp\tilde{z}_{\tilde{t}})}B^{\pm} + \bar{\omega}_{\mathrm{on}}B_{\tilde{t}}^{\pm}\right) = \bar{\omega}_{\mathrm{on}}\sqrt{\frac{\pi\beta}{2}}\left(A^{\pm} + A_{\tilde{t}}^{\pm}\right). \tag{5.38}$$

We will use (5.38) to construct a system of equations which describe the movements of the spindle in terms of the amplitudes of the peaks of the probability density functions and their relative diffusive widths.

5.2.4 Combining the whole system

We may now use expressions (5.10), (5.15) for $\bar{P}_{\mathrm{b}}^{\pm}$ and (5.27), (5.33) for $\bar{P}_{\mathrm{u}}^{\pm}$, and their coupling in region II (5.38) to close the system. Recalling that $\int_0^{\infty}\left(\bar{P}_{\mathrm{u}}^{\pm} + \bar{P}_{\mathrm{b}}^{\pm}\right)\mathrm{d}\bar{y} = 1$, then to leading order

$$\int_0^{\infty}\left(A^{\pm}e^{-\frac{1}{2\beta}\bar{y}^2} + B^{\pm}e^{\left(-\frac{1}{2\alpha}\left(\bar{y}-1\pm\tilde{z}_{\tilde{t}}\mp\bar{\omega}_{\mathrm{on}}\tilde{z}_{\tilde{t}\tilde{t}}\right)^2\right)}\right)\mathrm{d}\bar{y} = 1. \tag{5.39}$$

The first term of this integral is easily evaluated, while the second term is more complex. Consider only the leading-order terms of the exponent, due to $\bar{\omega}_{\mathrm{on}}$ being a small order parameter. Then

$$\int_0^{\infty} B^{\pm}e^{\left(-\frac{1}{2\alpha}\left(\bar{y}-1\pm\tilde{z}_{\tilde{t}}\mp\bar{\omega}_{\mathrm{on}}\tilde{z}_{\tilde{t}\tilde{t}}\right)^2\right)}\mathrm{d}\bar{y} \approx \int_0^{\infty} B^{\pm}e^{\left(-\frac{1}{2\alpha}\left(\bar{y}-\bar{y}_{\mathrm{c}}\right)^2\right)}\mathrm{d}\bar{y} \tag{5.40}$$

which we know is a peak contained within region III. That is, we integrate over the Gaussian, which does not intersect $\bar{y} = 0$ with any value of significance at leading order. Using this logic, the integral (5.40) may be evaluated and thus

$$A^{\pm}\sqrt{\frac{\pi\beta}{2}} + B^{\pm}\sqrt{2\pi\alpha} = 1. \tag{5.41}$$

This can be used to eliminate $A^{\pm}$ from (5.38) to give

$$2\bar{\omega}_{\mathrm{on}}\sqrt{2\pi\alpha}B_{\tilde{t}}^{\pm} = \bar{\omega}_{\mathrm{on}} - \sqrt{2\pi\alpha}\left(\bar{\omega}_0 e^{\gamma(1\mp\tilde{z}_{\tilde{t}})} + \bar{\omega}_{\mathrm{on}}\right)B^{\pm}. \tag{5.42}$$

Equation (5.42) predicts that $\sqrt{2\pi\alpha}B^{\pm}$ relaxes to $\frac{\bar{\omega}_{\mathrm{on}}}{\bar{\omega}_{\mathrm{on}}+\bar{\omega}_0 e^{\gamma\left(1\mp\tilde{z}_{\tilde{t}}\right)}}$ and (5.41) predicts that $\sqrt{\frac{\pi\beta}{2}}A^{\pm}$

relaxes to $\frac{\bar{\omega}_0 e^{\gamma\left(1\mp\tilde{z}_{\tilde{t}}\right)}}{\bar{\omega}_{\text{on}}+\bar{\omega}_0 e^{\gamma\left(1\mp\tilde{z}_{\tilde{t}}\right)}}$ provided $\tilde{z}$ does not change too rapidly.

Further to this, $\bar{P}_{\text{b}}^{\pm} = \bar{P}_{\text{b0}}^{\pm} + \bar{\omega}_{\text{on}}\bar{P}_{\text{b1}}^{\pm} + ...$ can be put into (5.1) to obtain a leading-order equation for the motion of the spindle pole. This requires the evaluation of

$$\int_0^{\bar{y}_{\text{max}}} \bar{y}\bar{P}_{\text{b}}^{\pm}\text{d}\bar{y} \sim \int_0^{\infty} \bar{y}B^{\pm}e^{\left(-\frac{1}{2\alpha}(\bar{y}-\bar{y}_{\text{c}})\right)^2}\text{d}\bar{y} + ... \tag{5.43}$$

where we assume $\bar{y}_{\text{max}}$ is sufficiently large that it exceeds the bounds of region III and can thus be taken as $\bar{y}_{\text{max}} \to \infty$. Again we let $\bar{y} = \bar{y}_{\text{c}} + \alpha^{1/2}\hat{Y}$, which is where $\bar{P}_{\text{b0}}^{\pm}$ has a significant value. Then

$$\int_0^{\infty} \bar{y}B^{\pm}e^{\left(-\frac{1}{2\alpha}(\bar{y}-\bar{y}_{\text{c}})^2\right)}\text{d}\bar{y} \sim \int_{-\infty}^{\infty} \left(\bar{y}_{\text{c}} + \alpha^{1/2}\hat{Y}\right) B^{\pm}e^{-\frac{1}{2}\hat{Y}^2}\alpha^{1/2}\text{d}\hat{Y}, \tag{5.44}$$

which to leading order becomes

$$\int_{-\infty}^{\infty} \left(\bar{y}_{\text{c}} + \alpha^{1/2}\hat{Y}\right) B^{\pm}e^{-\frac{1}{2}\hat{Y}^2}\alpha^{1/2}\text{d}\hat{Y} \sim \alpha^{1/2}\bar{y}_{\text{c}}B^{\pm}\int_{-\infty}^{\infty} e^{-\frac{1}{2}\hat{Y}^2}\text{d}\hat{Y} = \bar{y}_{\text{c}}B^{\pm}\sqrt{2\pi\alpha} + ... \tag{5.45}$$

Recalling that $\bar{y}_{\text{c}} = 1 \mp \tilde{z}_{\tilde{t}}$, (5.1) becomes

$$\bar{\xi}\tilde{z}_{\tilde{t}} = -\frac{K}{\bar{\omega}_{\text{on}}}\tilde{z} - N\sqrt{2\pi\alpha}\left(\left(1+\tilde{z}_{\tilde{t}}\right)B^{-} - \left(1-\tilde{z}_{\tilde{t}}\right)B^{+}\right) \tag{5.46}$$

and thus

$$\bar{\xi}\tilde{z}_{\tilde{t}} = -\frac{K}{\bar{\omega}_{\text{on}}}\tilde{z} - N\sqrt{2\pi\alpha}\left(B^{-}+B^{+}\right)\tilde{z}_{\tilde{t}} - N\sqrt{2\pi\alpha}\left(B^{-}-B^{+}\right). \tag{5.47}$$

This can be rewritten as

$$\left(\hat{\xi} + \hat{B}^{+} + \hat{B}^{-}\right)\tilde{z}_{\tilde{t}} + \hat{K}\tilde{z} = \hat{B}^{+} - \hat{B}^{-}, \tag{5.48}$$

where $\hat{B}^{\pm} = \sqrt{2\pi\alpha}B^{\pm}$, $\hat{K} = \frac{K}{\bar{\omega}_{\text{on}}N}$, and $\hat{\xi} = \frac{\bar{\xi}}{N}$. Recalling (5.42) which may be alternatively written as

$$\left(1 + \rho e^{\gamma(1\mp\tilde{z}_{\tilde{t}})}\right)\hat{B}^{\pm} + 2\hat{B}_{\tilde{t}}^{\pm} = 1 \tag{5.49}$$

where $\rho = \bar{\omega}_0/\bar{\omega}_{\text{on}}$, the coupled system (4.25a), (4.25b), and (4.32) is reduced to solving equations (5.48-5.49) along with initial conditions $\tilde{z}_0$ and $\hat{B}_0^{\pm}$.

5.3 Computational method

The following computational method was used to solve equations (5.48-5.49).

1. Initial conditions $\hat{B}_0^{\pm} = 0.3$ and $\tilde{z} = 0.05$ were defined.
2. The ODEs (5.48-5.49) and the initial conditions were passed to an ODE solver from Julia package `DifferentialEquations` [213].
3. The solver continued until a predefined end-time was achieved using automatic step selection.

Source code available at github.com/dionn-hargreaves/ODE_1D_spindle/. We note here the relative ease of this method compared with the additional steps required to solve the stochastic and PDE methods (Sections 4.2.3 and 4.3.2).

5.4 Results for the ODEs

5.4.1 Stability analysis

The simplicity of the ODE model lends itself to performing stability analysis on the system. To do stability analysis, small amplitude perturbations about the steady state are considered, where the steady-state solution $\hat{B}^{*\pm}$ is determined from (5.49) to be

$$(1 + \rho e^{\gamma})\, \hat{B}^{*\pm} = 1. \tag{5.50}$$

We rewrite this to give

$$\hat{B}^{*\pm} = \lambda^{-1}, \tag{5.51}$$

for $\lambda \equiv 1 + \rho e^{\gamma}$. Using (5.51) when determining the steady state solution $\tilde{z}^*$ by (5.48) gives

$$\tilde{z}^* = 0. \tag{5.52}$$

To analyse the stability of this solution, consider small amplitude perturbations to (5.51) and (5.52) such that

$$\hat{B}^{*\pm} = \lambda^{-1} + \epsilon \hat{b}^{\pm}\left(\tilde{t}\right) + ... \tag{5.53}$$

and

$$\tilde{z}^* = \epsilon \hat{z}\left(\tilde{t}\right) + ... \tag{5.54}$$

for small ϵ. Additionally,

$$\rho e^{\gamma(1 \mp \tilde{z}_{\tilde{t}})} = \rho e^{\gamma(1 \mp (\epsilon \hat{z}_{\tilde{t}} + ...))} \approx \rho e^{\gamma} \mp \epsilon \hat{z}_{\tilde{t}} \gamma \rho e^{\gamma} + ... \,. \tag{5.55}$$

Then to linear order in $\epsilon \ll 1$, equations (5.48-5.49) become

$$\left(\hat{\xi} + 2\lambda^{-1}\right) \hat{z}_{\tilde{t}} + \hat{K}\hat{z} = \hat{b}^{+} - \hat{b}^{-}, \tag{5.56a}$$

$$\mp \hat{z}_{\tilde{t}} \lambda^{-1} \rho \gamma e^{\gamma} + \lambda \hat{b}^{\pm} + 2\hat{b}^{\pm}_{\tilde{t}} = 0. \tag{5.56b}$$

Assuming exponential time-dependence $\hat{b}, \hat{z} \propto e^{s\tilde{t}}$ such that $\frac{\mathrm{d}}{\mathrm{d}\tilde{t}} \to s$, then (5.56) may alternatively be written

$$\left(\hat{\xi} + 2\lambda^{-1}\right) s\hat{z} + \hat{K}\hat{z} = \hat{b}^{+} - \hat{b}^{-}, \tag{5.57a}$$

$$\mp s\hat{z}\lambda^{-1}\gamma\rho e^{\gamma} + \lambda\hat{b}^{\pm} + 2s\hat{b}^{\pm} = 0. \tag{5.57b}$$

By explicitly writing the upper and lower cortex equations (5.57b) out as

$$-s\hat{z}\lambda^{-1}\gamma\rho e^{\gamma} + \lambda\hat{b}^{+} + 2s\hat{b}^{+} = 0, \tag{5.58a}$$

$$s\hat{z}\lambda^{-1}\gamma\rho e^{\gamma} + \lambda\hat{b}^{-} + 2s\hat{b}^{-} = 0, \tag{5.58b}$$

we can combine (5.58a)−(5.58b) to obtain an expression for $\hat{b}^{+} - \hat{b}^{-}$ which can be inserted into (5.57a). This is reduced further to

$$\left(\left(\hat{\xi} + 2/\lambda\right) s + \hat{K}\right)\left(\lambda\left(2s + \lambda\right)\right) = 2s\gamma\rho e^{\gamma}, \tag{5.59}$$

where we have assumed that $\hat{z} \neq 0$. Seeking solutions where $s = i\Omega$ at the onset of neutral oscillations, a natural frequency of

$$\Omega^2 = \frac{\hat{K}\lambda^2}{2\left(2 + \hat{\xi}\lambda\right)} \tag{5.60}$$

is returned when

$$\left(\hat{\xi}\lambda + 2\right)\lambda + 2\lambda\hat{K} = 2\gamma\rho e^{\gamma} \equiv 2\gamma\left(\lambda - 1\right). \tag{5.61}$$

Therefore at the onset of oscillations

$$\hat{K} = \frac{\gamma}{\lambda}\left(\lambda - 1\right) - \frac{1}{2}\left(\hat{\xi}\lambda + 2\right). \tag{5.62}$$

Recalling that $\hat{K} = K/\bar{\omega}_{\text{on}}N$, $\lambda = 1 + \left(\bar{\omega}_0/\bar{\omega}_{\text{on}}\right)e^{\gamma}$ and $\hat{\xi} = \bar{\xi}/N$, then (5.62) can be used to reveal the boundary in ($\bar{\omega}_{\text{on}}$, N) space at the onset of neutral oscillations (Figure 5.1A). The wedge shape of the oscillatory region described by (5.62) is similar to that returned by analysis of the PDE solutions across the parameter space (Figure 4.12), though the lowest N value capable of producing oscillations is increased using the ODEs from $N \approx 25$ to $N \approx 40$. Simulations of the Fokker-Planck model revealed that increasing the diffusive terms α and β promote oscillations below the stability threshold, thus the shifted threshold in the ODE system relative to the PDE system is likely due the assumption that diffusivity is low. Despite this discrepancy between the exact quantitative matching of the location of the stability boundary, we can use (5.62) to explore other factors which affect its location and shape. Interestingly, numerical solutions of the Fokker-Planck equations over $(N, \bar{\omega}_{\text{on}})$ space suggests an upper stability threshold between $0.006 < \bar{\omega}^{\dagger}_{\text{on}} < 0.007$ for $N \leq 80$, which is within 80% of the calculated stability threshold if $\bar{\omega}^{\dagger}_{\text{on}} = 0.0074$ using (5.69).

We first recall that in the Fokker-Planck model, decreasing the restoring force parameter

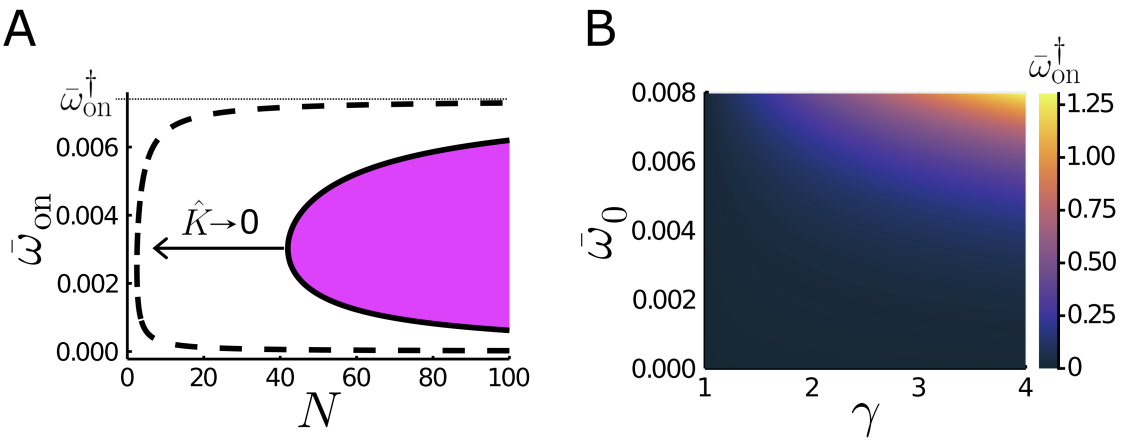

Figure 5.1. **Exploring the stability boundary between oscillatory and non-oscillatory solutions in the ODE model.** A) (Solid curve) The threshold separating oscillatory solutions (magenta) from non-oscillatory solutions in $(N, \bar{\omega}_{\text{on}})$ space, determined from (5.62) for parameters: $K = 5 \times 10^{-2}, \gamma = 2, \bar{\omega}_0 = 1 \times 10^{-3}, \bar{\xi} = 6.25 \times 10^{-1}$. (Dashed curve) The same threshold in the $\hat{K} \to 0$ limit determined by (5.64). B) A heat map of the value of the upper threshold $\bar{\omega}_{\text{on}}^{\dagger}$ by (5.69) which $\bar{\omega}_{\text{on}}$ asymptotically approaches for large N as parameters $\bar{\omega}_0$ and γ vary.

K promoted oscillations in the non-oscillatory region of parameter space (Figure 4.13C). To explore whether this behaviour is conserved in the ODE system, we look in the limit of $\hat{K} \to 0$ in equation (5.62) to describe how reducing K affects the stability boundary. In the limit of $\hat{K} \to 0$, (5.62) is dominated by the terms of the right hand side, so that it may be rewritten in this limit as

$$\hat{\xi}\lambda + 2 = \frac{2\gamma}{\lambda}(\lambda - 1). \tag{5.63}$$

As $\hat{\xi} = \bar{\xi}/N$ is the only parameter which depends on N, then rewriting (5.63) as

$$N = \frac{\bar{\xi}\lambda^2}{2\gamma(\lambda - 1) - 2\lambda} \tag{5.64}$$

gives the stability boundary for small $\hat{K}$ shown in Figure 5.1A (dashed line). This aligns with what was seen in simulations of the Fokker-Planck model, as decreasing $\hat{K}$ (by reduction of K), promotes oscillations in a greater region of the $(N, \bar{\omega}_{\text{on}})$ parameter space. As we cannot physically have $N < 0$, as it represents the number of cortical force generators, then the denominator of (5.64) must also be greater than zero. Then

$$\gamma(\lambda - 1) > \lambda, \tag{5.65}$$

and since $\lambda = 1 + (\bar{\omega}_0/\bar{\omega}_{\text{on}})\, e^{\gamma}$,

$$\bar{\omega}_{\text{on}} < (\gamma - 1)\, \bar{\omega}_0 e^{\gamma} \tag{5.66}$$

must be true for the establishment of non-decaying oscillations.

Analysis of (5.62) shows that $\bar{\omega}_{\text{on}}$ asymptotes to this value in the limit of large N. Recalling

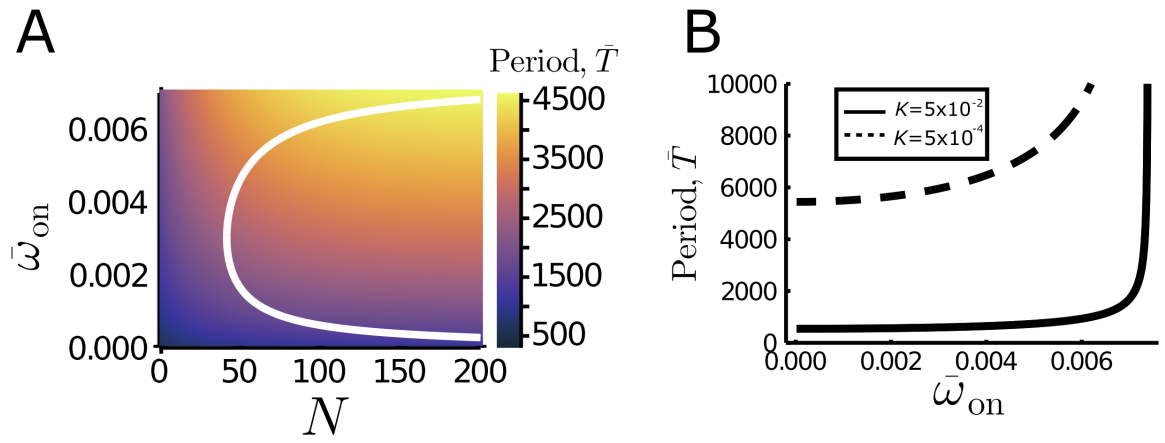

Figure 5.2. **The period of oscillation.** A) The period of oscillation as calculated from (5.60), in non-dimensionalised time as in Section 4, showing the boundary between oscillatory and non-oscillatory solutions (white). B) The relationship between the period of oscillation and the binding rate $\bar{\omega}_{\text{on}}$ using (5.60), along the neutral stability curve (5.62). The period $\bar{T}$ is reported in the non-dimensionalised time used in the stochastic simulations and Fokker-Planck system and is unbounded as $\bar{\omega}_{\text{on}} \to \bar{\omega}^{\dagger}_{\text{on}}$. Parameters used: $\gamma = 2, \bar{\omega}_0 = 1 \times 10^{-3}, \bar{\xi} = 6.25 \times 10^{-1}$. A) and B) (Solid curve) $K = 5 \times 10^{-2}$, B) (Dashed curve) $K = 5 \times 10^{-4}$

that $\hat{K} \propto 1/N$ and $\hat{\xi} \propto 1/N$, then (5.62) becomes

$$0 \sim \gamma(\lambda - 1) - \lambda, \tag{5.67}$$

which may equivalently be written as

$$\gamma \frac{\bar{\omega}_0}{\bar{\omega}_{\text{on}}} e^{\gamma} \sim 1 + \frac{\bar{\omega}_0}{\bar{\omega}_{\text{on}}} e^{\gamma}, \tag{5.68}$$

because $\lambda = 1 + \frac{\bar{\omega}_0}{\bar{\omega}_{\text{on}}} e^{\gamma}$. Algebraic rearrangement shows that as $N \to \infty$,

$$\bar{\omega}_{\text{on}} \to \bar{\omega}^{\dagger}_{\text{on}} \equiv (\gamma - 1)\, \bar{\omega}_0 e^{\gamma}. \tag{5.69}$$

Comparison of this result with that obtained by analysis of (5.64) is interesting as $\hat{K}$ is inversely proportional to N, thus a large value of N enforces a small value of $\hat{K}$. However, $\hat{K}$ may also become small independently of N due to the restoring force K. Thus it is not trivial that the boundaries on the upper threshold of the oscillatory region are the same for small $\hat{K}$ and large N. The expression (5.69) for the upper limit of $\bar{\omega}_{\text{on}}$ is interesting as it also reveals the necessity for the tension-sensitivity parameter γ to be greater than 1 for oscillations to occur. Indeed, removal of the tension-sensitivity of the unbinding rate in the stochastic simulations lead to a reduction of the coherence of the oscillatory behaviour of the spindle pole (Figure 4.7A). Thus the relative area of $(N, \bar{\omega}_{\text{on}})$ parameter space which hosts non-decaying oscillatory solutions (acknowledging that the area is infinite for unbounded N) decreases with the magnitude of $\hat{K}$ (representing a reduction of restoring forces relative to pulling forces), but increases with the tension-sensitivity of unbinding γ and the unbinding rate $\bar{\omega}_0$. The effect of changing $\bar{\omega}_0$ and γ on $\bar{\omega}^{\dagger}_{\text{on}}$ is shown in Figure 5.1B.

Analysis of the natural frequency predicted in (5.60) shows that the period of oscillation in-

creases with both N and $\bar{\omega}_{\text{on}}$ (Figure 5.2A). This mirrors what was seen in the solutions of the Fokker-Planck equations, where the period increased with both N and $\bar{\omega}_{\text{on}}$, and the solutions for increasing N increased their periods more rapidly when $\bar{\omega}_{\text{on}} = 0.003$ than they did when $\bar{\omega}_{\text{on}} = 0.001$ (Figure 4.10D). The period along the neutral stability curve predicted using (5.60) increases as K decreases (Figure 5.2B), thus reduction of restoring forces corresponds to longer periods of oscillation. The rapid increase of the period as $\bar{\omega}_{\text{on}} \to \bar{\omega}^{\dagger}_{\text{on}}$ coincides with $N \to \infty$. The values of the periods in Figure 5.2 have been converted into the non-dimensionalised time used in the stochastic and Fokker-Planck models by $\bar{T} = \left(\frac{2\pi}{\Omega}\right)\frac{1}{\bar{\omega}_{\text{on}}}$ for ease of comparison between solutions.

Stability analysis of the ODEs has revealed the boundary of the oscillatory region of $(\bar{\omega}_{\text{on}})$ parameter space, as well as the factors which affect its position and also estimates for the period of oscillation along the neutral curve. We now explore how the solutions of the ODE model compare with the simulations of the Fokker-Planck model.

5.4.2 Comparison with simulations of the Fokker-Planck model

Using the computational method outlined in Section 5.2, we obtain solutions in time for $\tilde{z}$ and $\hat{B}^{\pm}$. We use $\bar{y}^{\pm}_{\text{c}} = 1 \mp \tilde{z}_{\bar{t}}$ to obtain values for $\bar{y}^{\pm}_{\text{c}}$ for comparison with the PDE solutions. Note that ODE solutions are presented in terms of $\bar{z}$ and $\bar{t}$ for comparison with PDE solutions. Our aim is to determine whether or not the ODE model can be used as an appropriate simplification for this system.

In general, by overall comparison of the Fokker-Planck PDE solutions with the ODE solutions for equivalent parameters (Figure 5.3), the general dynamics of the solutions, most notably the history-dependent effect on the bound probability amplitude (Figure 5.3, third column), are captured in the ODE model. We will now look more closely at different features of the solutions in various regions of parameter space.

Relaxation oscillations occur when pulling forces dominate the spindle pole movement

If we reduce the magnitude of parameter $\widehat{K}$, the spindle pole oscillates with relaxation oscillations (Figure 5.3D) which match closely with the relaxation oscillations returned by the PDE model with equivalent parameters (Figure 5.3C), with similar period and amplitude as well as shape. When the restoring force modulated by $\widehat{K}$ is small, the structure of the oscillations in the PDE and ODE descriptions are more closely matched than in Figures 5.3A/B.

Alternatively, pulling forces may dominate if we have a very high number of force generators. The PDE model demonstrates that an increase from $N = 25$ to $N = 45$ leads to oscillations which tend to a relaxation structure (Figure 4.10). Parameter N exists in the ODE model within parameters $\widehat{\xi}$ and $\widehat{K}$. Altering these parameters such that they are equivalent to the PDE model for $N = 1000$ results in oscillations with a relaxation structure as expected (Figure 5.3E). Thus we conclude that the balance of pulling to restoring forces con-

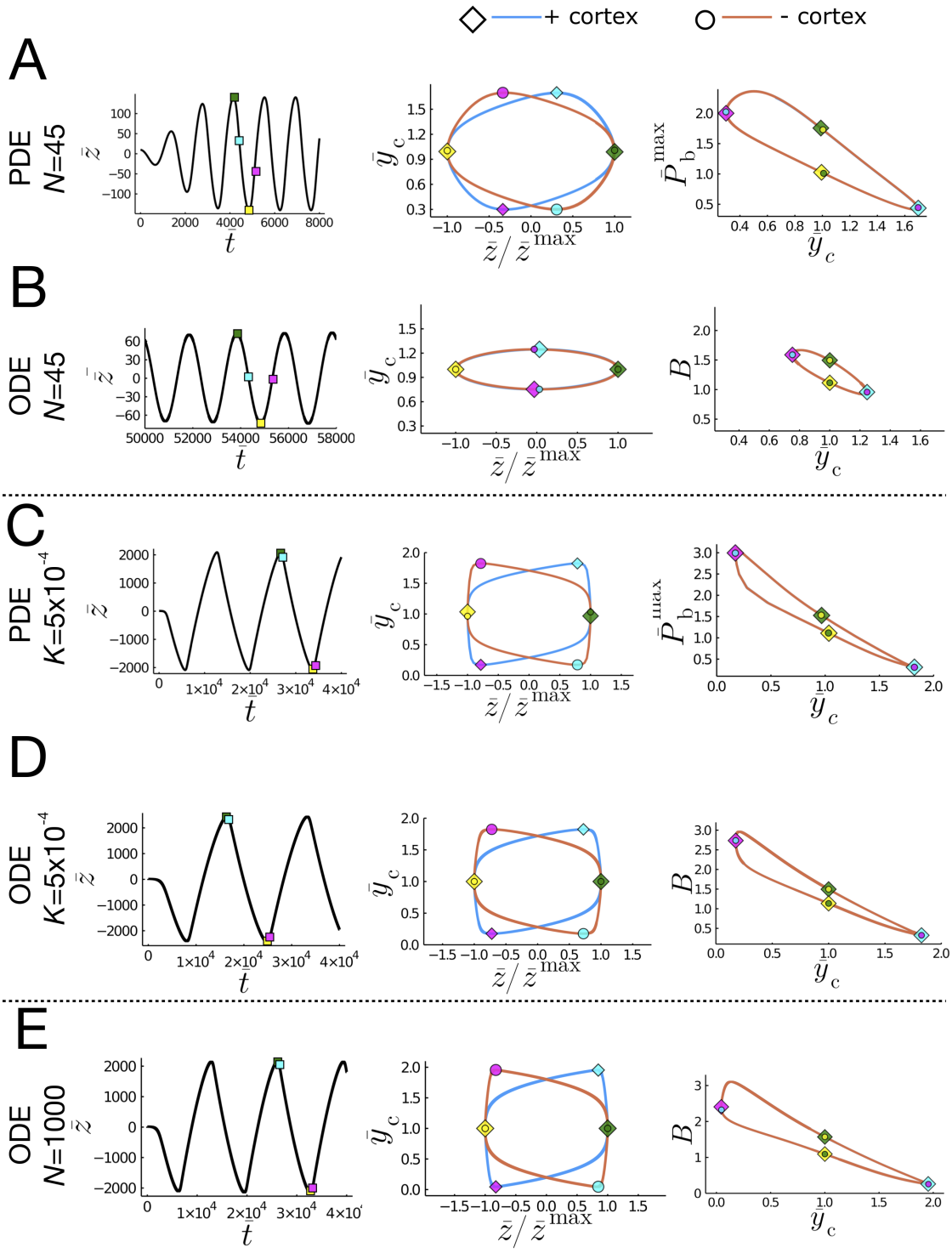

Figure 5.3. **Comparison of PDE and ODE solutions for equivalent parameters.** PDE and ODE solutions for equivalent parameters are presented, with non-equivalent solutions separated by a dotted line. A and C) represent solutions of the PDEs. B) D) and E) represent solutions of the ODEs. First column: spindle pole position $\bar{z}$. Second column: the centre of the bound probability density function as a function of pole position $\bar{y}_c^{\pm}(\bar{z})$. Third column: the amplitude of the bound probability density function as a function of the location of its centre ($\bar{P}_b^{\pm}(\bar{y}_c)$ for PDE solutions A,C); $B^{\pm} = \hat{B}^{\pm}/\sqrt{2\pi\alpha}$ for ODE solutions B, D, E). PDE solutions were obtained using parameters $\alpha = 8 \times 10^{-3}$, $\beta = 4 \times 10^{-3}$, $\bar{\xi} = 6.25 \times 10^{-1}$, $\bar{\omega}_0 = 1 \times 10^{-3}$, $\bar{\omega}_{on} = 3 \times 10^{-3}$, $\gamma = 2$, $\nu = 1 \times 10^3$ A) $K = 5 \times 10^{-2}$ and $N = 45$ and C) $K = 5 \times 10^{-4}$ and $N = 15$. ODE solutions obtained using B) equivalent parameters to A); D) equivalent parameters to C); and E) Equivalent parameters to A) with $N = 1000$. Line colours correspond to solutions in each cortex (blue = upper, orange = lower).

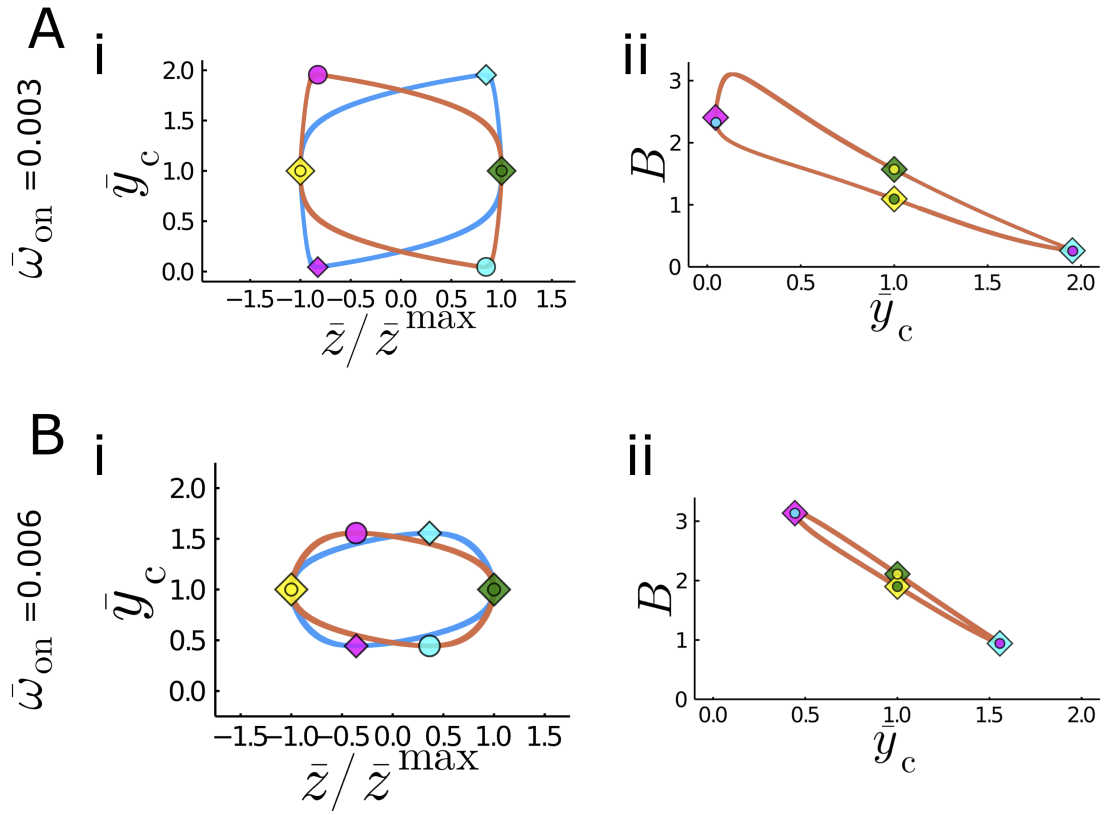

Figure 5.4. **Decreased binding rates increase the non-linearity of the oscillations in ODE solutions**. The centre of the bound probability density function $\bar{y}_c$ as a function of the normliased pole position $\bar{z}/\bar{z}^{\max}$ for A) $\bar{\omega}_{\text{on}} = 0.003$, B) $\bar{\omega}_{\text{on}} = 0.006$, using all other parameters equivalent to Figure 5.3E.

trols the structure of the oscillation of the spindle pole. Interestingly, the shape of the oscillations in the lower $\hat{K}$ and high N relaxation oscillation are slightly different. For low $\hat{K}$, the peak of the bound probability density function hits its maximum at the same time the spindle pole experiences its maximum velocity (when $\bar{y}_c^{\pm}$ is at its minimum value, Figure 5.3C,D). Alternatively, when N is increased, the maximum of the peak of the bound probability density function lags behind the spindle pole velocity (Figure 5.3E). This lag is interesting as it represents a delay between the binding of the force generators and the movements of the spindle pole, likely due to there being a greater number of force generators in the system to bind onto the microtubules before they are saturated. This delay is removed by increasing the binding rate $\bar{\omega}_{\text{on}}$ (Figure 5.4Aii, Bii), thus we attribute this lag to the rate of binding between the force generators and the microtubules. A higher affinity for binding also promotes more sinusoidal oscillations (Figure 5.4Ai, Bi).

5.4.3 Reduction in the limit of small $\hat{K}$

Since numerically reducing $\hat{K}$ leads to relaxation oscillations with fast and slow phases in both $\hat{B}^+$ and $\hat{B}^-$, we now explore whether a further simplification to the model can be implemented by exploiting $\hat{K}$ as a small parameter. The approximately linear sections of $\tilde{z}$ scale like $\hat{K}^{-1}$ in both time and amplitude, and correspond in time with slow phases. By

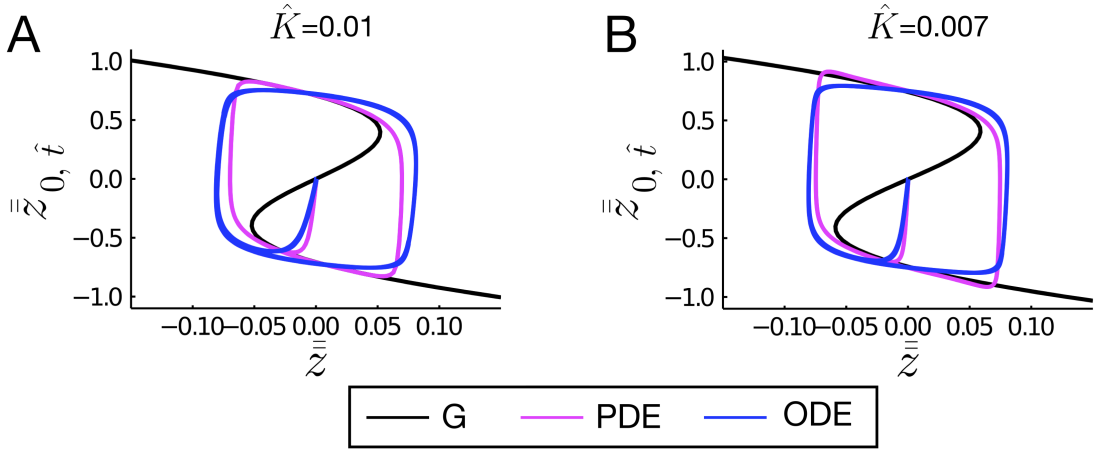

Figure 5.5. Overlaid phase portraits for the scaled solutions obtained by solving the ODE system (blue) and PDE system (magenta) for equivalent parameters where A) $\hat{K} = 0.01$, B) $\hat{K} = 0.007$. The inverted function G (black) given in (5.74) represents the expected limit cycle as $\hat{K} \to 0$. PDE parameters: $K = 5 \times 10^{-4}$, $\alpha = 8 \times 10^{-3}$, $\beta = 4 \times 10^{-3}$, $\bar{\xi} = 6.25 \times 10^{-1}$, $\bar{\omega}_0 = 1 \times 10^{-3}$, $\bar{\omega}_{\text{on}} = 3 \times 10^{-3}$, $\gamma = 2$, $\nu = 1 \times 10^3$ A) $N = 15$, B) $N = 25$. ODE parameters are equivalent.

re-scaling $\tilde{t} = \hat{t}/\hat{K}$ and $\tilde{z} = \bar{\bar{z}}/\hat{K}$ such that $\tilde{z}_{\tilde{t}} = \bar{\bar{z}}_{\hat{t}}$, the ODE equations (5.48-5.49) become

$$\left(1 + \rho e^{\gamma(1 \mp \bar{\bar{z}}_{\hat{t}})}\right) \hat{B}^{\pm} + 2\hat{K}\hat{B}^{\pm}_{\hat{t}} = 1 \tag{5.70}$$

and

$$\left(\hat{\xi} + \hat{B}^{+} + \hat{B}^{-}\right) \bar{\bar{z}}_{\hat{t}} + \bar{\bar{z}} = \hat{B}^{+} - \hat{B}^{-}. \tag{5.71}$$

By posing expansions $\hat{B}^{\pm} = \hat{B}^{\pm}_0 + \hat{K}\hat{B}^{\pm}_1 + \ldots$ and $\bar{\bar{z}} = \bar{\bar{z}}_0 + \hat{K}\bar{\bar{z}}_1 + \ldots$, then to leading order (5.70) and (5.71) become

$$\left(1 + \rho e^{\gamma\left(1 \mp \bar{\bar{z}}_{0,\hat{t}}\right)}\right) \hat{B}^{\pm}_0 = 1 \tag{5.72}$$

and

$$\left(\hat{\xi} + \hat{B}^{+}_0 + \hat{B}^{-}_0\right) \bar{\bar{z}}_{0,\hat{t}} + \bar{\bar{z}}_0 = \hat{B}^{+}_0 - \hat{B}^{-}_0. \tag{5.73}$$

We may rewrite (5.73) as

$$\bar{\bar{z}}_0 = \hat{B}^{+}_0 - \hat{B}^{-}_0 - \left(\hat{\xi} + \hat{B}^{+}_0 + \hat{B}^{-}_0\right) \bar{\bar{z}}_{0,\hat{t}} = G\left(\bar{\bar{z}}_{0,\hat{t}}\right), \tag{5.74}$$

with $\hat{B}^{\pm}_0$ defined by (5.72).

Equation (5.74) approximates the slow phases of the limit cycle in $(\bar{\bar{z}}_0, \bar{\bar{z}}_{0,\hat{t}})$ as $\hat{K} \to 0$ (Figure 5.5). Recalling that $\bar{y}^{\pm}_{\text{c}} = 1 \mp \bar{z}_{\text{t}}$ (Section 4.3), then following a parameter rescaling, (5.74) can also be used to describe the limit cycle in $(\bar{z}_0, \bar{y}^{\pm}_{\text{c}})$. The limit cycles obtained by solving the ODE and PDE systems with equivalent parameters are shown to closely match with this expected limit cycle (Figure 5.5A). As expected, this matching is improved as the value of $\hat{K}$ decreases (Figure 5.5A compared with Figure 5.5B). These cycles show the fast phases of the relaxation oscillation as the spindle pole changes its direction of motion (the approximately vertical sections at the maximum and minimum values of $\bar{\bar{z}}$). Then the maximum amplitude of oscillation can be estimated by the roots of G, which can be determined

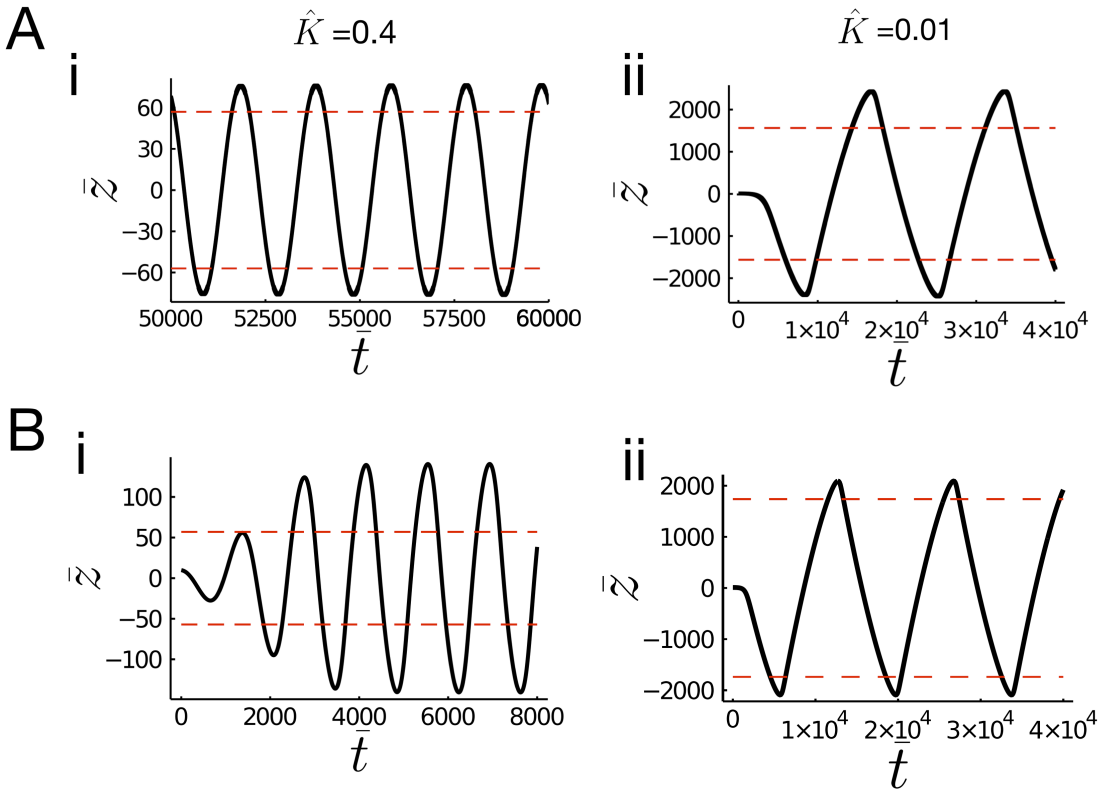

Figure 5.6. **Estimation of oscillation amplitude using G.** A) ODE solutions and B) PDE solutions of pole position, with the amplitude predicted by $\pm G_{\max}/\hat{K}$ (5.76) indicated by the red dashed lines. The parameters used are as in Ai) Figure 5.3B. Aii) Figure 5.3D. Bi) Figure 5.3A. Bii) Figure 5.3C.

by solving

$$\frac{\mathrm{d}G}{\mathrm{d}\bar{\bar{z}}_{0,\hat{t}}} = 0. \tag{5.75}$$

for roots $G_{\max}$ and $G_{\min}$. Then the amplitude of oscillation during relaxation oscillations can be estimated by

$$\tilde{z} = G_{\max}/\hat{K} + \epsilon \tag{5.76}$$

for ϵ a small correction parameter. Thus the amplitude of oscillation can be estimated from the ratio of pulling to pushing ($\hat{K}$), the effective drag $\hat{\xi}$, the ratio of the unbinding to binding rates (ρ) and the tension sensitivity of unbinding (γ). Surprisingly, the amplitude of oscillation in solutions of the ODE model are approximated well by (5.76), with little improvement as $\hat{K}$ is reduced (Figure 5.6A). However, the PDE solutions show a marked improvement in the matching of the estimation by (5.76) and the resulting amplitude as $\hat{K}$ is reduced (Figure 5.6B).

The tension-sensitivity of the cortical force generators, modulated by γ, is key for oscillations. Setting $\gamma = 0$ in (5.72) uncouples the values of $\hat{B}_0^{\pm}$ from the spindle pole dynamics, thus $\hat{B}_0^{+} = \hat{B}_0^{-}$ and (5.73) becomes

$$\bar{\bar{z}}_0 = -\left(\hat{\xi} + 2\left(1+\rho\right)^{-1}\right)\bar{\bar{z}}_{0,\hat{t}}. \tag{5.77}$$

This linear relationship between $\bar{\bar{z}}_0$ and $\bar{\bar{z}}_{0,\hat{t}}$ suggests that no oscillations occur in this case. The coupling of the populations of bound force generators through the tension-sensitive un-

binding rate is required for oscillations, as was shown by stability analysis of the ODE system (5.69).

5.5 Chapter Summary

In this chapter we have systematically reduced the Fokker-Planck PDEs introduced in Section 4.3 into a smaller system of ODEs using systematic asymptotic analysis. By assuming that diffusive terms α, β and the rates of binding and unbinding ($\bar{\omega}_{\text{on}}$ and $\bar{\omega}_0$ respectively) are small, we create a system of ODEs which are easily explored using linear stability analysis. We summarise the findings of this chapter with respect to the findings of Chapter 4, while its implications and comparison to the biological results we presented in Chapter 3 are postponed until Chapter 6.

This ODE system appropriately describes the push/pull model when non-dimensionalised binding and unbinding rates $\bar{\omega}_{\text{on}}$ and $\bar{\omega}_0$, and diffusion terms $\alpha^{1/2}$ and $\beta^{1/2}$ are small. The non-dimensionalisation method normalised binding, unbinding and diffusion to timescales set by the velocity of the force generators, thus they must be small relative to the unloaded motor protein velocity. In doing so, we assume further that relaxation of the unbound force generators relative to the unloaded motor protein velocity, Γ, is rapid.

The stability threshold identified by this analysis allowed us to determine the main factors which promote oscillations of the spindle pole. A wedge-shaped region in $(N, \bar{\omega}_{\text{on}})$ space supports oscillations (Figure 5.1A), bounded by an upper and lower threshold on the value of $\bar{\omega}_{\text{on}}$ and a lower threshold on the value of N. The stability boundary with this shape was also described by Grill *et al.* in their ODE reduction, though the factors which affect its position were not explicitly explored [80]. The upper threshold $\bar{\omega}_{\text{on}}^{\dagger}$ is solely dependent upon the unbinding parameters $\bar{\omega}_0$ and γ, and is independent of K, thus increased unbinding and increased tension-sensitivity to unbinding both promote oscillations across a wider region of binding affinities $\bar{\omega}_{\text{on}}$. This highlights the importance of unbinding of the force generators for the emergence of oscillations. We have identified that tension-sensitivity of unbinding is crucial for spindle pole oscillations to occur, with $\gamma > 1$ being necessary for any region of parameter space to host oscillations. Shee *et al.* (2021) describe a similar system of force generator loading/unloading upon a microtubule, where the microtubule is attached to a harmonic trap at one end and acted upon by the force generators at the other [152]. Their analysis uses mean field theory to describe the dynamics of the single population of force generators as a system of three ODEs in the position of the microtubule position, the number of bound force generators, and the extension of the bound force generators. They then connect this mean field model to a Fokker-Planck description similar to that presented here and in [80]. Interestingly, their analysis also highlights the requirement of a tension-sensitivity parameter in the unbinding rate of the force generators [152]. This result is interesting as the harmonic trap acts as a restoring force which is sufficient to create oscillatory dynamics of the microtubule by interaction with one population of force generators [152]. We therefore wonder whether the two opposing populations of force generators are required

for oscillations, or whether the presence of the microtubule restoring force combined with one-sided pulling of the spindle pole would be sufficient to create oscillations of the pole, though no longer centred around $\bar{z} = 0$, and we suggest this as a future direction for further analysis of the model.

Reducing the relative restoring force also resulted in an increase in the area of oscillatory space in $(N, \bar{\omega}_{\text{on}})$ (Figure 5.1A) This result matches what was suggested by the re-emergence of oscillations when K was reduced in the PDE simulations (Figure 4.13C). The period of oscillation also increases as the restoring force decreases (Figure 5.2B), thus the magnitude of the restoring force is important for promoting oscillations. Interestingly, in the limit of small $\hat{K}$ the ODEs may reduced to a single equation (5.74) capable of estimating the limit cycle of the relaxation oscillations (Figure 5.5) as well as the amplitude of oscillation (5.74) (Figure 5.6).

The ODE system has also revealed promoters of non-linearity in the resulting oscillations. The reduction of the restoring force relative to the pulling forces by either decreasing K or increasing N results in the emergence of relaxation oscillations (Figure 5.3D, E). Alternatively, increasing the binding rate $\bar{\omega}_{\text{on}}$ makes the oscillations more sinusoidal. Thus the balances of pulling and pushing forces, as well as the affinity for force generator-microtubule binding, can affect the shape of the oscillations.

The simplicity of the ODE system is key for expansion of this model into 2D. The complexity of the higher order models and their associated cost of computation restricts their usage to 1D. Further, reducing the higher order models has allowed us to identify the key parameters for promoting dynamic movements of the spindle pole. Thus the relative importance of the parameters for producing dynamic movements in 2D will be more easily determined. Unfortunately, due to time-constraints, results for the 2D model were not obtained in time to present here. However, an initial expansion to 2D is presented in Appendix A. In the next section we will discuss more directly the biological relevance of the mathematical models explored and how they can shed light on the modes of spindle movement we identified in Chapter 3.

Chapter 6

Conclusions and future directions: integrating experimental observations and mathematical modelling

Cell division is a crucial process to get right for a developing organism, driving tissue growth and determining the fate of the resulting daughter cells [31]. Cell divisions within tissues both affect, and are affected by, the tissue environment [219]–[221], thus reading and responding to the external environment via regulation of cell division is an important process for maintaining tissue homeostasis [8]–[11].

Cells in stretched epithelial tissue have been shown to increase their division rate and also reorient their divisions along the axis of stretch [15], though whether this division orientation response to stretch occurs due to cell shape-based mechanisms or direct force sensing is unclear as cell shape and force are highly coupled [15], [21], [40], [222]. The positioning of the mitotic spindle to determine division orientation has been attributed to interactions of the astral microtubules with the cell cortex, either by pushing or by pulling from cortical proteins [22], [23]. A key protein involved in spindle positioning is NuMA, a cortical protein which anchors dynein-dynactin to impart pulling forces on the spindle through the astral microtubules [64]. NuMA has also been implicated in stretch-induced spindle alignment [27], [103]. Specifically, the Woolner lab has recently shown that NuMA is required for tension-sensitive orientation of the spindle along the cell long axis, as defined by the locations of the TCVs, when cells experience an anisotropic stretch [27]. However the mechanisms by which the spindle is positioned differently in response to response to stretch remain unclear. Unpublished work from the Woolner lab suggests that NuMA directly senses force rather than cell shape [27], but how does the applied force affect NuMA to create a spindle response?

Our aim here was to shed light on the spindle pole positioning factors which may be affected by the application of an external stretch, by analysing the translational and rotational dynamics of the spindle pole at a high temporal resolution in stretched and unstretched tissues. We then analysed spindle dynamics in stretched tissues subject to a partial knockdown of NuMA, to assess how the spindle positioning mechanisms were perturbed. By using mathematical modelling to determine the factors which affect spindle dynamics, we

aimed to advance our understanding of how tension may affect NuMA-mediated spindle positioning.

Mathematically, we have built a direct link between stochastic simulations, a Fokker-Planck model, a system of nonlinear ODEs and an algebraic model of relaxation oscillations. The stochastic simulations qualitatively mimic the noisy time series data of spindle oscillations (Figure 4.5 compared with Figures 3.9 and 3.7). The amplitude and period of the stochastic simulation oscillations are well matched with measurements of spindle pole displacements and periods of the posterior pole of the *C. elegans* first division. As parameters pertinent to the *Xenopus laevis* system were difficult to find, we deferred to the parameters specific to *C. elegans* with the hope of exploring the parameter space to determine where may be more appropriate for *Xenopus laevis*. The simpler models reveal important relationships between parameters that are very hard to extract from simulations due to their complex formulation and also their computational cost, and we believe these relationships between parameters are important for spindle dynamics. Interestingly, the lower-order models presented can be used to estimate the upper stability boundary of $\bar{\omega}_{\text{on}}$ which is a function only of the unbinding rate and tension-sensitivity, and the value of $\bar{\omega}^{\dagger}_{\text{on}}$ was well conserved through the Fokker-Planck equations (Figure 4.12 and $\bar{\omega}^{\dagger}_{\text{on}} = 0.0074$, using (5.69)). When restoring forces are reduced, the algebraic equation (5.74) can be used to describe the slow phases of the limit cycle of the oscillations, as well as the amplitude of oscillation. For small $\hat{K}$, the amplitude of oscillation determined by (5.76) is well matched with the amplitude of oscillations produced by the Fokker-Planck equations (Figure 5.6Bii) but is less appropriate when $\hat{K}$ is larger, as is indicated by the poorer matching between the amplitude estimated by (5.76) and the oscillatory amplitude for $\hat{K} = 0.4$ (Figure 5.6Bi). Across the stochastic simulations, Fokker-Planck equations and the ODE system, we saw a reduction in oscillatory dynamics for increasing restoring forces and decreasing numbers of force generators, highlighting the importance of the balance of pulling and pushing on the spindle pole to create a dynamic response. How this would translate to a 2D model is an interesting thought, as oscillations in the spindle mitotic angle would require both spindle poles to oscillate in anti-phase to one another. We hope that the 2D model in development (Appendix A) will provide further insight into the dynamic spindle system.

Mathematical analysis has revealed that a spindle pole being acted upon by pulling forces from opposing populations of force generators and a restoring force from microtubules can oscillate when perturbed from a stable centre position [80]. Mitotic spindles are not formed precisely at the geometric centre of the cell and undergo net centring over the course of metaphase (Figure 3.2C). Thus the origin of this perturbation from the centre is biologically relevant, motivating the use of a theoretical model to explain their origin. Oscillations are predicted to occur in the spindle pole position in a specific region of parameter space, where the position of the stability boundary depends upon the factors which modulate the sizes of the restoring forces and the pulling forces (Figure 5.1). It is a requirement for oscillations that the unbinding rate of cortical force generators is sufficiently tension sensitive, i.e. $\gamma > 1$ (by (5.69)). This requirement may be met biologically given that dynein

forms a slip bond with microtubules [61], however the directional slip bond behaviour has been omitted from this model and may provide more interesting dynamics [62]. This directional slip bond behaviour could be incorporated into the stochastic descriptions of the model very simply, by imposing conditions on unbinding, such that if the force acting on dynein is greatest toward the spindle pole (for example, if the spindle pole is moving toward dynein faster than dynein's walking velocity), then $\bar{\omega}_0$ would be a smaller value. However, more work would need to be done to determine how this would carry through to the ODE description of the model.

The region of $(N, \bar{\omega}_{\text{on}})$ parameter space which gives rise to oscillations is also expanded when restoring forces are reduced relative to pulling forces (Figure 5.1A). Restoring forces may be altered by differences in microtubule stiffness parameter k_{MT} which defines the relative stiffness of the microtubule due to bending effects [135], [137] and also due to the process of dynamic instability, where highly dynamic microtubules contact and push against the cell cortex as they grow and shrink [137]. The most interesting augmentation of k_{MT} is its reduction when microtubules are assumed to hinge at their nucleation point rather than being held clamped at its end [135], [137]. Crucially, NuMA's role as a structural protein, focussing microtubules at the spindle poles [24], is suggested to act as a clamp for microtubules, preventing them from hinging and therefore increasing their flexural rigidity and subsequently their stiffness [135]. We suggest that a partial knockdown of NuMA may affect this clamping mechanism and lead to a reduced relative microtubule stiffness due to potential hinging of the microtubules at the spindle poles. When Tarannum (2022) subjected *Xenopus laevis* cells to a more complete morpholino-targetted knockdown of NuMA, the integrity of the mitotic spindle was perturbed and multipolar spindles formed, which supports this suggestion [27], along with similar defects in spindle pole structure upon overexpression of LGN which prevents NuMA from functioning at the spindle pole [113]. Reduction of restoring parameters K in the ODE model by two orders of magnitude resulted in oscillations with periods spanning approximately 120-300 s (using 5.60)), which is similar to the period of oscillation seen in NuMA KD tissues (Figure 3.10B), while for larger K the ODE model predicts a range of periods spanning 2-90 s, which is closer in magnitude to those measured in stretched and unstretched tissues (Figure 3.10B). Interestingly, reduction of restoring forces relative to pulling forces was shown to result in the emergence of relaxation oscillations (Figures 4.11 and 5.3C, D), though increasing binding was shown to return the oscillations to a more sinusoidal nature (Figure 5.4). Thus, relaxation oscillations may be an indicator of large pulling forces relative to restoring forces, though the degree of non-linearity of the oscillation may be less extreme if the binding rates of dynein are high.

The relevance of the emergence of relaxation oscillations is unclear. Relaxation oscillations have been shown to arise from interactions between coupled oscillators. It has been shown elsewhere that oscillations in the activation of cell cycle protein Cdk1 by early embryonic calcium waves have a relaxation structure due to the positive and negative feedback loops existing within the activation circuit [223]. Relaxation oscillations have also been used to describe the activation of the heartbeat [224]. Indeed, relaxation oscillations in biology

occur naturally under coupling of oscillators. Notably, relaxation oscillators have amplitudes which are independent of start conditions, and are characterised by segments of slow change interrupted by segments of fast change [225]. We have shown that the fast and slow phases encountered in the 1D model are due to the rapid unbinding rate $\bar{\omega}_0 e^{\gamma \bar{y}}$ when bound force generators are extended significantly. That is, in each population we have two coupled oscillators: the number of bound force generators (represented by the probability density function of the bound force generators $\bar{P}_{\mathrm{b}}^{\pm}$) oscillates in anti-phase with the average extension of the bound force generators $\bar{y}_{\mathrm{c}}^{\pm}$ due to the extension-sensitive off rate ($\gamma > 1$) and the constant binding rate $\bar{\omega}_{\mathrm{on}}$ which allows the numbers of bound force generators to recover. These oscillating populations in each cortex are then coupled to one another through their connection to the spindle pole. The detailed response of the spindle pole (little response for high restoring forces, large responses for low restoring forces) limits the coupling between these populations. Thus highly coupled oscillating populations, in the form of a highly responsive spindle pole position, leads to the emergence of relaxation oscillations. While our experimental analysis did not reveal obvious relaxation oscillations by visual analysis of the oscillatory tracks (e.g. Figures 3.7, 3.9 and 3.11), Larson and Bement (2017) identified that spindles in the epithelium of the *Xenopus laevis* embryo move away from the cell cortex quicker than they approach [77]. This non-linearity in the velocity of the spindle suggests that non-sinusoidal oscillations of the spindle may be revealed upon further probing of our collected data.

Unfortunately, 1D models of spindle orientation can only recapitulate the dynamics we see experimentally to a certain degree. We plan to develop the 2D framework we have established in Appendix A and observe how the 1D behaviour might translate in two dimensions. Experimentally, oscillations in the spindle angle require spindle poles to oscillate in anti-phase to one another to create measurable changes in the angle, and the additional complexity of torque on the spindle array is likely to affect force transfer through the structure and subsequent spindle positioning. Our estimation of the amplitude of the oscillations of the spindle pole (5.76) may be used to determine the relative order of magnitude of the parameters in the cells of the *Xenopus laevis*, by matching with cell length scales and/or analysis of the movements of individual poles. As this work was concerned with whole-spindle movements, analysis of the individual spindle poles was not undertaken.

The 1D model shows that factors which result in an increase in oscillation period also show an increase in oscillation amplitude, though within cells the amplitude will be limited by the size of the cell. This limit is not accounted for in the 1D model. How geometric constraints may influence the spindle behaviour will be paramount to determining which aspects of spindle movement are a result of cell shape alone and which are influenced by the application of an external force. Thus the data we collected on the translational movements of the spindle pole are open to interpretation. In particular, our analysis of the directions of major and minor orientations of the track traced by the centre of mitotic spindle yielded surprising results which we could not explain by analysis of the data alone (Figure 3.6). In particular, the tracks followed by the mitotic spindle were highly elongated relative to the

cell shapes (Figure 3.5) and showed a bias which was comparable to the division orientation but not cell shape in unstretched and stretched tissues (Figures 3.4E, G and Figures 3.6A, B).

Interestingly, the track orientations showed no significant bias toward or away from the cell shape orientation in either elongated or circular cells (Figure 3.4E, G), thus a force-sensing mechanism which is variable along the cell shape may contribute, though we have no clear proposals given the current data for what this may be. Due to the complex relationship between pulling and pushing forces, we propose that the changing spindle angle creates complicated dynamic translational movements, and we believe that a 2D model will contribute to our understanding. We believe that analysis of the spindle movements with respect to the spindle orientation through metaphase, such as the pole-pole kymographs employed in [18], will also help to shed light on this mechanism, particularly if we analyse the movements both along and perpendicular to the pole-pole axis.

What factors could lead to the difference in numbers of oscillating spindles? According to the 1D model, oscillations of the 1D spindle pole are promoted by decreasing restoring forces, increasing tension sensitivity of unbinding, increasing the base unbinding rate, increasing the number of force generators, and changing the binding affinity within two thresholds. As we saw no difference in the period of oscillation between stretched and unstretched cells, we assume that stretching a tissue does not affect the spindle restoring force, as changes in this have been shown to alter the period of oscillation (in (5.60)). We also note that the number of oscillating spindles increased between the first and second half of metaphase (Figure 3.13A), thus a change within the cell environment also promotes oscillations (Figure 3.13B,C). Unpublished work in the Woolner lab has shown that NuMA localises to the cell cortex along the pole-pole axis, and this localisation increases as metaphase proceeds [27]. This could result in more oscillations as metaphase proceeds because the number of force generators N is increased above the stability threshold (Figure 5.1A). If the number of force generators is limited within the cell and remains close to the stability threshold we would expect that, if there are sufficient force generators within the cell to create an oscillatory response, then the resulting period is unlikely to change once recruitment to the cell cortex is complete. If a cell has a large number of force generators, we would expect to see the onset of oscillations earlier in metaphase, and the period of oscillation may increase as metaphase proceeds (Figures 4.10 and 5.2A). A trend of an increased period in the second half of metaphase was observed in the unstretched tissues, though the increase was not statistically significant (Figure 3.13B). We suggest that this may be too subtle a difference to be significant without a larger dataset. Interestingly, in other work in the Woolner lab we have seen that the dynamic localisation of NuMA to the cortex was slightly more rapid in stretched cells, with recruitment to the polar cortex happening earlier in metaphase than in unstretched tissues [27]. This is interesting for two reasons. The first is that we would therefore expect a smaller difference between the periods of oscillation between the first and second half of metaphase as N saturates earlier in mitosis in stretched cells. We observed this as the trend of the increased period was eradicated in stretched tis-

sues (Figures 3.13C). The second is that we would therefore expect more oscillatory spindles in the stretched tissue vs the unstretched tissue, and for the number of oscillating spindles between the two halves of metaphase to remain relatively unchanged. Interestingly, we saw a reduction in the number of oscillating spindles in the stretched tissue when compared with the unstretched tissue. Further, the number of oscillating spindles in the second half of metaphase was elevated, though not significantly. We therefore suggest that an additional mechanism may exist which can push the system into an oscillatory region of parameter space, and that this mechanism is tension-sensitive, such that increased cell tension reduces the size of the oscillatory region and makes it more difficult to access. Pecreaux *et al.* (2006) propose that during the oscillation of the posterior pole during the asymmetric division of the single cell *C. elegans* embryo, the processivity of dynein increases [78]. That is, the binding rate of dynein to impart a pulling force increases as metaphase proceeds, an effect they believe to be mediated through LIN-5 [78] which has been speculated as being a homolog to NuMA due to its large coiled-coil and binding to GPR-1,2 (LGN) [67], [81]. While we have considered the number of binding force generators to change as NuMA localises differentially to the cortex in stretch conditions, we have not considered that the stretch itself may be altering the ability of dynein to bind to NuMA. Thus the binding rate parameter $\bar{\omega}_{\text{on}}$ could be used to describe dynein's binding to NuMA as well as the binding rate to microtubules, and stretch could then have an impact on the binding rate $\bar{\omega}_{\text{on}}$.

NuMA's dynein binding domain overlaps with the coiled-coil region [65]. It has been shown mathematically that it is possible for binding to cause amplified changes in the structure of coiled-coils [122], indeed, the binding of ATP to dynein produces sliding of the helices in one of dynein's coiled-coils which facilitates its walking motion [226], [227] and changes its affinity for microtubule binding [228]. In a similar mechanism, we suggest that an externally applied tension could be translated to NuMA via the 4.1 binding domain [103] to cause a conformational change in the structure of NuMA's coiled-coil, which would affect the binding affinity to dynein. Deletion of the 4.1 binding domain of NuMA has shown to result in spindle positioning defects [103] which suppoorts this suggestion. Interestingly, a recent study into spindle rotation in response to tension showed that while the spindle reoriented with respect to tension, the localisation of NuMA did not reorient [83]. Tension at the cortex was optogenetically enhanced by localised increase in RhoA activity leading to myosin contractility. Spindles rotated away from sites of contractility, though NuMA's localisation was unchanged following the activation of RhoA [83]. This supports our suggestion that tension increases NuMA's ability to bind with dynein. Increased sites of cortical contractility will result in tension away from the contraction, therefore NuMA which is localised further away from the site of contraction will be able to bind with dynein and create a net pulling force on the mitotic spindle to rotate it away from the contraction site. If NuMA's ability to bind with dynein is tension-dependent in this way, then NuMA does not need to relocalise in order to create this directed pulling response, as NuMA at the site of contraction will be less likely to bind with dynein to create a spindle-movement response.

This work has identified a number of interesting avenues to further explore. The results

of the mathematical model have highlighted a potential second mechanism for NuMA in spindle positioning which is less well defined, where its localisation at the spindle poles may not only be important for maintaining spindle structure, as has been previously shown, but also for correct spindle positioning by providing a scaffold for efficient transfer of microtubule pushing forces. We suggest that taking an alternative route of NuMA depletion through the application of chemical inhibitor MLN8237 would allow us to further explore this effect (as in [83]). Application of MLN8237 acts to inhibit Aurora-A-mediated phosphorylation of NuMA at the spindle poles, meaning that NuMA would not be sequestered from the spindle poles to the cell cortex [118]. Then we could assess the spindle dynamics due to a loss of cortical NuMA without depleting NuMA at the spindle pole. Alternatively, expressing a form of NuMA lacking its LGN binding domain has also been shown to lose its cortical localisation and remain at the spindle poles [103]. We would expect in either of these cases to see a cessation of spindle pole oscillations and movements as the number of cortical force generators should remain below the threshold required to induce oscillations, as the threshold will not be perturbed by a reduction of restoring forces.

Another avenue to explore would be the difference in the number of oscillators in stretched and unstretched cells. We have suggested the potential for tension-mediated conformational changes to NuMA's coiled-coil region resulting in a perturbation of its binding affinity with dynein/dynactin, though whether or not this change can result in the increase of the number of oscillators we see as metaphase proceeds is to be determined. We propose that truncations to NuMA's coiled-coil domain may be used to determine whether the coiled-coil region is important for tension-sensitive spindle positioning. We also propose that the development of the 2D model will help us to determine to what extent the movements of the mitotic spindle can be explained by cell shape alone and thus point to dynamics which may be a result of tension-sensitive effects.

Overall this study has revealed potential mechanisms for spindle positioning with respect to cell shape and cell tension. We propose that NuMA's role in spindle positioning is not restricted to its cortical localisation to pull on the spindle, but also affects the restoring forces provided by microtubules to centre the spindle within the cell due to its localisation at the spindle poles. We have demonstrated that oscillations of the mitotic spindle occur in both stretched and unstretched tissues with a similar period, though the threshold to enter an oscillatory regime is less easily crossed for stretched tissues, suggesting a tension-sensitive mechanism may be responsible. We propose that NuMA's large coiled-coil domain may undergo structural changes under tension which facilitate the binding of dynein and pushes tissues under tension closer to the upper threshold between stable and oscillatory solutions, reducing their chances of oscillating.

References

[1] D. T. Bergstralh and D. St Johnston, "Spindle orientation: What if it goes wrong?" In *Seminars in cell & developmental biology*, Elsevier, vol. 34, 2014, pp. 140–145.

[2] X. Morin and Y. Bellaïche, "Mitotic spindle orientation in asymmetric and symmetric cell divisions during animal development," *Developmental cell*, vol. 21, no. 1, pp. 102–119, 2011.

[3] R. Keller, L. A. Davidson, and D. R. Shook, "How we are shaped: The biomechanics of gastrulation," *Differentiation: original article*, vol. 71, no. 3, pp. 171–205, 2003.

[4] L. LeGoff, H. Rouault, and T. Lecuit, "A global pattern of mechanical stress polarizes cell divisions and cell shape in the growing drosophila wing disc," *Development*, vol. 140, no. 19, pp. 4051–4059, 2013.

[5] Y. Mao, A. L. Tournier, P. A. Bates, J. E. Gale, N. Tapon, and B. J. Thompson, "Planar polarization of the atypical myosin dachs orients cell divisions in drosophila," *Genes & development*, vol. 25, no. 2, pp. 131–136, 2011.

[6] P. Campinho, M. Behrndt, J. Ranft, T. Risler, N. Minc, and C.-P. Heisenberg, "Tension-oriented cell divisions limit anisotropic tissue tension in epithelial spreading during zebrafish epiboly," *Nature cell biology*, vol. 15, no. 12, pp. 1405–1414, 2013.

[7] M. Rauzi, U. Krzic, T. E. Saunders, M. Krajnc, P. Ziherl, L. Hufnagel, and M. Leptin, "Embryo-scale tissue mechanics during drosophila gastrulation movements," *Nature communications*, vol. 6, no. 1, p. 8677, 2015.

[8] Z. Tang, Y. Hu, Z. Wang, K. Jiang, C. Zhan, W. F. Marshall, and N. Tang, "Mechanical forces program the orientation of cell division during airway tube morphogenesis," *Developmental cell*, vol. 44, no. 3, pp. 313–325, 2018.

[9] N. I. Petridou, Z. Spiró, and C.-P. Heisenberg, "Multiscale force sensing in development," *Nature cell biology*, vol. 19, no. 6, pp. 581–588, 2017.

[10] C. Guillot and T. Lecuit, "Mechanics of epithelial tissue homeostasis and morphogenesis," *Science*, vol. 340, no. 6137, pp. 1185–1189, 2013.

[11] K. D. Irvine and B. I. Shraiman, "Mechanical control of growth: Ideas, facts and challenges," *Development*, vol. 144, no. 23, pp. 4238–4248, 2017.

[12] K. C. Hart, J. Tan, K. A. Siemers, J. Y. Sim, B. L. Pruitt, W. J. Nelson, and M. Gloerich, "E-cadherin and lgn align epithelial cell divisions with tissue tension independently of cell shape," *Proceedings of the National Academy of Sciences*, vol. 114, no. 29, E5845–E5853, 2017.

[13] J. Fink, N. Carpi, T. Betz, A. Bétard, M. Chebah, A. Azioune, M. Bornens, C. Sykes, L. Fetler, D. Cuvelier, *et al.*, "External forces control mitotic spindle positioning," *Nature cell biology*, vol. 13, no. 7, pp. 771–778, 2011.

[14] E. Scarpa, C. Finet, G. B. Blanchard, and B. Sanson, "Actomyosin-driven tension at compartmental boundaries orients cell division independently of cell geometry in vivo," *Developmental cell*, vol. 47, no. 6, pp. 727–740, 2018.

[15] A. Nestor-Bergmann, G. A. Stooke-Vaughan, G. K. Goddard, T. Starborg, O. E. Jensen, and S. Woolner, "Decoupling the roles of cell shape and mechanical stress in orienting and cueing epithelial mitosis," *Cell reports*, vol. 26, no. 8, pp. 2088–2100, 2019.

[16] M. S. Lam, A. Lisica, N. Ramkumar, G. Hunter, Y. Mao, G. Charras, and B. Baum, "Isotropic myosin-generated tissue tension is required for the dynamic orientation of the mitotic spindle," *Molecular Biology of the Cell*, vol. 31, no. 13, pp. 1370–1379, 2020.

[17] T. P. Wyatt, A. R. Harris, M. Lam, Q. Cheng, J. Bellis, A. Dimitracopoulos, A. J. Kabla, G. T. Charras, and B. Baum, "Emergence of homeostatic epithelial packing and stress dissipation through divisions oriented along the long cell axis," *Proceedings of the National Academy of Sciences*, vol. 112, no. 18, pp. 5726–5731, 2015.

[18] A. M. Corrigan, R. L. Shrestha, I. Zulkipli, N. Hiroi, Y. Liu, N. Tamura, B. Yang, J. Patel, A. Funahashi, A. Donald, *et al.*, "Automated tracking of mitotic spindle pole positions shows that lgn is required for spindle rotation but not orientation maintenance," *Cell Cycle*, vol. 12, no. 16, pp. 2643–2655, 2013.

[19] N. Minc, D. Burgess, and F. Chang, "Influence of cell geometry on division-plane positioning," *Cell*, vol. 144, no. 3, pp. 414–426, 2011.

[20] A. J. Quyn, P. L. Appleton, F. A. Carey, R. J. Steele, N. Barker, H. Clevers, R. A. Ridgway, O. J. Sansom, and I. S. Näthke, "Spindle orientation bias in gut epithelial stem cell compartments is lost in precancerous tissue," *Cell stem cell*, vol. 6, no. 2, pp. 175–181, 2010.

[21] A. Nestor-Bergmann, G. Goddard, S. Woolner, and O. E. Jensen, "Relating cell shape and mechanical stress in a spatially disordered epithelium using a vertex-

based model," *Mathematical medicine and biology: a journal of the IMA*, vol. 35, no. Supplement_1, pp. i1–i27, 2018.

[22] S. Kotak and P. Gönczy, "Mechanisms of spindle positioning: Cortical force generators in the limelight," *Current opinion in cell biology*, vol. 25, no. 6, pp. 741–748, 2013.

[23] F. J. McNally, "Mechanisms of spindle positioning," *Journal of Cell Biology*, vol. 200, no. 2, pp. 131–140, 2013.

[24] A. Merdes, K. Ramyar, J. D. Vechio, and D. W. Cleveland, "A complex of numa and cytoplasmic dynein is essential for mitotic spindle assembly," *Cell*, vol. 87, no. 3, pp. 447–458, 1996.

[25] A. Merdes, R. Heald, K. Samejima, W. C. Earnshaw, and D. W. Cleveland, "Formation of spindle poles by dynein/dynactin-dependent transport of numa," *The Journal of cell biology*, vol. 149, no. 4, pp. 851–862, 2000.

[26] T. Kiyomitsu and I. M. Cheeseman, "Chromosome-and spindle-pole-derived signals generate an intrinsic code for spindle position and orientation," *Nature cell biology*, vol. 14, no. 3, pp. 311–317, 2012.

[27] N. Tarannum, "Mechanical regulation of cell division orientation: Investigating the role of nuclear mitotic apparatus protein," Ph.D. dissertation, University of Manchester, 2022.

[28] B. Alberts, A. Johnson, J. Lewis, D. Morgan, M. Raff, K. Roberts, and P. Walter, *Molecular biology of the cell (6th ed.)* Garland Science, Taylor and Francis Group, 2015.

[29] Y. Zhai, P. J. Kronebusch, P. M. Simon, and G. G. Borisy, "Microtubule dynamics at the g2/m transition: Abrupt breakdown of cytoplasmic microtubules at nuclear envelope breakdown and implications for spindle morphogenesis.," *The Journal of cell biology*, vol. 135, no. 1, pp. 201–214, 1996.

[30] A. V. Taubenberger, B. Baum, and H. K. Matthews, "The mechanics of mitotic cell rounding," *Frontiers in cell and developmental biology*, p. 687, 2020.

[31] J. C. Pease and J. S. Tirnauer, "Mitotic spindle misorientation in cancer–out of alignment and into the fire," *Journal of cell science*, vol. 124, no. 7, pp. 1007–1016, 2011.

[32] T. Lechler and E. Fuchs, "Asymmetric cell divisions promote stratification and differentiation of mammalian skin," *Nature*, vol. 437, no. 7056, pp. 275–280, 2005.

[33] C. Luxenburg, H. Amalia Pasolli, S. E. Williams, and E. Fuchs, "Developmental roles for srf, cortical cytoskeleton and cell shape in epidermal spindle orientation," *Nature cell biology*, vol. 13, no. 3, pp. 203–214, 2011.

[34] S. K. McConnell, "Constructing the cerebral cortex: Neurogenesis and fate determination," *Neuron*, vol. 15, no. 4, pp. 761–768, 1995.

[35] X. Morin, F. Jaouen, and P. Durbec, "Control of planar divisions by the g-protein regulator lgn maintains progenitors in the chick neuroepithelium," *Nature neuroscience*, vol. 10, no. 11, pp. 1440–1448, 2007.

[36] N. D. Poulson and T. Lechler, "Robust control of mitotic spindle orientation in the developing epidermis," *Journal of Cell Biology*, vol. 191, no. 5, pp. 915–922, 2010.

[37] D. T. Bergstralh, T. Haack, and D. St Johnston, "Epithelial polarity and spindle orientation: Intersecting pathways," *Philosophical Transactions of the Royal Society B: Biological Sciences*, vol. 368, no. 1629, p. 20 130 291, 2013.

[38] G. Costa, K. I. Harrington, H. E. Lovegrove, D. J. Page, S. Chakravartula, K. Bentley, and S. P. Herbert, "Asymmetric division coordinates collective cell migration in angiogenesis," *Nature cell biology*, vol. 18, no. 12, pp. 1292–1301, 2016.

[39] S. M. da Silva and J.-P. Vincent, "Oriented cell divisions in the extending germband of drosophila," 2007.

[40] A. Nestor-Bergmann, G. Goddard, and S. Woolner, "Force and the spindle: Mechanical cues in mitotic spindle orientation," in *Seminars in cell & developmental biology*, Elsevier, vol. 34, 2014, pp. 133–139.

[41] T. M. Finegan, D. Na, C. Cammarota, A. V. Skeeters, T. J. Nádasi, N. S. Dawney, A. G. Fletcher, P. W. Oakes, and D. T. Bergstralh, "Tissue tension and not interphase cell shape determines cell division orientation in the drosophila follicular epithelium," *The EMBO journal*, vol. 38, no. 3, e100072, 2019.

[42] O. Hertwig, "Ueber den werth der ersten furchungszellen für die organbildung des embryo experimentelle studien am frosch-und tritonei," *Archiv für mikroskopische Anatomie*, vol. 42, no. 4, pp. 662–807, 1893.

[43] F. Bosveld, O. Markova, B. Guirao, C. Martin, Z. Wang, A. Pierre, M. Balakireva, I. Gaugue, A. Ainslie, N. Christophorou, *et al.*, "Epithelial tricellular junctions act as interphase cell shape sensors to orient mitosis," *Nature*, vol. 530, no. 7591, pp. 495–498, 2016.

[44] C. B. O'Connell and Y.-l. Wang, "Mammalian spindle orientation and position respond to changes in cell shape in a dynein-dependent fashion," *Molecular biology of the cell*, vol. 11, no. 5, pp. 1765–1774, 2000.

[45] M. Théry, A. Jiménez-Dalmaroni, V. Racine, M. Bornens, and F. Jülicher, "Experimental and theoretical study of mitotic spindle orientation," *Nature*, vol. 447, no. 7143, pp. 493–496, 2007.

[46] A. Desai and T. J. Mitchison, "Microtubule polymerization dynamics," *Annual review of cell and developmental biology*, vol. 13, no. 1, pp. 83–117, 1997.

[47] E. Karsenti and I. Vernos, "The mitotic spindle: A self-made machine," *Science*, vol. 294, no. 5542, pp. 543–547, 2001.

[48] T. Mitchison and E. Salmon, "Mitosis: A history of division," *Nature cell biology*, vol. 3, no. 1, E17–E21, 2001.

[49] D. A. Compton, "Spindle assembly in animal cells," *Annual review of biochemistry*, vol. 69, no. 1, pp. 95–114, 2000.

[50] M. Moritz, M. B. Braunfeld, J. W. Sedat, B. Alberts, and D. A. Agard, "Microtubule nucleation by γ-tubulin-containing rings in the centrosome," *Nature*, vol. 378, no. 6557, pp. 638–640, 1995.

[51] T. Mitchison and M. Kirschner, "Dynamic instability of microtubule growth," *nature*, vol. 312, no. 5991, pp. 237–242, 1984.

[52] N. B. Gudimchuk and J. R. McIntosh, "Regulation of microtubule dynamics, mechanics and function through the growing tip," *Nature reviews Molecular cell biology*, vol. 22, no. 12, pp. 777–795, 2021.

[53] M. P. Yaffe, N. Stuurman, and R. D. Vale, "Mitochondrial positioning in fission yeast is driven by association with dynamic microtubules and mitotic spindle poles," *Proceedings of the National Academy of Sciences*, vol. 100, no. 20, pp. 11 424–11 428, 2003.

[54] M. Dogterom, J. W. Kerssemakers, G. Romet-Lemonne, and M. E. Janson, "Force generation by dynamic microtubules," *Current opinion in cell biology*, vol. 17, no. 1, pp. 67–74, 2005.

[55] J. Kajtez, A. Solomatina, M. Novak, B. Polak, K. Vukušić, J. Rüdiger, G. Cojoc, A. Milas, I. Šumanovac Šestak, P. Risteski, *et al.*, "Overlap microtubules link sister k-fibres and balance the forces on bi-oriented kinetochores," *Nature communications*, vol. 7, no. 1, p. 10 298, 2016.

[56] M. E. Tanenbaum and R. H. Medema, "Mechanisms of centrosome separation and bipolar spindle assembly," *Developmental cell*, vol. 19, no. 6, pp. 797–806, 2010.

[57] J. M. Scholey, "Kinesin-5 in drosophila embryo mitosis: Sliding filament or spindle matrix mechanism?" *Cell motility and the cytoskeleton*, vol. 66, no. 8, pp. 500–508, 2009.

[58] T. J. Mitchison, P. Maddox, J. Gaetz, A. Groen, M. Shirasu, A. Desai, E. D. Salmon, and T. M. Kapoor, "Roles of polymerization dynamics, opposed motors, and a tensile element in governing the length of xenopus extract meiotic spindles," *Molecular biology of the cell*, vol. 16, no. 6, pp. 3064–3076, 2005.

[59] T. Gaglio, A. Saredi, J. B. Bingham, M. J. Hasbani, S. R. Gill, T. A. Schroer, and D. A. Compton, "Opposing motor activities are required for the organization of the mammalian mitotic spindle pole.," *The Journal of cell biology*, vol. 135, no. 2, pp. 399–414, 1996.

[60] L. A. Jones, C. Villemant, T. Starborg, A. Salter, G. Goddard, P. Ruane, P. G. Woodman, N. Papalopulu, S. Woolner, and V. J. Allan, "Dynein light intermediate chains maintain spindle bipolarity by functioning in centriole cohesion," *Journal of Cell Biology*, vol. 207, no. 4, pp. 499–516, 2014.

[61] Y. Ezber, V. Belyy, S. Can, and A. Yildiz, "Dynein harnesses active fluctuations of microtubules for faster movement," *Nature physics*, vol. 16, no. 3, pp. 312–316, 2020.

[62] L. Rao, F. Berger, M. P. Nicholas, and A. Gennerich, "Molecular mechanism of cytoplasmic dynein tension sensing," *Nature communications*, vol. 10, no. 1, p. 3332, 2019.

[63] R. J. McKenney, W. Huynh, M. E. Tanenbaum, G. Bhabha, and R. D. Vale, "Activation of cytoplasmic dynein motility by dynactin-cargo adapter complexes," *Science*, vol. 345, no. 6194, pp. 337–341, 2014.

[64] M. Okumura, T. Natsume, M. T. Kanemaki, and T. Kiyomitsu, "Dynein–dynactin–numa clusters generate cortical spindle-pulling forces as a multi-arm ensemble," *Elife*, vol. 7, e36559, 2018.

[65] S. Kotak, C. Busso, and P. Gönczy, "Cortical dynein is critical for proper spindle positioning in human cells," *Journal of Cell Biology*, vol. 199, no. 1, pp. 97–110, 2012.

[66] S. Busson, D. Dujardin, A. Moreau, J. Dompierre, and J. R. De Mey, "Dynein and dynactin are localized to astral microtubules and at cortical sites in mitotic epithelial cells," *Current biology*, vol. 8, no. 9, pp. 541–544, 1998.

[67] Q. Du and I. G. Macara, "Mammalian pins is a conformational switch that links numa to heterotrimeric g proteins," *Cell*, vol. 119, no. 4, pp. 503–516, 2004.

[68] M. Gloerich, J. M. Bianchini, K. A. Siemers, D. J. Cohen, and W. J. Nelson, "Cell division orientation is coupled to cell–cell adhesion by the e-cadherin/lgn complex," *Nature communications*, vol. 8, no. 1, p. 13 996, 2017.

[69] E. Peyre, F. Jaouen, M. Saadaoui, L. Haren, A. Merdes, P. Durbec, and X. Morin, "A lateral belt of cortical lgn and numa guides mitotic spindle movements and planar division in neuroepithelial cells," *Journal of Cell Biology*, vol. 193, no. 1, pp. 141–154, 2011.

[70] M. Wühr, E. S. Tan, S. K. Parker, H. W. Detrich, and T. J. Mitchison, "A model for cleavage plane determination in early amphibian and fish embryos," *Current Biology*, vol. 20, no. 22, pp. 2040–2045, 2010.

[71] K. Kimura and A. Kimura, "Intracellular organelles mediate cytoplasmic pulling force for centrosome centration in the caenorhabditis elegans early embryo," *Proceedings of the National Academy of Sciences*, vol. 108, no. 1, pp. 137–142, 2011.

[72] M. De Luca, P. Lavia, and G. Guarguaglini, "Report a functional interplay between aurora-a, plk1 and tpx2 at spindle poles," *Cell cycle*, vol. 5, no. 3, pp. 296–303, 2006.

[73] G. Eot-Houllier, M. Venoux, S. Vidal-Eychenié, M.-T. Hoang, D. Giorgi, and S. Rouquier, "Plk1 regulates both asap localization and its role in spindle pole integrity [s]," *Journal of Biological Chemistry*, vol. 285, no. 38, pp. 29 556–29 568, 2010.

[74] S. Sana, R. Keshri, A. Rajeevan, S. Kapoor, and S. Kotak, "Plk1 regulates spindle orientation by phosphorylating numa in human cells," *Life Science Alliance*, vol. 1, no. 6, 2018.

[75] P. Kalab and R. Heald, "The rangtp gradient–a gps for the mitotic spindle," *Journal of cell science*, vol. 121, no. 10, pp. 1577–1586, 2008.

[76] A. Dimitracopoulos, P. Srivastava, A. Chaigne, Z. Win, R. Shlomovitz, O. M. Lancaster, M. Le Berre, M. Piel, K. Franze, G. Salbreux, *et al.*, "Mechanochemical crosstalk produces cell-intrinsic patterning of the cortex to orient the mitotic spindle," *Current Biology*, vol. 30, no. 18, pp. 3687–3696, 2020.

[77] M. E. Larson and W. M. Bement, "Automated mitotic spindle tracking suggests a link between spindle dynamics, spindle orientation, and anaphase onset in epithelial cells," *Molecular biology of the cell*, vol. 28, no. 6, pp. 746–759, 2017.

[78] J. Pecreaux, J.-C. Röper, K. Kruse, F. Jülicher, A. A. Hyman, S. W. Grill, and J. Howard, "Spindle oscillations during asymmetric cell division require a threshold number of active cortical force generators," *Current Biology*, vol. 16, no. 21, pp. 2111–2122, 2006.

[79] J. Pecreaux, S. Redemann, Z. Alayan, B. Mercat, S. Pastezeur, C. Garzon-Coral, A. A. Hyman, and J. Howard, "The mitotic spindle in the one-cell c. elegans embryo is positioned with high precision and stability," *Biophysical Journal*, vol. 111, no. 8, pp. 1773–1784, 2016.

[80] S. W. Grill, K. Kruse, and F. Jülicher, "Theory of mitotic spindle oscillations," *Physical review letters*, vol. 94, no. 10, p. 108 104, 2005.

[81] K. H. Siller, C. Cabernard, and C. Q. Doe, "The numa-related mud protein binds pins and regulates spindle orientation in drosophila neuroblasts," *Nature cell biology*, vol. 8, no. 6, pp. 594–600, 2006.

[82] C. P. Samora, B. Mogessie, L. Conway, J. L. Ross, A. Straube, and A. D. McAinsh, "Map4 and clasp1 operate as a safety mechanism to maintain a stable spindle position in mitosis," *Nature cell biology*, vol. 13, no. 9, pp. 1040–1050, 2011.

[83] M. Kelkar, P. Bohec, M. B. Smith, V. Sreenivasan, A. Lisica, L. Valon, E. Ferber, B. Baum, G. Salbreux, and G. Charras, "Spindle reorientation in response to mechanical stress is an emergent property of the spindle positioning mechanisms," *Proceedings of the National Academy of Sciences*, vol. 119, no. 26, e2121868119, 2022.

[84] M. Gai, F. T. Bianchi, C. Vagnoni, F. Vernì, S. Bonaccorsi, S. Pasquero, G. E. Berto, F. Sgrò, A. M. Chiotto, L. Annaratone, *et al.*, "Aspm and citk regulate spindle orientation by affecting the dynamics of astral microtubules," *EMBO reports*, vol. 17, no. 10, pp. 1396–1409, 2016.

[85] E. Moreno, L. Valon, F. Levillayer, and R. Levayer, "Competition for space induces cell elimination through compaction-driven erk downregulation," *Current Biology*, vol. 29, no. 1, pp. 23–34, 2019.

[86] H. Lavoie, J. Gagnon, and M. Therrien, "Erk signalling: A master regulator of cell behaviour, life and fate," *Nature reviews Molecular cell biology*, vol. 21, no. 10, pp. 607–632, 2020.

[87] N. Borghi, M. Sorokina, O. G. Shcherbakova, W. I. Weis, B. L. Pruitt, W. J. Nelson, and A. R. Dunn, "E-cadherin is under constitutive actomyosin-generated tension that is increased at cell–cell contacts upon externally applied stretch," *Proceedings of the National Academy of Sciences*, vol. 109, no. 31, pp. 12 568–12 573, 2012.

[88] S. Yonemura, Y. Wada, T. Watanabe, A. Nagafuchi, and M. Shibata, "Aα-catenin as a tension transducer that induces adherens junction development," *Nature cell biology*, vol. 12, no. 6, pp. 533–542, 2010.

[89] E. E. Weiss, M. Kroemker, A.-H. Rüdiger, B. M. Jockusch, and M. Rüdiger, "Vinculin is part of the cadherin–catenin junctional complex: Complex formation between α-catenin and vinculin," *The Journal of cell biology*, vol. 141, no. 3, pp. 755–764, 1998.

[90] N. Tarannum, R. Singh, and S. Woolner, "Sculpting an embryo: The interplay between mechanical force and cell division," *Journal of Developmental Biology*, vol. 10, no. 3, p. 37, 2022.

[91] K. E. Kasza and J. A. Zallen, "Dynamics and regulation of contractile actin–myosin networks in morphogenesis," *Current opinion in cell biology*, vol. 23, no. 1, pp. 30–38, 2011.

[92] R. Levayer and T. Lecuit, "Biomechanical regulation of contractility: Spatial control and dynamics," *Trends in cell biology*, vol. 22, no. 2, pp. 61–81, 2012.

[93] P. Skoglund, A. Rolo, X. Chen, B. M. Gumbiner, and R. Keller, "Convergence and extension at gastrulation require a myosin iib-dependent cortical actin network," 2008.

[94] J. H. Gutzman, S. U. Sahu, and C. Kwas, "Non-muscle myosin iia and iib differentially regulate cell shape changes during zebrafish brain morphogenesis," *Developmental biology*, vol. 397, no. 1, pp. 103–115, 2015.

[95] M. Murrell, P. W. Oakes, M. Lenz, and M. L. Gardel, "Forcing cells into shape: The mechanics of actomyosin contractility," *Nature reviews Molecular cell biology*, vol. 16, no. 8, pp. 486–498, 2015.

[96] B. R. Acharya, A. Nestor-Bergmann, X. Liang, S. Gupta, K. Duszyc, E. Gauquelin, G. A. Gomez, S. Budnar, P. Marcq, O. E. Jensen, *et al.*, "A mechanosensitive rhoa pathway that protects epithelia against acute tensile stress," *Developmental cell*, vol. 47, no. 4, pp. 439–452, 2018.

[97] T. R. Arnold, R. E. Stephenson, and A. L. Miller, "Rho gtpases and actomyosin: Partners in regulating epithelial cell-cell junction structure and function," *Experimental cell research*, vol. 358, no. 1, pp. 20–30, 2017.

[98] G. Charras and A. S. Yap, "Tensile forces and mechanotransduction at cell–cell junctions," *Current Biology*, vol. 28, no. 8, R445–R457, 2018.

[99] S. Sluysmans, E. Vasileva, D. Spadaro, J. Shah, F. Rouaud, and S. Citi, "The role of apical cell–cell junctions and associated cytoskeleton in mechanotransduction," *Biology of the Cell*, vol. 109, no. 4, pp. 139–161, 2017.

[100] S. A. Gudipaty, J. Lindblom, P. D. Loftus, M. J. Redd, K. Edes, C. Davey, V. Krishnegowda, and J. Rosenblatt, "Mechanical stretch triggers rapid epithelial cell division through piezo1," *Nature*, vol. 543, no. 7643, pp. 118–121, 2017.

[101] F. Sachs, "Stretch-activated ion channels: What are they?" *Physiology*, vol. 25, no. 1, pp. 50–56, 2010.

[102] N. den Elzen, C. V. Buttery, M. P. Maddugoda, G. Ren, and A. S. Yap, "Cadherin adhesion receptors orient the mitotic spindle during symmetric cell division in mammalian epithelia," *Molecular biology of the cell*, vol. 20, no. 16, pp. 3740–3750, 2009.

[103] L. Seldin, N. D. Poulson, H. P. Foote, and T. Lechler, "Numa localization, stability, and function in spindle orientation involve 4.1 and cdk1 interactions," *Molecular biology of the cell*, vol. 24, no. 23, pp. 3651–3662, 2013.

[104] C. W. Chiu, C. Monat, M. Robitaille, M. Lacomme, A. M. Daulat, G. Macleod, H. McNeill, M. Cayouette, and S. Angers, "Sapcd2 controls spindle orientation and asymmetric divisions by negatively regulating the gαi-lgn-numa ternary complex," *Developmental cell*, vol. 36, no. 1, pp. 50–62, 2016.

[105] Z. Zheng, H. Zhu, Q. Wan, J. Liu, Z. Xiao, D. P. Siderovski, and Q. Du, "Lgn regulates mitotic spindle orientation during epithelial morphogenesis," *Journal of Cell Biology*, vol. 189, no. 2, pp. 275–288, 2010.

[106] D. A. Compton and D. W. Cleveland, "Numa is required for the proper completion of mitosis.," *The Journal of cell biology*, vol. 120, no. 4, pp. 947–957, 1993.

[107] J. Lee, T. Miyano, and R. M. Moor, "Spindle formation and dynamics of γ-tubulin and nuclear mitotic apparatus protein distribution during meiosis in pig and mouse oocytes," *Biology of reproduction*, vol. 62, no. 5, pp. 1184–1192, 2000.

[108] C. M. Price and D. E. Pettijohn, "Redistribution of the nuclear mitotic apparatus protein (numa) during mitosis and nuclear assembly: Properties of purified numa protein," *Experimental cell research*, vol. 166, no. 2, pp. 295–311, 1986.

[109] D. Parry, "Numa/centrophilin: Sequence analysis of the coiled-coil rod domain," *Biophysical journal*, vol. 67, no. 3, pp. 1203–1206, 1994.

[110] C. H. Yang and M. Snyder, "The nuclear-mitotic apparatus protein is important in the establishment and maintenance of the bipolar mitotic spindle apparatus.," *Molecular biology of the cell*, vol. 3, no. 11, pp. 1259–1267, 1992.

[111] J. Harborth, K. Weber, and M. Osborn, "Epitope mapping and direct visualization of the parallel, in-register arrangement of the double-stranded coiled-coil in the numa protein.," *The EMBO journal*, vol. 14, no. 11, pp. 2447–2460, 1995.

[112] C. H. Yang, E. J. Lambie, and M. Snyder, "Numa: An unusually long coiled-coil related protein in the mammalian nucleus.," *The Journal of cell biology*, vol. 116, no. 6, pp. 1303–1317, 1992.

[113] Q. Du, L. Taylor, D. A. Compton, and I. G. Macara, "Lgn blocks the ability of numa to bind and stabilize microtubules: A mechanism for mitotic spindle assembly regulation," *Current Biology*, vol. 12, no. 22, pp. 1928–1933, 2002.

[114] L. Haren and A. Merdes, "Direct binding of numa to tubulin is mediated by a novel sequence motif in the tail domain that bundles and stabilizes microtubules," *Journal of cell science*, vol. 115, no. 9, pp. 1815–1824, 2002.

[115] Q. Du, P. T. Stukenberg, and I. G. Macara, "A mammalian partner of inscuteable binds numa and regulates mitotic spindle organization," *Nature cell biology*, vol. 3, no. 12, pp. 1069–1075, 2001.

[116] T. K. Tang, C. Tang, Y.-J. Chao, and C.-W. Wu, "Nuclear mitotic apparatus protein (numa): Spindle association, nuclear targeting and differential subcellular localization of various numa isoforms," *Journal of cell science*, vol. 107, no. 6, pp. 1389–1402, 1994.

[117] J. Harborth, J. Wang, C. Gueth-Hallonet, K. Weber, and M. Osborn, "Self assembly of numa: Multiarm oligomers as structural units of a nuclear lattice," *The EMBO journal*, vol. 18, no. 6, pp. 1689–1700, 1999.

[118] S. Gallini, M. Carminati, F. De Mattia, L. Pirovano, E. Martini, A. Oldani, I. A. Asteriti, G. Guarguaglini, and M. Mapelli, "Numa phosphorylation by aurora-a orchestrates spindle orientation," *Current Biology*, vol. 26, no. 4, pp. 458–469, 2016.

[119] O. Kisurina-Evgenieva, G. Mack, Q. Du, I. Macara, A. Khodjakov, and D. A. Compton, "Multiple mechanisms regulate numa dynamics at spindle poles," *Journal of cell science*, vol. 117, no. 26, pp. 6391–6400, 2004.

[120] L. Seldin, A. Muroyama, and T. Lechler, "Numa-microtubule interactions are critical for spindle orientation and the morphogenesis of diverse epidermal structures," *Elife*, vol. 5, e12504, 2016.

[121] Z. Zheng, Q. Wan, G. Meixiong, and Q. Du, "Cell cycle–regulated membrane binding of numa contributes to efficient anaphase chromosome separation," *Molecular biology of the cell*, vol. 25, no. 5, pp. 606–619, 2014.

[122] O. N. Yogurtcu, C. W. Wolgemuth, and S. X. Sun, "Mechanical response and conformational amplification in α-helical coiled coils," *Biophysical journal*, vol. 99, no. 12, pp. 3895–3904, 2010.

[123] I. A. Asteriti, E. Di Cesare, F. De Mattia, V. Hilsenstein, B. Neumann, E. Cundari, P. Lavia, and G. Guarguaglini, "The aurora-a inhibitor mln8237 affects multiple mitotic processes and induces dose-dependent mitotic abnormalities and aneuploidy," *Oncotarget*, vol. 5, no. 15, p. 6229, 2014.

[124] D. Oriola, D. J. Needleman, and J. Brugués, "The physics of the metaphase spindle," *Annual review of biophysics*, vol. 47, pp. 655–673, 2018.

[125] Y. Bellaïche, "Cell division in the light of modeling," *Developmental cell*, vol. 38, no. 6, pp. 584–586, 2016.

[126] I. M. Tolić and N. Pavin, "Mitotic spindle: Lessons from theoretical modeling," *Molecular Biology of the Cell*, vol. 32, no. 3, pp. 218–222, 2021.

[127] W. T. Gibson, J. H. Veldhuis, B. Rubinstein, H. N. Cartwright, N. Perrimon, G. W. Brodland, R. Nagpal, and M. C. Gibson, "Control of the mitotic cleavage plane by local epithelial topology," *Cell*, vol. 144, no. 3, pp. 427–438, 2011.

[128] E. Nazockdast, A. Rahimian, D. Needleman, and M. Shelley, "Cytoplasmic flows as signatures for the mechanics of mitotic positioning," *Molecular biology of the cell*, vol. 28, no. 23, pp. 3261–3270, 2017.

[129] T. Shinar, M. Mana, F. Piano, and M. J. Shelley, "A model of cytoplasmically driven microtubule-based motion in the single-celled caenorhabditis elegans embryo," *Proceedings of the National Academy of Sciences*, vol. 108, no. 26, pp. 10 508–10 513, 2011.

[130] A. Kimura and S. Onami, "Computer simulations and image processing reveal length-dependent pulling force as the primary mechanism for c. elegans male pronuclear migration," *Developmental cell*, vol. 8, no. 5, pp. 765–775, 2005.

[131] B. Ibrahim, "Mathematical modeling and numerical simulation of the mitotic spindle orientation system," *Mathematical Biosciences*, vol. 303, pp. 46–51, 2018.

[132] A. Mogilner, R. Wollman, G. Civelekoglu-Scholey, and J. Scholey, "Modeling mitosis," *Trends in cell biology*, vol. 16, no. 2, pp. 88–96, 2006.

[133] M. Kurachi, M. Hoshi, and H. Tashiro, "Buckling of a single microtubule by optical trapping forces: Direct measurement of microtubule rigidity," *Cell motility and the cytoskeleton*, vol. 30, no. 3, pp. 221–228, 1995.

[134] F. Pampaloni, G. Lattanzi, A. Jonáš, T. Surrey, E. Frey, and E.-L. Florin, "Thermal fluctuations of grafted microtubules provide evidence of a length-dependent persistence length," *Proceedings of the National Academy of Sciences*, vol. 103, no. 27, pp. 10 248–10 253, 2006.

[135] B. Rubinstein, K. Larripa, P. Sommi, and A. Mogilner, "The elasticity of motor–microtubule bundles and shape of the mitotic spindle," *Physical biology*, vol. 6, no. 1, p. 016 005, 2009.

[136] M. Dogterom and B. Yurke, "Measurement of the force-velocity relation for growing microtubules," *Science*, vol. 278, no. 5339, pp. 856–860, 1997.

[137] J. Howard, "Elastic and damping forces generated by confined arrays of dynamic microtubules," *Physical biology*, vol. 3, no. 1, p. 54, 2006.

[138] T. L. Hill and Y. Chen, "Phase changes at the end of a microtubule with a gtp cap.," *Proceedings of the National Academy of Sciences*, vol. 81, no. 18, pp. 5772–5776, 1984.

[139] A. Mogilner and G. Oster, "The polymerization ratchet model explains the force-velocity relation for growing microtubules," *European Biophysics Journal*, vol. 28, no. 3, pp. 235–242, 1999.

[140] G. S. van Doorn, C. Tănase, B. M. Mulder, and M. Dogterom, "On the stall force for growing microtubules," *European Biophysics Journal*, vol. 29, pp. 2–6, 2000.

[141] J. Krawczyk and J. Kierfeld, "Stall force of polymerizing microtubules and filament bundles," *Europhysics letters*, vol. 93, no. 2, p. 28 006, 2011.

[142] M. Dogterom and S. Leibler, "Physical aspects of the growth and regulation of microtubule structures," *Physical review letters*, vol. 70, no. 9, p. 1347, 1993.

[143] J. Zhu, A. Burakov, V. Rodionov, and A. Mogilner, "Finding the cell center by a balance of dynein and myosin pulling and microtubule pushing: A computational study," *Molecular biology of the cell*, vol. 21, no. 24, pp. 4418–4427, 2010.

[144] Z.-Y. Liu, B. Li, Z.-L. Zhao, G.-K. Xu, X.-Q. Feng, and H. Gao, "Mesoscopic dynamic model of epithelial cell division with cell-cell junction effects," *Physical Review E*, vol. 102, no. 1, p. 012 405, 2020.

[145] J. Li, L. Cheng, and H. Jiang, "Cell shape and intercellular adhesion regulate mitotic spindle orientation," *Molecular Biology of the Cell*, vol. 30, no. 19, pp. 2458–2468, 2019.

[146] J. Li and H. Jiang, "Geometric asymmetry induces upper limit of mitotic spindle size," *Biophysical journal*, vol. 112, no. 7, pp. 1503–1516, 2017.

[147] L. Laan, N. Pavin, J. Husson, G. Romet-Lemonne, M. Van Duijn, M. P. López, R. D. Vale, F. Jülicher, S. L. Reck-Peterson, and M. Dogterom, "Cortical dynein controls microtubule dynamics to generate pulling forces that position microtubule asters," *Cell*, vol. 148, no. 3, pp. 502–514, 2012.

[148] M. Akiyama, M. Nonomura, A. Tero, and R. Kobayashi, "Numerical study on spindle positioning using phase field method," *Physical biology*, vol. 16, no. 1, p. 016 005, 2018.

[149] A. M. Corrigan, R. Shrestha, V. M. Draviam, and A. M. Donald, "Modeling of noisy spindle dynamics reveals separable contributions to achieving correct orientation," *Biophysical journal*, vol. 109, no. 7, pp. 1398–1409, 2015.

[150] H. Tanimoto, A. Kimura, and N. Minc, "Shape–motion relationships of centering microtubule asters," *Journal of Cell Biology*, vol. 212, no. 7, pp. 777–787, 2016.

[151] F. Schwietert and J. Kierfeld, "Bistability and oscillations in cooperative microtubule and kinetochore dynamics in the mitotic spindle," *New Journal of Physics*, vol. 22, no. 5, p. 053 008, 2020.

[152] A. Shee, S. Ghosh, and D. Chaudhuri, "Filament-motor protein system under loading: Instability and limit cycle oscillations," *Soft Materials*, vol. 19, no. 3, pp. 323–333, 2021.

[153] D. Oriola, H. Gadêlha, C. Blanch-Mercader, and J. Casademunt, "Subharmonic oscillations of collective molecular motors," *Europhysics Letters*, vol. 107, no. 1, p. 18 002, 2014.

[154] D. Lee-Liu, E. E. Méndez-Olivos, R. Muñoz, and J. Larraín, "The african clawed frog xenopus laevis: A model organism to study regeneration of the central nervous system," *Neuroscience letters*, vol. 652, pp. 82–93, 2017.

[155] M. J. Lohka and J. L. Maller, "Induction of nuclear envelope breakdown, chromosome condensation, and spindle formation in cell-free extracts.," *The Journal of cell biology*, vol. 101, no. 2, pp. 518–523, 1985.

[156] G. A. Stooke-Vaughan, L. A. Davidson, and S. Woolner, "Xenopus as a model for studies in mechanical stress and cell division," *genesis*, vol. 55, no. 1-2, e23004, 2017.

[157] M. Fisher, C. James-Zorn, V. Ponferrada, A. J. Bell, N. Sundararaj, E. Segerdell, P. Chaturvedi, N. Bayyari, S. Chu, T. Pells, *et al.*, "Xenbase: Key features and resources of the xenopus model organism knowledgebase," *Genetics*, vol. 224, no. 1, iyad018, 2023.

[158] U. Hellsten, R. M. Harland, M. J. Gilchrist, D. Hendrix, J. Jurka, V. Kapitonov, I. Ovcharenko, N. H. Putnam, S. Shu, L. Taher, *et al.*, "The genome of the western clawed frog xenopus tropicalis," *Science*, vol. 328, no. 5978, pp. 633–636, 2010.

[159] J. R. Masters, "Hela cells 50 years on: The good, the bad and the ugly," *Nature Reviews Cancer*, vol. 2, no. 4, pp. 315–319, 2002.

[160] D. Mittelman and J. H. Wilson, "The fractured genome of hela cells," *Genome biology*, vol. 14, pp. 1–4, 2013.

[161] W. Zhou, X. Wang, L. Li, X. Feng, Z. Yang, W. Zhang, and R. Hu, "Depletion of tubulin polymerization promoting protein family member 3 suppresses hela cell proliferation," *Molecular and cellular biochemistry*, vol. 333, pp. 91–98, 2010.

[162] A. H. Hyman and K. Simons, "Beyond hela cells," *Nature*, vol. 480, no. 7375, pp. 34–34, 2011.

[163] A. Zuasti, C. Jiménez-Cervantes, J. García-Borrón, and C. Ferrer, "The melanogenic system of xenopus laevis," *Archives of histology and cytology*, vol. 61, no. 4, pp. 305–316, 1998.

[164] D. S. Hewapathirane, D. Dunfield, W. Yen, S. Chen, and K. Haas, "In vivo imaging of seizure activity in a novel developmental seizure model," *Experimental neurology*, vol. 211, no. 2, pp. 480–488, 2008.

[165] D. S. Hewapathirane and K. Haas, "The albino xenopus laevis tadpole as a novel model of developmental seizures," *Animal Models of Epilepsy: Methods and Innovations*, pp. 45–57, 2009.

[166] W. S. Hoogenboom, D. K. Douwel, and P. Knipscheer, "Xenopus egg extract: A powerful tool to study genome maintenance mechanisms," *Developmental biology*, vol. 428, no. 2, pp. 300–309, 2017.

[167] A. Desai, A. Murray, T. J. Mitchison, and C. E. Walczak, "The use of xenopus egg extracts to study mitotic spindle assembly and function in vitro," *Methods in cell biology*, vol. 61, pp. 385–412, 1998.

[168] B. T. French and A. F. Straight, "The power of xenopus egg extract for reconstitution of centromere and kinetochore function," *Centromeres and Kinetochores: Discovering the Molecular Mechanisms Underlying Chromosome Inheritance*, pp. 59–84, 2017.

[169] M. Sheehan, A. Mills, A. Sleeman, R. Laskey, and J. Blow, "Steps in the assembly of replication-competent nuclei in a cell-free system from xenopus eggs.," *The Journal of cell biology*, vol. 106, no. 1, pp. 1–12, 1988.

[170] D. L. Levy and R. Heald, "Nuclear size is regulated by importin α and ntf2 in xenopus," *Cell*, vol. 143, no. 2, pp. 288–298, 2010.

[171] R.-H. Chen, "The spindle checkpoint in xenopus laevis," *Frontiers in Bioscience-Landmark*, vol. 13, no. 6, pp. 2231–2237, 2008.

[172] K. Pfister, D. R. Shook, C. Chang, R. Keller, and P. Skoglund, "Molecular model for force production and transmission during vertebrate gastrulation," *Development*, vol. 143, no. 4, pp. 715–727, 2016.

[173] L. Beloussov, J. Dorfman, and V. Cherdantzev, "Mechanical stresses and morphological patterns in amphibian embryos," 1975.

[174] Y. Hara, K. Nagayama, T. S. Yamamoto, T. Matsumoto, M. Suzuki, and N. Ueno, "Directional migration of leading-edge mesoderm generates physical forces: Implication in xenopus notochord formation during gastrulation," *Developmental biology*, vol. 382, no. 2, pp. 482–495, 2013.

[175] M. Moruzzi, A. Nestor-Bergmann, G. K. Goddard, N. Tarannum, K. Brennan, and S. Woolner, "Generation of anisotropic strain dysregulates wild-type cell division at the interface between host and oncogenic tissue," *Current biology*, vol. 31, no. 15, pp. 3409–3418, 2021.

[176] R. Feroze, J. H. Shawky, M. von Dassow, and L. A. Davidson, "Mechanics of blastopore closure during amphibian gastrulation," *Developmental biology*, vol. 398, no. 1, pp. 57–67, 2015.

[177] L. Wolpert, C. Tickle, and A. M. Arias, *Principles of development*. Oxford University Press, USA, 2015.

[178] L. Lu-Sha, Z. Lan-Ying, W. Shou-Hong, and J.-P. Jiang, "Research proceedings on amphibian model organisms," *Zoological Research*, vol. 37, no. 4, p. 237, 2016.

[179] S. Woolner, A. L. Miller, and W. M. Bement, "Imaging the cytoskeleton in live xenopus laevis embryos," *Cytoskeleton Methods and Protocols*, pp. 23–39, 2010.

[180] G. A. Anderson, L. Gelens, J. C. Baker, and J. E. Ferrell, "Desynchronizing embryonic cell division waves reveals the robustness of xenopus laevis development," *Cell reports*, vol. 21, no. 1, pp. 37–46, 2017.

[181] Y.-H. Chien, R. Keller, C. Kintner, and D. R. Shook, "Mechanical strain determines the axis of planar polarity in ciliated epithelia," *Current Biology*, vol. 25, no. 21, pp. 2774–2784, 2015.

[182] G. K. Goddard, N. Tarannum, and S. Woolner, "Applying tensile and compressive force to xenopus animal cap tissue," *Cold Spring Harbor Protocols*, vol. 2020, no. 3, pdb–prot105551, 2020.

[183] R. Keller, "Early embryonic development of xenopus laevis," *Methods in cell biology*, vol. 36, pp. 61–113, 1991.

[184] A. Szabo, I. Cobo, S. Omara, S. McLachlan, R. Keller, and R. Mayor, "The molecular basis of radial intercalation during tissue spreading in early development," *Developmental cell*, vol. 37, no. 3, pp. 213–225, 2016.

[185] M. Ravi, V. Paramesh, S. Kaviya, E. Anuradha, and F. P. Solomon, "3d cell culture systems: Advantages and applications," *Journal of cellular physiology*, vol. 230, no. 1, pp. 16–26, 2015.

[186] A. M. Session, Y. Uno, T. Kwon, J. A. Chapman, A. Toyoda, S. Takahashi, A. Fukui, A. Hikosaka, A. Suzuki, M. Kondo, *et al.*, "Genome evolution in the allotetraploid frog xenopus laevis," *Nature*, vol. 538, no. 7625, pp. 336–343, 2016.

[187] S. D. Joshi and L. A. Davidson, "Live-cell imaging and quantitative analysis of embryonic epithelial cells in xenopus laevis," *JoVE (Journal of Visualized Experiments)*, no. 39, e1949, 2010.

[188] C. A. Schneider, W. S. Rasband, and K. W. Eliceiri, "Nih image to imagej: 25 years of image analysis," *Nature methods*, vol. 9, no. 7, pp. 671–675, 2012.

[189] J. Rudnick and G. Gaspari, *Elements of the random walk: an introduction for advanced students and researchers*. Cambridge University Press, 2004.

[190] C. Stringer, T. Wang, M. Michaelos, and M. Pachitariu, "Cellpose: A generalist algorithm for cellular segmentation," *Nature methods*, vol. 18, no. 1, pp. 100–106, 2021.

[191] B. Illowsky and S. Dean, "Introductory statistics," 2018.

[192] S. Inoué, "Cell division and the mitotic spindle," *The Journal of cell biology*, vol. 91, no. 3, p. 131, 1981.

[193] A. Burakov, E. Nadezhdina, B. Slepchenko, and V. Rodionov, "Centrosome positioning in interphase cells," *The Journal of cell biology*, vol. 162, no. 6, pp. 963–969, 2003.

[194] S. Woolner and N. Papalopulu, "Spindle position in symmetric cell divisions during epiboly is controlled by opposing and dynamic apicobasal forces," *Developmental cell*, vol. 22, no. 4, pp. 775–787, 2012.

[195] R. Rappaport, "Cytokinesis in animal cells," *International review of cytology*, vol. 31, pp. 169–214, 1971.

[196] R. L. Klemke, S. Cai, A. L. Giannini, P. J. Gallagher, P. d. Lanerolle, and D. A. Cheresh, "Regulation of cell motility by mitogen-activated protein kinase," *The Journal of cell biology*, vol. 137, no. 2, pp. 481–492, 1997.

[197] K. Oegema, A. Desai, S. Rybina, M. Kirkham, and A. A. Hyman, "Functional analysis of kinetochore assembly in caenorhabditis elegans," *The Journal of cell biology*, vol. 153, no. 6, pp. 1209–1226, 2001.

[198] J.-C. Labbé, E. K. McCarthy, and B. Goldstein, "The forces that position a mitotic spindle asymmetrically are tethered until after the time of spindle assembly," *The Journal of cell biology*, vol. 167, no. 2, pp. 245–256, 2004.

[199] N. E. Phillips, C. Manning, N. Papalopulu, and M. Rattray, "Identifying stochastic oscillations in single-cell live imaging time series using gaussian processes," *PLoS Computational Biology*, vol. 13, no. 5, e1005479, 2017.

[200] C. S. Manning, V. Biga, J. Boyd, J. Kursawe, B. Ymisson, D. G. Spiller, C. M. Sanderson, T. Galla, M. Rattray, and N. Papalopulu, "Quantitative single-cell live imaging links hes5 dynamics with cell-state and fate in murine neurogenesis," *Nature communications*, vol. 10, no. 1, p. 2835, 2019.

[201] V. J. Allan, "Cytoplasmic dynein," *Biochemical Society Transactions*, vol. 39, no. 5, pp. 1169–1178, 2011.

[202] M. Trokter, N. Mücke, and T. Surrey, "Reconstitution of the human cytoplasmic dynein complex," *Proceedings of the National Academy of Sciences*, vol. 109, no. 51, pp. 20 895–20 900, 2012.

[203] D. T. Gillespie, "Exact stochastic simulation of coupled chemical reactions," *The journal of physical chemistry*, vol. 81, no. 25, pp. 2340–2361, 1977.

[204] V. Belyy, N. L. Hendel, A. Chien, and A. Yildiz, "Cytoplasmic dynein transports cargos via load-sharing between the heads," *Nature communications*, vol. 5, no. 1, pp. 1–9, 2014.

[205] R. Milo and R. Phillips, *Cell biology by the numbers*. Garland Science, 2015.

[206] M. Chen and Y. Cao, "Analysis and remedy of negativity problem in hybrid stochastic simulation algorithm and its application," in *Proceedings of the 2018 ACM International Conference on Bioinformatics, Computational Biology, and Health Informatics*, 2018, pp. 585–586.

[207] M. A. Gibson and J. Bruck, "Efficient exact stochastic simulation of chemical systems with many species and many channels," *The journal of physical chemistry A*, vol. 104, no. 9, pp. 1876–1889, 2000.

[208] D. T. Gillespie, "Approximate accelerated stochastic simulation of chemically reacting systems," *The Journal of chemical physics*, vol. 115, no. 4, pp. 1716–1733, 2001.

[209] M. Rathinam, L. R. Petzold, Y. Cao, and D. T. Gillespie, "Stiffness in stochastic chemically reacting systems: The implicit tau-leaping method," *The Journal of Chemical Physics*, vol. 119, no. 24, pp. 12 784–12 794, 2003.

[210] Y. Cao, H. Li, and L. Petzold, "Efficient formulation of the stochastic simulation algorithm for chemically reacting systems," *The journal of chemical physics*, vol. 121, no. 9, pp. 4059–4067, 2004.

[211] Y. Cao, D. T. Gillespie, and L. R. Petzold, "Efficient step size selection for the tau-leaping simulation method," *The Journal of chemical physics*, vol. 124, no. 4, p. 044 109, 2006.

[212] Y. Cao, D. T. Gillespie, and L. R. Petzold, "Adaptive explicit-implicit tau-leaping method with automatic tau selection," *The Journal of Chemical physics*, vol. 126, no. 22, p. 224 101, 2007.

[213] C. Rackauckas and Q. Nie, "Differentialequations.jl–a performant and feature-rich ecosystem for solving differential equations in julia," *Journal of Open Research Software*, vol. 5, no. 1, 2017.

[214] C. Tsitouras, "Runge–kutta pairs of order 5 (4) satisfying only the first column simplifying assumption," *Computers & Mathematics with Applications*, vol. 62, no. 2, pp. 770–775, 2011.

[215] J.-M. Ginoux and C. Letellier, "Van der pol and the history of relaxation oscillations: Toward the emergence of a concept," *Chaos: An Interdisciplinary Journal of Nonlinear Science*, vol. 22, no. 2, p. 023 120, 2012.

[216] S. H. Strogatz, *Nonlinear dynamics and chaos with student solutions manual: With applications to physics, biology, chemistry, and engineering*. CRC press, 2018.

[217] L. S. Tsimring, "Noise in biology," *Reports on Progress in Physics*, vol. 77, no. 2, p. 026 601, 2014.

[218] B. F. McEwen, A. B. Heagle, G. O. Cassels, K. F. Buttle, and C. L. Rieder, "Kinetochore fiber maturation in ptk1 cells and its implications for the mechanisms of chromosome congression and anaphase onset," *The Journal of cell biology*, vol. 137, no. 7, pp. 1567–1580, 1997.

[219] J. Ranft, M. Basan, J. Elgeti, J.-F. Joanny, J. Prost, and F. Jülicher, "Fluidization of tissues by cell division and apoptosis," *Proceedings of the National Academy of Sciences*, vol. 107, no. 49, pp. 20 863–20 868, 2010.

[220] B. G. Godard and C.-P. Heisenberg, "Cell division and tissue mechanics," *Current opinion in cell biology*, vol. 60, pp. 114–120, 2019.

[221] S. Huang and D. E. Ingber, "Cell tension, matrix mechanics, and cancer development," *Cancer cell*, vol. 8, no. 3, pp. 175–176, 2005.

[222] M. J. Siedlik, V. D. Varner, and C. M. Nelson, "Pushing, pulling, and squeezing our way to understanding mechanotransduction," *Methods*, vol. 94, pp. 4–12, 2016.

[223] L. Gelens, K. C. Huang, and J. E. Ferrell, "How does the xenopus laevis embryonic cell cycle avoid spatial chaos?" *Cell reports*, vol. 12, no. 5, pp. 892–900, 2015.

[224] B. van der Pol D.Sc. and J. van der Mark, "Lxxii. the heartbeat considered as a relaxation oscillation, and an electrical model of the heart," *The London, Edinburgh, and Dublin Philosophical Magazine and Journal of Science*, vol. 6, no. 38, pp. 763–775, 1928. DOI: 10.1080/14786441108564652. eprint: https://doi.org/10.1080/14786441108564652. [Online]. Available: https://doi.org/10.1080/14786441108564652.

[225] J. Grasman, *Asymptotic methods for relaxation oscillations and applications*. Springer Science & Business Media, 2012, vol. 63.

[226] A. P. Carter, "Crystal clear insights into how the dynein motor moves," *Journal of cell science*, vol. 126, no. 3, pp. 705–713, 2013.

[227] L. Truebestein and T. A. Leonard, "Coiled-coils: The long and short of it," *Bioessays*, vol. 38, no. 9, pp. 903–916, 2016.

[228] Y. Nishikawa, M. Inatomi, H. Iwasaki, and G. Kurisu, "Structural change in the dynein stalk region associated with two different affinities for the microtubule," *Journal of molecular biology*, vol. 428, no. 9, pp. 1886–1896, 2016.

Appendices

Appendix A

Expansion to two dimensions

We present our expansion of the model described in Chapters 4 and 5 into 2D by defining the 2D mitotic spindle and deriving equations of motion for the spindle array due to forces acting on the spindle poles.

The mitotic spindle in the cell is comprised of two spindle poles, connected by interactions between interpolar microtubules and also by the kinetochore microtubules attachments to the chromosomes which form the metaphase plate (Figure 1.3). Here we expand the 1D model of an individual spindle pole described and explored in Chapters 4 and 5 to 2D. First, the individual spindle poles will be considered in 2D. We expand the two isolated populations of force generators above and below the pole into one distributed population of force generators which occupies the entire perimeter of the cell. Microtubules extending fan-like from the spindle pole with an angular width of Θ (Figure A.1A) will interact with cortical force generators at the cell perimeter, as well as provide a restoring force. This set-up will apply to both spindle poles which will result in a net force on the central spindle array, whose centre $\mathbf{R}_{\mathrm{s}}\left(\bar{t}\right)$ is positioned half way between the positions of the two spindle poles, $\mathbf{R}_{\mathrm{p1}}\left(\bar{t}\right)$ and $\mathbf{R}_{\mathrm{p2}}\left(\bar{t}\right)$ (Figure A.1A). We henceforth refer to this pole-pole array as "the spindle", whose orientation is defined by

$$\mathbf{n} = \begin{bmatrix} \cos\phi \\ \sin\phi \end{bmatrix}, \tag{A.1}$$

which lies parallel to the spindle at an angle $\phi\left(\bar{t}\right)$ to the horizontal (Figure A.1A). Any position along the spindle is thus given for fixed x as

$$\mathbf{x}\left(\bar{t}\right) = \mathbf{R}_{\mathrm{s}}\left(\bar{t}\right) + x\mathbf{n}\left(\bar{t}\right), \tag{A.2}$$

where $x \in [-l/2, l/2]$ for a spindle of length l.

By the chain rule, $\mathrm{d}\mathbf{n}\left(\phi\left(\bar{t}\right)\right)/\mathrm{d}\bar{t} = \frac{\mathrm{d}\mathbf{n}}{\mathrm{d}\phi}\frac{\mathrm{d}\phi}{\mathrm{d}\bar{t}} = \mathbf{Z} \times \mathbf{n}\phi_{\bar{t}}$, then any point on the spindle moves with velocity

$$\mathbf{x}_{\bar{t}} = \mathbf{R}_{\mathrm{s},\bar{t}} + x\phi_{\bar{t}}\left(\mathbf{Z} \times \mathbf{n}\right), \tag{A.3}$$

where $\mathbf{Z} = [0\ 0\ 1]$ is the vector pointing out of the 2D plane. It is noted here that vector $\mathbf{Z}$ is the only vector with a component out of the 2D plane and is therefore the only vector which is written with x, y, z components in this work. By considering the tensor product

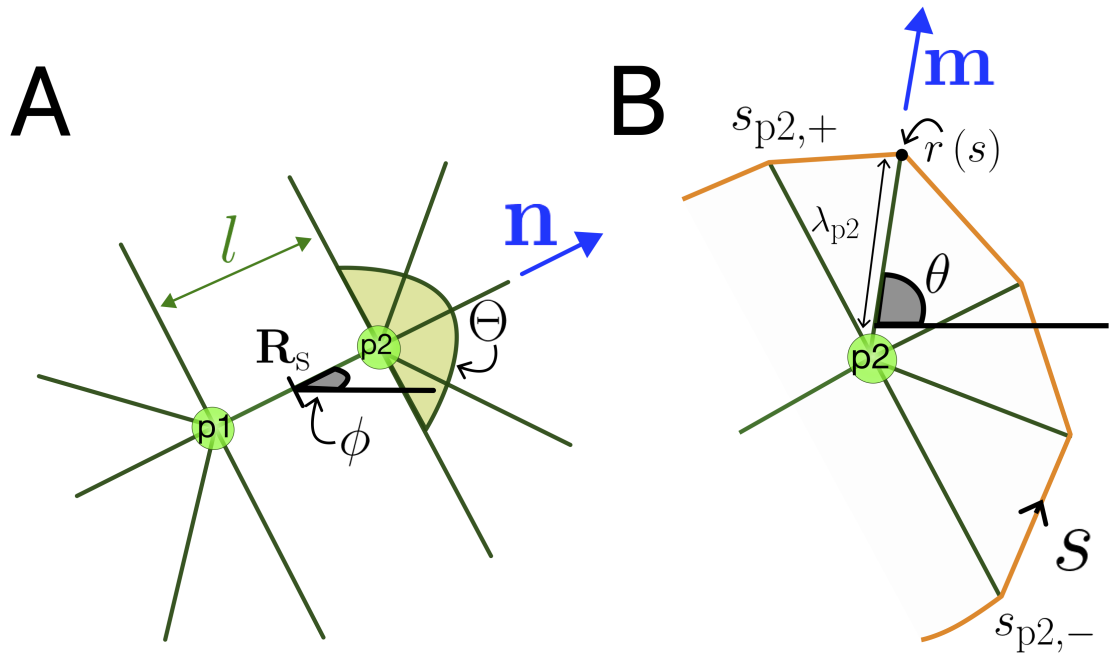

Figure A.1. **2D spindle schematic**. A) The spindle array, showing the microtubule angular width Θ, the spindle orientation vector $\mathbf{n}(\phi)$, the spindle centre $\mathbf{R}_s$ and the spindle length l. B) The geometry of microtubule-cortex interactions from spindle pole p2. The cell edge is parametrised by arclength s and described by function $r(s)$. The microtubule at an angle θ from the horizontal has length λ_{p2} and orientation vector $\mathbf{m}$. The angular width of the microtubule fan contacts the cell periphery at $s_{p2,-} < s < s_{p2,+}$, defining the interaction zone.

$\mathbf{nn} \equiv \mathbf{n} \otimes \mathbf{n}$, we may write the drag on the spindle in terms of the tensor

$$\mathsf{D} = b_{\parallel}\mathbf{nn} + b_{\perp}\left(\mathsf{I} - \mathbf{nn}\right), \tag{A.4}$$

the summation of drag parallel ($b_{\parallel}\mathbf{nn}$) and perpendicular ($b_{\perp}\left(\mathsf{I} - \mathbf{nn}\right)$) to the spindle, where I is the identity matrix. This can be used to determine the force balance on the spindle,

$$\mathcal{F} = \int_{-l/2}^{l/2} \mathbf{F} \mathrm{d}x = \int_{-l/2}^{l/2} \mathsf{D} \cdot \mathbf{x}_{\bar{t}}\, \mathrm{d}x, \tag{A.5}$$

where $\mathbf{F}$ is the net force per unit length exerted by microtubules and $\mathcal{F}$ is the total force. The torque then follows as

$$\tau = \mathbf{Z} \cdot \left(\int_{-l/2}^{l/2} x\mathbf{n} \mathrm{d}x \times \mathbf{F} \right) = \mathbf{Z} \cdot \left(\int_{-l/2}^{l/2} x\mathbf{n} \mathrm{d}x \times \left(\mathsf{D} \cdot \mathbf{x}_{\bar{t}}\right) \right) \tag{A.6}$$

The force (A.5) can be rewritten as

$$\mathcal{F} = \int_{-l/2}^{l/2} \mathsf{D} \cdot \mathbf{x}_{\bar{t}} \mathrm{d}x = \int_{-l/2}^{l/2} \mathsf{D} \cdot \left(\mathbf{R}_{s,\bar{t}} + x\phi_{\bar{t}} \left(\mathbf{Z} \times \mathbf{n} \right) \right) \mathrm{d}x, \tag{A.7}$$

and thus

$$\mathcal{F} = \int_{-l/2}^{l/2} \mathsf{D} \cdot \mathbf{R}_{\mathrm{s},\bar{t}} \mathrm{d}x. \tag{A.8}$$

Then it follows by integration that the equation of motion of the spindle pole is given

$$\mathcal{F} = l\mathsf{D} \cdot \mathbf{R}_{\mathrm{s},\bar{t}}. \tag{A.9}$$

If we consider torque in a similar way,

$$\tau = \mathbf{Z} \cdot \int_{-\frac{l}{2}}^{\frac{l}{2}} x\mathbf{n} \times \mathsf{D} \cdot \mathbf{x}_{\bar{t}} \mathrm{d}x = \mathbf{Z} \cdot \int_{-\frac{l}{2}}^{\frac{l}{2}} x\mathbf{n} \times \mathsf{D} \cdot \left(\mathbf{R}_{\mathrm{s},t} + x\phi_{\bar{t}} \left(\mathbf{Z} \times \mathbf{n}\right)\right) \mathrm{d}x, \tag{A.10}$$

then

$$\tau = \mathbf{Z} \cdot \int_{-l/2}^{l/2} x\mathbf{n} \times \left(\mathsf{D} \cdot \mathbf{R}_{\mathrm{s},\bar{t}}\right) \mathrm{d}x + \mathbf{Z} \cdot \int_{-l/2}^{l/2} x^2 \phi_{\bar{t}} \mathbf{n} \times \left(\mathsf{D} \cdot \left(\mathbf{Z} \times \mathbf{n}\right)\right) \mathrm{d}x. \tag{A.11}$$

The first integral here vanishes, while the $\mathbf{Z} \times \mathbf{n}$ term in the second integral pulls out the perpendicular component of the total drag. Then,

$$\tau = \mathbf{Z} \cdot \int_{-l/2}^{l/2} b_{\perp} x^2 \phi_{\bar{t}} \mathbf{n} \times \left(\mathbf{Z} \times \mathbf{n}\right) \mathrm{d}x, \tag{A.12}$$

and $\mathbf{n} \times \left(\mathbf{Z} \times \mathbf{n}\right) = \mathbf{Z}$ which results in

$$\tau = \int_{-l/2}^{l/2} b_{\perp} x^2 \phi_{\bar{t}} \mathrm{d}x. \tag{A.13}$$

By integration this becomes

$$\tau = \mu_{\mathrm{D}} \phi_{\bar{t}} \tag{A.14}$$

with $\mu_{\mathrm{D}} = \frac{l^3}{12} b_{\perp}$ the rotational drag. (Here, μ_{D} is separate from the μ defined in the 1D model as a relaxation rate.)

We will now define the forces which generate motion in (A.5) and (A.6).

A.1 Calculating the forcing terms in 2D

The forcing terms $\mathbf{F}$ in (A.5) arise from force generators at the cortex pulling on microtubules, as well as restoring forces provided by the microtubules themselves. These forces affect the spindle positioning through their connection to the two spindle poles which lie at positions $\mathbf{R}_{\mathrm{p1}}\left(\bar{t}\right) = \mathbf{R}_{\mathrm{s}} - \frac{1}{2} l\mathbf{n}$ and $\mathbf{R}_{\mathrm{p2}}\left(\bar{t}\right) = \mathbf{R}_{\mathrm{s}} + \frac{1}{2} l\mathbf{n}$ respectively. We consider the force as being produced from the combination of pulling and pushing on each spindle pole individually ($\mathbf{F}_{\mathrm{p1}}$ and $\mathbf{F}_{\mathrm{p2}}$). Then we may write

$$\mathbf{F} = \mathbf{F}_{\mathrm{p1}} \delta\left(x + \frac{l}{2}\right) + \mathbf{F}_{\mathrm{p2}} \delta\left(x - \frac{l}{2}\right) \tag{A.15}$$

so

$$\mathcal{F} = \mathbf{F}_{\text{p1}} + \mathbf{F}_{\text{p2}}, \tag{A.16}$$

and

$$\tau = \tau_{\text{p1}} + \tau_{\text{p2}} = \frac{l}{2}\mathbf{Z}.\left(\mathbf{n} \times \mathbf{F}_{\text{p2}} - \mathbf{n} \times \mathbf{F}_{\text{p1}}\right). \tag{A.17}$$

If we parameterise the cell perimeter by arclength s such that the perimeter is described by $\mathbf{r}(s)$ (Figure A.1B), then we may discretise the perimeter into segments of fixed arclength and only include segments $s_{\text{p}i,-} < s < s_{\text{p}i,+}$ for $i = 1, 2$, which lie within the angular width Θ of the microtubule fan. Then a microtubule of length λ_{p2} extending from pole $\mathbf{R}_{\text{p2}}$ will contact the perimeter at point $\mathbf{r}\,(s)$ for

$$\lambda_{\text{p2}}\mathbf{m} = \mathbf{r}\,(s) - \mathbf{R}_{\text{p2}}, \tag{A.18}$$

where $\mathbf{m} = \mathbf{m}\,(t;\theta)$ is a unit vector along the microtubule (Figure A.1B. The spindle pole velocity, is related to the changing microtubule length and orientation via

$$\mathbf{R}_{\text{p2},\bar{t}} = \left(\mathbf{r}\,(s) - \lambda_{\text{p2}}\mathbf{m}\right)_{\bar{t}} = -\left(\lambda_{\text{p2}}\mathbf{m}\right)_{\bar{t}}. \tag{A.19}$$

Vector $\mathbf{m}$ may be written

$$\mathbf{m} = \begin{bmatrix}\cos\theta \\ \sin\theta\end{bmatrix}, \tag{A.20}$$

therefore

$$\mathbf{m}_{\bar{t}} = \mathbf{Z} \times \mathbf{m}\theta_{\bar{t}}, \tag{A.21}$$

and thus $\mathbf{m}.\mathbf{m}_{\bar{t}} = 0$. Then expanding (A.19) to

$$\mathbf{R}_{\text{p2},\bar{t}} = -\lambda_{\text{p2}}\mathbf{m}_{\bar{t}} - \lambda_{\text{p2},\bar{t}}\mathbf{m}, \tag{A.22}$$

it follows that

$$\mathbf{R}_{\text{p2},\bar{t}}.\mathbf{m} = \lambda_{\text{p2},\bar{t}} \tag{A.23}$$

is the pole velocity in the direction $\mathbf{m}$. Thus the velocity of the bound force generators along the microtubule may be written as in (4.28) like

$$\bar{v}_{\text{p2,b}} = -\left(1 - \bar{y} + \lambda_{\text{p2},\bar{t}}\right). \tag{A.24}$$

This velocity term may be used in the evolution equation for the bound probability density function, which we take to be of the same form as in Section 4.3, but now as a function of s rather cortex position (upper or lower). That is, for $\bar{P}_{\text{p}i,\text{u}}$ and $\bar{P}_{\text{p}i,\text{b}}$ for $i = 1, 2$ in (4.25b) and (4.25a) become

$$\bar{P}_{\text{p}i,\text{u},\bar{t}} = -\bar{\omega}_{\text{on}}\bar{P}_{\text{p}i,\text{u}} + \bar{\omega}_0 e^{\gamma\bar{y}}\bar{P}_{\text{p}i,\text{b}} - \Gamma\left(-\bar{y}\bar{P}_{\text{p}i,\text{u}} - \beta\bar{P}_{\text{p}i,\text{u},\bar{y}}\right)_{\bar{y}} \tag{A.25a}$$

$$\bar{P}_{\text{p}i,\text{b},\bar{t}} = \bar{\omega}_{\text{on}}\bar{P}_{\text{p}i,\text{u}} - \bar{\omega}_0 e^{\gamma\bar{y}}\bar{P}_{\text{p}i,\text{b}} - \left(\bar{v}_{\text{p}i,\text{b}}\bar{P}_{\text{p}i,\text{b}} - \alpha\bar{P}_{\text{p}i,\text{b},\bar{y}}\right)_{\bar{y}} \tag{A.25b}$$

for $\bar{P}_{\mathrm{p}i,\mathrm{b(u)}}\left(\bar{t},\bar{y};s\right)$ at fixed s Then the net pulling force on pole p2 may be calculated by

$$\mathbf{F}_{\mathrm{p2}}^{\mathrm{Pull}} = N_{\rho}\int_{s_{\mathrm{p2},-}}^{s_{\mathrm{p2},+}} \mathrm{d}s \int_{0}^{\bar{y}_{\max}} \mathrm{d}\bar{y}\bar{P}_{\mathrm{p2,b}}\bar{y}\mathbf{m}, \tag{A.26}$$

where N_{ρ} is the density of available cortical force generators distributed across the cell perimeter. The form of the force in (A.26) mirrors the force in the 1D PDE model (4.31), altered to describe the 2D force acting on the spindle pole from the array of microtubules spanning an angular width Θ.

The restoring force provided by the microtubules is described as

$$\mathbf{F}_{\mathrm{p2}}^{\mathrm{R}} = K\int_{s_{\mathrm{p2},-}}^{s_{\mathrm{p2},+}} \mathrm{d}s\left(\lambda_{\mathrm{p2}} - L\right)\mathbf{m}, \tag{A.27}$$

provided $\lambda_{\mathrm{p2}}(\theta) < L$. Then the total force on pole p2 is given

$$\mathbf{F}_{\mathrm{p2}} = \mathbf{F}_{\mathrm{p2}}^{\mathrm{Pull}} + \mathbf{F}_{\mathrm{p2}}^{R}. \tag{A.28}$$

We note that similarly

$$\mathbf{F}_{\mathrm{p1}} = \mathbf{F}_{\mathrm{p1}}^{\mathrm{Pull}} + \mathbf{F}_{\mathrm{p1}}^{R}, \tag{A.29}$$

with $\mathbf{F}_{\mathrm{p1}}^{\mathrm{Pull}}$ and $\mathbf{F}_{\mathrm{p1}}^{R}$ are as in (A.26) and (A.27) except with λ_{p1} measured relative to the pole p1. That is,

$$\mathbf{F}_{\mathrm{p1}}^{\mathrm{Pull}} = N_{\rho}\int_{s_{\mathrm{p1},-}}^{s_{\mathrm{p1},+}} \mathrm{d}s \int_{0}^{\bar{y}_{\max}} \mathrm{d}\bar{y}\bar{P}_{\mathrm{p1,b}}\bar{y}\mathbf{m}, \tag{A.30}$$

where the integral limits have changed in order to integrate over the microtubule fan emanating from pole p1. Similarly,

$$\mathbf{F}_{\mathrm{p1}}^{\mathrm{R}} = K\int_{s_{\mathrm{p1},-}}^{s_{\mathrm{p1},+}} \mathrm{d}\theta\left(\lambda_{\mathrm{p1}} - L\right)\mathbf{m}. \tag{A.31}$$

Thus, we have that

$$\begin{aligned} l\mathsf{D}\cdot\mathbf{R}_{\mathrm{s},\bar{t}} = K&\left(\int_{s_{\mathrm{p1},-}}^{s_{\mathrm{p1},+}} \mathrm{d}s\left(\lambda_{\mathrm{p1}} - L\right)\mathbf{m} + \int_{s_{\mathrm{p2},-}}^{s_{\mathrm{p2},+}} \mathrm{d}s\left(\lambda_{\mathrm{p2}} - L\right)\mathbf{m}\right) \\ &+ N_{\rho}\left(\int_{s_{\mathrm{p1},-}}^{s_{\mathrm{p1},+}}\mathrm{d}s\int_{0}^{\bar{y}_{\max}}\mathrm{d}\bar{y}\bar{P}_{\mathrm{p1,b}}\bar{y}\mathbf{m} + \int_{s_{\mathrm{p2},-}}^{s_{\mathrm{p1},+}}\mathrm{d}s\int_{0}^{\bar{y}_{\max}}\mathrm{d}\bar{y}\bar{P}_{\mathrm{p2,b}}\bar{y}\mathbf{m}\right). \end{aligned} \tag{A.32}$$

By (A.14) and (A.17), the angular equation of motion is given

$$\begin{aligned} \mu_{\mathrm{D}}\phi_{\bar{t}} = l\mathbf{Z}\cdot&\left(-K\left(\int_{s_{\mathrm{p1},-}}^{s_{\mathrm{p1},+}} \mathrm{d}s\left(\lambda_{\mathrm{p1}} - L\right)\mathbf{n}\times\mathbf{m} - \int_{s_{\mathrm{p2},-}}^{s_{\mathrm{p2},+}} \mathrm{d}s\left(\lambda_{\mathrm{p2}} - L\right)\mathbf{n}\times\mathbf{m}\right)\right. \\ &\left.-N_{\rho}\left(\int_{s_{\mathrm{p1},-}}^{s_{\mathrm{p1},+}}\mathrm{d}s\int_{0}^{\bar{y}_{\max}}\mathrm{d}\bar{y}\bar{P}_{\mathrm{p1,b}}\bar{y}\mathbf{n}\times\mathbf{m} - \int_{s_{\mathrm{p2},-}}^{s_{\mathrm{p2},+}}\mathrm{d}s\int_{0}^{\bar{y}_{\max}}\mathrm{d}\bar{y}\bar{P}_{\mathrm{p2,b}}\bar{y}\mathbf{n}\times\mathbf{m}\right).\right) \end{aligned} \tag{A.33}$$

Now that we have extended our 1D model to 2D, we apply the reduction to ODEs used in Chapter 5 to produce an easily solvable system of equations from (A.25), (A.32) and (A.33).

A.2 Reduction of the 2D model to ordinary differential equations

Following the methods used in Chapter 5 we re-scale by writing $\bar{t} = \tilde{t}/\bar{\omega}_{\text{on}}$ and $\mathbf{R}_{\text{s}} = \tilde{\mathbf{R}}_{\text{s}}/\bar{\omega}_{\text{on}}$, $\phi = \tilde{\phi}/\bar{\omega}_{\text{on}}$. All re-scaled parameters will now be denoted with tildes. Then we rewrite (A.25) as

$$\bar{\omega}_{\text{on}}\bar{P}_{\text{p}i,\text{u},\tilde{t}} = -\bar{\omega}_{\text{on}}\bar{P}_{\text{p}i,\text{u}} + \bar{\omega}_0 e^{\gamma\bar{y}}\bar{P}_{\text{p}i,\text{b}} - \Gamma\left(-\bar{y}\bar{P}_{\text{p}i,\text{u}} - \beta\bar{P}_{\text{p}i,\text{u},\bar{y}}\right)_{\bar{y}} \tag{A.34a}$$

$$\bar{\omega}_{\text{on}}\bar{P}_{\text{p}i,\text{b},\bar{t}} = \bar{\omega}_{\text{on}}\bar{P}_{\text{p}i,\text{u}} - \bar{\omega}_0 e^{\gamma\bar{y}}\bar{P}_{\text{p}i,\text{b}} - \left(\bar{v}_{\text{p}i,\text{b}}\bar{P}_{\text{p}i,\text{b}} - \alpha\bar{P}_{\text{p}i,\text{b},\bar{y}}\right)_{\bar{y}} \tag{A.34b}$$

at fixed arclength s. Additionally, the equations of motion (A.32) and (A.33) are rescaled as

$$\begin{aligned} l\mathsf{D}\cdot\tilde{\mathbf{R}}_{\text{s},\tilde{t}} = \frac{K}{\bar{\omega}_{\text{on}}}&\left(\int_{s_{\text{p1},-}}^{s_{\text{p1},+}} \mathrm{d}s\left(\tilde{\lambda}_{\text{p1}} - \tilde{L}\right)\mathbf{m} + \int_{s_{\text{p2},-}}^{s_{\text{p2},+}} \mathrm{d}s\left(\tilde{\lambda}_{\text{p2}} - \tilde{L}\right)\mathbf{m}\right) \\ &+ \frac{N_\rho}{\bar{\omega}_{\text{on}}}\left(\int_{s_{\text{p1},-}}^{s_{\text{p1},+}}\mathrm{d}s\int_0^{\bar{y}_{\text{max}}}\mathrm{d}\bar{y}\bar{P}_{\text{p1,b}}\bar{y}\mathbf{m} + \int_{s_{\text{p2},-}}^{s_{\text{p2},+}}\mathrm{d}s\int_0^{\bar{y}_{\text{max}}}\mathrm{d}\bar{y}\bar{P}_{\text{p2,b}}\bar{y}\mathbf{m}\right) \end{aligned} \tag{A.35}$$

and

$$\begin{aligned} \mu_{\text{D}}\tilde{\phi}_{\tilde{t}} = \frac{\tilde{l}}{\bar{\omega}_{\text{on}}}\mathbf{Z}\cdot&\left(-\frac{K}{\bar{\omega}_{\text{on}}}\left(\int_{s_{\text{p1},-}}^{s_{\text{p1},+}}\mathrm{d}s\left(\tilde{\lambda}_{\text{p1}} - \tilde{L}\right)\mathbf{n}\times\mathbf{m} - \int_{s_{\text{p2},-}}^{s_{\text{p2},+}}\mathrm{d}s\left(\tilde{\lambda}_{\text{p2}} - \tilde{L}\right)\mathbf{n}\times\mathbf{m}\right)\right. \\ &\left.-\frac{N_\rho}{\bar{\omega}_{\text{on}}}\left(\int_{s_{\text{p1},-}}^{s_{\text{p1},+}}\mathrm{d}s\int_0^{\bar{y}_{\text{max}}}\mathrm{d}\bar{y}\bar{P}_{\text{p1,b}}\bar{y}\mathbf{n}\times\mathbf{m} - \int_{s_{\text{p2},-}}^{s_{\text{p2},+}}\mathrm{d}s\int_0^{\bar{y}_{\text{max}}}\mathrm{d}\bar{y}\bar{P}_{\text{p2,b}}\bar{y}\mathbf{n}\times\mathbf{m}\right)\right). \end{aligned} \tag{A.36}$$

We again assume that $\alpha^{1/2}$, $\beta^{1/2}$ are small parameters such that $\bar{P}_{\text{p}i,\text{b}}$ and $\bar{P}_{\text{p}i,\text{u}}$ are strongly peaked about $\bar{y}_{\text{c}} = 1 + \tilde{\lambda}_{\tilde{t}}$ and $\bar{y}_{\text{c}} = 0$ respectively within regions I and III in $\bar{y}$ space (Figure 4.8H)

For $\bar{\omega}_{\text{on}} \sim \bar{\omega}_0 \ll 1$, we assume that the expressions for $\bar{P}^{\pm}_{\text{b(u)}}$ determined in Chapter 5 hold similarly for $\bar{P}_{\text{p}i,\text{b(u)}}$. That is, we may write $\bar{P}_{\text{p}i,\text{b}} = \bar{P}_{\text{p}i,\text{b0}} + \bar{\omega}_{\text{on}}\bar{P}_{\text{p}i,\text{b1}} + ...$, with

$$\bar{P}_{\text{p}i,\text{b0}} = B_{\text{p}i}\left(\tilde{t}, s\right)e^{\left(-\frac{1}{2\alpha}\left(\bar{y}-\bar{y}_{\text{c}}+\bar{\omega}_{\text{on}}\tilde{\lambda}_{\text{p}i,\tilde{t}\tilde{t}}\right)^2\right)} \tag{A.37}$$

for $B_{\text{p}i}$ the amplitude of the peak of the bound probability density function at arclength s

(subject to small corrections). Similarly, $\bar{P}_{\mathrm{p}i,\mathrm{u}} = \bar{P}_{\mathrm{p}i,\mathrm{u}0} + \bar{\omega}_{\mathrm{on}}\bar{P}_{\mathrm{p}i,\mathrm{u}1} + ...$, with

$$\bar{P}_{\mathrm{p}i,\mathrm{u}0} = A_{\mathrm{p}i}\left(\tilde{t}, s\right) e^{-\frac{1}{2\beta}\bar{y}^2} \tag{A.38}$$

for $A_{\mathrm{p}i}$ the amplitude of the peak of the unbound probability density function at arclength s (subject to small corrections). It follows by the methodology in Chapter 5 that

$$\left(1 + \rho e^{\gamma\left(1+\tilde{\lambda}_{\mathrm{p}i,\tilde{t}}\right)}\right)\hat{B}_{\mathrm{p}i} + 2\hat{B}_{\mathrm{p}i,\tilde{t}} = 1 \tag{A.39}$$

at fixed arclength s for $\hat{B}_{\mathrm{p}i} = \sqrt{2\pi\alpha}B_{\mathrm{p}i}$.

Inserting $\bar{P}_{\mathrm{p}i,\mathrm{b}} = \bar{P}_{\mathrm{p}i,\mathrm{b}0} + \bar{\omega}_{\mathrm{on}}\bar{P}_{\mathrm{p}i,\mathrm{b}1} + ...$ into (A.35) requires the evaluation of

$$\int_0^{\bar{y}_{\max}} \mathrm{d}\bar{y}\bar{P}_{\mathrm{p}i,\mathrm{b}0}\bar{y} \approx \int_0^{\infty} \mathrm{d}\bar{y}B_{\mathrm{p}i}e^{\left(-\frac{1}{2\alpha}(\bar{y}-\bar{y}_{\mathrm{c}})^2\right)}\bar{y} \tag{A.40}$$

where we assume that $\bar{y}_{\max}$ is sufficiently large that it exceeds the bounds of region III, where $\bar{P}_{\mathrm{p}i,\mathrm{b}0}$ is of significant value, and can thus be taken as $\bar{y}_{\max} \to \infty$. Setting $\bar{y} = \bar{y}_{\mathrm{c}} + \alpha^{1/2}\hat{Y}$, then

$$\int_0^{\infty} \mathrm{d}\bar{y}B_{\mathrm{p}i}e^{\left(-\frac{1}{2\alpha}(\bar{y}-\bar{y}_{\mathrm{c}})^2\right)}\bar{y} \approx \int_{-\infty}^{\infty} \mathrm{d}\hat{Y}B_{\mathrm{p}i}e^{\left(-\frac{1}{2}\hat{Y}^2\right)}\alpha^{1/2}\left(\bar{y}_{\mathrm{c}} + \alpha^{1/2}\hat{Y}\right), \tag{A.41}$$

which to leading order becomes

$$\int_{-\infty}^{\infty} \mathrm{d}\hat{Y}B_{\mathrm{p}i}e^{\left(-\frac{1}{2}\hat{Y}^2\right)}\alpha^{1/2}\left(\bar{y}_{\mathrm{c}} + \alpha^{1/2}\hat{Y}\right) \approx \alpha^{1/2}\bar{y}_{\mathrm{c}}B_{\mathrm{p}i}\int_{-\infty}^{\infty} \mathrm{d}\hat{Y}e^{\left(-\frac{1}{2}\hat{Y}^2\right)} = \bar{y}_{\mathrm{c}}B_{\mathrm{p}i}\sqrt{2\pi\alpha} \tag{A.42}$$

with $\bar{y}_{\mathrm{c}} = 1 + \tilde{\lambda}_{\mathrm{p1(p2)},\tilde{t}}$. Then recalling $\hat{B}_{\mathrm{p}i} = \sqrt{2\pi\alpha}B_{\mathrm{p}i}$,

$$\bar{y}_{\mathrm{c}}B_{\mathrm{p}i}\sqrt{2\pi\alpha} = \left(1 + \tilde{\lambda}_{\mathrm{p1(p2)},\tilde{t}}\right)\hat{B}_{\mathrm{p}i} \tag{A.43}$$

and (A.35) becomes

$$\begin{aligned} l\mathsf{D}\cdot\tilde{\mathbf{R}}_{\mathrm{s},\tilde{t}} = \frac{K}{\bar{\omega}_{\mathrm{on}}}&\left(\int_{s_{\mathrm{p1},-}}^{s_{\mathrm{p1},+}} \mathrm{d}s\left(\tilde{\lambda}_{\mathrm{p1}} - \tilde{L}\right)\mathbf{m} + \int_{s_{\mathrm{p2},-}}^{s-\mathrm{p2},+} \mathrm{d}s\left(\tilde{\lambda}_{\mathrm{p2}} - \tilde{L}\right)\mathbf{m}\right) \\ &+ \frac{N_\rho}{\bar{\omega}_{\mathrm{on}}}\left(\int_{s_{\mathrm{p1},-}}^{s_{\mathrm{p1},+}} \mathrm{d}s\left(1 + \tilde{\lambda}_{\mathrm{p1},\tilde{t}}\right)\hat{B}_{\mathrm{p1}}\mathbf{m} + \int_{s_{\mathrm{p2},-}}^{s-\mathrm{p2},+} \mathrm{d}s\left(1 + \tilde{\lambda}_{\mathrm{p2},\tilde{t}}\right)\hat{B}_{\mathrm{p2}}\mathbf{m}\right) \end{aligned} \tag{A.44}$$

and similarly (A.36) becomes

$$\mu_{\mathrm{D}}\tilde{\phi}_{\tilde{t}} = \frac{\tilde{l}}{\bar{\omega}_{\mathrm{on}}}\mathbf{Z}\cdot\left(-\frac{K}{\bar{\omega}_{\mathrm{on}}}\left(\int_{s_{\mathrm{p1},-}}^{s_{\mathrm{p1},+}} \mathrm{d}s\left(\tilde{\lambda}_{\mathrm{p1}} - \tilde{L}\right)\mathbf{n}\times\mathbf{m} - \int_{s_{\mathrm{p2},-}}^{s-\mathrm{p2},+} \mathrm{d}s\left(\tilde{\lambda}_{\mathrm{p2}} - \tilde{L}\right)\mathbf{n}\times\mathbf{m}\right)\right.$$

$$-\frac{N_\rho}{\bar{\omega}_{\text{on}}}\left(\int_{s_{\text{p1},-}}^{s_{\text{p1},+}} \mathrm{d}s\left(1+\tilde{\lambda}_{\text{p1},\tilde{t}}\right)\hat{B}_{\text{p1}}\mathbf{n}\times\mathbf{m}-\int_{s_{\text{p2},-}}^{s-\text{p2},+} \mathrm{d}s\left(1+\tilde{\lambda}_{\text{p2},\tilde{t}}\right)\hat{B}_{\text{p2}}\mathbf{n}\times\mathbf{m}\right)\right). \tag{A.45}$$

Therefore, solving equations (A.39), (A.44) and (A.45) along with initial conditions $\tilde{\phi}_0$, $\tilde{\mathbf{R}}_{\text{s0}}$ and $B_0^{\text{p1(p2)}}(s)$ should result in 2D dynamics of the mitotic spindle.